

Thèse

# A Molecular Dynamics Approach to Nano-scale Lubrication

Présentée devant

L'Institut National des Sciences Appliquées de Lyon

Pour obtenir

Le grade de Docteur

Formation doctorale : Mécanique

Ecole doctorale : Mécanique, Energétique, Génie civil, Acoustique (MEGA)

Par

**Hassan Berro**

(Ingénieur)

Soutenue le 11 Octobre 2010 devant la commission d'examen

Jury MM.

---

Examineur	L. Bocquet	Professeur (Université Claude Bernard Lyon 1)
Examineur	P. Chantrenne	Professeur (INSA de Lyon)
Co-directeur	N. Fillot	Maître de Conférences (INSA de Lyon)
Rapporteur	J. F. Molinari	Professeur (EPFL, Suisse)
Rapporteur	S. Sinnott	Professeur (University of Florida, USA)
Directeur	P. Vergne	Directeur de recherche (CNRS – INSA de Lyon)
Invité	M. Zaccheddu	Ingénieur de recherche Ph.D. (SKF ERC, Pays-Bas)

---

Laboratoire de recherche : Laboratoire de Mécanique des Contacts et des Structures  
(LaMCoS, INSA – Lyon CNRS UMR 5259)



**INSA Direction de la Recherche - Ecoles Doctorales - Quadriennal  
2007-2010**

<b>SIGLE</b>	<b>ECOLE DOCTORALE</b>	<b>NOM ET COORDONNEES DU RESPONSABLE</b>
<b>CHIMIE</b>	<b>CHIMIE DE LYON</b> <a href="http://sakura.cpe.fr/ED206">http://sakura.cpe.fr/ED206</a>  M. Jean Marc LANCELIN  Insa : R. GOURDON	M. Jean Marc LANCELIN Université Claude Bernard Lyon 1 Bât CPE 43 bd du 11 novembre 1918 69622 VILLEURBANNE Cedex Tél : 04.72.43 13 95 Fax : lancelin@hikari.cpe.fr
<b>E.E.A.</b>	<b>ELECTRONIQUE, ELECTROTECHNIQUE, AUTOMATIQUE</b> <a href="http://www.insa-lyon.fr/eea">http://www.insa-lyon.fr/eea</a> M. Alain NICOLAS Insa : C. PLOSSU ede2a@insa-lyon.fr Secrétariat : M. LABOUNE AM. 64.43 – Fax : 64.54	M. Alain NICOLAS Ecole Centrale de Lyon Bâtiment H9 36 avenue Guy de Collongue 69134 ECULLY Tél : 04.72.18 60 97 Fax : 04 78 43 37 17 eea@ec-lyon.fr Secrétariat : M.C. HAVGOUDOUKIAN
<b>E2M2</b>	<b>EVOLUTION, ECOSYSTEME, MICROBIOLOGIE, MODELISATION</b> <a href="http://biomserv.univ-lyon1.fr/E2M2">http://biomserv.univ-lyon1.fr/E2M2</a>  M. Jean-Pierre FLANDROIS Insa : H. CHARLES	M. Jean-Pierre FLANDROIS CNRS UMR 5558 Université Claude Bernard Lyon 1 Bât G. Mendel 43 bd du 11 novembre 1918 69622 VILLEURBANNE Cédex Tél : 04.26 23 59 50 Fax 04 26 23 59 49 06 07 53 89 13 e2m2@biomserv.univ-lyon1.fr
<b>EDISS</b>	<b>INTERDISCIPLINAIRE SCIENCES- SANTÉ</b>  Sec : Safia Boudjema M. Didier REVEL Insa : M. LAGARDE	M. Didier REVEL Hôpital Cardiologique de Lyon Bâtiment Central 28 Avenue Doyen Lépine 69500 BRON Tél : 04.72.68 49 09 Fax :04 72 35 49 16 Didier.revel@creatis.uni-lyon1.fr
<b>INFOMATHS</b>	<b>INFORMATIQUE ET MATHEMATIQUES</b> <a href="http://infomaths.univ-lyon1.fr">http://infomaths.univ-lyon1.fr</a> M. Alain MILLE	M. Alain MILLE Université Claude Bernard Lyon 1 LIRIS - INFOMATHS Bâtiment Nautibus 43 bd du 11 novembre 1918 69622 VILLEURBANNE Cedex Tél : 04.72. 44 82 94 Fax 04 72 43 13 10 infomaths@bat710.univ-lyon1.fr - alain.mille@liris.cnrs.fr
<b>Matériaux</b>	<b>MATERIAUX DE LYON</b>  M. Jean Marc PELLETIER  Secrétariat : C. BERNAVON 83.85	M. Jean Marc PELLETIER INSA de Lyon MATEIS Bâtiment Blaise Pascal 7 avenue Jean Capelle 69621 VILLEURBANNE Cédex Tél : 04.72.43 83 18 Fax 04 72 43 85 28 Jean-marc.Pelletier@insa-lyon.fr
<b>MEGA</b>	<b>MECANIQUE, ENERGETIQUE, GENIE CIVIL, ACOUSTIQUE</b>  M. Jean Louis GUYADER  Secrétariat : M. LABOUNE PM : 71.70 –Fax : 87.12	M. Jean Louis GUYADER INSA de Lyon Laboratoire de Vibrations et Acoustique Bâtiment Antoine de Saint Exupéry 25 bis avenue Jean Capelle 69621 VILLEURBANNE Cedex Tél :04.72.18.71.70 Fax : 04 72 43 72 37 mega@lva.insa-lyon.fr
<b>ScSo</b>	<b>ScSo*</b>  M. OBADIA Lionel  Insa : J.Y. TOUSSAINT	M. OBADIA Lionel Université Lyon 2 86 rue Pasteur 69365 LYON Cedex 07 Tél : 04.78.77.23.88 Fax : 04.37.28.04.48 Lionel.Obadia@univ-lyon2.fr

\*ScSo : Histoire, Géographie, Aménagement, Urbanisme, Archéologie, Science politique, Sociologie, Anthropologie



---

## **A Molecular Dynamics Approach to Nano-scale Lubrication**

### **Abstract**

---

A numerical approach based on Molecular Dynamics simulations was developed in the purpose of investigating the local mechanisms of lubrication at nano-scales. The model elements were introduced and characterized in order to yield the most realistic material and interfacial properties of the contact. Due to their tight relationship with friction at the nanometre scale, the energetic dissipation methods used in molecular dynamics were revisited and guidelines were set for choosing a correct dissipation method for a variety of operating conditions. Moreover, a novel method combining physical relevance and simplicity was introduced for studying heat dissipation in the high-shear regime.

The model was then employed to investigate the effects related to the molecular structure of the surfaces and that of the confined lubricant. On one hand, for studying different tribological surfaces, an original method was used to quantitatively measure the physical adsorption and corrugation potentials. These properties directly influence the structuring and boundary flow in confined films. On the other hand, the influence of lubricant molecular shape and molecular mixing on the tribological performance was investigated for both wetting and non-wetting surfaces. The simulations allowed local analysis of lubricated friction to be performed from the molecular scale and thus a better understanding of the physical interaction between the involved elements.

Keywords: tribology, friction, lubrication, energy dissipation, molecular dynamics.

---

## **Une Approche Dynamique Moléculaire de la Lubrification à l'Echelle Nanométrique**

### **Résumé**

---

Une approche numérique basée sur des simulations Dynamique Moléculaire a été développée dans le but d'étudier les mécanismes locaux de la lubrification à l'échelle nanométrique. Les éléments du modèle ont été présentés et caractérisés afin de reproduire les propriétés les plus réalistes des matériaux et de l'interface du contact. En raison de leur relation étroite avec le frottement, les méthodes de dissipation énergétique pour la dynamique moléculaire ont été revisitées et des recommandations ont été proposées pour le choix d'une méthode correcte adaptée aux différentes conditions opératoires. Pour le régime de fort cisaillement et donc de forte dissipation, une nouvelle méthode mieux fondée physiquement a été développée, combinant simplicité et vitesse de calcul.

Le modèle a ensuite été utilisé pour étudier les effets liés à la structure moléculaire des surfaces et du lubrifiant confiné. Afin d'étudier différentes surfaces tribologiques, une méthode originale a été utilisée pour mesurer quantitativement les potentiels physiques d'adsorption et de corrugation. Ces propriétés influencent directement la stratification dans le film et son glissement à l'interface solide. D'autre part, l'influence de la forme moléculaire du lubrifiant sur sa performance tribologique a été étudiée, en solution pure et en mélange, pour les surfaces mouillantes et non-mouillantes. Les simulations moléculaires ont permis une analyse locale du frottement lubrifié à l'échelle moléculaire et ainsi une meilleure compréhension des interactions physiques entre les éléments mis en jeu.

Mots clés : tribologie, frottement, lubrification, dissipation d'énergie, dynamique moléculaire.



# Preface

---

This thesis is submitted in partial fulfillment for the requirements of a Ph.D. degree in mechanical engineering from the “Institut National des Sciences Appliquées” (INSA) de Lyon. The contained research has been carried out from September 2007 to August 2010 at the Contacts and Structural Mechanics laboratory (LaMCoS) of CNRS and INSA de Lyon.

I would like to start by expressing my gratitude to the French Ministry of National Education and Scientific Research for their financial support during the whole duration of my Ph.D. I am sincerely grateful to my two supervisors Drs. Philippe Vergne and Nicolas Fillot. This thesis would certainly have not seen the light without their continuous support and advice on all levels. I also wish to thank the P2CHPD (Pôle de Compétence en Calcul Haute Performance Dédié) and LaMCoS for the computing facilities that were put at my disposition and without which this work would not have been possible.

I would also like to thank the Global Center of Education (GCOE) and especially Prof. Taku Ohara and Ass. Prof. Takashi Tokumasu who welcomed me at the Institute of Fluid Sciences at Tohoku University in Sendai during a two-month internship from September to November 2009 and with whom I had very interesting discussions about advanced simulation methods. Special thanks also go to Drs. Maurizio Zaccheddu and Rihard Pasaribu from SKF who showed interest in my work and provided me with experimental results on the ZDDP additive and invited me to visit the Engineering and Research Center in the Netherlands.

Special thanks go to Prof. Patrice Chantrenne from CETHIL laboratory of INSA-Lyon with whom I had several important discussions on the thermal aspects of MD simulations. I would also like to thank Profs. Susan Sinnott from the University of Florida and Jean-François Molinari from the Ecole Polytechnique Fédérale de Lausanne for accepting to review the manuscript and to be present among the jury for my Ph.D. defense. I am also grateful for Prof. Lydéric Bocquet from Université Claude Bernard for his interest in my research and for accepting to participate in the jury.

I also wish to thank all members of the Lubrication and Lubricants Modeling group of LaMCoS laboratory with whom I shared much more than a workplace. I notably thank Nathalie, Nicolas, and Thomas, my office colleagues as well as Vincent and Fida for all the pleasant moments that we shared. I wish you all the best in your future projects.

Last but certainly not least, I would like to thank all my friends and family for their continuous support. I am extremely grateful for my two big brothers Wissam and Khodor for always

being there for me and Mom and Dad for their sacrifices over the years and their love that keeps amazing me everyday. Thank you for your presence for my Ph.D. defense, no words can express how much this means to me. I also wish to thank my dear Sophie for her continuous encouragement and love during the good as well as difficult moments in the last three years.

# Table of Contents

---

<b>Résumé Etendu</b>	<b>viii</b>
<b>Introduction</b>	<b>viii</b>
<b>0.1 Etat de l'art</b>	<b>x</b>
0.1.1 Introduction	x
0.1.2 Etudes expérimentales	xii
0.1.3 Etudes numériques	xiii
0.1.4 Conclusion	xiv
<b>0.2 Conception du modèle</b>	<b>xv</b>
0.2.1 Introduction	xv
0.2.2 Méthode de la Dynamique Moléculaire	xv
0.2.3 Eléments du modèle	xvi
0.2.4 Initialisation et échantillonnage	xvii
0.2.5 Conclusion	xviii
<b>0.3 Du frottement aux mécanismes de dissipation d'énergie</b>	<b>xix</b>
0.3.1 Bilan énergétique	xix
0.3.2 Algorithmes de thermostat	xx
0.3.3 Début de l'échauffement	xxi
0.3.4 Méthodes avancées de dissipation	xxi
0.3.5 Conclusion	xxii
<b>0.4 Adsorption et corrugation des surfaces</b>	<b>xxiii</b>
0.4.1 Caractérisation physique des surfaces	xxiv
0.4.2 Simulation du cisaillement	xxv
0.4.3 Conclusion	xxvi
<b>0.5 Effet de la structure moléculaire du lubrifiant et de la mouillabilité des surfaces</b>	<b>xxvii</b>
0.5.1 Effet de la longueur de la chaîne moléculaire	xxvii
0.5.2 Effet de la ramification de la chaîne moléculaire	xxviii
0.5.3 Mélanges de lubrifiants non-polaires	xxx
0.5.4 Mélanges de lubrifiants polaires	xxxi
0.5.5 Conclusion	xxxiii
<b>Conclusion générale et perspectives</b>	<b>xxxiv</b>
<b>Nomenclature</b>	<b>xxxvii</b>

<b>Introduction</b>	<b>1</b>
<b>1. State of the art</b>	<b>4</b>
<b>1.1 Tribology: historical review</b>	<b>4</b>
<b>1.2 Lubrication regimes</b>	<b>7</b>
1.2.1 Full film lubrication	7
1.2.2 Mixed lubrication	8
1.2.3 Boundary lubrication	8
<b>1.3 Molecular lubrication</b>	<b>9</b>
1.3.1 Experimental work	10
1.3.1.1 Structuring and solvation force	10
1.3.1.2 Nano-rheology	12
1.3.1.3 Friction curves	15
1.3.1.4 Boundary flow	17
1.3.2 Numerical work	19
1.3.2.1 Simulation methods	20
1.3.2.2 Structural effects and solvation forces	21
1.3.2.3 Nano-rheology	24
1.3.2.4 Boundary flow	27
<b>Conclusion</b>	<b>29</b>
<b>2. Numerical Model of Molecular Lubrication</b>	<b>32</b>
<b>Introduction</b>	<b>32</b>
<b>2.1 Molecular dynamics method</b>	<b>32</b>
2.1.1 Principle	33
2.1.2 Integration methods	33
2.1.2.1 The Verlet algorithm	33
2.1.2.2 Other algorithms	34
2.1.3 Initial conditions	34
<b>2.2 Construction of the molecular lubrication model</b>	<b>34</b>
2.2.1 Model overview	34
2.2.2 Solid surfaces	36
2.2.2.1 Crystalline structure and interactions	36
2.2.2.2 Thermal and mechanical properties	39
2.2.3 Lubricant	42
2.2.3.1 Molecular architecture and interactions	43
2.2.3.2 Dynamic and thermal properties	44
2.2.4 Surface-Lubricant interface	47
<b>2.3 Initialization and sampling</b>	<b>49</b>
2.3.1 Geometry	49
2.3.2 Initial density	50
2.3.3 Compression	51
2.3.4 Shear	52
2.3.5 Sampling effects	53
2.3.5.1 Spatial sampling: system size	53

2.3.5.2 Time sampling: time-step and simulation duration	54
Conclusion	56
<b>3. Friction and Energetic Dissipation Mechanisms</b>	<b>58</b>
<b>Introduction</b>	<b>58</b>
<b>3.1 Energy balance in confined films under shear</b>	<b>59</b>
3.1.1 Energetic path	59
3.1.2 Balance validation in confined shear simulation	61
3.1.3 Cause-effect relationship between friction and thermostat dissipation	63
<b>3.2 Sliding boundary thermostat method</b>	<b>63</b>
3.2.1 Thermostating algorithms	64
3.2.2 Heating onset by shearing	66
<b>3.3 Advanced dissipation methods</b>	<b>68</b>
3.3.1 The Phantom-Molecules method	69
3.3.2 The variable boundary temperature method	71
3.3.2.1 Principle	71
3.3.2.2 Validation	73
3.3.2.3 Temperature update interval	74
3.3.3 Assessment on the dissipation methods	75
<b>Conclusion</b>	<b>76</b>
<b>4. Effect of Surface Adsorption and Corrugation</b>	<b>78</b>
<b>Introduction</b>	<b>78</b>
<b>4.1 Surface characterization</b>	<b>79</b>
4.1.1 Surface scanning method	79
4.1.2 Application to different surface types	81
<b>4.2 Overview of the molecular model</b>	<b>83</b>
<b>4.3 Results and discussion</b>	<b>84</b>
4.3.1 Film structure	84
4.3.2 Boundary flow	85
4.3.3 Apparent shear stress	87
<b>Conclusion</b>	<b>88</b>
<b>5. Effect of lubricant molecular structure and surface wettability</b>	<b>92</b>
<b>Introduction</b>	<b>92</b>
<b>5.1 Effect of molecular chain length</b>	<b>92</b>
5.1.1 Molecular domain	93
5.1.2 Results	94
5.1.2.1 Film structure	94
5.1.2.2 Boundary flow	95
5.1.2.3 Apparent shear stress	96
<b>5.2 Effect of molecular branching</b>	<b>98</b>
5.2.1 Molecular domain	98

5.2.2 Results	99
5.2.2.1 Film structure	99
5.2.2.2 Boundary flow	100
5.2.2.3 Apparent shear stress	101
<b>5.3 Non polar lubricant mixtures</b>	<b>102</b>
5.3.1 Molecular domain	102
5.3.2 Results	103
5.3.2.2 Film structure	103
5.3.2.3 Boundary flow	105
5.3.2.4 Apparent shear stress	106
<b>5.4 Polar lubricant mixtures</b>	<b>107</b>
5.4.1 Molecular domain	107
5.4.2 Molecular migration of ZDDP molecules	109
5.4.3 Effect on the boundary flow and friction	111
<b>Conclusion</b>	<b>112</b>
<b>General conclusion and prospects</b>	<b>115</b>
<b>Appendix 1: Temperature-control Algorithms</b>	<b>118</b>
<b>A1.1 Introduction</b>	<b>118</b>
<b>A1.2 Thermostating algorithms</b>	<b>119</b>
A1.2.1 Velocity-rescaling	119
A1.2.2 Nosé-Hoover algorithm	119
A1.2.3 Langevin algorithm	121
<b>A1.3 Phantom-Molecules method</b>	<b>122</b>
A1.3.1 Scope of applicability	122
A1.3.2 Practical application	122
A1.3.2.1 Primary-Phantom atoms interactions	123
A1.3.2.2 Phantom-Fixed atoms interactions	125
<b>Appendix 2: Heat Conduction in a Semi-infinite Solid with a Constant Boundary Flux</b>	<b>128</b>
<b>A2.1 Introduction</b>	<b>128</b>
<b>A2.2 1-D Heat conduction with constant boundary flux</b>	<b>128</b>
A2.2.1 Integration	129
A2.2.2 Time evolution of the wall temperature	130
<b>A.2.3 Discrete formulation of the boundary temperature change with flux</b>	<b>130</b>
<b>Appendix 3: Calculation methods of macroscopic quantities from microscopic data</b>	<b>132</b>
<b>Introduction</b>	<b>132</b>
<b>A3.1 Characteristic profiles</b>	<b>132</b>
A3.1.1 Lubricant density profile	132
A3.1.2 Lubricant velocity profile	133
A3.1.3 Lubricant temperature profile	134
<b>A3.2 Time-variable quantities</b>	<b>134</b>

A3.2.1 Lubricant film thickness	134
A3.2.2 Lubricant density	135
A3.2.3 Apparent shear rate	135
A3.2.4 Apparent shear stress	135
A3.2.4 Lubricant temperature	136
<b>A3.3 Deduced quantities</b>	<b>136</b>
A3.3.1 Effective shear rate	136
A3.3.2 Effective viscosity	136
<b>References</b>	<b>137</b>
<b>Publications</b>	<b>144</b>



# Résumé Etendu

viii

<b>Introduction</b>	<b>viii</b>
<b>0.1 Etat de l'art</b>	<b>x</b>
0.1.1 Introduction	x
0.1.2 Etudes expérimentales	xii
0.1.3 Etudes numériques	xiii
0.1.4 Conclusion	xiv
<b>0.2 Conception du modèle</b>	<b>xv</b>
0.2.1 Introduction	xv
0.2.2 Méthode de la Dynamique Moléculaire	xv
0.2.3 Eléments du modèle	xvi
0.2.4 Initialisation et échantillonnage	xvii
0.2.5 Conclusion	xviii
<b>0.3 Du frottement aux mécanismes de dissipation d'énergie</b>	<b>xix</b>
0.3.1 Bilan énergétique	xix
0.3.2 Algorithmes de thermostat	xx
0.3.3 Début de l'échauffement	xxi
0.3.4 Méthodes avancées de dissipation	xxi
0.3.5 Conclusion	xxii
<b>0.4 Adsorption et corrugation des surfaces</b>	<b>xxiii</b>
0.4.1 Caractérisation physique des surfaces	xxiv
0.4.2 Simulation du cisaillement	xxv
0.4.3 Conclusion	xxvi
<b>0.5 Effet de la structure moléculaire du lubrifiant et de la mouillabilité des surfaces</b>	<b>xxvii</b>
0.5.1 Effet de la longueur de la chaîne moléculaire	xxvii
0.5.2 Effet de la ramification de la chaîne moléculaire	xxviii
0.5.3 Mélanges de lubrifiants non-polaires	xxx
0.5.4 Mélanges de lubrifiants polaires	xxxi
0.5.5 Conclusion	xxxiii
<b>Conclusion générale et perspectives</b>	<b>xxxiv</b>

# Résumé Etendu

---

## Introduction

Le frottement est la force résistante au mouvement relatif de deux corps en contact. Sans le frottement, nous ne serions pas en mesure d'accomplir de nombreuses tâches simples comme tenir debout et marcher, se raser, se brosser les dents, s'habiller, faire du feu en frottant deux bâtons l'un contre l'autre, ou même démarrer et arrêter nos voitures. Une vie sans frottement est certainement difficile à imaginer, mais une vie avec un frottement maîtrisé est sans aucun doute l'un des buts ultimes de la technologie moderne.

Une part importante de la recherche en ingénierie vise à optimiser l'efficacité énergétique des technologies qui opèrent sur des sources non renouvelables d'énergie telles que les produits électroménagers ou les dispositifs de transport. Ces produits génèrent de l'énergie mécanique sous forme de mouvement. Malheureusement, dès que le mouvement apparaît, le frottement intervient. La perte d'énergie due au frottement entre les composants mécaniques compte pour la plus grande part du total des pertes énergétiques. Ce phénomène a donc un impact non négligeable sur les deux plans, économique et environnemental.

La lubrification vise à réduire les pertes qui sont dues au contact direct entre les corps solides et à améliorer la longévité des composants mécaniques. Le principe est simple : en ajoutant un lubrifiant (solide, liquide ou gaz) pour séparer les surfaces en contact, les effets négatifs du frottement sec, tels que l'adhérence et l'usure, peuvent être évités. Le frottement se produisant en présence de lubrifiant est notamment inférieur à celui produit entre les deux mêmes surfaces en contact sec. En même temps, un compromis est recherché entre la performance tribologique des lubrifiants et leur effet secondaire sur l'environnement. Comme lubrifiants, les huiles minérales ont des propriétés satisfaisantes dans les applications aux vitesses, pressions et températures modérées de fonctionnement. Toutefois, dans des conditions plus sévères, comme celles affrontées dans les processus d'usinage ou à l'intérieur des moteurs à combustion interne, l'utilisation d'additifs devient indispensable pour garantir les performances tribologiques.

La conception des lubrifiants est confrontée à des défis technologiques croissants, tels que la réduction de la taille des systèmes mécaniques afin de limiter la consommation d'huile à des fins environnementales. Dans les systèmes compacts comme les dispositifs de stockage optique et les micromoteurs, les lubrifiants opèrent souvent sous confinement moléculaire. Sur un autre plan, la présence de films très minces de lubrifiant devient courante même dans des applications classiquement considérées de grande échelle comme les roulements, pour des raisons économiques et environnementales. Dans de telles circonstances et dans les conditions d'exploitation industrielle, des films nanométriques peuvent être facilement trouvés à

l'intérieur des mécanismes au cours du processus normal de marche ou bien pendant des périodes critiques comme la mise en marche ou l'arrêt.

Le travail présenté dans cette thèse porte sur la lubrification moléculaire, où l'épaisseur du fluide de lubrification est de seulement quelques nanomètres. Dans ce genre de contact confiné, les propriétés tribologiques des lubrifiants sont très différentes de celles obtenues dans des contacts de plus grandes dimensions. Elles dépendent des effets qui se produisent aux échelles nanoscopiques d'espace et de temps et sont étroitement liées à la structure moléculaire et aux interactions entre les molécules de lubrifiant et les surfaces. Une approche numérique exploitant des simulations en dynamique moléculaire est utilisée dans cette thèse pour accéder aux mécanismes locaux de la lubrification sous confinement sévère. Parmi les effets considérés, on s'intéresse aux propriétés physiques des surfaces comme la corrugation et l'adsorption ainsi qu'à la structure moléculaire du lubrifiant. Un autre effet de grande importance concerne les mécanismes de transformation de l'énergie mécanique en chaleur par le frottement et sa dissipation subséquente dans le contact.

Le manuscrit commence par une revue de l'état de l'art. Les phénomènes particuliers se produisant dans les films confinés comprennent la stratification et la solidification du film et le glissement aux parois. La compréhension récente de ces phénomènes, grâce aux techniques expérimentales et numériques, offre une base solide pour l'interprétation des résultats des simulations présentés dans le reste de la thèse.

Un modèle numérique de la lubrification moléculaire est développé en se basant sur la méthode de la dynamique moléculaire. Ce modèle permet de modéliser un large choix de surfaces tribologiques et de lubrifiants réalistes. Le modèle est paramétré pour reproduire les propriétés thermiques et mécaniques des surfaces, du lubrifiant ainsi que de leur interface.

La dissipation d'énergie est étroitement liée au frottement. Cette problématique essentielle pour l'étude de la lubrification est donc discutée en détail. Pour différentes conditions opératoires, des recommandations sont données pour le choix correct de la méthode de dissipation de l'énergie. Pour les cas fortement cisailés, une nouvelle méthode est également présentée, qui permet de modéliser la dissipation de chaleur de façon réaliste.

Le modèle est ensuite exploité pour étudier plusieurs effets moléculaires se produisant dans les films confinés. Dans un premier temps, on considère l'effet de la structure atomique des surfaces sur la structuration et le glissement du fluide aux parois. Ensuite, on étudie la relation entre la structure moléculaire du lubrifiant et sa performance tribologique pour les deux cas typiques des surfaces mouillantes et non mouillantes.

Enfin, la conclusion générale récapitule les idées principales évoquées dans le manuscrit, les principaux résultats présentés tout au long des différentes sections, et enfin des suggestions pour les travaux futurs.

## 0.1 Etat de l'art

### 0.1.1 Introduction

Il ne fait aucun doute que l'Homme a pensé au frottement et aux moyens de le réduire depuis très longtemps [1, 2, 3]. En fait, les premiers systèmes mécaniques (bois/pierre) datent de 4000 ans avant J.-C. et certains ont été effectivement lubrifiés avec des graisses animales. Dans l'histoire documentée des dernières années, l'étude du frottement a été limitée à la conception des machines. Ce ne fut que rarement, jusqu'à récemment, un sujet tiré de façon indépendante par les chercheurs. C'est peut-être en raison des complexités qui surgissent dues à la nature multi-physique des mécanismes de frottement. Toutefois, avec la révolution industrielle est venu le développement des machines lourdement chargées et comportant des liaisons mécaniques plus que jamais complexes. Elle a ainsi introduit un besoin essentiel pour l'analyse sérieuse du frottement, de l'usure et de la lubrification. La maîtrise des pertes dues au frottement contribue non seulement à la durée de vie des éléments de machines, mais aussi à la fiabilité et à la productivité des filières industrielles complètes.

Les premiers travaux sur le frottement lubrifié ont été réalisés par Hirn en 1847. Il a étudié expérimentalement l'évolution du coefficient de frottement sous charge constante et vitesse variable, dans les deux cas des contacts secs et lubrifiés. Pour le cas lubrifié, il a pu constater que le coefficient de frottement augmente proportionnellement à la vitesse ; un résultat rejeté par la communauté scientifique de l'époque en raison de son apparent conflit avec la troisième loi de frottement (pour un coefficient de frottement constant). Ces résultats ont cependant montré qu'une nouvelle analyse était nécessaire pour étudier les contacts entièrement lubrifiés.

En 1886, Reynolds a proposé sa théorie de la lubrification hydrodynamique en réduisant les équations générales de la dynamique des fluides (équations de Navier-Stokes) au problème de lubrification en couche mince [4]. Reynolds a discuté les origines physiques de la pression hydrodynamique qui se développe dans des paliers lubrifiés; une constatation expérimentale par Tower en 1883. Il a également expliqué que, dans certains cas de cisaillement élevés et tandis que le lubrifiant sépare complètement les surfaces, le coefficient de frottement ne devient plus proportionnel à la vitesse à cause des effets thermiques qui influencent la résistance à l'écoulement du lubrifiant.

La théorie hydrodynamique de Reynolds a été la pierre angulaire de la plupart des recherches au cours du dernier siècle. Des solutions théoriques de l'équation de Reynolds ont été proposées pour de nombreux systèmes simples et cela a eu un grand impact sur la conception des paliers et roulements. Sur le plan expérimental, un schéma récapitulatif de différents régimes de lubrification a été proposé par Stribeck en 1902, basé sur ses expériences approfondies sur des paliers lubrifiés. La courbe de Stribeck (Fig. 0.1) montre que le frottement dépend de la nature du lubrifiant, de la charge normale et de la vitesse. Dans des conditions opératoires sévères, une transition se produit à partir de la lubrification hydrodynamique, avec une séparation complète des surfaces et un frottement relativement faible, à la lubrification limite où la charge devient supportée par les aspérités en contact et non plus par la pression hydrodynamique au sein du lubrifiant. Un régime de lubrification mixte existe entre ces deux extrémités. Dans ce régime, la charge est supportée dans certaines

régions par les aspérités déformées et dans d'autres régions par la pression du lubrifiant qui sépare les surfaces en mouvement relatif.

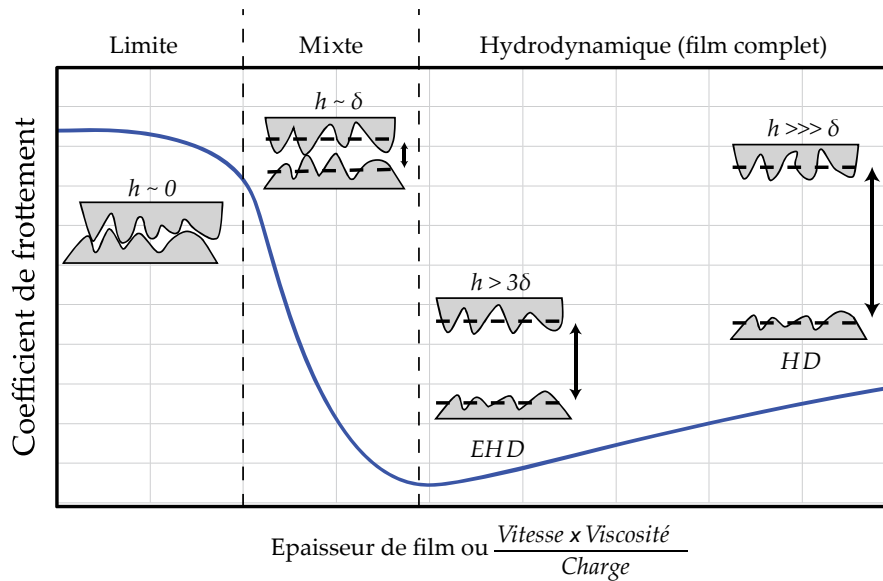


**Fig. 0.1 : Courbe de Stribeck illustrant les trois régimes de lubrification: limite, mixte et hydrodynamique. La transition entre ces régimes dépend de la viscosité du lubrifiant, de la vitesse et de la charge normale.  $\delta$  est la valeur effective de la rugosité des surfaces.**

L'étude du frottement lubrifié peut donc suivre celle du régime de lubrification concerné. Ce dernier dépend du type d'application et des conditions opératoires. Bien que ce point de vue de la lubrification soit largement accepté dans la communauté de tribologues, il reste incapable de prédire même qualitativement le frottement dans les systèmes lubrifiés à l'échelle moléculaire [6]. Les particularités de tels systèmes n'ont été que récemment accessibles par l'expérimentation.

La lubrification moléculaire est le processus consistant à séparer deux surfaces en contact par un lubrifiant dont l'épaisseur est comparable à l'échelle moléculaire (nanomètre). Comme la plupart des surfaces dans les applications d'ingénierie classique ont des rugosités qui s'étendent bien au-delà l'échelle du nanomètre, la lubrification moléculaire idéale existait rarement comme mode unique de lubrification.

Aujourd'hui, la situation a changé. Des applications classiquement lubrifiées par des films épais et complets comme les roulements sont actuellement conçus pour fonctionner avec des films beaucoup plus minces. L'épaisseur du film devient de l'ordre de seulement quelques nanomètres [9]. En outre, l'ensemble des nouvelles technologies évolue autour des techniques de micro fabrication où la connaissance de l'échelle nanométrique est essentielle [10]. Les périphériques de stockage informatique et les dispositifs micromécaniques sont des exemples où la tribologie des revêtements et des lubrifiants confinés à l'échelle moléculaire représente un véritable défi pour leur optimisation et leur maintenance.

L'étude de la lubrification moléculaire a néanmoins été limitée en raison de difficultés d'accès aux échelles caractéristiques des phénomènes moléculaires. En outre, dû à la complexité des effets physiques et chimiques qui interviennent, il est difficile de construire des modèles universels pour les régimes mixtes et limites de la lubrification. Toutefois, grâce à l'évolution récente des méthodes expérimentales et de simulation pouvant désormais accé-

der directement à l'échelle nanométrique, il est devenu possible d'étudier de nombreuses particularités de lubrification moléculaire. Des études expérimentales et numériques ont été en mesure de se compléter mutuellement dans la description des phénomènes moléculaires et donner un aperçu fascinant de ce qui se produit à un lubrifiant sous confinement sévère.

### 0.1.2 Etudes expérimentales

Jusqu'à présent, il a été impossible d'expérimenter la lubrification moléculaire dans les conditions réelles des applications [11]. L'échelle la plus petite de la lubrification qui est accessible est celle d'un contact entre deux aspérités. Cela a été possible grâce au SFA (appareil à force de surface) et à l'AFM (microscope à force atomique). Ces deux appareils permettent d'étudier à l'échelle moléculaire les propriétés statiques (structurelles) et dynamiques des films confinés entre deux aspérités [12].

Sous confinement moléculaire, il est inapproprié de considérer un film lubrifiant comme un domaine continu et sans structure. La raison en est que les surfaces solides peuvent modifier l'ordre à l'intérieur du lubrifiant conduisant à des forces structurelles lorsque elles se rapprochent.

En 1981, Horn et Israelachvili [16], en utilisant le SFA ont trouvé que la force normale entre deux surfaces séparées par un film très mince est oscillatoire. Cette force varie entre attraction et répulsion avec une périodicité égale au diamètre moléculaire du liquide confiné. Ces oscillations décroissent exponentiellement lorsque les surfaces sont éloignées. Ce phénomène est dû à la structuration du film sous forme des couches parallèles aux surfaces solides. Quand la séparation varie, l'énergie libre atteint des maxima et minima successifs, et la force de surface oscille de la même manière.

La littérature rapporte de nombreuses études SFA pour déterminer la forces des surfaces séparées par toutes sortes de liquides : simple polaires [16, 17, 18, 19], non polaires avec des liaisons d'hydrogène [20], des solutions polymères [21], etc. Les principales conclusions sont que la force de surface est insensible à la polarité et à la température, mais est très sensible à la présence d'eau.

En ce qui concerne les propriétés dynamiques de lubrifiants, en 1985 Chan et Horn ont mesuré le taux de drainage des films moléculaires des liquides Newtoniens entre des feuilles lisses de mica [15]. Ils ont trouvé que la viscosité effective augmente dans les films de moins de 10 nm. Cette augmentation en viscosité a aussi été observé par Van Alsten et Granick en 1988 [13] quand la séparation des surface devient plus petite que la longueur de la molécule du fluide confiné. En outre, une forte dépendance de la viscosité de la pression a été signalée. Quand l'épaisseur devient inférieure à 3 couches moléculaires, une transition réversible vers à un état solide est observée. Cet état est caractérisé par une réponse élastique du film au cisaillement.

Enfin, il est fréquent de trouver expérimentalement que les fluides confinés à l'échelle moléculaire glissent aux parois si ils sont forcés au-delà d'une contrainte limite [34-38]. Ce glissement dépend à la fois à la structure moléculaire [34] et de la morphologie de la surface [36, 37]. Les longues molécules ont plus tendance à glisser aux parois que les plus courtes.

L'état de la surface est également un facteur crucial car les fluides ne glissent pas près des surfaces irrégulières [37]. Dans d'autres travaux [31], il est montré que le glissement diminue quand l'épaisseur du film augmente, justifiant ainsi la condition de non glissement dans les films confinés mais à l'échelle macroscopique.

Néanmoins, il existe un autre aspect du glissement aux parois lorsque les films sont confinés à l'échelle moléculaire. Dans certains cas, les couches fluides peuvent adhérer aux surfaces comme cela a été montré par Chan et Horn [15]. Des couches fluides stagnantes à proximité de chaque surface ont été observées dans des films confinés d'épaisseur comprise entre 10 et 50 nm. Le débat reste donc ouvert sur le sujet de l'écoulement à l'interface, en particulier pour les systèmes de taille moléculaire.

### 0.1.3 Etudes numériques

Des études numériques ont été menées pour interpréter et même parfois pour prédire les propriétés des films confinés. La majorité de ces études est fondée sur les méthodes de la mécanique moléculaire : Monte Carlo (MC) et Dynamique Moléculaire (DM).

Les premières simulations [45, 46, 47] ont montré qu'un liquide, adsorbé sur une surface, a une structure très particulière. Les molécules du liquide forment plusieurs couches très bien définies. La densité du fluide à travers le film oscille en fonction de la distance à la surface. En cas de confinement entre deux surfaces, un nombre entier de couches est formé dans la direction parallèle à la surface [49]. Lorsque les deux surfaces s'approchent, le film est compressé jusqu'à ce qu'une couche complète soit évincée. En conséquence, la force entre les surfaces est oscillante et change entre répulsion et attraction.

Des simulations par la dynamique moléculaire ont montré qu'en plus de la structuration normale, un ordre epitaxial (dans le plan) est présent à l'intérieur des couches [55]. Cet ordre dépend de deux facteurs essentiels : la force d'interaction surface-fluide et de la commensurabilité des densités des solides et liquides. La commensurabilité pourrait être définie comme le registre entre les topologies de deux surfaces en contact, quelle que soit les phases concernées. Elle est maximale lorsque les topologies de surface sont similaires.

La nature moléculaire du liquide a également une influence notable sur la structuration des milieux confinés. Bien que les oscillations de la densité sont encore perçues dans le cas de longues molécules tels que les alcanes et les polymères [56, 57], la stratification est plus douce et se dissipe plus vite que dans les fluides composés de molécules sphériques. Finalement, le branchement moléculaire influence également le phénomène de stratification [60, 61, 62]. Les molécules linéaires s'organisent en couches mieux définies que dans le cas de molécules ramifiées.

Quant aux propriétés dynamiques des films confinés, il s'avère que la viscosité effective augmente avec le confinement, en accord avec les expériences [51, 54]. Elle oscille également avec l'épaisseur du film d'une manière analogue à la force de surface et la période de l'oscillation est fonction du diamètre moléculaire [54].

À pression constante, la viscosité augmente de plusieurs ordres de grandeur lorsque l'épaisseur est réduite [53, 66, 67]. Dans les molécules sphériques, cette augmentation de la

viscosité est due à la cristallisation du film [66]. Dans les molécules longues, elle est due à l'établissement de ponts entre les surfaces [67].

A épaisseur constante, la viscosité augmente significativement avec la pression parce que le fluide est amené dans un état plus proche de la transition vitreuse. En outre, à des taux de cisaillement accessibles à la simulation, les liquides se montrent très aminçissants (shear-thinning) et la viscosité apparente suit une loi de puissance quasi universelle [11, 66, 68, 65]. Une viscosité constante se manifeste aux taux de cisaillement faibles. Cette viscosité constante est supérieure à la valeur Newtonienne du fluide non confiné. Quand l'épaisseur du film diminue, ou lorsque la pression augmente, ce plateau de viscosité constante est déplacé vers des taux de cisaillement plus faibles et il atteint des valeurs très importantes [66].

Enfin, la structure des surfaces [63, 65, 64, 71] et leur dynamique [72] influencent également la viscosité effective des films confinés. En frustrant la structuration dans le fluide, l'effet du confinement sur la viscosité devient moins prononcé à proximité des surfaces rugueuses [64, 63].

Parmi les effets moléculaires les plus intéressants observés dans les simulations de films confinés on trouve ceux qui se manifestent à l'interface écoulement - solide. En raison de leur caractère local, il a été difficile d'explorer ces phénomènes directement par l'expérience. Ils sont pourtant cruciaux pour la bonne compréhension et l'interprétation de la dynamique des films confinés. Les facteurs qui influencent l'écoulement à l'interface sont nombreux et varient selon la nature chimique du liquide et celle des surfaces, les interactions entre les deux, la morphologie de la surface, les conditions opératoires et, bien sûr, l'épaisseur du film confiné.

Dès les premières simulations [51, 53] employant des surfaces lisses, un glissement aux parois a toujours été observé. Toutefois, lorsque des surfaces structurées ont été employées, un phénomène inverse d'adhérence à la surface a été remarqué [52]. Le glissement augmente aussi avec la longueur des chaînes moléculaires. Plusieurs études portant sur des alcanes détecte le glissement pour une variété de forces d'interaction [11, 68, 65]. Quant aux molécules ramifiées, leur structure joue un rôle important dans l'augmentation du glissement à l'interface [62]. Près des surfaces souples et rugueuses, ou lorsque la température augmente, le glissement est réduit. D'autre part, lorsque le taux de cisaillement augmente, le glissement augmente.

#### **0.1.4 Conclusion**

Bien que les conditions de l'expérimentation et de la simulation des films confinés à l'échelle moléculaire soient différentes, les simulations ont permis de comprendre de nombreux effets à l'origine des observations expérimentales. L'oscillation des forces de surfaces, la structuration du film, l'augmentation de la viscosité, la solidification du fluide et le glissement à l'interface représentent des phénomènes qui ont été observés dans les expériences et retrouvés dans les simulations. En accédant aux détails des effets locaux, les simulations ont permis d'identifier les vrais facteurs responsables de ces phénomènes. Cette procédure est souvent compliquée, voire impossible, à accomplir par les méthodes expérimentales existantes.

La connaissance de tous les effets reportés dans ce chapitre fournit une base pour comprendre la problématique de la lubrification à l'échelle moléculaire. Dans la section suivante, les détails de la conception d'un modèle de simulation moléculaire dans un cadre thermodynamique bien défini sont présentés.

## 0.2 Conception du modèle

### 0.2.1 Introduction

En général, la modélisation numérique des problèmes physiques est basée sur les théories fondamentales et les équations associées. En lubrification hydrodynamique, par exemple, la modélisation est basée sur la théorie de Reynolds. Toutefois, une telle modélisation continue n'est pas pertinente pour le cas de la lubrification moléculaire, à cause de l'aspect discontinu. La définition des grandeurs thermodynamiques est très délicate dans de tels systèmes et devient encore plus complexe dans des conditions de non équilibre du cisaillement. Heureusement, les modèles numériques qui incluent une description moléculaire explicite sont capables de détecter de nombreux effets à l'échelle locale de la lubrification moléculaire.

La dynamique moléculaire est une méthode de simulation moléculaire de type déterministe. Les trajectoires de toutes les molécules dans un système peuvent être prédites avec précision en utilisant les potentiels d'interactions inter et intra moléculaires.

### 0.2.2 Méthode de la Dynamique Moléculaire

La dynamique moléculaire est basée sur l'application des équations de mouvement de Newton sur tous les atomes qui interagissent dans le système moléculaire. La force agissant sur chaque atome est déterminée comme le gradient de l'énergie potentielle des interactions avec les atomes voisins. L'accélération peut éventuellement être calculée à partir des équations du mouvement.

La connaissance des trajectoires atomiques au cours du temps nécessite la résolution de l'équation différentielle du mouvement. L'approche standard consiste à utiliser des méthodes de différences finies. Étant donné que les positions et la dynamique (vitesses, accélérations, etc.) de tous les atomes sont connues à un instant donné, ces propriétés après un court pas de temps peuvent être déduites avec précision. Les équations différentielles du mouvement de tous les atomes sont donc résolues à chaque pas de temps. Le choix du pas de temps a ainsi une influence directe sur l'exactitude de l'intégration. L'algorithme d'intégration principalement utilisé pour résoudre les équations du mouvement et utilisé dans cette thèse est celui de Verlet.

A l'échelle de la modélisation moléculaire, un système de seulement quelques nanomètres de large dans chaque direction peut être explicitement considéré. Il est donc hors de question de modéliser un contact dans son ensemble avec les zones d'entrée et sortie. Le modèle de lubrification moléculaire construit pour cette thèse se compose d'un lubrifiant

confiné entre deux surfaces comme montré dans la Fig. 0.2. Des conditions périodiques aux limites en  $x$  et  $y$  permettent au modèle élémentaire de se répéter à l'infini dans ces directions.

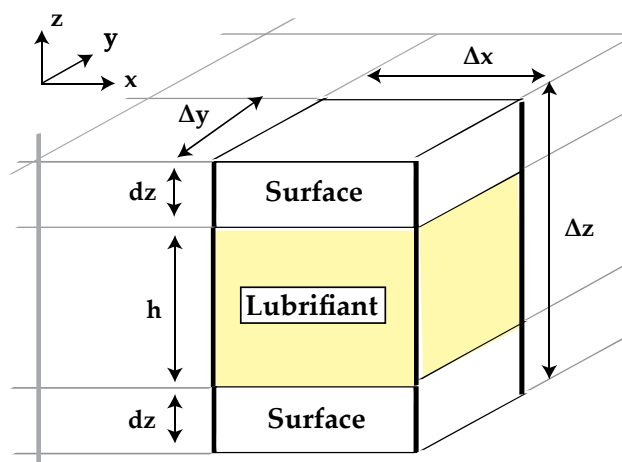


**Fig. 0.2 :** Schéma du modèle de lubrification moléculaire. La boîte de simulation est délimitée par des lignes noires en gras. Les extensions en gris représentent les copies de la boîte de simulation obtenues en appliquant les conditions périodiques.

Les éléments qui constituent le modèle sont étudiés de manière indépendante. Ces éléments comprennent les surfaces solides, le lubrifiant confiné, et les interfaces entre les deux. Après cette étape, les éléments sont réunis dans la configuration de la Fig. 0.2 pour construire le modèle complet de lubrification moléculaire.

### 0.2.3 Eléments du modèle

Bien que l'intérêt principal du modèle de lubrification soit de reproduire le comportement du lubrifiant, il est important d'avoir un modèle suffisamment représentatif pour les surfaces. Le modèle qui sera utilisé est basé sur des surfaces cristallines structurées avec la réplique la plus réaliste possible des propriétés mécaniques et thermiques. A cet effet, des simulations moléculaires ont été menées pour calculer la conductivité thermique et le coefficient d'élasticité. Les paramètres optimaux des interactions entre les atomes solides ont été déterminés pour reproduire au mieux les valeurs expérimentales.

Le processus de modélisation d'un lubrifiant liquide présente trois complications par rapport à celui des surfaces solides. D'abord et contrairement à la structure bien ordonnée (cristalline) dans les solides, il n'y a pas d'ordre global dans un liquide. Deuxièmement, les molécules du lubrifiant sont en mesure de se déplacer les unes par rapport aux autres. Troisièmement, les chaînes moléculaires sont flexibles, et donc toutes sortes de déformation et rotations des liaisons doivent être prises en compte. L'architecture moléculaire d'un liquide est représentée schématiquement dans la Fig. 0.3.

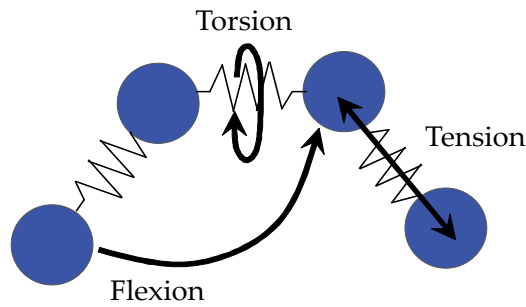


Fig. 0.3 : Schéma montrant les trois types d'interactions intermoléculaires utilisé pour modéliser la flexibilité des molécules de lubrifiant.

Pour les modèles d'interaction, les propriétés thermiques et dynamiques ont été déterminées pour des molécules d'alcanes de différentes tailles. Il s'est avéré que les modèles explicites et grossiers donnent généralement des prédictions acceptables de ces propriétés pour les courtes molécules. Pour les longues molécules, les résultats sont moins précis en comparaison des données expérimentales, mais restent dans le même ordre de grandeur.

Enfin, les interactions à l'interface déterminent comment les surfaces influencent la structure du lubrifiant confiné. En outre, ces interactions permettent aux surfaces de transmettre la compression et le cisaillement au lubrifiant. Les interactions entre la surface et le lubrifiant sont généralement modélisées en utilisant un potentiel de Lennard Jones. Dans cette thèse, les paramètres du modèle ont été ajustés pour reproduire les données expérimentales d'énergie d'adsorption moléculaire des surfaces [87, 88].

## 0.2.4 Initialisation et échantillonnage

Le modèle de la lubrification moléculaire est construit à partir des trois éléments constitutifs décrits précédemment : les surfaces, le lubrifiant, et de leur interface. Un aperçu d'un modèle avec des surfaces d'or qui confinent 2,4 nm de pentane comme lubrifiant est donné dans la Fig. 0.4.

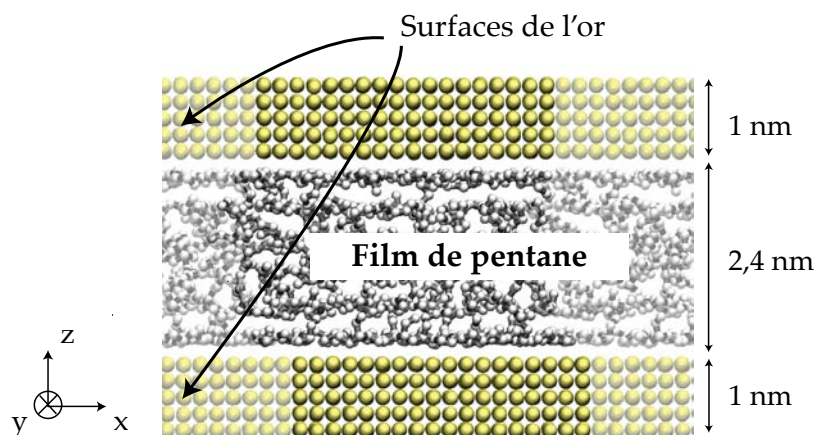


Fig. 0.4 : Aperçu du modèle complet de lubrification moléculaire comprenant des surface d'or et un film lubrifiant de pentane d'une épaisseur de 2,4 nm. Les zones ombrées correspondent aux copies du système par les frontières périodiques.

Le lubrifiant est comprimé en appliquant une charge unidirectionnelle normale à la surface. Sous charge constante, l'épaisseur du film présente des oscillations amorties avec le temps. Quand le système atteint l'équilibre, les surfaces sont mises en mouvement relatif à vitesses constantes, égales mais opposées.

Enfin, il est important d'analyser l'influence de l'échantillonnage spatial et temporel sur le résultat des simulations moléculaires. L'échantillonnage spatial est lié à la taille du domaine dans les directions  $x$  et  $y$ , où les conditions périodiques sont appliquées. L'échantillonnage temporel dépend du choix du pas de temps ainsi que de la durée totale de la simulation.

En effectuant des simulations avec des surfaces de différentes dimensions, il s'est avéré que, dans certains cas, un échantillon plus large est nécessaire pour éliminer les erreurs statistiques. Ainsi un plus grand domaine est réellement nécessaire pour simuler de longues chaînes moléculaires et/ou de faibles vitesses de glissement.

Quant à l'échantillonnage temporel, le pas de temps doit être suffisamment petit pour que l'hypothèse que toutes les forces d'interaction sont constantes entre deux pas reste valable et donc l'énergie totale du système reste constante. Néanmoins, il y a un intérêt évident dans l'utilisation de grands pas de temps car cela permet d'étudier des phénomènes sur une plus longue période de temps. Une valeur optimale de 1 fs a été choisie pour assurer la stabilité et la précision de l'intégration temporelle.

Enfin, il est difficile d'établir une recommandation unique pour le choix de la durée totale simulée. Plus la durée d'échantillonnage est longue, plus précises sont les statistiques recueillies. De plus, si le système est de grande taille une durée plus courte serait suffisante. Toutefois, dans tous les cas la durée de simulation doit être supérieure à l'échelle de temps du phénomène à étudier. Par exemple, dans le modèle de lubrification moléculaire présenté précédemment, la simulation devra être plus longue que le temps nécessaire pour atteindre l'état stationnaire de cisaillement du système.

## 0.2.5 Conclusion

Après une brève présentation de la méthode de simulation choisie, un modèle de lubrification moléculaire a été conçu et développé élément par élément. Chaque élément a été étudié séparément et paramétré afin d'obtenir des propriétés réalistes des matériaux et des interactions à l'interface. Les éléments ont finalement été assemblés pour produire un modèle de lubrification moléculaire. Ce modèle a ensuite été testé et il a permis de reproduire de nombreuses tendances trouvées dans la littérature, sous des conditions statiques et dynamiques.

Des problématiques liées à l'échantillonnage spatial et temporel ont aussi été traitées. Cela a permis de faire différents choix de paramètres numériques du modèle pour assurer la stabilité et la précision des simulations ainsi que la pertinence des statistiques déterminées à partir de l'échelle moléculaire, pour différentes conditions de fonctionnement.

Dans le but de modéliser la lubrification moléculaire, l'un des points faibles de cet outil numérique est la méthode de dissipation de la chaleur. L'énergie mécanique, injectée en continu dans le système par compression et cisaillement, est transformée en chaleur. La chaleur

est ensuite transférée par conduction et convection à l'intérieur du lubrifiant, à travers l'interface, et jusqu'aux surfaces où elle est dissipée. Si la méthode de dissipation employée n'est pas réaliste, la température du lubrifiant peut augmenter de façon non physique. Cela influence à son tour la dynamique du lubrifiant et peut donner des résultats incorrects sur le frottement.

Il est donc essentiel de modéliser de façon appropriée la dissipation de la chaleur en particulier dans les études de frottement. Le chapitre suivant est consacré à la résolution de cette problématique pour les problèmes de lubrification moléculaire.

## 0.3 Du frottement aux mécanismes de dissipation d'énergie

Un modèle numérique de lubrification moléculaire a été construit et caractérisé. Dans ce modèle, toutes les interactions qui gouvernent l'évolution du système avec le temps sont conservatives. L'énergie mécanique supplémentaire apportée par la pression et le glissement appliqués aux surfaces ne peut être dissipée que sous forme de chaleur. Pour une étude de type lubrification, la dissipation d'énergie est un facteur clé qui doit être soigneusement manipulé car la réponse de l'interface est par nature très dépendante de la température locale. La présente section est donc consacrée à l'étude de l'influence de la méthode de dissipation d'énergie sur l'état thermodynamique du film confiné et sur le frottement global pour différentes conditions opératoires. Un nouveau modèle de dissipation d'énergie dédié aux simulations sous cisaillement élevé est présenté. Ce modèle prend en compte un transfert de chaleur réaliste du lubrifiant confiné vers les surfaces.

Pour des systèmes simples et homogènes, tels que les solides et liquides de taille macroscopique, la température peut être contrôlée en utilisant l'un des nombreux algorithmes existants. Toutefois, dans le cas des films confinés, certains problèmes peuvent survenir en raison de la nature non homogène du système [96]. Cette non-homogénéité est due principalement à l'interface solide / liquide et se manifeste sous la forme de fluctuations de la densité à travers le film. Le problème devient encore plus compliqué en présence de cisaillement. La chaleur générée par effet visqueux doit être évacuée hors du contact, sinon la température augmente indéfiniment. Plusieurs transformations énergétiques se produisent donc dans le contact et les champs caractéristiques de température et de vitesse ne peuvent être capturés que si les molécules de lubrifiant sont libres de toute contrainte thermique directe [97]. La chaleur supplémentaire doit donc être dissipée au niveau des surfaces [97].

Afin de mieux comprendre les différentes transformations énergétiques survenant à l'intérieur du film lubrifiant, l'équilibre énergétique dans des conditions de lubrification limite est étudié dans la section suivante. Cette analyse sera utilisée pour démontrer qu'il existe une relation étroite entre la dissipation d'énergie, le thermostat et la force de frottement dans le contact.

### 0.3.1 Bilan énergétique

Depuis son application sous forme mécanique, l'énergie subit trois étapes essentielles : l'absorption, la transformation, et enfin la dissipation. L'énergie est ajoutée au système par

compression et mouvement relatif des surfaces. La différence de quantité de mouvement entre les deux surfaces se diffuse à l'intérieur du lubrifiant cisailé qui absorbe cette énergie mécanique. L'énergie est ensuite transformée sous forme thermique, la chaleur visqueuse générée à l'intérieur du film cisailé. L'augmentation de la température à l'intérieur du film lubrifiant crée un gradient avec la température contrôlée des surfaces. Il en résulte un flux de chaleur par conduction et convection vers les surfaces où l'énergie est enfin dissipée.

Au cours de la simulation, à la fin de la phase transitoire qui se produit en début de cisaillement, un équilibre est établi entre les énergies entrantes et sortantes du contact. L'apport d'énergie mécanique est complètement dissipé par les thermostats des surfaces. C'est le début de l'état stationnaire de cisaillement. L'épaisseur moyen du film est également constante et donc la puissance générée par la compression est nulle. Le rôle du film lubrifiant est d'absorber l'énergie mécanique de cisaillement, la transformer en chaleur, et enfin transporter cette dernière vers les surfaces. La boucle énergétique « surfaces – lubrifiant – surfaces » continue sans cesse une fois l'état stationnaire de cisaillement atteint.

Il y a deux scénarios possibles pour décrire la relation de cause à effet entre l'énergie dissipée et le frottement dans le contact :

1. L'énergie dissipée est la conséquence des forces de frottement. Indépendamment des paramètres numériques du thermostat, l'énergie dissipée dépend uniquement des conditions opératoires.
2. Le frottement mesuré est la conséquence de la dissipation d'énergie. Par exemple, numériquement si le thermostat est réglé pour extraire rapidement de l'énergie, la température du lubrifiant n'augmente pas assez. En conséquence, la résistance à l'écoulement ainsi que le frottement augmentent significativement.

Afin de pouvoir répondre à ce paradoxe, différentes méthodes de dissipation sont comparés.

### **0.3.2 Algorithmes de thermostat**

La méthode de dissipation classique utilisée dans des simulations de films confinés sous cisaillement est le thermostat des parois glissantes (SBT). Dans cette méthode, la température de chaque surface solide est maintenue fixe et aucune contrainte thermique n'est appliquée au lubrifiant. Cette méthode a été employée par plusieurs auteurs [96, 97, 65, 94] pour substituer les thermostats homogènes utilisés auparavant et qui contrôle directement la température du lubrifiant. Néanmoins, il est intéressant de voir si les différentes implémentations de cette méthode peuvent avoir un effet sur le frottement obtenu pour les mêmes conditions opératrices du contact. Dans cette section, trois algorithmes ont été testés: le « velocity-rescaling », le thermostat « Nosé-Hoover », et le thermostat « Langevin ».

Les résultats des simulations avec ces trois algorithmes montrent une influence importante sur l'augmentation de température à l'intérieur du lubrifiant ainsi que sur le frottement. Les thermostats très dissipatifs atténuent l'augmentation de température ce qui augmente la force nécessaire pour cisailier le lubrifiant.

### 0.3.3 Début de l'échauffement

La littérature rapporte que les méthodes de thermostat ne deviennent influentes que dans le régime de cisaillement où l'échauffement est en fait susceptible de se produire à l'intérieur du lubrifiant [97, 65]. On constate de plus qu'il y a un taux de cisaillement critique à partir duquel le lubrifiant commence à s'échauffer [3]. Le système étudié ici est plus complexe que les systèmes de la littérature. Il est donc nécessaire de déterminer, pour ce système particulier, le taux de cisaillement critique qui correspond au début de l'échauffement du lubrifiant.

Des simulations ont donc été menées avec des vitesses variables des surfaces. Une large gamme de taux de cisaillement a donc été étudiée. L'augmentation de température à l'intérieur du lubrifiant en fonction du taux de cisaillement apparent est donnée en Fig. 0.5. Pour des taux de cisaillement inférieur à  $6 \times 10^9 \text{ s}^{-1}$ , aucun échauffement n'a pu être détecté et, au-delà, le lubrifiant commence à chauffer significativement.

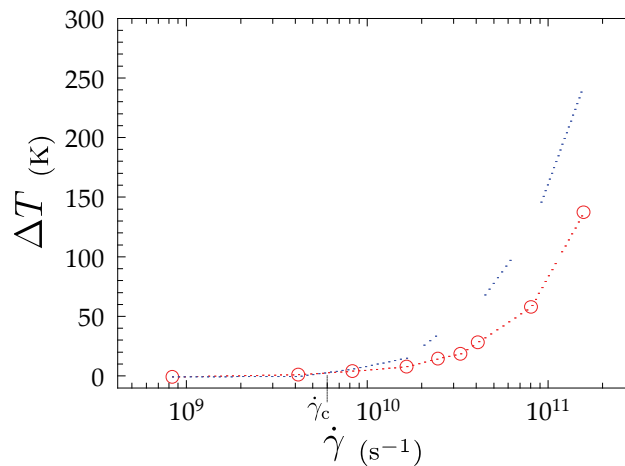


Fig. 0.5 : Augmentation de la température du lubrifiant en fonction du taux de cisaillement apparent.

### 0.3.4 Méthodes avancées de dissipation

Dans la méthode du thermostat des parois glissantes (SBT), la température des surfaces est constante et choisie égale à la température ambiante (en dehors du contact). Ainsi, pour tout flux de chaleur généré dans le contact, il n'y a pas de gradient de température dans les solides. Cela équivaut à supposer que ces derniers ont des conductivités et capacités thermiques infinies. En réalité, de telles propriétés n'existent pas. De plus, les flux de chaleur générés pouvant atteindre des valeurs de l'ordre du  $\text{GW/m}^2$ , on peut prédire par un modèle analytique une augmentation significative de la température des parois pendant l'échelle de temps des simulations.

Il est donc très important de modéliser avec précision la dissipation par conduction non seulement à l'intérieur du lubrifiant, mais aussi à travers les surfaces solides lorsque les conditions opératoires sont sévères. Il est particulièrement important de permettre à la température de surface de s'accommoder naturellement de l'échauffement du lubrifiant. Deux méthodes avancées de dissipation sont présentées et comparées. La première est la méthode

des molécules fantômes [113] et la seconde est appelée VBT (variable boundary temperature) : c'est une nouvelle méthode basée sur la mise à jour régulière de la température des surfaces en fonction du flux de chaleur sortant du contact.

L'aspect le plus important en comparant les deux méthodes avancées est que la température de surface augmente lorsque le lubrifiant s'échauffe. L'augmentation de la température de surface avec les deux méthodes est du même ordre de grandeur. En fait, la contrainte de cisaillement totale et donc le frottement sont également très proches (voir Tableau 0.1).

Méthode de dissipation	Augmentation de température (K)		Contrainte de cisaillement (MPa)
	Surface	Lubrifiant	
SBT	0	57,8	65,4
Molécules fantômes	32,1	84,7	60,6
VBT	30,5	82,3	60,8

**Tableau 0.1 : Augmentation de température, dans les surfaces et à l'intérieur du film lubrifiant, et la contrainte de cisaillement apparente obtenues dans les simulations avec les différentes méthodes de dissipation d'énergie.**

La méthode VBT présente cependant trois avantages par rapport à la méthode des molécules fantômes. D'abord, elle ne nécessite pas d'ajouter des atomes (degrés de liberté) supplémentaires à l'intérieur du système. Deuxièmement, elle est plus facile à mettre en œuvre surtout si la structure cristalline des surfaces est complexe, ce qui est souvent vérifié dans le cas des surfaces tribologiques réelles. Troisièmement, dans la méthode des molécules fantômes un solide semi-infini est modélisé avec une température constante alors que dans la méthode de VBT, une telle hypothèse n'est plus nécessaire. La conduction de la chaleur hors du contact est donc traitée de façon plus physique et réaliste.

### 0.3.5 Conclusion

Les résultats de cette section ont prouvé que la méthode de dissipation de la chaleur employée peut quantitativement influencer le frottement. Cela est premièrement dû au fait que, si les surfaces dissipent la chaleur plus rapidement, le lubrifiant s'échauffe moins et sa viscosité effective est plus élevée. Le deuxième point évoqué dans la section 0.3.1, qui indique que le frottement est influencé par la méthode de dissipation d'énergie semble être plus persuasif.

Toutefois, il a aussi été montré que l'échauffement du lubrifiant n'est significatif que si un taux de cisaillement critique est dépassé. Ainsi, si le taux de cisaillement est faible, la méthode de dissipation n'a aucune influence sur les propriétés du film lubrifiant et le frottement dans le contact. Dans ce régime, le frottement est indépendant de la méthode de dissipation et le premier scénario de section 0.3.1 est valide.

Le frottement dans les simulations moléculaires n'est pas le résultat direct de la méthode numérique de dissipation mais il n'est pas toujours indépendant de cette dernière. Dans des conditions de contact sévères, les méthodes employées pour la dissipation d'énergie commencent à intervenir. Dans ce cas, deux méthodes avancées ont été présentées pour permettre une modélisation physique de la conduction de chaleur à travers les surfaces.

Basé sur ces conclusions, le modèle de lubrification moléculaire est ensuite employé dans le régime de faible cisaillement (au sens de l'insignifiance de la dissipation thermique) pour étudier l'influence de la structure moléculaire des surfaces et du lubrifiant sur l'écoulement à l'interface et le frottement. Les conditions opératoires simulées sont proches de celles trouvées dans les applications réelles où la vitesse de glissement des surfaces et l'épaisseur du film sont respectivement de l'ordre de 10 m/s et 4 nm.

## 0.4 Adsorption et corrugation des surfaces

Des expériences ont montré que, dans les géométries confinées, la structure et la dynamique des lubrifiants sont fortement influencées par la nature des surfaces [15, 16]. La structure bien organisée des surfaces solides se transmet, à travers les interactions interfaciales, à l'ensemble des "vallées" du potentiel physique que les molécules du lubrifiant sont susceptibles d'occuper [55, 100]. Toute surface, qu'elle soit géométriquement lisse ou rugueuse, se manifeste par une sorte d'empreinte qui peut interagir physiquement avec les couches voisines de lubrifiant.

Le potentiel d'interaction des surfaces avec le lubrifiant est une combinaison de deux effets : le potentiel d'adsorption et le potentiel de corrugation [101]. L'adsorption augmente avec la densité atomique et l'énergie de surface [55]. Les molécules de lubrifiant sont plus attirées par les surfaces ayant un potentiel d'adsorption élevé et, en conséquence, une couche dense de lubrifiant se forme près de chaque surface. Le potentiel de corrugation, d'autre part, dépend des variations du potentiel d'interaction physique dans le plan de l'interface. Ces variations sont dues à la densité et la structure cristalline des surfaces [55, 87]. Par analogie avec l'exemple d'une empreinte dans le sable, le potentiel de corrugation représente la forme de l'empreinte alors que le potentiel d'adsorption représente la profondeur dont celle-ci est repoussée dans le sable.

Avec des surfaces modèles, il est possible de modifier tout paramètre pour changer l'adsorption et la corrugation [55]. Par exemple, augmenter la densité atomique de la surface donne une plus forte adsorption mais une plus faible corrugation. Dans les problèmes réels de lubrification moléculaire, les matériaux de surface tels que les oxydes sont amorphes. Ils peuvent être constitués de deux ou plusieurs types d'atomes et ont des structures cristallines assez complexes. Les méthodes classiques d'analyse qui s'appliquent aux surfaces modèles deviennent inefficaces, car de nombreux facteurs entrent en jeu. Il n'y a pas de façon claire dans la littérature pour combiner tous ces facteurs dans des paramètres représentatifs et comparables pour caractériser les différents types de surface.

Une méthode simple est donc proposée dans la section suivante afin de comparer les propriétés de cinq surfaces composées de différents matériaux. Ces surfaces seront ensuite utilisées pour confiner un film lubrifiant dans des conditions de lubrification moléculaire. Les effets moléculaires dans le film seront analysés en fonction des propriétés d'adsorption et corrugation des surfaces.

## 0.4.1 Caractérisation physique des surfaces

Une méthode de caractérisation est développée pour permettre de caractériser les potentiels d'adsorption et de corrugation de différentes surfaces. Le principe est le suivant : un ensemble d'atomes « balayeurs » sont positionnés à une élévation ( $d$ ) au-dessus de la surface en question, comme illustré dans la Fig. 0.6. Ces atomes sont uniformément répartis et s'étendent sur toute la dimension  $x$  de la surface. L'énergie potentielle, venant des interactions avec les atomes de la surface, est alors enregistrée à chaque instant pendant que les atomes « balayeurs » se déplacent selon la direction  $y$ . Les données acquises permettent d'établir un balayage précis de l'énergie d'interaction de la surface.

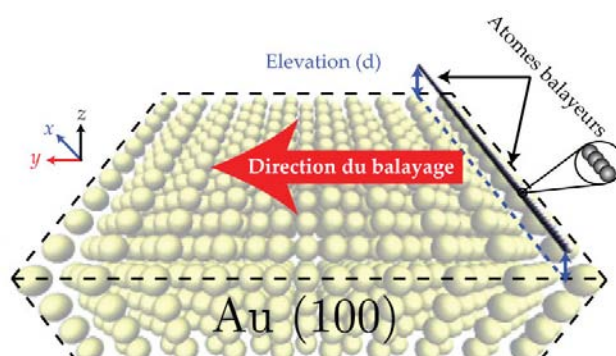


Fig. 0.6 : Schéma explicatif de la méthode de balayage pour effectuer la caractérisation physique d'une surface d'or Au (100).

Par exemple, une vue de dessus d'une surface modèle est donnée dans la Fig. 0.7. L'analyse révèle la présence de vallées d'énergie potentielle périodiquement répétée. Ces sites sont ceux que les atomes de lubrifiant occuperont préférentiellement.

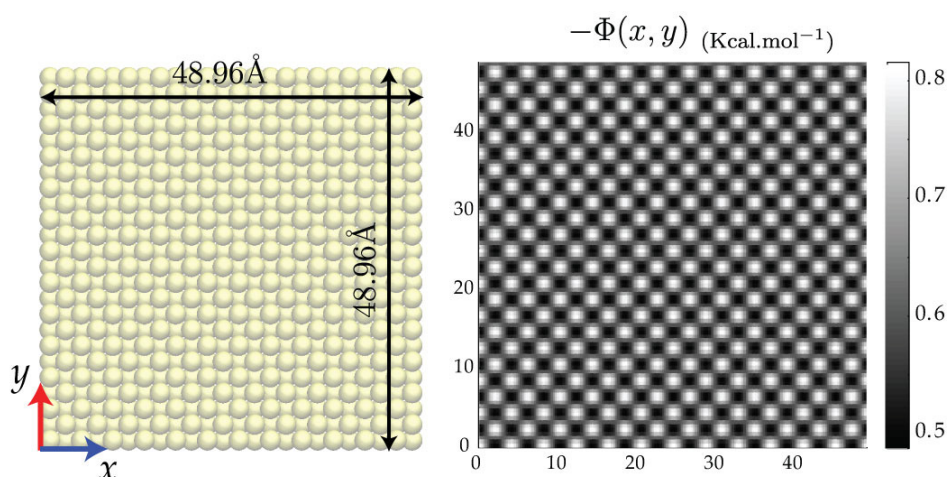


Fig. 0.7 : Aperçu dans le plan d'une surface d'or Au (111) avec son potentiel déterminé par la méthode de balayage montrée en Fig. 0.6.

Le paramètre d'adsorption ( $\epsilon_{\text{ads}}$ ) est déterminé comme la moyenne de l'énergie d'interaction LJ effective sur toute la surface. Le paramètre de corrugation ( $\epsilon_{\text{corr}}$ ) en unité d'énergie est l'écart moyen entre l'énergie d'interaction et l'adsorption moyenne ( $\epsilon_{\text{ads}}$ ).

La procédure a été appliquée à cinq types de surfaces. Les paramètres d'adsorption et de corrugation sont comparés dans la Fig. 0.8. Les résultats montrent que les surfaces ont des potentiels d'adsorption et de corrugation très différents. Une telle observation n'aurait pas été simple sans la méthode de caractérisation.

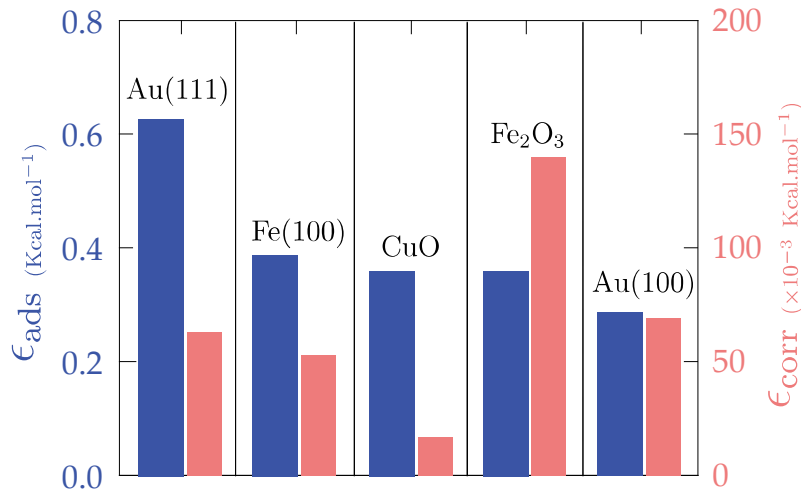


Fig. 0.8 : Paramètres d'adsorption et de corrugation de cinq surfaces déterminés par la méthode de caractérisation décrite en Fig. 0.6.

Afin d'étudier la relation entre les résultats du balayage, les potentiels physiques d'adsorption et de corrugation, et les propriétés des films confinés, ces cinq surfaces ont été mises dans des conditions de lubrification moléculaire pour confiner le même film nanométrique d'hexadécane.

## 0.4.2 Simulation du cisaillement

Les simulations ont été réalisées sur un système comprenant un film d'hexadécane de 4nm d'épaisseur confiné entre les cinq surfaces caractérisées précédemment. Une pression constante de 500 MPa a été appliquée et les surfaces ont été déplacées dans des directions opposées à une vitesse constante de 10 m/s : le taux de cisaillement apparent est donc de  $5 \times 10^9 \text{ s}^{-1}$ . Selon les conclusions de la section précédente, aucun échauffement n'est censé se produire dans ces conditions. Ainsi, un thermostat (SBT) avec une implémentation Langevin a été utilisé pour maintenir la température des surfaces à 300 K.

Le résultat de ces simulations montre que la nature des surfaces est un facteur essentiel qui influence la structuration dans le film lubrifiant. Cette structuration est significativement amplifiée par le potentiel d'adsorption et faiblement atténuée par la corrugation. Quant au glissement interfacial, le potentiel de corrugation se présente comme un facteur dominant. Le lubrifiant ne glisse pas en présence de surfaces corruguées (Fig. 0.9).

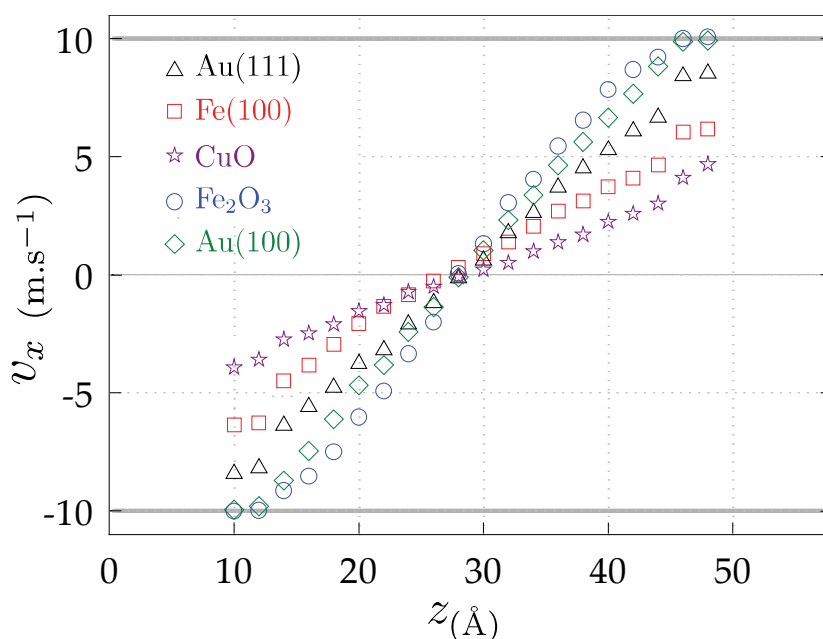


Fig. 0.9 : Profils de vitesses à travers un film d'hexadécane confiné entre cinq différents types de surface.

Les molécules d'hexadécane glissent plus facilement à proximité de surfaces ayant des faibles potentiels de corrugation. La raison en est que, dans de tels cas, le potentiel d'interaction varie peu à travers la surface. Les atomes du lubrifiant sont ainsi facilement en mesure d'échapper aux « vallées » du potentiel et de circuler librement. Lorsque les surfaces sont corruguées, elles présentent un grand nombre de « vallées » de potentiel. Les molécules du lubrifiant trouvent presque toujours des positions d'équilibre dans ces sites et se déplacent ainsi à la vitesse des surfaces.

Quant au frottement, la contrainte de cisaillement apparente la plus importante est trouvée pour la surface de  $\text{Fe}_2\text{O}_3$  et la plus faible pour  $\text{CuO}$ . En considérant les résultats de caractérisation de la Fig. 0.8, il est clair que les surfaces corruguées engendrent un frottement plus élevé. Ceci est principalement dû au glissement faible du lubrifiant près de ces surfaces.

### 0.4.3 Conclusion

La méthode de caractérisation a été appliquée à cinq surfaces réalistes avec des différentes densités, structures cristallines, et paramètres de l'interaction. Les résultats ont montré que certaines surfaces peuvent avoir un fort potentiel d'adsorption avec une faible corrugation et vice-versa.

Ces surfaces ont ensuite été employées dans des simulations de lubrification moléculaire avec un film nanométrique d'hexadécane. Le résultat des simulations a montré des propriétés structurelles et dynamiques différentes pour chacune des surfaces. Étant donné que les analyses de surface étaient disponibles, les facteurs qui influencent ces propriétés ont pu être identifiés.

Pour les conditions opératoires étudiées, le potentiel d'adsorption de la surface s'est avéré être un facteur dominant qui amplifie la densité de la couche de fluide située près de la surface. Quant à l'écoulement interfacial, le glissement lubrifiant/surface est fortement in-

fluencé par la corrugation. Les molécules de lubrifiant peuvent bien glisser sur une surface à fort potentiel d'adsorption si elle présente une faible corrugation.

Enfin, en terme de frottement, il a été constaté que la corrugation est le facteur le plus influant grâce à sa relation étroite avec le glissement aux parois et donc finalement avec la mouillabilité des surfaces. La dernière section de ce résumé étendu traite des effets de la structure moléculaire du lubrifiant sur le frottement, en fonction de la mouillabilité des surfaces.

## **0.5 Effet de la structure moléculaire du lubrifiant et de la mouillabilité des surfaces**

Les lubrifiants réels sont des mélanges de différents composants chimiques. Leur viscosité est liée à la forme de leurs molécules constitutives et à leurs interactions. Les molécules ramifiées et celles composées de longues chaînes ont souvent des viscosités plus élevées que les molécules à courtes chaînes linéaires. Dans les problèmes classiques de lubrification, les coefficients intrinsèques de transport sont souvent suffisants pour expliquer la relation entre le frottement et la structure moléculaire des lubrifiants.

Cependant, cette relation devient bien plus complexe dans des géométries confinées à l'échelle moléculaire. La notion de viscosité est totalement insuffisante pour expliquer le frottement à cette échelle [101]. En raison de la petite taille du domaine, les interactions entre les surfaces et le lubrifiant jouent en effet un rôle essentiel. Ces interactions dépendent autant des propriétés des surfaces que de la forme et de la nature des molécules du lubrifiant.

Les lubrifiants commerciaux sont des mélanges de différents types de composants chimiques tels que les huiles minérales, additifs anti-usure et additifs de friction, anti-oxydants, détergents, etc. Les molécules constitutives peuvent être saturées avec des chaînes linéaires ou ramifiées, mais peuvent aussi être polaires et présenter des interactions physico-chimiques avec les surfaces. Contrairement à la section précédente, où l'hexadécane a été le seul fluide considéré, dans ce chapitre les effets de la forme et de la nature moléculaire du lubrifiant vis-à-vis de surfaces de différentes caractéristiques de mouillage sont étudiés. Il est essentiel de comprendre ces effets afin d'améliorer la capacité prédictive dans la conception des lubrifiants pour des applications entièrement ou partiellement concernées par la lubrification moléculaire.

### **0.5.1 Effet de la longueur de la chaîne moléculaire**

La longueur des molécules d'un lubrifiant est un facteur crucial pour déterminer ses performances tribologiques en régime moléculaire [103]. Les molécules courtes ont généralement des viscosités faibles, mais en confinement sévère elles peuvent plus facilement atteindre un état d'ordre élevé (état solide ou vitreux) que les molécules plus longues [61].

Cinq types de molécules d'alcane, saturées et linéaires, de différentes longueurs de chaîne ont été étudiés dans des conditions de lubrification moléculaire. Les simulations ont montré d'abord que le phénomène de stratification est plus prononcé pour les molécules

courtes. Pour les molécules longues on montre un alignement parallèle à la direction de cisaillement. En outre, la proportion de molécules contenues dans chaque couche peut varier et devenir élevée. Par exemple avec du tétracosane (C32), dans la première couche près de la surface, 44% des molécules forment des ponts vers la deuxième couche, comparé à seulement 15% avec du pentane (C5). La formation de ponts (bridging) est représentative de la cohésion interne du fluide qui est également liée à sa résistance à l'écoulement (viscosité) [103].

Les profils de vitesse à travers chacun des cinq films lubrifiants sont donnés dans la Fig. 0.10. Pour la surface non mouillante (CuO), un glissement aux parois se produit dans tous les cas, mais il augmente significativement avec la longueur de chaîne (Fig. 0.10-a). Ces effets ne sont pas observés avec la surface mouillante ( $\text{Fe}_2\text{O}_3$ ).

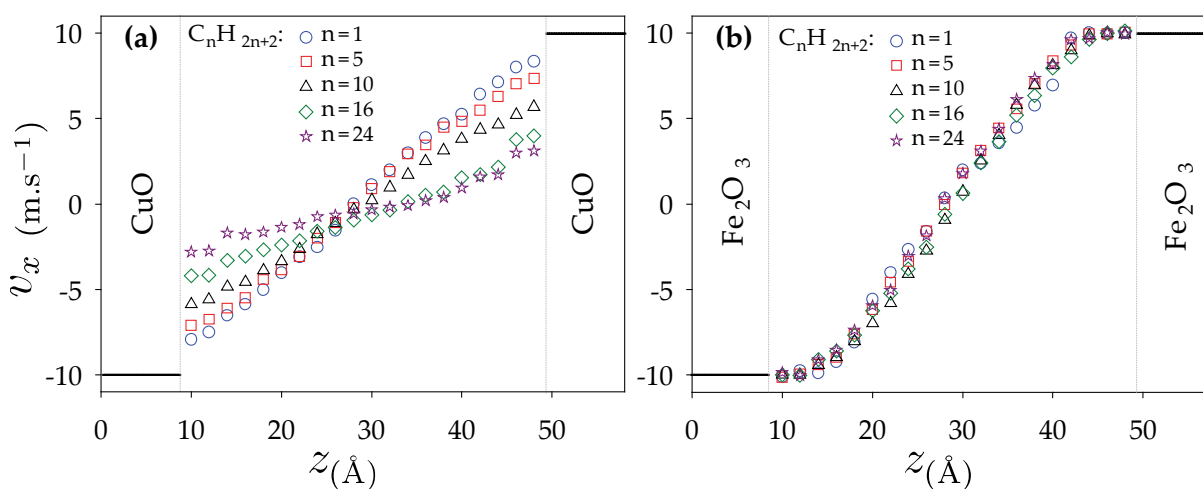


**Fig. 0.10 : Profils de vitesses à travers cinq films de différentes longueurs de chaînes moléculaire, pour deux types de surfaces : CuO (non-mouillante) et  $\text{Fe}_2\text{O}_3$  (mouillante).**

En raison d'une cohésion interne, entre les couches du fluide, bien plus forte que la cohésion vis-à-vis des surfaces non-mouillantes, les molécules longues glissent aux parois. Lorsque la cohésion interne est faible, comme dans le cas des molécules courtes, les couches adsorbées préfèrent suivre le mouvement des surfaces et un faible glissement est observé.

Quant au frottement, le glissement qui se produit près des surfaces non-mouillantes et qui augmente avec la longueur de chaîne contrebalance l'augmentation de la viscosité. Cela conduit à une stabilisation du frottement pour les longues chaînes. Par contre, en l'absence de glissement près des surfaces mouillantes, le frottement augmente globalement avec la longueur de chaîne en raison de l'augmentation naturelle de la viscosité avec de telles molécules.

## 0.5.2 Effet de la ramification de la chaîne moléculaire

Au delà de la longueur de la chaîne moléculaire du lubrifiant, le degré de ramification est un autre facteur relié à la forme moléculaire et qui influe sur les propriétés de lubrification moléculaire. Entre molécules linéaires et ramifiées, ces dernières ont généralement des viscosités plus élevées. Sous confinement sévère cependant, l'inverse a pu être observé expé-

rimentalement [23]. Par ailleurs, des simulations moléculaires ont montré que la ramification peut influencer les propriétés locales des films, comme leur structuration en couches [105] et le glissement aux parois [62].

Afin d'étudier l'effet de la ramification des molécules sur la structure et la dynamique des films confinés, des simulations moléculaires ont été réalisées sur deux types de films de décane composés respectivement de molécules linéaires et de molécules ramifiées.

Les résultats montrent d'abord que la densité de la première couche du lubrifiant près de la surface n'est pas influencée par la ramification. Toutefois, une atténuation de la structuration est constatée dans le film de décane ramifié. En raison de leur cohésion interne forte, les molécules ramifiées sont effectivement moins influencées par les interactions de surface et retrouvent un comportement macroscopique (bulk) à une distance assez proche de la surface.

En ce qui concerne l'ordre tangentiel, les molécules linéaires forment très peu de pont entre les couches. Dans le cas des molécules ramifiées, une grande proportion de molécules forme des ponts entre les couches internes. La cohésion interne du film lubrifiant est donc plus forte que dans le cas des molécules linéaires.

Quant à l'écoulement à l'interface, on observe l'absence de glissement pour les deux molécules dans le cas des surfaces mouillantes. Cependant, une influence remarquable de la ramification sur les profils de vitesse peut être observée avec la surface non-mouillante. Le glissement aux parois est significativement plus important dans le cas des molécules ramifiées. Dans ce cas, la cohésion interne est devenue plus forte que la cohésion avec la surface ce qui explique l'existence d'un glissement très important.

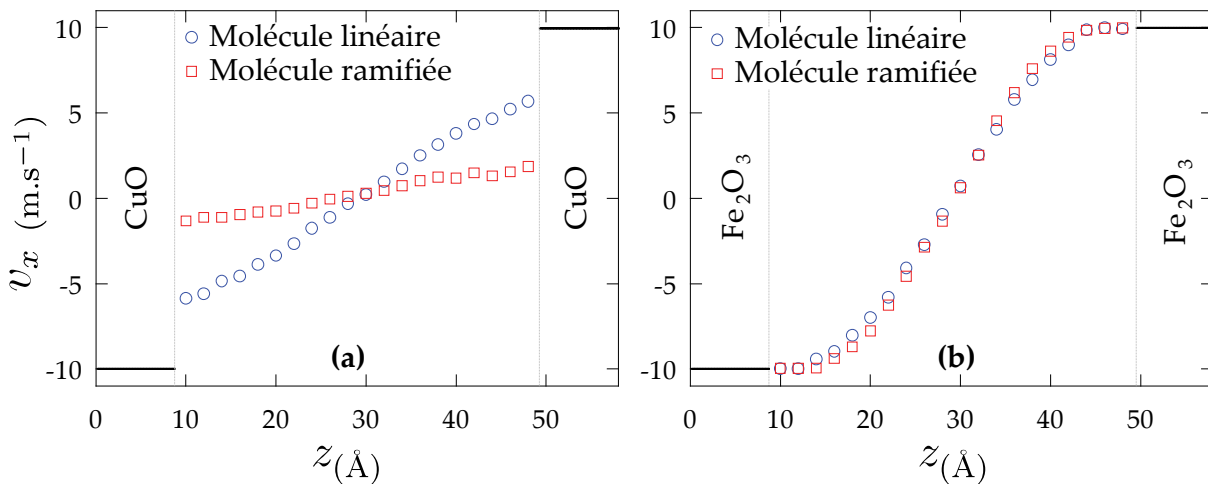


**Fig. 0.11 : Profils de vitesse à travers des films composés des molécules linéaires et ramifiés de décane, confinés entre des surfaces de CuO et Fe<sub>2</sub>O<sub>3</sub>.**

La ramification augmente la cohésion interne du fluide, la viscosité et entraîne un frottement significativement élevé pour le cas des surfaces mouillantes. Dans le cas des surfaces non-mouillantes, le glissement aux parois joue un rôle important pour limiter l'augmentation de frottement. Dans la limite des conditions opératoires considérées, le frottement est toujours plus élevé pour les molécules ramifiées.

### 0.5.3 Mélanges de lubrifiants non-polaires

Le plus simple des lubrifiants commerciaux est un mélange d'hydrocarbures saturés de différentes structures moléculaires. La forme des molécules influence la performance tribologique autant dans les conditions de large séparation que dans le cas de séparations moléculaires. Dans ce dernier cas, la réponse tribologique dépend également de la nature des surfaces.

Dans cette section, un lubrifiant composé d'un mélange de longues et courtes chaînes d'alcane (50% d'hexadécane et 50 % de méthane) a été considéré. Un film de 4 nm d'épaisseur de ce mélange est confiné entre les deux types de surfaces, mouillantes et non-mouillantes. Un aperçu de la configuration initiale du système est donné dans la Fig. 0.12. Les différentes molécules du mélange sont initialement réparties de façon homogène dans tout le domaine du modèle.

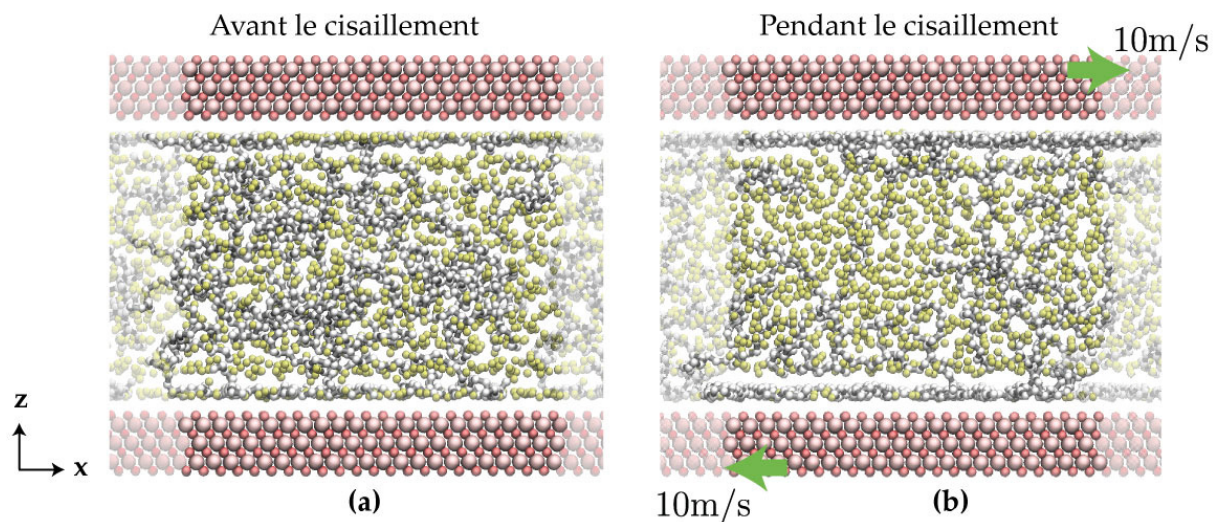


**Fig. 0.12 : Aperçu d'un film de 4 nm d'épaisseur constitué d'un mélange méthane-hexadécane : (a) état initial (b) au cours de cisaillement. Les molécules de méthane sont représentées en jaune tandis que celles d'hexadécane sont représentées en noir et blanc.**

Au cours du cisaillement, un phénomène très intéressant de ségrégation moléculaire se produit dans le film. Les longues molécules d'hexadécane (couleurs noir et blanc) migrent vers la surface tandis que les courtes molécules de méthane restent au centre du film.

Les profils de vitesse à travers le mélange confiné sont représentés dans la Fig. 0.13. Du fait qu'il y a souvent un lien étroit entre la structure du film et son écoulement à l'interface, ils sont comparés aux profils obtenus avec des solutions pures de ses molécules constitutives (hexadécane et le méthane).

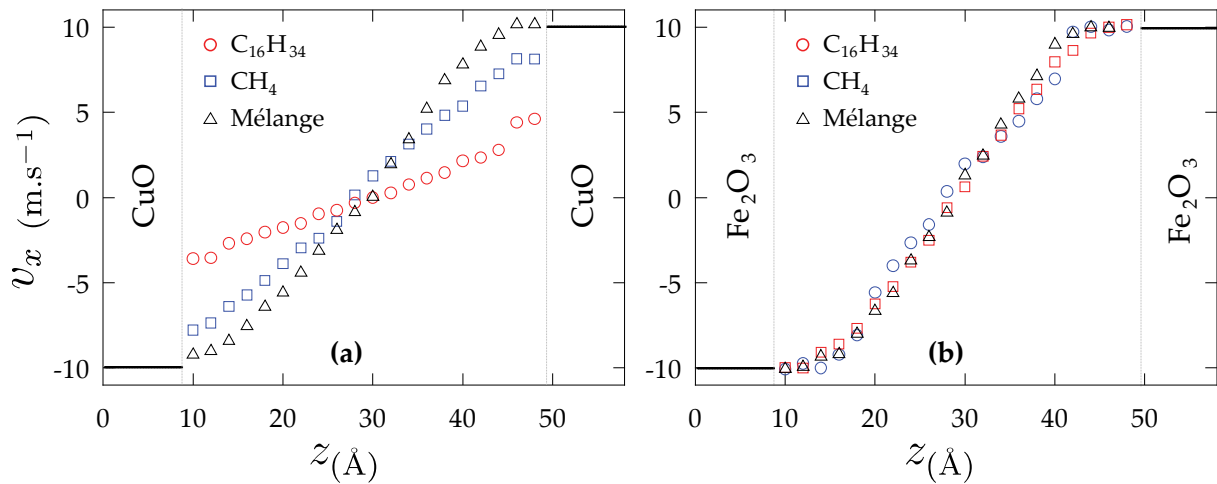


**Fig. 0.13 : Profils de vitesses pour des films d'hexadécane, de méthane, et de leur mélange entre des surfaces de CuO et Fe<sub>2</sub>O<sub>3</sub>.**

Avec la surface mouillante, le profil de vitesses du mélange coïncide avec ceux obtenus avec l'hexadécane et le méthane purs. Toutefois, avec la surface non-mouillante, on constate l'absence de glissement dans le cas du mélange (fig. 5.13-a).

En raison de l'hétérogénéité du domaine (Fig. 0.12), les molécules d'hexadécane masquent la morphologie lisse de la surface non-mouillante pour les couches internes du lubrifiant qui sont composées principalement de méthane. En outre, la cohésion entre les molécules de méthane et la couche dense d'hexadécane est assez faible pour que cette dernière préfère coller aux surfaces. Le glissement aux parois disparaît complètement.

La majorité des molécules situées au centre du film est constituée de méthane (de faible viscosité), le frottement est ainsi remarquablement plus faible dans le cas du mélange que dans le cas de la solution pure d'hexadécane.

## 0.5.4 Mélanges de lubrifiants polaires

Les additifs anti-usure sont des composés chimiques qui sont fréquemment ajoutés pour améliorer les performances des huiles. Ces additifs protègent les surfaces par des processus d'adsorption physique ou chimique. Les couches protectrices réduisent considérablement le frottement et l'usure et améliorent la durée de vie des éléments mécaniques.

Le ZDDP (Zinc dialkyl-dithio-phosphate) est un exemple représentatif d'un additif anti-usure classique utilisé dans les huiles commerciales pour moteurs à combustion interne [108]. En dépit de ses excellentes propriétés anti-usure, cet additif est connu pour produire un frottement plus important dans les conditions de la lubrification mixte [108]. Des études expérimentales récentes [109] ont montré que l'ajout de 5% de concentration en masse de ZDDP à une solution d'huile de base d'hexadécane donne environ 40% d'augmentation de frottement par rapport à l'hexadécane pur. En utilisant la simulation dynamique moléculaire, cette section vise à identifier les principales raisons de ce comportement dans des conditions de confinement moléculaire.

Dans la configuration moléculaire initiale (Fig. 0.14), les molécules de ZDDP sont positionnées au centre du film. Cependant, dès que le cisaillement commence, les molécules de ZDDP s'orientent vers les surfaces d'oxyde de Fer. Cela se produit avec les deux types de surfaces mouillantes et non-mouillantes. Des aperçus du système au cours du cisaillement sont donnés dans la Fig. 0.14 pour le cas des surfaces non-mouillantes.

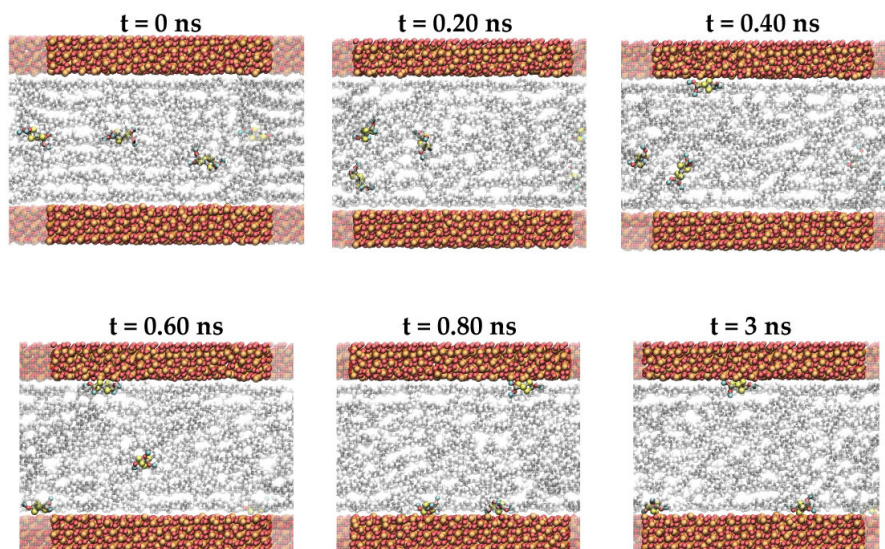


**Fig. 0.14 : Aperçus du système moléculaire au cours du cisaillement dans le cas des surfaces non-mouillantes de l'oxyde de fer. Les molécules de ZDDP sont en couleur tandis que les molécules d'hexadécane sont représentées en noir et blanc.**

Ce phénomène peut s'expliquer par la nature polaire des molécules de ZDDP. Les charges atomiques interagissent par des forces électrostatiques avec les surfaces oxydées. En revanche, les molécules saturées d'hexadécane ne présentent pas de telles interactions à longue distance avec les surfaces. De plus, le cisaillement joue un rôle encourageant de ce phénomène car elle provoque un alignement des molécules de lubrifiant.

Les profils de vitesse dans les films d'hexadécane et le mélange d'hexadécane et de ZDDP sont donnés dans la Fig. 0.15. Avec la surface mouillante, les profils de vitesse avec et sans ZDDP sont très proches, avec une absence du glissement aux parois. Dans le cas des surfaces non-mouillantes, la présence de ZDDP produit une atténuation significative du glissement par rapport au cas de l'hexadécane pur.

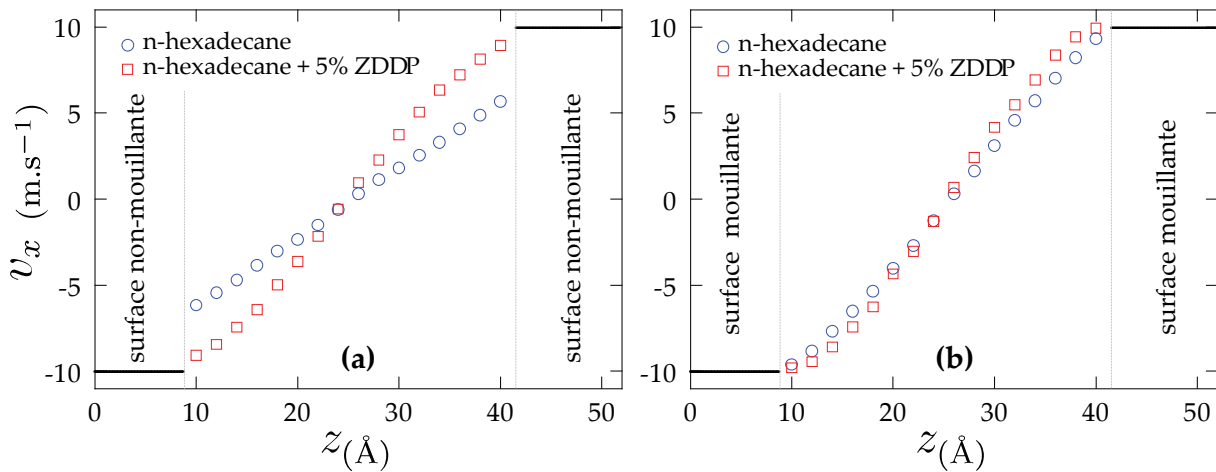


**Fig. 0.15 : Profils de vitesses à travers des films d'hexadécane pur et d'un mélange d'hexadécane et de ZDDP. Le taux de cisaillement apparent dans toutes les simulations est de  $6,9 \times 10^9 \text{ s}^{-1}$ .**

La réduction du glissement est due à la migration moléculaire du ZDDP. Quand les molécules de ZDDP sont adsorbées à la surface (Fig. 0.14), la corrugation effective des surfaces est augmentée. Cela améliore le transfert d'énergie cinétique vers le film d'hexadécane.

La présence de ZDDP augmente la valeur du taux de cisaillement moyen dans le centre du film. Ceci provoque une augmentation du frottement dans le cas du mélange par rapport au cas de l'hexadécane pur.

## 0.5.5 Conclusion

Le frottement dans les films confinés à l'échelle moléculaire est influencé autant par les propriétés de surface que par la nature moléculaire du film lubrifiant. Dans les films constitués d'un seul type de molécules, l'augmentation de la longueur de chaîne moléculaire et la ramification atténuent le phénomène de structuration moléculaire à travers le film lubrifiant. La cohésion interne du lubrifiant devient aussi plus forte. Dans le cas des surfaces mouillantes, la longueur moléculaire et le degré de ramification influencent le frottement via la variation de la viscosité. Cependant près des surfaces non-mouillantes, la cohésion interne des molécules longues et ramifiées peut devenir plus forte que leur cohésion avec les surfaces. Il en résulte un glissement plus important près des parois et une atténuation marquée du frottement.

Dans les mélanges de molécules saturées de longues et courtes chaînes, le film devient hétérogène sous cisaillement. Les molécules longues se rapprochent des surfaces tandis que la partie centrale du film reste occupée par les molécules courtes. En raison de la faible viscosité des molécules courtes, une faible résistance à l'écoulement est observée dans le cas du mélange comparé à la solution composée de molécules longues.

Enfin, un mélange d'hexadécane et ZDDP, représentatif de lubrifiants commerciaux, a été étudié dans les conditions de la lubrification moléculaire. En accord avec les expériences, la présence de ZDDP a entraîné une augmentation de frottement par rapport à l'hexadécane pur. La migration moléculaire et l'adsorption physique des molécules de ZDDP sur les surfaces sont à l'origine de ce phénomène. Lorsque ces molécules sont collées aux surfaces, elles

réduisent considérablement le glissement qui se produit naturellement avec de l'hexadécane pur. Il en résulte une augmentation globale du taux de cisaillement moyen au centre du film qui est cisailé à un taux plus élevé et finalement, un frottement plus élevé est obtenu, en accord avec les résultats expérimentaux.

## Conclusion générale et perspectives

Dans cette thèse, une approche numérique basée sur des simulations de dynamique moléculaire a été développée dans le but d'étudier les mécanismes locaux de la lubrification à l'échelle nanométrique. Les éléments du modèle ont été explicitement caractérisés de façon à reproduire les propriétés des matériaux et un comportement interfacial du système moléculaire les plus réalistes

Une attention particulière a été accordée à la méthodologie de dissipation de la chaleur dans les simulations, notamment en raison de sa relation avec le frottement. Les mécanismes de transformation et de dissipation d'énergie dans les films confinés ont été étudiés en détail. Lorsque les surfaces glissent à une vitesse modérée, l'énergie mécanique est totalement adsorbée par le lubrifiant, convertie en chaleur et complètement dissipée par le thermostat. En conséquence, la température globale reste constante. Toutefois, quand un taux de cisaillement critique est dépassé, le système commence à s'échauffer et, à partir de ce point, une méthode appropriée de dissipation d'énergie devient nécessaire.

Des méthodes avancées ont été comparées dans le régime d'échauffement et les résultats ont montré que si les surfaces sont autorisées à s'échauffer, elles s'adaptent plus naturellement à l'augmentation de la température du lubrifiant. Une nouvelle méthode pour appliquer des conditions aux limites thermiques originales a été introduite à cet effet. Le principe est que la température des surfaces peut être mise à jour lors de la simulation, selon le flux de chaleur provenant du contact.

Le modèle moléculaire et les conclusions acquises sur les effets thermiques ont été mis en application afin d'étudier différents effets se produisant à l'échelle nanoscopique et qui donnent sa particularité à la lubrification moléculaire.

Premièrement, l'influence de la nature des surfaces sur le frottement a été considérée. Une nouvelle procédure a été développée pour caractériser des surfaces réalistes avec deux paramètres qui représentent les potentiels physiques d'adsorption et de corrugation. Les simulations ont montré qu'un film de lubrifiant présente des propriétés structurales et dynamiques différentes selon le type de surfaces entre lesquelles il est confiné. Le phénomène de structuration devient plus prononcé près des surfaces caractérisées par un potentiel d'adsorption élevé. D'autre part, les variations du potentiel d'interaction (corrugation) influencent le glissement du lubrifiant par rapport aux parois. La résistance des molécules du lubrifiant au mouvement relatif des surfaces, qui donne le frottement du contact, s'est avérée essentiellement dépendante de la condition de glissement (mouillabilité). Dans le cas des surfaces de faible corrugation (surfaces non mouillantes), le lubrifiant glisse aux parois et le film devient effectivement cisailé à un taux de cisaillement inférieur au taux apparent. Il en résulte un plus faible coefficient de frottement.

Deuxièmement, l'influence de la structure moléculaire du lubrifiant sur les propriétés tribologiques du contact a été étudiée pour des surfaces mouillantes et non-mouillantes. L'influence de différents paramètres a été examinée : la longueur de chaîne, le degré de ramification, le mélange de lubrifiants non-polaires et, enfin, le mélange de fluides polaires. Les simulations ont montré que la longueur de chaîne influence considérablement le glissement aux parois. Les longues molécules glissent plus facilement à l'interface solide. Cela pourrait s'expliquer par la forte cohésion interne qui est due à la formation de ponts (liaisons) entre les couches consécutives au travers du film lubrifiant. En dépit de leur viscosité supérieure, les films lubrifiants constitués de longues molécules ne génèrent pas de frottement nettement supérieur à celui obtenu avec des molécules plus courtes dans le cas de surfaces non-mouillantes, en raison du phénomène de glissement. D'autre part, avec des surfaces mouillantes, puisque aucun glissement ne se produit, le frottement augmente naturellement avec la longueur de chaîne en raison de la viscosité qui croît également. La présence de ramifications a les mêmes conséquences que l'augmentation de la longueur des chaînes moléculaires. Du fait de leur viscosité élevée, les molécules ramifiées génèrent un frottement plus important que les molécules linéaires. Par contre, elles montrent un glissement plus prononcé aux parois en raison de leur forte cohésion interne, ce qui limite l'augmentation de frottement.

Dans les films lubrifiants constitués d'un mélange des molécules saturées de différentes longueurs de chaîne, le cisaillement provoque une ségrégation moléculaire. Les longues molécules se rapprochent des surfaces tandis que les molécules plus courtes restent au centre du film. Cette structuration hétérogène influence les propriétés d'écoulement et donc le frottement du mélange confiné. D'une part le glissement, présent dans le cas des solutions pures, disparaît complètement même en présence de surfaces non-mouillantes. Par ailleurs la partie centrale du film est principalement constituée de molécules courtes, donc de faible viscosité. En conséquence, le coefficient de frottement mesuré pour le mélange est relativement faible.

Enfin, un mélange modèle d'un lubrifiant commercial, comprenant de l'hexadécane comme huile de base et du ZDDP comme additif anti-usure a été étudié. La nature des surfaces, la composition du lubrifiant et les conditions de la simulation ont été choisies pour être représentatives d'une application industrielle. Les simulations ont montré que les molécules polaires de l'additif sont attirées par les surfaces oxydées où elles se trouvent finalement adsorbées. A l'interface des surfaces non-mouillantes, cette migration provoque une atténuation complète du glissement aux parois. Par ailleurs elle entraîne une augmentation du taux de cisaillement effectif au centre du film. Les simulations ont montré que le frottement mesuré était plus élevé en présence de ZDDP, comme observé lors des expériences de référence réalisées dans des conditions similaires.

Il existe de nombreuses possibilités d'utilisation du modèle développé dans ce travail pour étudier un large choix de structures de surfaces et de types de lubrifiants. Des études plus approfondies sur l'influence de la forme moléculaire et la polarité du lubrifiant à proximité de surfaces réalistes peuvent être entreprises pour généraliser les effets présentés dans cette thèse. En outre, en étudiant de nouveaux modèles de surfaces, il pourrait être intéressant de déduire des lois globales qui rapportent, depuis l'échelle moléculaire, le glissement lubrifiant/surface au potentiel d'adsorption des surfaces. Ces lois pourraient être intégrées dans des simulations à grande échelle comme en élastohydrodynamique, pour prendre compte du glissement interfacial qui joue un rôle important à l'échelle nanométrique.

Bien que les effets moléculaires présentés dans ce mémoire aient été établis pour un nombre limité de conditions opératoires, ils pourraient également être étudiés dans des conditions plus sévères de vitesse, pression, température et confinement. Pour accéder à ces régimes de cisaillement élevé, les méthodes appropriées de dissipation énergétique développées dans cette thèse constitueraient une base solide.

Il serait également intéressant d'étudier l'effet de la rugosité réelle (géométrique) des surfaces sur la structure et la dynamique des lubrifiants confinés. Ce travail serait complémentaire de celui entrepris dans cette thèse sur les effets de la corrugation physique. Dans la configuration surfaces rugueuses, le modèle moléculaire pourrait être utilisé pour simuler les conditions conduisant à la perte du contact fluide solide (rupture de lubrification). A partir de l'analyse de ces simulations, il serait envisageable de fournir des indications sur les propriétés souhaitables des lubrifiants dédiés aux conditions de fonctionnement sévères telles que celles rencontrées dans les régimes de lubrification mixte ou limite.

# Nomenclature

---

## Roman symbols

$a$	[Å]	Distance between unit cells in a lattice along the first principle axis.
$a(t)$	[Å.fs <sup>-2</sup> ]	Atomic acceleration at instant t.
$c$	[Å]	Distance between unit cells in a lattice along the third principle axis.
$C_\theta$	[Kcal.mol <sup>-1</sup> rd <sup>-2</sup> ]	Half of the angular spring constant in molecular bending interactions.
$C_{\text{Bridge}}$	dimensionless	Bridging coefficient.
$c_L$	dimensionless	Lindemann criterion.
$\tilde{d}$	[Å]	Distance to the nearest atom.
$d$	[Å]	Scan elevation.
$\bar{d}_c$	dimensionless	Reduced average distance of the ZDDP molecules from the film centre.
$dz$	[Å]	Surface thickness in the molecular model.
$E_0$	[Kcal.mol <sup>-1</sup> ]	Total initial energy of the system.
$E_{\text{ads}}$	[Kcal.mol <sup>-1</sup> ]	Per-molecule lubricant adsorption energy on solid surfaces.
$E_{\text{in}}$	[Kcal.mol <sup>-1</sup> ]	Input mechanical energy by surface sliding and normal loading.
$E_k$	[Kcal.mol <sup>-1</sup> ]	Total kinetic energy of the molecular system
$E_{\text{out}}$	[Kcal.mol <sup>-1</sup> ]	Output (dissipated) energy by the thermostat.
$E(t)$	[Kcal.mol <sup>-1</sup> ]	Total energy of the system at instant t.
$F$	[Kcal.mol <sup>-1</sup> ]	Embedded energy function depending on the electron density.
$f_i$	[nN]	Total force acting on atom "i".
$F_c, F_f, F_r$	[Kcal.mol <sup>-1</sup> .Å <sup>-1</sup> ]	Conservative, friction, and random forces in Langevin thermostat.
$F_x$	[nN]	Total resistive force to the constant velocity surface sliding.
$h$	[Å]	Thickness of the confined film (on the z-dimension).

$\hbar$	[J.s <sup>-1</sup> ]	Plank angular constant
$K$	[Kcal.mol <sup>-1</sup> Å <sup>-2</sup> ]	Half of the spring constant in the Harmonic bonds interaction model.
$K_0$	[GPa]	Bulk modulus.
$k_B$	[J.K <sup>-1</sup> ]	Boltzmann constant.
$l$	[Å]	Bond-length at a given instant.
$l_0$	[Å]	Equilibrium bond-length.
$m$	[amu][Kg]	Atomic/molecular mass.
$M$	[amu]	Mass of a single lubricant molecule.
$m_i$	[amu]	Mass of atom "i".
$n$	dimensionless	Number of carbons in alkane molecules.
$\tilde{n}$	dimensionless	Index of temperature update.
$N$	dimensionless	Total number of atoms in the system.
$N_c$	dimensionless	Total number of constraints.
$N_{dof}$	dimensionless	Number of degrees of freedom in the molecular system.
$N_x$	dimensionless	Number of scanning atoms in the surface scan procedure.
$N_y$	dimensionless	Number of snapshots taken during a surface scan.
$P$	[Kg.m.s <sup>-1</sup> ]	Total linear momentum transferred in NEMD simulations.
$p_i$	[Kg.m.s <sup>-1</sup> ]	Linear momentum of atom i.
$q$	[e <sup>-</sup> ]	Atomic charge.
$Q$	[Kcal.mol <sup>-1</sup> ]	Exchanged heat in the NEMD simulations.
$Q_b$		Thermal inertia (mass) of the Nosé-Hoover heat bath.
$r$	[Å]	Distance between two interacting atoms.
$r(t)$	[Å]	Atomic position at instant t.
$r_i$	[Å]	Position vector of atom "i".
$\ddot{r}_i$	[Å.fs <sup>-2</sup> ]	Acceleration vector of atom "i".
$S$	[Å <sup>2</sup> ]	Surface area normal to the heat transfer direction (z).
$\tilde{s}$		Added degree of freedom in Nosé-Hoover extended system method.
$t$	[ns]	Time.
$T$	[K]	Temperature calculated in layers normal to the heat transfer direction.
$T_t$	[K]	Target temperature.
$T(t)$	[K]	Instantaneous kinetic temperature.
$T_0$	[K]	Initial temperature of the molecular system.

$T_w$	[K]	Temperature of the wall (surface) in direct interaction with the confined film.
$T_\infty$	[K]	Surroundings temperature, far from the contact.
$u, v_x$	[m.s <sup>-1</sup> ]	Fluid shear velocity calculated in normal layers to the momenta transfer.
$V$	[Kcal.mol <sup>-1</sup> ]	Total potential energy due to the intermolecular interactions with surrounding atoms.
$\bar{v}$	dimensionless	Ratio of the average streaming velocity of the ZDDP molecules to the surface sliding speed.
$\bar{v}_i$	[m.s <sup>-1</sup> ]	Streaming velocity (in the shear direction) of ZDDP molecule i.
$v(t)$	[Å.fs <sup>-1</sup> ]	Atomic velocity at instant t.
$V_{\text{angle}}$	[Kcal.mol <sup>-1</sup> ]	Molecular bending angle interactions potential energy.
$V_{\text{bond}}$	[Kcal.mol <sup>-1</sup> ]	Molecular bonding interactions potential energy.
$V_{\text{torsion-X}}$	[Kcal.mol <sup>-1</sup> ]	Molecular twisting (dihedral angle) interactions potential energy (model X).
$V_{\text{(EAM)}}$	[Kcal.mol <sup>-1</sup> ]	Embedded Atoms Method interaction model potential energy.
$V_{\text{(HB)}}$	[Kcal.mol <sup>-1</sup> ]	Harmonic bonds interactions potential energy.
$V_{\text{(LJ)}}$	[Kcal.mol <sup>-1</sup> ]	Lennard Jones model interactions potential energy.
$x_O, z_{\text{Fe}}$	dimensionless	Internal degrees of freedom for the respective atoms in the crystalline structure.
$Z_c$	[Å]	Z elevation of the center plane of the film.
$Z_i$	[Å]	Z coordinate of the center of mass of ZDDP molecule i.

## Greek symbols

$\alpha$	[m <sup>2</sup> .s <sup>-1</sup> ]	Thermal diffusivity of the boundary surface.
$\alpha_d$	[N.s.m <sup>-1</sup> ]	Damping coefficient for phantom layer-fixed layer atomic interactions
$\dot{\gamma}, \dot{\gamma}_{\text{app}}$	[s <sup>-1</sup> ]	Apparent shear rate.
$\dot{\gamma}_c$	[s <sup>-1</sup> ]	Critical shear rate beyond which a hexadecane confined lubricant starts heating.
$\dot{\gamma}_{\text{eff}}$	[s <sup>-1</sup> ]	Effective shear rate in the central part of the film.
$\delta t$	[fs]	Simulation time-step.
$\Delta t$	[fs]	Velocity rescaling interval.
$\Delta \tilde{t}$	[ns]	Wall temperature update interval in the VBT method.

$\Delta T$	[K]	Lubricant average temperature increase due to shearing.
$\langle \delta u^2 \rangle$	[Å]	Average Mean square displacement of the atoms in the system.
$\Delta x$	[Å]	Simulation box length on the x-dimension.
$\Delta y$	[Å]	Simulation box length on the y-dimension.
$\Delta z$	[Å]	Simulation box length on the z-dimension.
$\epsilon$	[K]	Lennard Jones potential well-depth / energy parameter.
$\epsilon_{\text{ads}}$	[Kcal.mol <sup>-1</sup> ]	Adsorption parameter obtained from the surface scan.
$\epsilon_{\text{AB}}$	[Kcal.mol <sup>-1</sup> ]	LJ interaction well-depth between atoms of types A and B.
$\epsilon_{\text{corr}}$	[Kcal.mol <sup>-1</sup> ]	Corrugation parameter obtained from the surface scan.
$\epsilon_{\text{wf}}$	[ε]	Wall fluid interaction well depth in LJ reduced units.
$\eta_0$	[mPa.s]	Estimated Newtonian (zero-shear) viscosity.
$\eta_{\text{eff}}, \eta$	[mPa.s]	Dynamic viscosity of the confined film.
$\theta_{\text{d}}$	[K]	Debye temperature of the boundary surface.
$\theta$	[rd]	Angle between three consecutively bonded atoms at a given instant.
$\theta_0$	[rd]	Equilibrium angle between three consecutively bonded atoms.
$\kappa$	dimensionless	The ratio of the wall-fluid to the fluid-fluid LJ well-depths.
$\lambda$	[W.m <sup>-1</sup> K <sup>-1</sup> ]	Thermal conductivity.
$\tilde{\lambda}$	dimensionless	Velocity rescaling factor
$\rho$	[Kg.m <sup>-3</sup> ]	Mass density across the confined film.
$\bar{\rho}$	[Kg.m <sup>-3</sup> ]	Average density across the confined lubricant film.
$\rho_e$		Electron density from the surrounding atoms in the EAM model.
$\rho_{\text{max}}$	[Kg.m <sup>-3</sup> ]	Density peak in the first lubricant layer adjacent to the surface.
$\sigma$	[Å]	Lennard Jones distance parameter.
$\sigma_{\text{AB}}$	[Å]	LJ distance parameter for interactions between atoms of types A and B.
$\tau$	[ps]	Lennard Jones time scale.
$\tau_{\text{xz}}^{\text{ex}}$	[MPa]	Total shear stress due to the exchanged linear momenta.
$\tau_{\text{NH}}, \tau_{\text{L}}$	[fs]	Nosé-Hoover and Langevin thermostats temperature relaxation time.
$\tau_{\text{xz}}$	[MPa]	Apparent (total) shear stress calculated at the surfaces level.
$\phi$	[rd]	Dihedral angle between four consecutively bonded atoms.
$\phi^{\text{ex}}$	[W.m <sup>-2</sup> ]	Exchanged heat flux in the non-equilibrium simulations.

$\phi^{pw}$	[Kcal.mol <sup>-1</sup> ]	Pairwise interaction potential in the EAM model.
$\phi_w$	[GW.m <sup>-2</sup> ]	Heat flux generated and conducted from the film to the boundary wall.
$\Phi(x, y)$	[Kcal.mol <sup>-1</sup> ]	Potential energy felt by a scanning atom at position (x,y).
$\omega_B$	[rd.s <sup>-1</sup> ]	Debye frequency of the surface



# Introduction

---

Friction is the resistive force to the relative motion of two bodies in contact. Without friction, we would not be able to accomplish many simple tasks like starting and stopping our cars, standing and walking on the ground, shaving, brushing our teeth, wearing clothes or making fire by rubbing two wooden sticks together. A life without friction is certainly hard to imagine, but a life with controlled friction is undoubtedly one of the ultimate goals of modern technology.

A significant portion of research aims to optimize the energetic efficiencies of everyday technology products that operate on non-renewable sources of energy such as household items, robots and transportation devices. Many of these products generate mechanical energy by motion. Unfortunately, whenever there is motion, there is friction. Friction losses between mechanical components account to the largest portion of the total energetic losses. Friction thus has a non-negligible economical as well as environmental impact.

Lubrication technology aims to reduce the losses which are due to direct solid-solid contact and to improve the longevity of mechanical components. The principle is simple: by adding a lubricant (solid, liquid, or gas) that separates any two contacting surfaces, the negative effects of dry sliding such as surface adhesion and wear can be avoided. Friction between the surfaces and a lubricant is notably lower than between the two surfaces in dry contact. At the same time, a compromise is made between the tribological performance of lubricants and their environmental side-effects. As lubricants, organic oils have satisfactory performance in applications with moderate velocities, pressures, and operating temperatures. However, under more severe conditions like those encountered in machining processes or inside internal-combustion engines, the use of additives becomes indispensable for improving the tribological performance.

Modern lubricant design is facing increasing technological challenges such as component downsizing and limiting the oil consumption for environmental purposes. In compacted systems such as optical storage devices and micro motors, lubricants are often found operating under molecular scale confinements. On another level, there is an increasing demand for using very thin lubricant films, even in larger scale applications such as rolling-element bearings, for both environmental and economical factors. In such circumstances and under current industrial operating conditions, nano-meter films can be easily found in contact sub-regions either during the normal running process or during critical periods like start up and shutdown.

The work presented in this thesis deals with molecular lubrication problems where the lubricating fluid is only a few nanometers thick. In such confined contacts, the tribological properties of lubricants are very different than those in large separations. They depend on

effects occurring over nano scales of time and space and are closely related to the molecular structure and interactions between lubricant molecules and the bounding surfaces. A numerical approach using Molecular Dynamics simulations is used throughout this thesis for accessing the local mechanisms of lubrication under severe confinement. Among the considered effects are those of the surface physical properties of corrugation and adsorption with respect to the lubricant molecular structure. Another effect of importance concerns the transformation of mechanical energy into heat and its subsequent dissipation.

The presented research begins with a review on the state of the art (Chapter 1) on the structural and dynamic properties of confined liquids sheared between two solid substrates. The experimental and numerical works from the literature are presented in separate sections. Particular phenomena occurring in confined films are presented including film structuring, solidification and boundary slip. This review on the state of the art offers a strong foundation for interpreting the simulation results presented in the following chapters.

In Chapter 2, a numerical MD model of molecular lubrication is developed which allows a wide choice of realistic tribological surfaces and lubricants to be modeled. The model is parameterized to give realistic thermal and mechanical properties of the surfaces, the lubricant as well as their interface.

Energy dissipation in the model which is closely related to the friction is discussed in details in Chapter 3. For different operating conditions, guidelines are given in this chapter for employing the correct energetic dissipation method. For highly sheared cases, a novel method is also presented which allows physical and representative heat dissipation from the contact to be modeled.

The molecular model is then employed for investigating several molecular effects occurring in confined lubricant films. In Chapter 4, the effect of surface atomic structure is studied by comparing how the same lubricant behaves when confined between five different realistic surface materials. The structural and dynamic behaviors of the confined lubricant are explained according to the surface properties of physical adsorption and corrugation. Finally, in Chapter 5, the relationship between the lubricant molecular structure and its tribological performance is investigated for the two typical cases of wetting and non-wetting surfaces. Lubricants of different chain lengths and branching degrees are studied in pure solutions as well as in mixtures.

The general conclusion and prospects part of this manuscript recapitulates the main ideas of the conducted research, the main results presented throughout the different chapters, and finally suggestions for future work.

<b>1   State of the art</b>	<b>4</b>
<b>1.1 Tribology: historical review</b>	<b>4</b>
<b>1.2 Lubrication regimes</b>	<b>7</b>
1.2.1 Full film lubrication	7
1.2.2 Mixed lubrication	8
1.2.3 Boundary lubrication	8
<b>1.3 Molecular lubrication</b>	<b>9</b>
1.3.1 Experimental work	10
1.3.1.1 Structuring and solvation force	10
1.3.1.2 Nano-rheology	12
1.3.1.3 Friction curves	15
1.3.1.4 Boundary flow	17
1.3.2 Numerical work	19
1.3.2.1 Simulation methods	20
1.3.2.2 Structural effects and solvation forces	21
1.3.2.3 Nano-rheology	24
1.3.2.4 Boundary flow	27
<b>Conclusion</b>	<b>29</b>

# 1. State of the art

---

Friction is a reaction force which hampers or resists the relative motion of two bodies in contact. It is directly related to the normal reaction force with a coefficient, given experimentally, called the friction coefficient. Dry friction between machine elements results in material wear, fatigue, elastic/plastic deformations, and surface adhesion with the generated heat in the contact. Intermolecular friction also occurs inside fluids giving rise to the notion of viscosity.

When a third body (solid, liquid, or gas) separates the two principle bodies in motion, it can gently accommodate their velocity difference resulting in reduced friction and wear. This is the phenomenon of lubrication. Tribology, the science of friction, lubrication, and wear, is without doubt a multidisciplinary science as it is often related to material and thermal sciences, rheology and fluid dynamics, as well as surface chemistry. When it comes to the nano-scale limit, tribology becomes involved with molecular scale mechanics and quantum physics.

## 1.1 Tribology: historical review

There is no doubt that Man thought about friction and the means of reducing it a very long time ago [1, 2, 3]. In fact, the first wood/stone mechanical systems date to earlier than 4000 B.C. and some of these systems were actually lubricated using animal fat. In recent documented history, the study of friction was limited to machinery design. It was only rarely, until recently, a subject taken independently by researchers. This is perhaps due to the complexities that arise due to the multiphysics nature of the friction mechanisms. However, with the industrial revolution came the development of heavy loaded machinery that incorporate complex mechanical couplings, contacts, and relative motions. It thus brought an essential need for a serious analysis of the friction, wear and lubrication phenomena. The control of frictional losses contributes not only to the longer lifespan of single machine elements but also the reliability and productivity of complete industrial chains.

Leonardo da Vinci is known to be one of the fathers of modern tribology. Although his manuscripts were lost for a quarter of a millennium, it is established that he was the first to quantify friction forces and introduce the notion of friction coefficient (first law of friction). In his work on dry friction, he showed that the apparent surface of contact between two moving bodies has no influence on the friction force (second law of friction, Fig. 1.1). He studied several related topics such as wear and its mechanisms, the design of lubrication systems, gears, screw-jacks, and rolling-element bearings. His work shows an incredible procession to the existing knowledge and technology of his era.

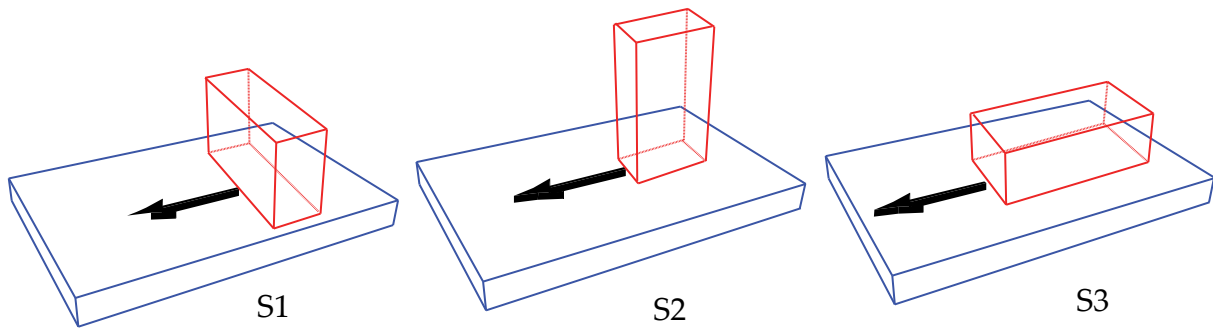


**Fig. 1.1 : A schematic of Leonardo da Vinci's experiment which he used to prove that the friction force is independent of the apparent area of contact.**

Amontons was among the pioneers to put standards in friction science as he rediscovered the two da Vinci friction laws [1]. He was succeeded by others to perform dry contact experiments between different materials in order to study the heat generation and solid adhesion as well as to analyze the effect of surface roughness on friction. However, the very first theoretical approach to the problem was by Euler in 1750 in two papers in which he defined the concept of friction and the friction angle; concepts which are still considered nowadays in many engineering applications. He also differentiated between static and dynamic friction and represented surface roughness as pyramid models.

During the industrial revolution, Coulomb conducted several experiments in order to identify the parameters which influence friction in sliding and rolling conditions. Among these parameters are the material nature, fluid lubrication, apparent area of the contact, loading pressure, and finally the relaxation time of the contacting surfaces prior to experiment. His experiments were able to confirm Amontons laws and to show in addition that the friction coefficient depends on the surface roughness. He also showed that, in many cases, the dynamic friction coefficient does not vary with the sliding velocity; this was later attributed to him as the third law of friction.

The first significant work on lubricated friction was carried out by Hirn in 1847 [1]. He studied experimentally the evolution of the friction coefficient under constant load but variable velocity in both dry and lubricated contacts. In lubricated contacts, he found that the friction coefficient is unstable for low velocities. When velocity is increased, friction becomes stable and then decreases until it reaches a minimum. At constant temperature, the friction coefficient then increases proportional to the velocity. Due to their apparent conflict with Coulomb's third law of friction (for a constant friction coefficient with velocity) Hirn's results were rejected and were not published until 1854. These results however showed that a novel analysis of the dynamic friction in fully lubricated contacts was needed and that the three friction laws for dry contacts were no longer applicable.

Theoretical formulation of the fluid dynamics equations was established by the mathematician Navier in 1822. Navier based his equations on Euler's previous work and introduced the viscosity (flow resistance) into the fluid dynamics equations. These equations are referred to as the Navier-Stokes equations; Stokes being the first to solve them for simple cases. In 1886, Reynolds proposed the theory of hydrodynamic lubrication by reducing the general Navier-Stokes equations for a thin full film lubrication problem [4]. Reynolds discussed the physical origins of hydrodynamic pressure which develops in lubricated journal bearings; an experimental finding by Tower in 1883. He also explained that in some cases of high shearing, while a lubricant still completely separates the sliding surfaces, the friction

coefficient becomes no longer proportional to the velocity due to thermal effects that influence the flow resistance of the lubricant.

Considerable research on dry friction was carried out throughout the twentieth century. The friction results of Coulomb are still widely applied for studying dry contacts [1]. In 1938, Holm observed that plastic deformation of the asperities between contacting surfaces gives rise to the formation of junctions. Friction represents the force needed for shearing these junctions. Such a view is called the adhesion theory of friction. In the same context, Bowden and Tabor introduced in 1950 the notion of real contact area. It represents the total surface area of the plastically deformed summits which effectively bear the contact load. The real contact area, much smaller than the apparent ones, depends on the applied load and can be directly related to the friction coefficient.

As for fluid-lubricated contacts, Reynolds theory of hydrodynamic lubrication has been the cornerstone for most research over the last century. Theoretical solutions of the Reynolds equation were proposed for many simple lubricated systems and this had a big impact on bearings design. A recapitulative friction diagram which distinguishes three lubrication regimes was first proposed by Stribeck in 1902, based on his extensive experiments on lubricated journal bearings. The Stribeck diagram (Fig. 1.2) illustrates that the friction depends on the nature of the lubricant, the normal load, and the velocity. Under severe operating conditions, a transition occurs from hydrodynamic lubrication with full contact separation and relatively low friction to boundary lubrication where the load is carried by the contacting asperities and no longer by the hydrodynamic pressure of the lubricant. An intermediate mixed lubrication regime exists between these two extremities. In this regime, the load is distributed in some regions to deformed asperities as in dry contacts and in other regions to the confined lubricant which separates the interacting surfaces.

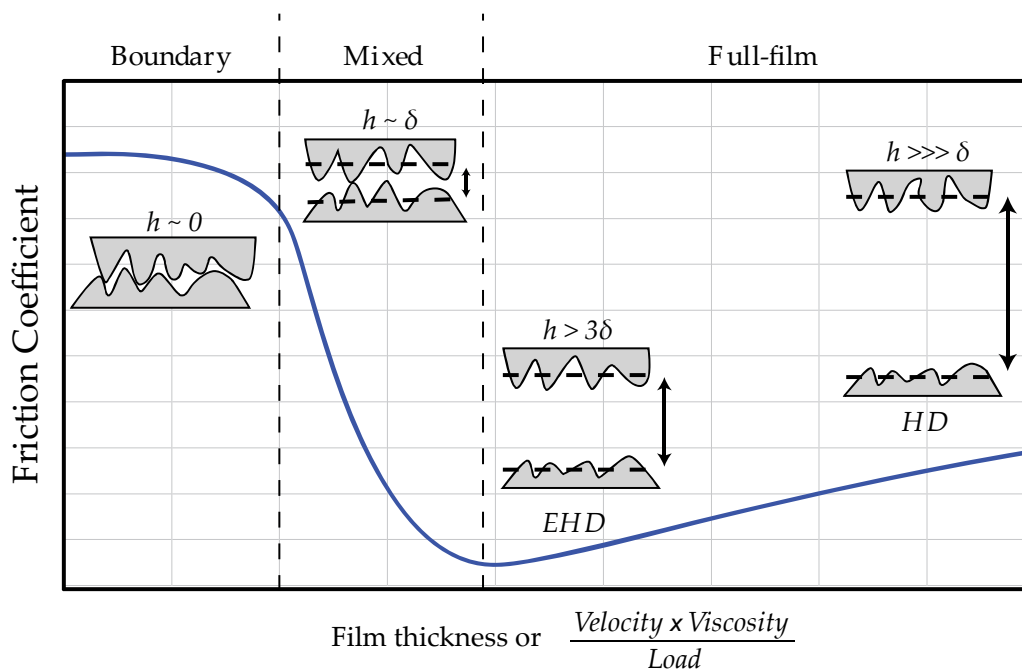


**Fig. 1.2 : Stribeck friction diagram illustrating the three lubrication regimes: boundary, mixed, and full-film lubrication. The transition between these regimes depends on the lubricant viscosity, velocity, and the normal load.  $\delta$  is the surface roughness rms. (based on [5])**

The research in lubricated friction can thus be classified according to the concerned lubrication regime which depends on the foreseen application. A detailed review on all of the work done in these areas is well beyond the scope of this section. Nevertheless, some generalities on the dominant lubrication mechanisms in each of the three regimes will be presented briefly. In the third section of this chapter, the transition is presented from the classic point of view given by the Stribeck diagram to the particular case of molecularly confined lubrication where the essential part of this thesis is set to contribute.

## 1.2 Lubrication regimes

The classification of lubrication regimes in this section is based on the classical view as originally demonstrated by the Stribeck diagram and experimental master curves [5]. Although this view of lubrication is widely accepted in the tribology community, it may still have some discrepancies while predicting friction in lubricated systems of molecular-scale confinement [6]. These particular aspects have only been recently accessible through experimentation and more details about them will be given in section 1.3. For the time being, the presented classification in this section is thus based on a global description of friction mechanisms in a lubricated contact problem with no special consideration of molecular scale effects.

### 1.2.1 Full film lubrication

The full film lubrication regime corresponds to the case where a continuous lubricant film separates the sliding bodies. If the formed lubricant film is sufficiently thick, the bodies do not contact each other directly. As a result, wear hardly occurs, and the load is carried out completely by the hydrodynamic pressure of the lubricant film. The frictional force is thus low and can be attributed to the viscosity of the lubricant. If the lubricant is Newtonian, meaning that its viscosity does not change with shear, the friction increases linearly with the shear rate. This ideal lubrication process is called Hydrodynamic Lubrication and generally occurs in low pressure contacts such as journal bearings where the contacting surfaces are conforming.

The equations describing this lubrication regime are derived from the basic equations of fluid dynamics with the assumptions of Reynolds hydrodynamic lubrication theory [4]. The general equations are reduced by considering the particular geometry of typical lubricant thin films (small thickness relative to the lateral extent). Moreover, the lubricant fluid is typically considered to be incompressible, Newtonian, and does not slip with respect to the bounding bodies.

Nevertheless, in many cases, the contact load may cause surface deformation. This occurs for example in rolling-element bearings or human and animal joints where elastic deformations take place. The elevated contact pressure may also influence the lubricant density and viscosity. When these phenomena occur, the system is said to operate in the Elasto-Hydrodynamic Lubrication (EHL) mode. This lubrication mode is thus characterized by quite elevated contact pressures which result in large elastic deformations of the contacting

bodies with respect to the film thickness in addition to important piezo-viscous effects inside the film.

The understanding of EHL mode is thus more complicated than hydrodynamic lubrication due to the multi-physics nature of the problem. An appropriate coupling is necessary between Reynolds equation giving the film thickness and classical structural mechanics equation giving the solid deformations. The problem becomes more complicated at high shear rates where viscous heating occurs inside the lubricant. Additional temperature-viscosity and temperature-density relationships need to be employed and thermal diffusion must be explicitly modeled inside the lubricant film and out of the bounding bodies in order to accurately describe the energy dissipation.

For these reasons, EHL is still an open subject for scientific research. The solutions of EHL problems are often given by using numerical methods that couple (fully or partially) as many physics as possible. The purpose is to have the best agreement with experimental results and eventually permit improved designs of EHL industrial applications such as rolling-contact bearings, gears, cam-tappets, etc.

### **1.2.2 Mixed lubrication**

From the hydrodynamic lubrication regime, when the Stribeck parameter (abscissa of Fig. 1.2) is lowered by increasing the load or decreasing the velocity, friction decreases gently until it reaches a minimum point (Fig. 1.2). At this point, the lubricant film becomes so thin that the surfaces, no matter how “smooth” they are, start interacting at the asperity level. In consequence, the friction increases as the number of asperity interactions increases. The load is thus carried in part by the interacting asperities and another part by the lubricant hydrodynamic pressure. Friction represents thus the force needed for shearing the lubricant and the formed junctions between micro-asperities

Machine elements that normally operate in full film lubrication often experience mixed lubrication during start-up and stopping [7]. The tribological performance of lubricants in this regime depends essentially on the ability of forming load-bearing layers (tribo-layers) that protect surfaces from direct contact, adhesion, and wear. A careful choice of the base oil and additives is thus necessary for lubricating machine elements which operate completely or partially under mixed lubrication.

### **1.2.3 Boundary lubrication**

When complete lubricant film rupture occurs, a boundary regime is established that depends uniquely on the nature of the interacting surfaces and their respective roughness. Thin load bearing layers from the lubricant are formed either by tribo-chemical reactions which are triggered by the temperature and pressure increase or by physical adsorption (Fig. 1.3). The load is carried only by the surface asperities and the effect of lubricant hydrodynamic pressure is completely lost. In this boundary regime, friction is independent of the load, velocity and lubricant viscosity. It is similar to dry kinetic friction and the ratio of tangential traction force to normal load is almost constant (Fig. 1.2).

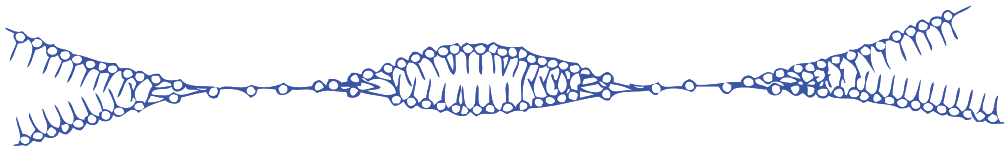


**Fig. 1.3: A schematic showing the interface between relatively moving bodies in boundary lubrication conditions. Although a high friction occurs, the thin adsorption layers of boundary additives can still protect the surfaces from seizure and wear in ideal dry friction scenarios. [8]**

### 1.3 Molecular lubrication

Molecular lubrication is the process which involves separating two relatively moving surfaces by a lubricant whose thickness is comparable to the molecular (nanometer) scale. Since most surfaces in engineering applications have roughness that extends well beyond the nanometer scale, ideal molecular lubrication hardly exists as a unique lubrication mode and is often present in sub-regions of mixed or boundary lubricated contacts. In these regions, a particular behavior emerges for molecularly confined films between interacting asperities. This has been classically conveyed by Hardy and Bowden models (Fig. 1.3) for boundary lubrication where a physically or chemically adsorbed lubricant monolayer was thought to play a tribological role in the severe confinement conditions [3].

Nowadays, the picture has changed. Classically full-film lubricated applications such as rolling element bearings are currently designed to employ thinner films. The predicted film thickness can be in the order of magnitude of only a few nanometers [9]. Moreover, whole new technologies have evolved around novel micro-fabrication techniques where the knowledge of the nano-scale is essential [10]. Information storage devices and micro-mechanical devices are examples where the tribology of coatings and lubricants in molecular confinement represents a real challenge for optimization and maintenance.

The study of molecular lubrication has nevertheless been limited due to difficulties in accessing the local time and length scales of molecular phenomena. Moreover, the complexity of the intervening physical and chemical effects makes it hard to construct universally representative models for the mixed and boundary lubrication regimes. However, thanks to recent developments of experimental and simulation methods that can access the molecular scale, it has become possible to investigate many of the particularities of molecular lubrication. Experimental and numerical studies were able to complement each other in describing molecular phenomena and giving intriguing insights about what occurs to a lubricant in molecular confinement.

The review on the state of the art is organized as follows. Experimental and numerical studies are considered in separate sections. Each section begins with a brief introduction on the methods employed for studying molecularly confined films. Subsequent results are then classified into three categories: structural properties, nano-rheology, and boundary flow. These effects being unique for molecular lubrication, the experimental and numerical results are compared in the conclusion at the end of this chapter.

### 1.3.1 Experimental work

Until now, it has been impossible to experimentally investigate molecular lubrication under the conditions of real engineering applications [11]. The smallest accessible lubrication scale is that of a single asperity contact. This has been possible thanks to the SFA (surface forces apparatus) and the AFM (atomic force microscope). These two experimental apparatus have undergone several modifications to allow the study of structural and dynamic properties of molecularly confined films between two contacting asperities [12]. In both apparatus, a careful calibration is needed for interpreting deflections and displacements (by optical or capacitance methods) into the equivalent normal and tangential forces [10, 12].

In the SFA, asperity contact is achieved by using a crossed cylinder set-up [12]. The cylinders are traditionally identical, of about one centimeter radius, made of silica, and are covered by molecularly smooth mica sheets. Although using mica is very common in SFA, a thin layer of any material can be deposited [12]. In an SFA experiment, the surfaces are pressed together using sensitive motors for coarse control and piezo crystals for molecular scale control. The surface separation and the area of the circular contact are measured with a resolution of about an Angstrom [10, 12, 13] using optical (transparent mediums) or capacitive methods [14] (opaque mediums). A spring is used to measure the normal force between the surfaces; it gives a force-measuring resolution in the range of 10 nN. The SFA set-up can be completely immersed in a lubricant or any controlled environment. This technique was improved by Israelachvili in 1986 to allow relative motions of the surfaces to be applied and lateral deformations, friction forces and effective viscosity of molecularly confined films to be measured with precision [12, 13, 15].

The AFM set-up is very similar to that of the SFA except that the forces are measured between a small tip and a sample surface instead of two macroscopic surfaces [10]. There is a large choice of material for the tip and cantilever which holds it and the tip radius can range from one atom to a micrometer [12], smaller tips being more interesting. In the range of commonly used tip sizes (10-100 nm), the adhesion forces can be in the order of 0.1-1 nN [12]. For that reason, high sensitivity micron-sized sensors have been specifically developed for the AFM, allowing 0.01 nm accuracy in cantilever deflection measurements for determining forces. Nevertheless, this technique has the disadvantage that the absolute separation between the tip and the surface and the real tip geometry is not exactly known since the tip can deform elastically or plastically during a measurement [12]. AFMs can operate in various environments but the signals need to be accurately calibrated to yield forces [10]. This technique has been extended to measure the lateral (friction) force and is sometimes referred to as the FFM (friction force microscope) [10].

#### 1.3.1.1 Structuring and solvation force

Under molecular confinement, it is inappropriate to consider lubricant films as a structureless continuum. The reason is that solid surfaces can modify the ordering inside the lubricant leading to structural forces when the two solids approach.

In 1981 Horn and Israelachvili [16] pioneered the SFA studies between two molecularly smooth mica surfaces that were separated by a molecular liquid film. In measurements with OMCTS fluid (Octamethylcyclotetrasiloxane, a non polar quasi-spherical molecule of a diameter that is approximately 0.9 nm), the normal (solvation) force is oscillatory as surfaces

are approached, varying between attraction and repulsion and with a periodicity that is equal to the molecular diameter of OMCTS (Fig. 1.4). The oscillations decay exponentially and within 6-10 molecular diameters, they almost vanish. Temperature has little effect on the solvation forces. The chemical properties of the surfaces and the liquid were shown, however, to quantitatively influence these forces. The presence of water in particular results in a decrease of oscillations to the limit where the forces become always attractive. The absolute value of the adhesion force increases about 7 times in the presence of water.

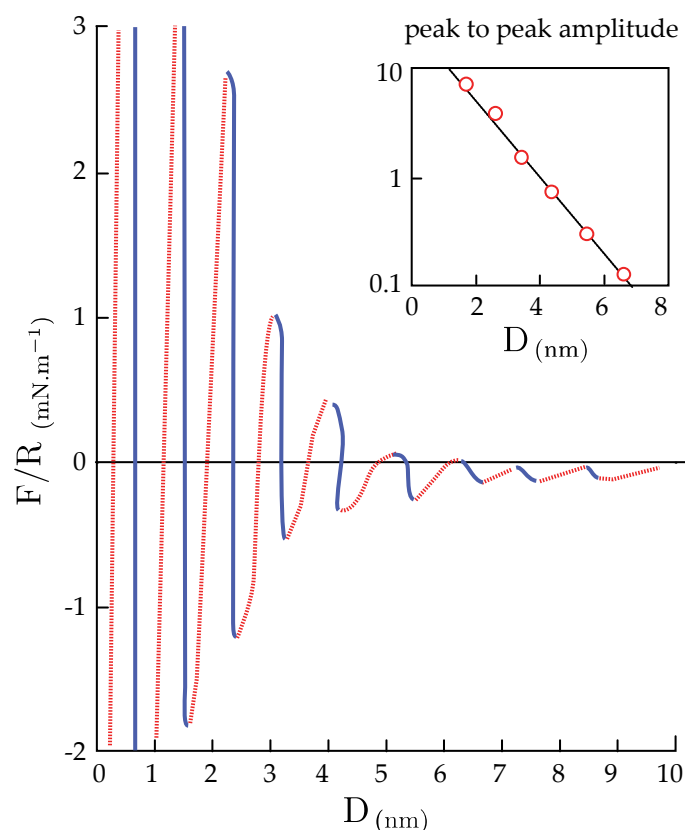


**Fig. 1.4: SFA experimental results of surface forces between curved mica surfaces separated by an OMCTS liquid. The red dotted segments correspond to unstable regions encountered when the surfaces are approached, characterized by abrupt jumps between two stable positions (blue continuous segments) (Results of Horn and Israelachvili [16])**

The surface force oscillation and its relationship with the liquid molecular diameter were explained by the phenomenon of liquid molecules being packed up into layers between the smooth solid surfaces [16]. As the separation is varied, the free energy has successive maxima and minima, and the surface force oscillates in the same manner.

The literature reports many SFA studies for determining the solvation forces between mica surfaces that are separated by all kinds of liquids: simple polar [16, 17, 18, 19], non-polar [20], hydrogen bonding, polymer solutions [21], and others. The main conclusions are that the short-range oscillatory solvation force is insensitive to polarity or temperature, but is very sensitive to the presence of water.

Liquid alkanes of different molecular weights show identical solvation force oscillations with a periodicity that is equal to a molecular width (0.4 nm) [19]. The molecular length hav-

ing no detectable effect, this indicates that simple alkanes are aligned parallel to the surfaces (unlike the classical Bowden model of Fig. 1.3). Furthermore, only 6 minima in the oscillatory force with alkanes can be detected by the SFA compared to 9-10 minima for spherical molecules (Fig. 1.4). This means that with alkane chains, the phenomenon of layering becomes undetectable beyond 3 molecular diameters from each surface.

Finally, in polymers, the force oscillations also exist but they can extend to separations that exceed the polymer radius of gyration [21].

### 1.3.1.2 Nano-rheology

In addition to the structural effects presented previously, dynamic properties of lubricants are also strongly influenced by the level of confinement.

In 1985, Chan and Horn used the SFA to measure the drainage rates of molecularly confined films of saturated Newtonian liquids between smooth mica sheets [15]. It was found that Reynolds hydrodynamic theory of lubrication accurately predicts the drainage rate down to a separation of about 50nm with no apparent change in bulk viscosity. From 50nm down to 10nm, a steady viscosity enhancement can be measured and can be empirically accounted for by considering an immobile thickness of about two molecular diameters from each surface. Below 10 nm, when the surfaces are moved together, abrupt jumps of one molecular diameter are recorded. Since the liquid molecules are organized in layers parallel to the surfaces [16], surfaces can only approach one another by squeezing out a complete liquid layer. This molecular phenomenon results in a significant enhancement in the apparent viscosity.

The first tribological experiment done using the SFA in the sense that the surfaces underwent oscillatory motions creating shear was done by Van Alsten and Granick in 1988 [13]. The dynamic response of hexadecane film to oscillatory shear was reported as a dynamic apparent viscosity. A remarkable viscosity enhancement was found when hexadecane was in a restricted geometry (Fig. 1.5). The viscosity increase was more important at separations thinner than the molecular length of the molecule ( $\approx 1.8\text{nm}$ ). In confined geometry, the film thickness is quantized to integral multiples of 0.4nm, the molecular width of hexadecane in accordance with previous equilibrium studies with hexadecane and other alkanes [19].

When pressure is increased, the surfaces approach in abrupt jumps corresponding to the squeezing of full hexadecane layer (Fig. 1.5). As for the dynamic response of confined hexadecane, a large dependence of the dynamic viscosity on the pressure was reported. As shown in Fig. 1.5 at constant surface separation of 0.8nm ( $8\text{\AA}$ ), a slight pressure increase from 6 to 14 MPa results in an enormous increase of viscosity (up to 4 orders of magnitude). This important pressure dependence of viscosity at constant thicknesses was also seen in larger separations up to 2.4nm i.e. 6 molecular layers.

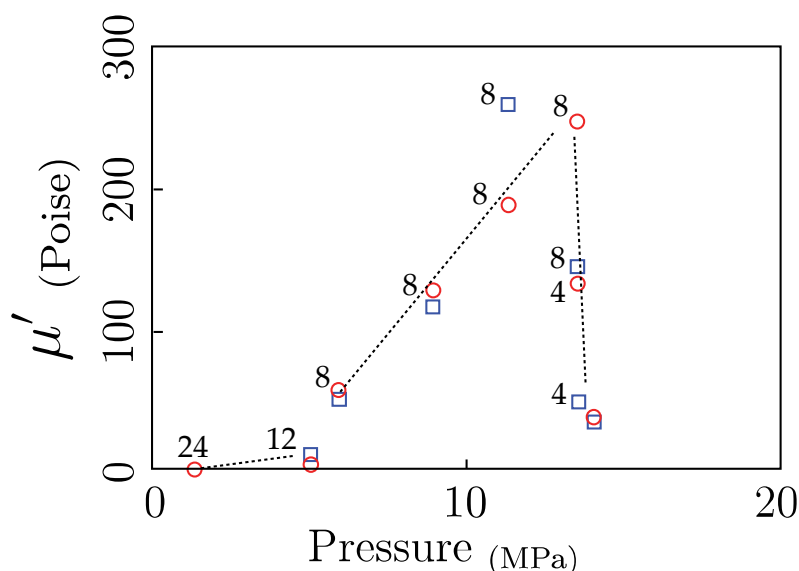


**Fig. 1.5:** The apparent dynamic viscosity of confined hexadecane as a function of the applied pressure. Numbers signify the thickness in Angstroms. The oscillations amplitude is 200 Å (squares) and 1000 Å (circles). [13]

At high pressures, a reversible transition to a solid like state was observed in liquids of different natures and molecular forms [13]. This state is characterized by an elastic response of the confined film to shear. Sliding can only be initiated if a critical shear stress is surpassed. The solid-like response was seen in confined films of less than 3 molecular layers.

Viscosity enhancement in molecularly confined films was also found by Israelachvili et al. using a modified SFA that allows measuring the shear force, velocity, as well as any lateral deformations of the surfaces [22]. When only one or two liquid molecular layers separate the surfaces in relative motion, the measured effective shear viscosity was 5-7 orders of magnitude higher than the bulk value. Moreover, such confined films exhibit solid-like behavior that can be characterized by a yield point and non dependence of the shear stress on the shear rate. A solid-like response to shear (stick-slip motion) is observed in the case of spherical molecules, and the average shear stress is quantized with the number of layers. The lower the number of layers, the higher is the shear stress.

The transition from liquid-like to solid-like behavior in confined films was investigated by Gee et al. [23]. A liquid-like dynamic behavior was detected for film thicknesses greater than 5 molecular diameters. At smaller thicknesses, when the surfaces are moved solid-like behavior was instantly seen in short and spherical molecules. In contrast, with long molecular chains a liquid-like behavior persisted and it was only after a certain time of shearing that a solid-like response evolved. By shear, preferential molecular alignment is influenced in the film which encourages the formation of organized solid-like structures. Molecules with a high level of branching have low tendency to solidify in confinement.

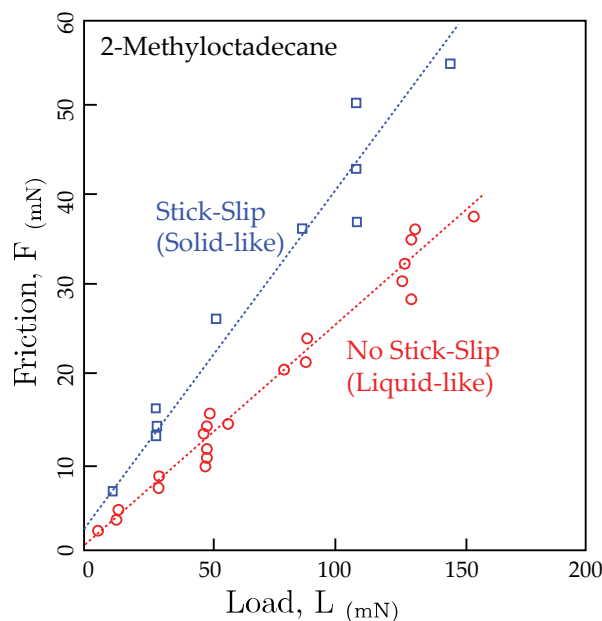


**Fig. 1.6: Frictional force of 2-methyloctadecane. In the beginning of shear, the film is liquid like (empty circles) and the friction coefficient is about 0.25. After some sliding, the film changes to a solid-like state accompanied by stick-slip; the friction coefficient increases to 0.35. (Results of Gee et al. [23])**

The transition from liquid to solid-like response is accompanied with an increase in the frictional force as shown in Fig. 1.6. Film solidification is encouraged if the walls have strong interactions and if they are in registry (commensurate). When the film solidifies, it pins the walls together (sticking phase). In order for the sliding to occur, the films flows plastically and eventually melts (slipping phase) before solidifying again when the walls become in registry again (next cycle sticking). These solid-liquid transitions that occur in solid-like films are responsible of the observed stick-slip motions. When the sliding velocity is higher than a critical value stick-slip vanishes and a smooth sliding regime is found. Smooth sliding is also seen when the film is contaminated by another molecule.

In confined films of sufficient thicknesses to exhibit liquid-like behavior, Dhinojwala et al. [24] found that a stick-slip motion occurs when the film is deformed faster than its intrinsic relaxation time, this is different from the stick-slip in solid-like films. Granick et al. [25, 26] observed viscosity decay with the shearing velocity in these kinds of films (Fig. 1.7). The decay follows a power law of  $\eta_{\text{eff}} = \dot{\gamma}^{-n}$  with  $n$  found experimentally to be in the range of  $0.5 - 1$  [25, 26, 27]. Luengo et al. [28] found that at sufficiently high shear rates, the viscosity joins again the bulk Newtonian viscosity plateau as shown in Fig. 1.8.

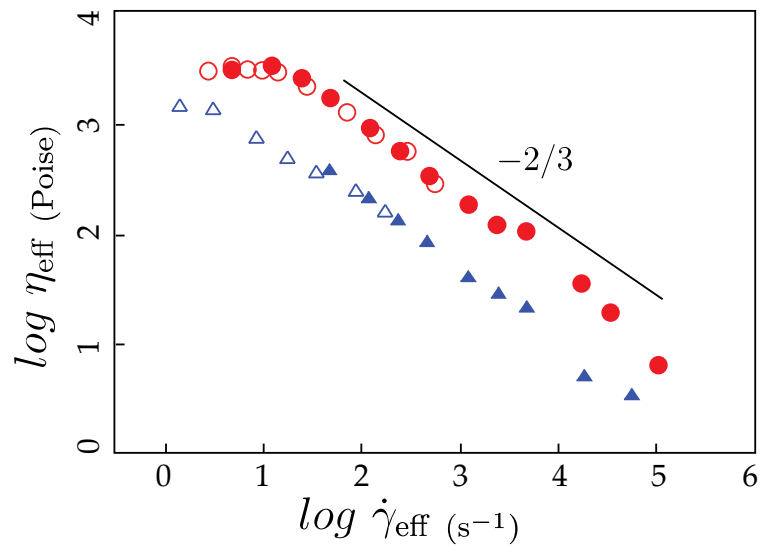


Fig. 1.7: Effective viscosity as a function of the shear rate for 2.7 nm dodecane (circles) and OMCTS (triangles) films. Filled symbols: constant oscillation amplitude, changing frequency. Empty symbols: constant oscillation frequency, varying amplitude. (Results of Hu et al. [26])

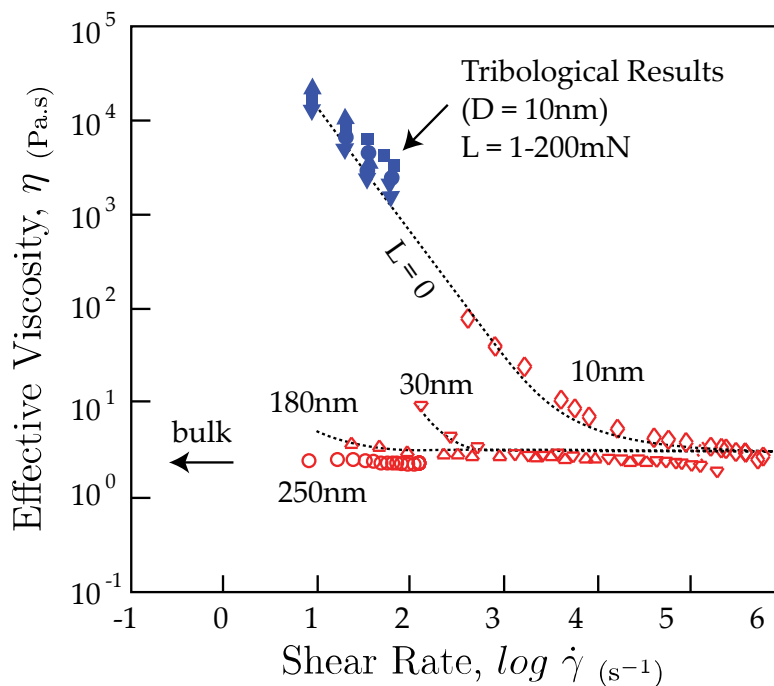


Fig. 1.8: Effective viscosity as a function of shear rate for a polybutadiene at 4 different thicknesses. Open data points were obtained by oscillatory shear and closed points denoted as “Tribological Results” were obtained by constant shear velocity. (Results of Luengo et al. [28])

### 1.3.1.3 Friction curves

The use of master curves for representing complex behavior of systems is a common trade in all fields of science. In classical lubrication problems, the Stribeck curve (Fig. 1.2) is used to predict the evolution tendencies of friction in terms of the bulk lubricant viscosity, the applied load and velocity. In molecular lubrication, the frictional behavior depends on different factors. For example, an inverse proportionality exists between friction and the (bulk) viscos-

ity of lubricants when they are in molecular confinement [29]. Viscous lubricants usually have irregular molecular structures. In molecular confinement conditions, the irregular molecular structure allows the lubricants to remain liquid-like, giving lower resistance to sliding compared to symmetrical molecules which can solidify. In order to explain the tendencies in the tribological properties of molecularly confined lubricants, friction curves based on molecular-scale findings on the shear resistance of fluids in confinement are needed.

Luengo et al. [30] proposed nano-rheology and friction maps that compile the SFA experimental results by different researchers. Nano-rheology maps are important in describing the flow resistance of lubricants in moderate to large thicknesses where they exhibit liquid-like behavior. In severe confinement (boundary regime), the film solidifies and sliding only occurs if a film-characteristic yield stress is surpassed (static friction  $F_s$ ).

The effective viscosity of the confined film and the friction force are given in Fig. 1.9 as a function of the shear rate and the sliding velocity respectively. Each curve corresponds to a constant applied load and film thickness. Three classes of rheological behavior to shear can be distinguished according to Fig. 1.9-a. In “thick” films which correspond to very low loading force in the experiments, the lubricant properties are identical to the bulk. Note that films referred to as “thick” are of a few nanometers thickness and can be found in heavily loaded elastohydrodynamic contacts. The notion of zero-load for these films is thus only an SFA property notion but the thickness notion is global. In these films, the viscosity is Newtonian over a wide range but undergoes shear thinning at high shear rates (green part of the figure).

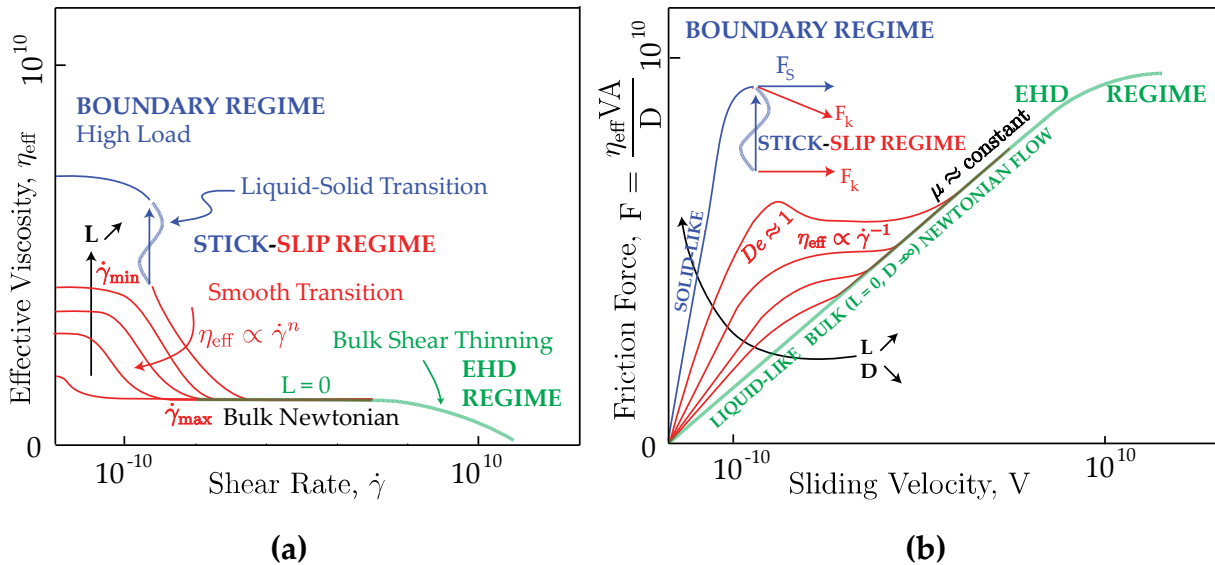


**Fig. 1.9: Proposed generalized log-log scale (a) viscosity-shear rate and (b) friction-velocity maps for molecularly confined films deduced from experimental measurements by Luengo, Israelachvili, and Granick [30]. The curves in each figure correspond to constant load ( $L$ ) (and constant film thickness ( $D$ )) evolutions.  $F_s$  and  $F_k$  represent static and kinetic friction forces when the film solidifies in the boundary regime.**

In films of intermediate thickness (between 2 and 10 molecular diameters) obtained with relatively higher loads, a Newtonian regime is still observed but at very small shear rates. The viscosity here is many orders of magnitude larger than the bulk one and increases with confinement. From this point when the shear rate is increased beyond a limiting value  $\dot{\gamma}_{\text{min}}$ , viscosity drops with a power-law dependence on the shear rate of  $\eta_{\text{eff}} = \dot{\gamma}^{-n}$ , where

$n = 0.5 - 1$ . The viscosity continues to decrease until it joins the bulk Newtonian plateau at  $\dot{\gamma}_{\max}$ .

The third class of behavior emerges in boundary films (very small thicknesses at high loads). The effective viscosity is high and the film response to shear continues to be Newtonian with the condition that the shear rate is extremely low. The transition to high velocity in such films is discontinuous and is of stick-slip nature involving repeated cycles of solidification and melting.

Fig. 1.9-b illustrates the influence of molecular confinement on a frictional force-velocity diagram. For Newtonian fluids lubricating under hydrodynamic full film conditions, a linear equation relates friction to velocity at constant loading (see Stribeck curve Fig. 1.2). In analogy, the two Newtonian plateaus of Fig. 1.9-a are translated into linear friction-velocity relationships in two regimes. The first is for all thicknesses but at very small velocities and the second corresponds to the bulk for small loads (large thicknesses) denoted by EHD on Fig. 1.9-b. The slope of these lines depends on the value of the viscosity. In thick films at high velocities, the film undergoes a limiting shear stress response.

In solidified boundary films occurring at the highest loads and smallest film thickness, friction passes by a maximum value  $F_s$  (static friction) and then it drops to  $F_k$  (kinetic friction), remaining constant with the sliding velocity. In intermediate films, the non Newtonian behavior between the two plateaus is conveyed by a gentle continuous decrease in the initial slope of the force-velocity curves. When the Deborah number  $De = 1$ , the applied shear rate is higher than the inverse of the fluid intrinsic relaxation time and in Fig. 1.9 the frictional force is maximum. The film becomes solid like [24] with a constant kinetic friction whatever the velocity.

#### 1.3.1.4 Boundary flow

The knowledge of boundary conditions such as boundary velocity is essential in solving lubrication problems. Near a stationary boundary, a fluid is classically supposed to be, also, stationary. This supposition has intrigued the likes of Maxwell, Helmholtz, and Thompson [31] who argued against the universal validity of the no-slip boundary condition that has neither a rigorous theoretical proof nor compelling argument. The topic of boundary slip still rouses great interest especially due to its practical implications in the domains of polymer processing and lubrication which involve fluid flow in molecularly small dimensions [32].

The first to experimentally show and measure boundary slip was Mooney in 1931 [33]. In his capillary viscometer experiments, Mooney found that the flow curves in non-Newtonian fluids can depend on the diameter of the capillary dies once the applied stress exceeds a critical value. Fluid slipping at the capillary boundaries can only explain the intriguing change in the flow curves.

Many other workers have investigated the slip problematic (for reviews, see [34, 35, 36]). It is experimentally common to find that in capillary or parallel-plate viscometer setups, confined fluids slip near the boundaries if they are forced beyond a critical stress [37, 38]. In these experiments, slip is detected when the slope of the flow curve changes i.e. the stress transmitted from the fluid to the boundary changes slope (with respect to the strain rate) as shown in Fig. 1.10. This behavior is seen at relatively small shear rates ( $10^2 - 10^3 \text{ s}^{-1}$ ) and thus is different than shear thinning at high shear rates which usually occurs while the fluid still sticks to the surface.

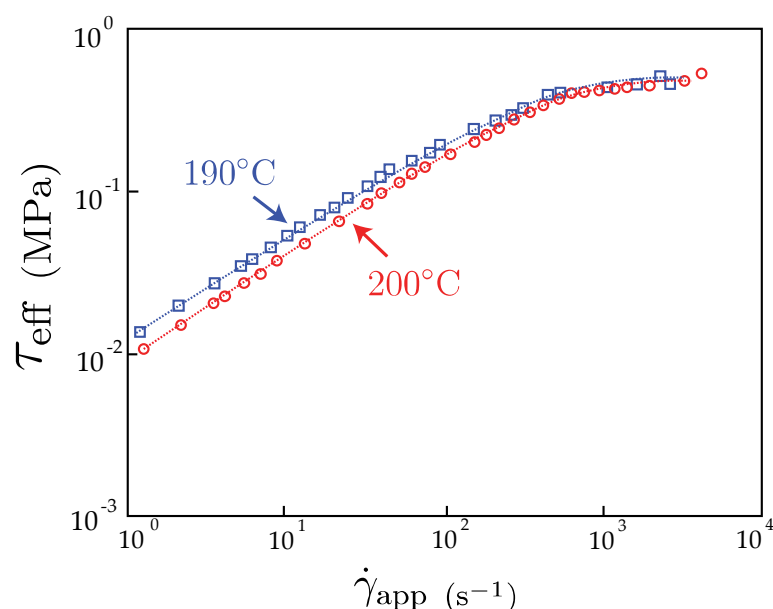


**Fig. 1.10: Apparent flow curve for a polyethylene polymer at 190 °C and 220 °C in a 1 mm diameter and 20 L/D capillary. The change in slope of the apparent stress is indicative of the slip at the capillary boundaries. (Results of Ramamurthy [37])**

Slip in these systems was found to depend on the molecular structure [34] as well as on the surface morphology [36, 37]. Long molecules have high tendencies to slip past walls compared to short ones. The state of the surfaces is also a crucial factor as fluids do not slip past surfaces with gross irregularities [37]. In other work involving a Quartz-crystal oscillator setup with molecularly thin films [31] on gold substrates, slip length was found to decrease with the film thickness, justifying thus the no-slip boundary condition in macroscopic scale films.

Migler et al. presented in 1993 the first direct measurements of the local velocity of a sheared polymer at a solid interface [39]. As shown in Fig. 1.11 for weak solid-polymer interactions, a strong slip is detected at high velocity of shearing. In strongly interacting surface-polymers, slip was found to be strongly reduced. Other experimental work showed that slip is also reduced by pressure and boundary roughness [35]. Zhu and Granick showed that even wetting fluids can experience slip if the surfaces are smooth enough [40]. Slip occurs when at the fluid is sheared beyond a critical shear rate, suggesting that in molecularly thin films boundary slip can occur for moderate sliding velocities.

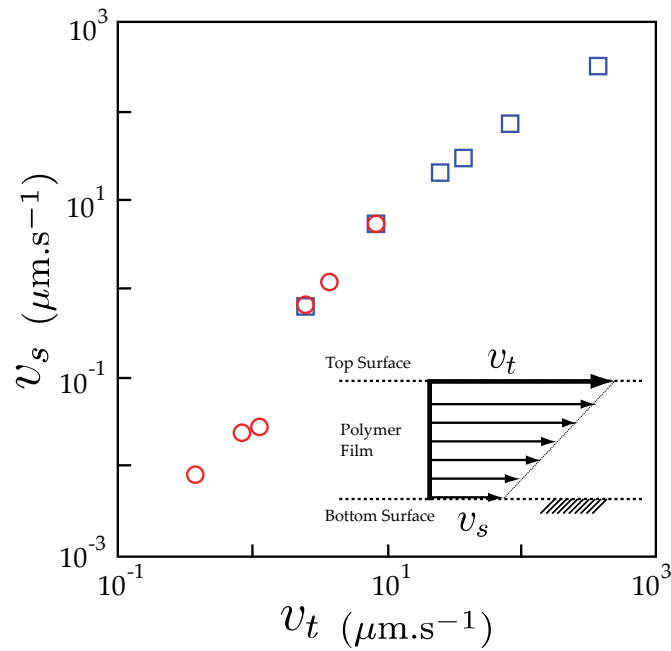


**Fig. 1.11: Slip velocity ( $v_s$ ) of polydimethylsiloxane (PDMS) on silanated silica surfaces as a function of the top surface velocity ( $v_t$ ). (Results of Migler et al. [39])**

Nevertheless, there is another side to the story of boundary flow when films are confined to molecular scales. In some cases, fluid layers can be stuck to the bounding surfaces and this was shown in early SFA drainage experiments by Chan and Horn [15]. Stagnant fluid layers near each surface were seen in confined films between 10 and 50 nm. The debate remains open in the subject of interfacial flow, especially for molecularly confined systems.

In conclusion to the state of art on the experimental work on molecular lubrication, many interesting properties of confined lubricants have been evoked in the literature. Confinement greatly influences the structure and homogeneity of lubricant films. The dynamic properties are also significantly influenced, often leading to increased stress and friction. However, a local phenomenon of boundary slip seems to emerge in confined films. Wall slippage is thought to be the way to controlling friction in molecularly confined films [35].

In parallel with and sometimes leading experiments, numerical studies have been conducted to interpret and predict many of the properties of confined films. Most of these studies were based on Molecular Dynamics and Monte Carlo simulation methods. The most significant numerical work in the literature related to confined films is reviewed in the next section.

### 1.3.2 Numerical work

Molecular simulations have greatly evolved during the last 30 years. Over this period, many of the fluid properties, in the bulk as well as near interfaces were investigated by simulation [41], providing information at scales hardly accessible to experiments. As will be conveyed in this section of the state of the art, in molecular lubrication problems, simulations predicted many of the properties of confined films years before the development of experimental techniques capable of providing results at the same scale.

Simulations are characterized by their low cost yet good predictive ability and the possibility to access the local information in very small systems [42]. The resemblance between molecular simulations and constitutive (ab-initio) physical principles gives them their predictive ability. Simulations play two essential roles side by side with experiment. In unexplored systems, molecular simulations can orient experiment to the conditions where interesting phenomena are susceptible to occur. In such a situation, experiment aims to validate what is observed by simulations. On the other hand in systems that are already explored by experiments, simulations can be employed to complete the understanding of the occurring phenomena from the tiniest scale and not uniquely from integrated effects seen at the whole scale of experiments.

Molecular simulations have, nevertheless, a general limitation related to the processing and data handling speed of computers. This unfortunately impacts one or more of the three essential properties of simulations: system size, simulation duration, and size of the smallest element in the model. Fortunately, simulation algorithms have not ceased developing for giving realistic models while reducing the computational costs [43].

The most commonly used simulation methods are briefly introduced in the next section. In the remaining part of this chapter, the most significant simulation work in molecular lubrication is presented.

### **1.3.2.1 Simulation methods**

Monte-Carlo (MC) and Molecular Dynamics (MD) are the simulation methods most commonly employed for studying confined films in molecular lubrication. These methods are based on a classical definition of the system Hamiltonian [41]. In other words, the energy is defined as the sum of kinetic and potential energies of the atoms modeled as point masses on the center of their nuclei. The kinetic energy, representing the atomic vibrations, depends essentially on the temperature while the potential energy depends on the atomic configuration and on the set of inter-atomic interaction laws which constitute a force-field.

Monte Carlo is a stochastic molecular simulation method classically used to determine the equilibrium properties and configuration of molecular systems in precise thermodynamic ensembles. Starting from an atomic configuration, the method uses random steps for moving atoms around the domain. Steps are accepted or rejected according to the change they produce in the potential energy. Since forces are not explicitly calculated on all atoms, MC is relatively economic in terms of calculation time and can be used to simulate relatively large systems. Moreover, it is convenient when systems are only defined by an energy prescription or when there is incertitude in the inputs. However, there is no notion of time in classical MC; it neglects dynamics which is a major drawback for simulating flow.

Molecular Dynamics is a deterministic molecular simulation method based on applying Newton's equations of motion on all atoms in a molecular system. At each iteration (time step), forces on all atoms are calculated explicitly and atomic accelerations are computed. Then, by numerical integration, the new positions and velocities of all atoms are determined. Since time is included explicitly, the atomic motions in MD are realistic provided the interactions are properly chosen. More details on the Molecular Dynamics simulation method are presented in Chapter 2, dedicated to MD modeling for molecular lubrication.

In what follows, a review on the simulation literature related to confined films and lubricants is presented. The review is classified in three categories: structural effects and solvation forces, nano-rheology, and boundary flow.

### 1.3.2.2 Structural effects and solvation forces

Since the late 1970's, a considerable attention was dedicated to the understanding of the structure and adsorption of fluids near solid surfaces and a few analytical theories were proposed in this regards [44]. However, a major contribution to this subject was through molecular simulation [45, 46, 47].

When an ideal mono-atomic (Lennard Jones) fluid is adsorbed onto a model surface (potential field [48]), it forms more than one well-defined layer [45, 46, 47]. The fluid density across the adsorbed film oscillates with the distance from the surface. In molecularly confined films, a discrete number of layers are formed parallel to the surfaces [49]. As shown in Fig. 1.12, across films of different thicknesses the density oscillates with maximum values located near the solid interface. When two surfaces are moved together, the film is compressed until a complete layer (due to the structural effects) is squeezed out. In consequence, the surface solvation force is oscillatory and changes between repulsion and attraction [49].

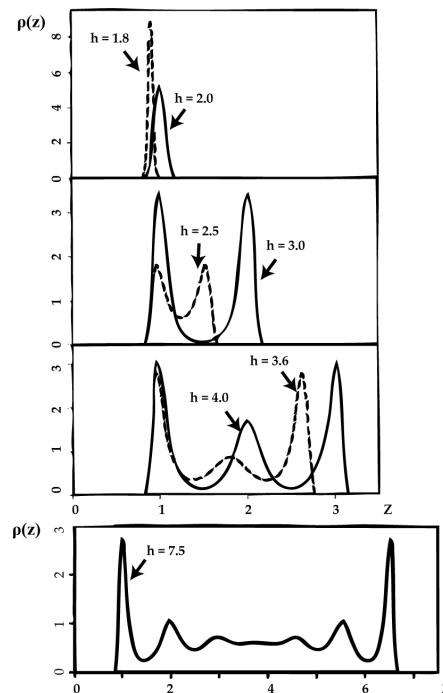


**Fig. 1.12:** Density profiles of a LJ model liquid (mono-atomic) confined at a thickness “ $h$ ” between two FCC (100) surfaces represented as a potential field acting on the liquid atoms. The film thickness is given in Lennard Jones reduced units (Results of Snook and van Megen [49])

In ideal LJ fluids, the effects of fluid structuring, notably on the diffusion properties and solvation force, extend to about ten molecular diameters [50]. In thicker films, the diffusion coefficient becomes very close to the bulk value and the solvation force equals the pressure. Shearing the confined film has no effect on the equilibrium structure [51, 52, 53, 54].

MD simulations showed also that an epitaxial (in-plane) order is present inside the formed layers in confined LJ films between crystalline surfaces [55]. The epitaxial ordering depends on two essential factors: the surface-fluid interaction strength and the commensurability of the solid and fluid densities. The commensurability could be defined as the registry between the topologies of two contacting surfaces (whatever the phase). It is maximal when the surface topologies are similar and can be interlocked together.

As shown in Fig. 1.13, when the surface-fluid interactions are strong a high level of epitaxial ordering is induced in the fluid. The first fluid layer crystallizes and the ordering may extend to the third fluid layer if the solid and the fluid have equal densities. If the densities are not equal, the first fluid layer no longer crystallizes but instead becomes highly ordered and commensurate with the surface. Fig. 1.14 shows an example of such a high-order commensurate structure [55]. In this case, in-plane order does not extend deep inside the fluid. When the surface-fluid interactions are weak, the fluid does not crystallize and in-plane order is limited to the layer adjacent to the solid surface (Fig. 1.13).

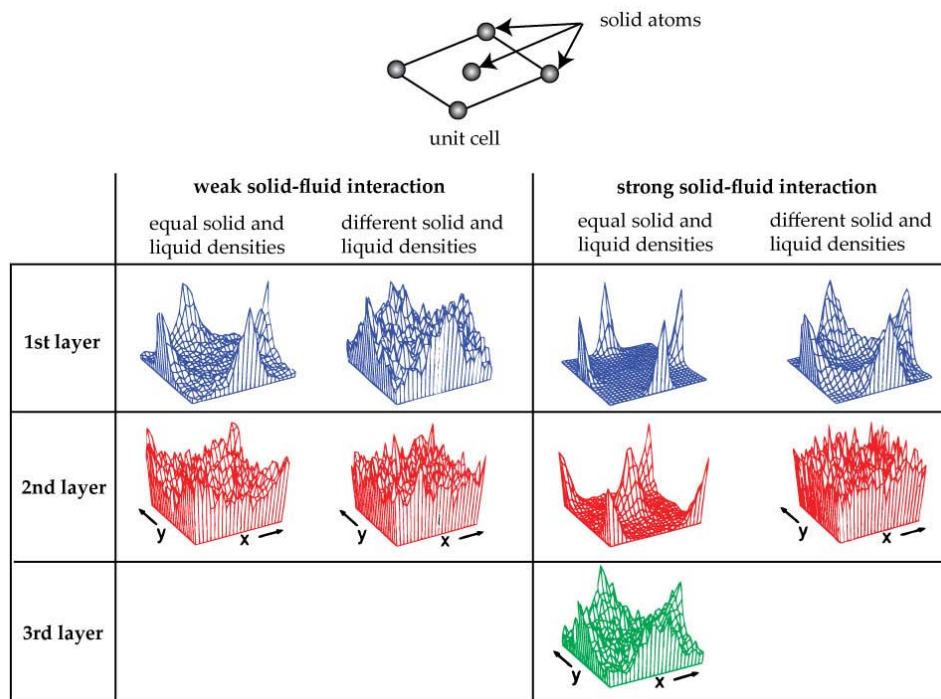


**Fig. 1.13: Atomic probability distribution functions, parallel to a lattice unit cell of the solid, for the first three fluid layers adjacent to the surfaces. These functions are given for different surface interaction strengths and density commensurability between the solid and the fluid. The solid unit cell is represented in the top of figure, where atoms are disposed in the corners and the center of the cell. (Results of Thompson and Robbins [55])**

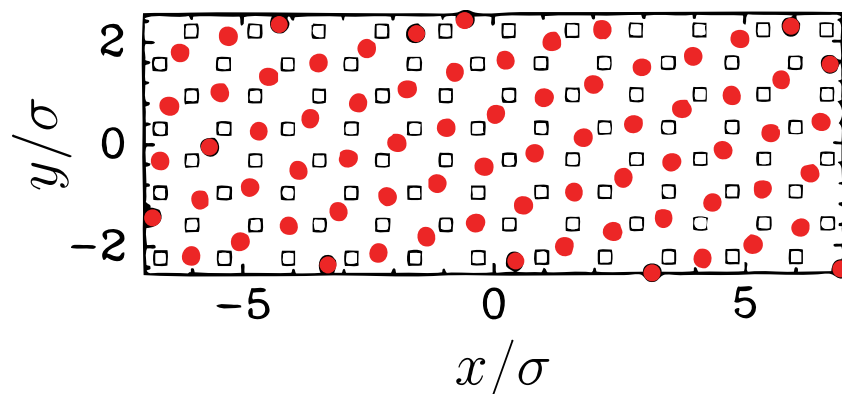


**Fig. 1.14: XY plane projections (parallel to the surface) of the positions of the atoms of the surface (open squares) and those of the adjacent fluid layer (closed circles). Although in this case the solid and fluid densities are not equal, the atomic configuration of surface-adjacent fluid layer is commensurate with the surface structure. (Results of Thompson and Robbins [55])**

The molecular nature of the fluid has also significant influence on the structuring in confined geometries. Although density oscillations are still seen in long molecules such as alkanes and polymers [56, 57], the layering is softer and decays faster than in ideal LJ fluids.

In polymer fluids, the bulk structure is perturbed and the molecular chains are flattened near the solid interface [56, 58]. The interfacial region extends to about twice the segment diameter [58]. Away from the surfaces, the bulk structure is gradually recovered and bulk properties are found at a distance comparable to the polymer radius of gyration [56, 58].

Similar effects are seen in alkanes of ten to twenty monomers [59, 57]. Molecules in the interfacial region are flattened and are preferentially oriented parallel to the surfaces. The characteristic layer thickness is about 0.4 nm corresponding to the molecular width of an alkane chain (see Fig. 1.15). Layering disappears in linear alkanes at a distance comparable to the molecular length.

Molecular branching also influences the confined structuring [60, 61, 62]. As shown in Fig. 1.15, linear molecules show sharper layering than branched ones. The solvation force is also significantly influenced by branching [61]. As shown in Fig. 1.16, in linear and spherical fluids the oscillation of solvation forces is pronounced and exhibits attractive and repulsive regions. In branched molecules, on the other hand, the density oscillations are less pronounced, the forces are overall repulsive (positive) and are generally stronger than in straight chain and spherical molecules.

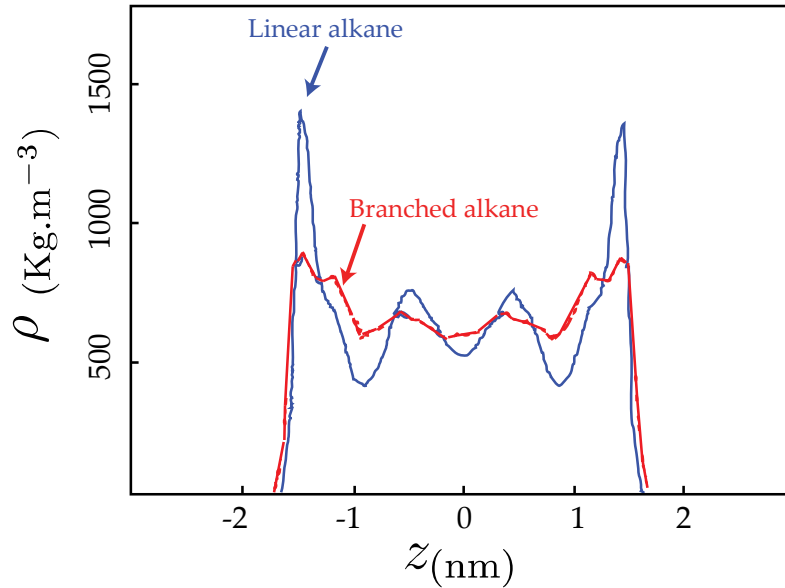


Fig. 1.15: Comparison between the density profiles of a linear alkane (n-decane) and a branched alkane (4-propyl-heptate) confined between fictional surfaces at 188.91 MPa. (Results of Padilla [60])

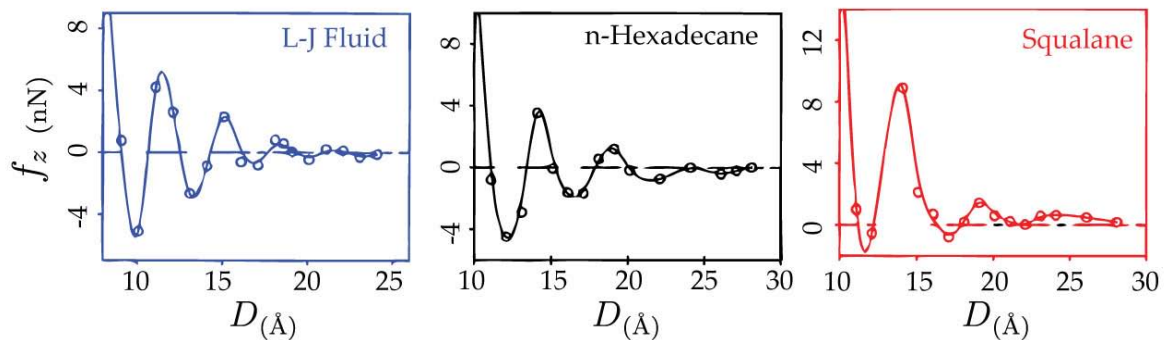


Fig. 1.16: Equilibrium solvation forces as a function of the film thickness computed for a simple mono-atomic LJ fluid, linear chain (n-hexadecane) and a branched alkane (squalane). (Results of Gao et al. [61])

Finally, the surface corrugation has an effect on the structure of the confined fluid [63, 64, 65]. It is seen that the layering is frustrated near rough surfaces compared to molecularly smooth ones.

This inhomogeneous nature of confined films, characterized by oscillating densities has certainly an impact on the dynamics of these films. A review on the dynamics of confined films is presented in the next section.

### 1.3.2.3 Nano-rheology

Equilibrium molecular simulations showed much of the inhomogeneities of confined films. The earliest work on the dynamics of confined films is based on the hypothesis that the inhomogeneous confined film can be considered as a set of homogeneous layers [51]. Each layer has its own density and eventually, its local viscosity. This is the basis of the local aver-

age density model (LADM) which gave very satisfactory results in predicting the flow in moderately confined ideal fluids (Fig. 1.17). However, this model fails to predict many properties of confined films especially the enhanced viscosities in very confined geometries where the densities only cannot explain the local dynamic properties of films [53].

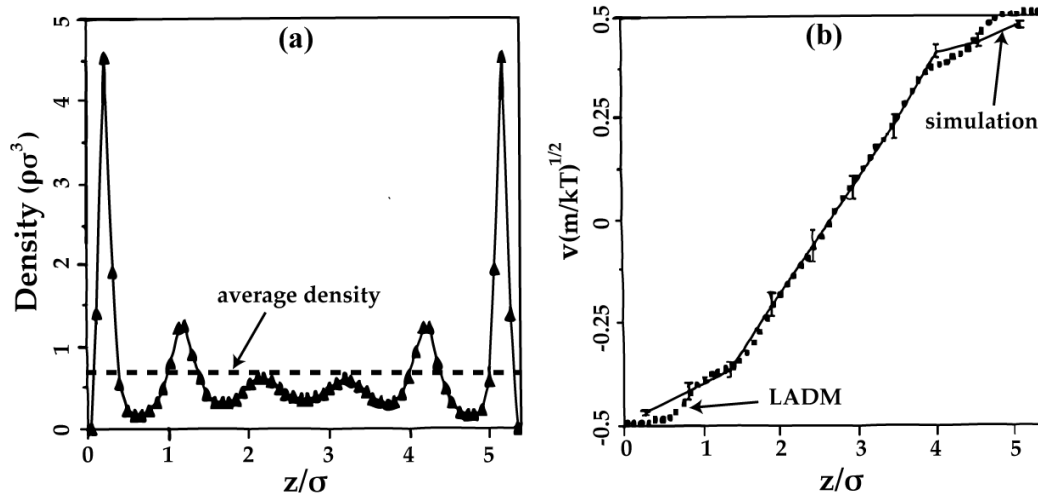


Fig. 1.17: Density (a) and velocity (b) profiles of a confined LJ fluid between structureless surfaces. (Results of Bitsanis et al. [51])

Since the dynamics of confined fluids are influenced by factors that are not always intrinsic to the fluid, it is basically inappropriate to define a global “viscosity” within the traditional rheological notion of the term. However, a flow resistance, in viscosity units, determined as the ratio of the shear stress to the shear rate gives an idea on the global dynamics of confined film and can also be compared to experiment [51, 54]. Most work on the nano-rheology of confined films reports this value as the effective shear viscosity.

The effective shear viscosity of a confined spherical fluid increases with confinement [51, 54]. As shown in Fig. 1.18, it also oscillates with the film thickness in an analogous manner to the solvation force where the period is equal to the molecular diameter [54].

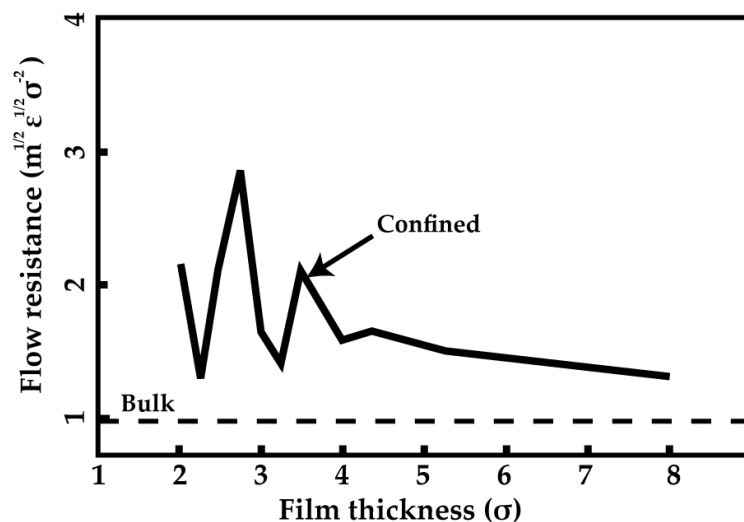
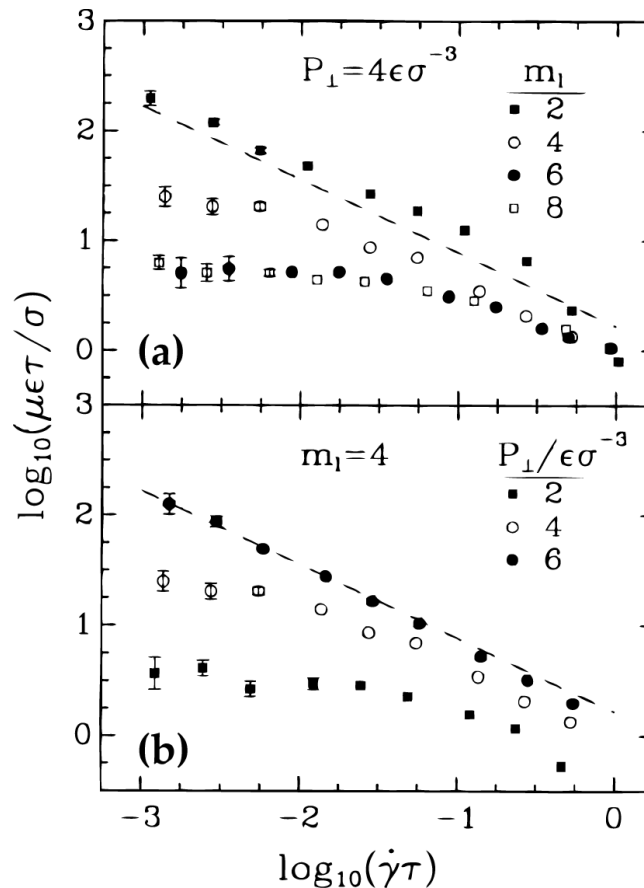


Fig. 1.18: Flow resistance (effective viscosity) in a confined film of a LJ fluid between structured surfaces as a function of the film thickness. (Results of Somers and Davis [54])

At constant pressure, the effective viscosity increases by several orders of magnitude when the thickness is reduced (Fig. 1.19-a) [53, 66, 67]. In spherical molecules, this viscosity enhancement is due to the crystallization of the film [66]. In long molecules, the viscosity enhancement is due to the formation of crystalline bridges between the approaching surfaces [67].

At constant thickness, the effective viscosity increases significantly with pressure as the fluid is pushed closer to a glassy phase transition (Fig. 1.19-b). Moreover, at shear rates accessible to simulation ( $10^9 - 10^{11} \text{ s}^{-1}$ ), fluids can be highly thinning. A universal viscosity-shear rate power law of  $\mu \propto \dot{\gamma}^{-n}$  with  $n = [0.5, 1]$  is observed for different pressures and thicknesses [11, 66, 68, 65]. A constant viscosity manifesting a linear shear stress-rate relationship is seen at low shear rates. The constant viscosity is higher than the Newtonian bulk value. When the film is thinner or when the pressure is increased, the constant-viscosity plateau is displaced to extremely low shear rates. The viscosity is expected to be orders of magnitude larger than the bulk [66].



**Fig. 1.19:** Variation of the effective viscosity, of a fluid with a linear chain of  $n=6$ , with the shear rate: (a) at constant pressure but variable thickness (number of layers); (b) at a constant thickness but variable pressure. The dashed lines have slopes of  $-2/3$ . (Results of Thompson et al. [66])

Beyond a critical pressure, a glassy phase is seen in confined fluids [66]. Glass transition is accompanied by a significant decrease in the diffusion coefficient representing the atomic mobility (Fig. 1.20) and an increase in the effective viscosity and relaxation times [61, 66, 69].

In commensurate spherical films, this transition occurs within film thicknesses smaller than 5-6 molecular diameters [61]. Upon shearing, the glassy film has a linear elastic response (the stress increases linearly with strain). The dynamic response becomes highly non-linear when a critical (yield) stress is attained beyond which the film yields to shearing [61, 69]. If the shearing is stopped prior to the yield point [61], the deformed film maintains the stress; this is the signature of a solid-like behavior.

The critical pressure of glass transition decreases with the chain length. Thus, an ideal LJ fluid may exhibit glass transition at a pressure where a fluid of a longer chain is still disordered (fluid like). Branched and flexible molecules are also more resistant to solidification and are seen fluid-like even in severe conditions of confinement and pressure [62, 70].

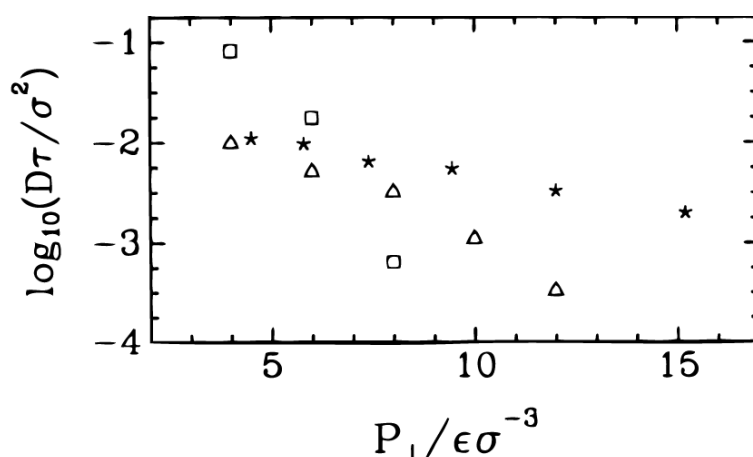


Fig. 1.20: Variation of the diffusion coefficient as a function of the normal pressure in 2 layer thin films. Squares: mono-atomic fluid ( $n=1$ ), triangles: 6 monomers linear chain ( $n=6$ ), stars: diffusion in the bulk for  $n=6$  fluid. (Results of Thompson et al. [66])

Finally, the surface structure [63, 65, 64, 71] and dynamics [72] also influence the effective viscosity of confined films. By frustrating the ordering of the neighboring fluid, the effects of confinement on the effective viscosity are less pronounced near rough surfaces [64, 63]. In consequence, the film remains fluid-like.

### 1.3.2.4 Boundary flow

Among the most interesting molecular effects seen in simulations of confined films are those on boundary flow. Due to their localized nature, boundary flow effects are usually difficult to access directly by experiment. They are yet crucial for the correct understanding and interpretation of the dynamics of confined films.

Three boundary flow patterns can be seen in confined films: slip, no-slip, and locking. Factors that influence the boundary flow are numerous and vary from the chemical nature of the fluid, that of the surfaces, the interactions between the two, surface morphology, operating conditions, and of course the level of confinement.

The first factor which influences the boundary flow in molecular simulations is the surface corrugation. In early simulations [51, 53] which employed ideal fluid molecules and smooth potential fields [48] to represent the solid surfaces, boundary slip was always observed. However when structured surfaces were employed, the opposite phenomenon of

fluid locking to the surfaces was seen [52]. A comparison of the velocity profiles obtained with smooth and structured surfaces is given in Fig. 1.21. The slip observed with smooth surfaces is completely attenuated with structured ones. When the film thickness is larger than 8 molecular diameters, a no-slip boundary condition is re-established for both cases.

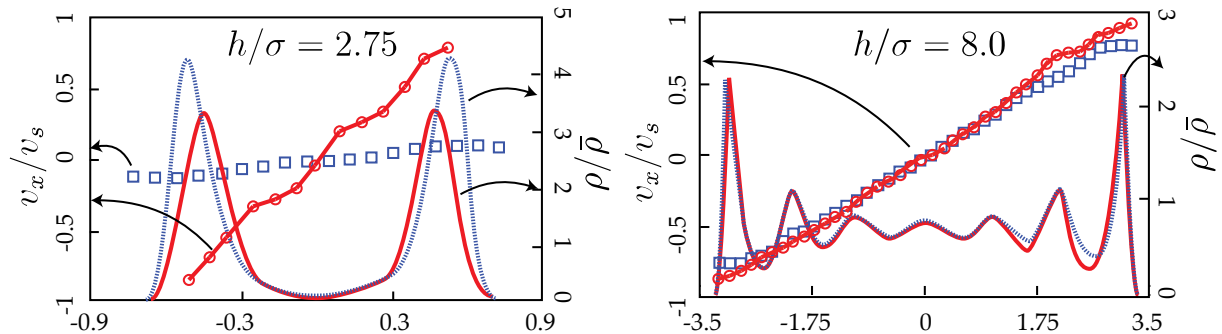


**Fig. 1.21: Density and velocity profiles of sheared LJ films in nano confinement. Solid lines and circles correspond to structured surfaces and dotted lines with square symbols correspond to smooth surface models.  $v_x$  and  $v_s$  are the fluid streaming and the surface sliding velocities respectively.  $h$  is the film thickness and  $\sigma$  is the LJ distance parameter. (Results of Heinbuch and Fischer [52])**

In ideal LJ fluids, the commensurability of fluid molecules with the surfaces is important in predicting the boundary flow [55]. As shown in Fig. 1.22, commensurate fluids show a no-slip boundary condition even for low solid-fluid interaction strengths. In the case of strong interactions, a state of locking can be observed in such films where more than one fluid layer moves at the same speed as the surface [52, 55]. On the other hand, incommensurate fluids slip at the solid boundary for low interaction strength. In the case of strong interactions, the first fluid layer crystallizes and is locked to the surface, but slip occurs inside the fluid from the second layer and on.

Slip increases with the length of the molecular chains. Several studies involving alkanes detected slip for a variety of interaction strengths [11, 68, 65]. As for branched molecules, branching plays an important role in increasing the slip [62].

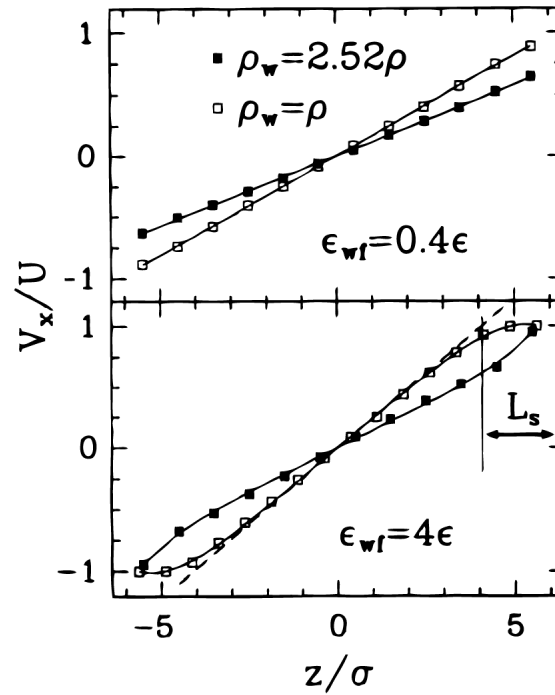


Fig. 1.22: Velocity profiles across ideal LJ films confined between structured surfaces for different surface-fluid interaction strengths. Closed squares: incommensurate solid and fluid densities. Empty squares: commensurate solid and fluid densities. (Results of Thompson and Robbins [55])

Among several other factors that influence slip are the surface flexibility [73], roughness [64, 63], temperature [52], forcing level [52, 73, 74]. In flexible or rough surfaces, or when the temperature is increased, slip is reduced. On the other hand, when the forcing level (such as the shear rate) is increased, slip also increases.

## Conclusion

Although the conditions of experiment and simulation of molecularly confined films are different, simulations have allowed many of the molecular effects behind the experimental observations to be understood. Oscillatory solvation forces and viscosities, film solidification, viscosity thinning, and boundary slip are phenomena that have been seen in experiments and simulations. By accessing the underlying local effects behind any global observation, simulations studied ranges of parameters in order to identify which are responsible of the phenomenon. This procedure is often complicated if not impossible to do in experiments.

The knowledge of all the effects reviewed in this chapter provides an indispensable basis to understand the simplest problem in molecular lubrication. In the next chapter, the details of constructing a molecular simulation model within a well-defined thermodynamic framework are presented.



# 2

# Numerical Model of Molecular Lubrication

<b>Introduction</b>	<b>32</b>
<b>2.1 Molecular dynamics method</b>	<b>32</b>
2.1.1 Principle	33
2.1.2 Integration methods	33
2.1.2.1 The Verlet algorithm	33
2.1.2.2 Other algorithms	34
2.1.3 Initial conditions	34
<b>2.2 Construction of the molecular lubrication model</b>	<b>34</b>
2.2.1 Model overview	34
2.2.2 Solid surfaces	36
2.2.2.1 Crystalline structure and interactions	36
2.2.2.2 Thermal and mechanical properties	39
2.2.3 Lubricant	42
2.2.3.1 Molecular architecture and interactions	43
2.2.3.2 Dynamic and thermal properties	44
2.2.4 Surface-Lubricant interface	47
<b>2.3 Initialization and sampling</b>	<b>49</b>
2.3.1 Geometry	49
2.3.2 Initial density	50
2.3.3 Compression	51
2.3.4 Shear	52
2.3.5 Sampling effects	53
2.3.5.1 Spatial sampling: system size	53
2.3.5.2 Time sampling: time-step and simulation duration	54
<b>Conclusion</b>	<b>56</b>

# 2. Numerical Model of Molecular Lubrication

---

## Introduction

A numerical model is used to represent a “non-numerical” problem in mathematical terms. When the problem of interest is of a physical nature, modeling is based on the underlying fundamental theories and governing equations. In full lubrication for instance, modeling is based on Reynolds hydrodynamic lubrication theory and energy equations. Modeling work involves determining a set of numerically resolvable relationships whose results are approximations of the accurate physical solution to the problem.

In molecular lubrication however, continuum-type modeling is irrelevant due to the discontinuity of the domain. The definition of thermodynamic quantities is very delicate in such systems and becomes even more complicated in non-equilibrium conditions of shearing. Fortunately, numerical models with an explicit molecular description can detect many of the local scale effects behind the mechanisms of molecular lubrication.

Molecular dynamics is a deterministic molecular simulation method. The trajectories of all molecules in a system, due to all molecular interactions, can be accurately predicted. This chapter begins with an introduction on the principle of this simulation method. The remaining part of the chapter presents a step-by-step model construction and validation plan for realistic surfaces and lubricants in the purpose of investigating molecular lubrication.

## 2.1 Molecular dynamics method

The history of molecular dynamics is not so short. Before becoming a “numerical” technique, the thought of simulating matter by gelatin balls goes back to 1936 [41]. In the late fifties, Alder and Wainwright launched the idea of molecular dynamics as a numerical simulation method. They worked on solving Newton’s classical equations of motions for a small set of molecules modeled as hard spheres. Rahman, in 1964, was the first to employ the method with a continuous potential (Lennard Jones) between molecules. Since forces change all the time, he introduced a step by step integration procedure to approximate the molecular trajectories [41].

Originally employed to investigate phase transitions and interfacial behavior, molecular dynamics also found its application in physics, physical chemistry, material sciences, bio-

chemistry, and biophysics since the late seventies. Currently, molecular dynamics is employed in all domains where molecular scale effects play a role.

### 2.1.1 Principle

Molecular dynamics is based on applying Newton's equations of motion on all interacting atoms in the molecular system. For an atom  $i$  with a position vector  $r_i$  and interacting with a potential energy  $V$ , one defines:

$$(2.1) \quad f_i = -\nabla_{r_i} V$$

$$(2.2) \quad \ddot{r}_i = f_i/m_i$$

The force  $f_i$  acting on each atom is thus determined as the gradient of the potential energy from the interactions with all neighboring atoms. The acceleration vector  $\ddot{r}_i$  can eventually be calculated from Newton's equations of motion (Eq. (2.2)).

### 2.1.2 Integration methods

Knowledge of atomic trajectories during time requires solving the differential equation of motion (2.2). The standard way is by using finite difference methods.

Given that the positions and dynamics (velocities, accelerations, etc.) of all atoms are known at time  $t$ , the same information can be calculated at  $t + \delta t$  with sufficient accuracy. The differential equations of motion of all atoms are solved on a step by step basis. The choice of the time step  $\delta t$  has direct influence on the accuracy of the integration.  $\delta t$  must be significantly smaller than the typical time needed by a molecule to travel its own length [41]. The choice of  $\delta t$  also depends on the integration algorithm. The most commonly used integration scheme for the equations of motion, the Verlet algorithm, is presented in the next section.

#### 2.1.2.1 The Verlet algorithm

The Verlet algorithm gives a direct solution to the equation of motion [41]. The atomic position  $r(t)$ , acceleration  $a(t)$ , and position  $r(t - \delta t)$  at the previous step are used to calculate the atomic position for the next step:

$$(2.3) \quad r(t + \delta t) = 2r(t) - r(t - \delta t) + \delta t^2 a(t)$$

This algorithm is easy to implement, time reversible, and doesn't require any velocity to calculate the trajectory. The positions are exact except for errors of order  $\delta t^4$ . However when the velocity is needed, for example to calculate the kinetic energy, it can only be defined as:

$$(2.4) \quad v(t) = \frac{r(t + \delta t) - r(t - \delta t)}{2\delta t}$$

The velocity  $v(t)$  can thus only be computed if the position  $r(t + \delta t)$  at the next step is known. Moreover, velocities are subject to errors of order  $\delta t^2$ . Modifications to the original algorithm were proposed in order to minimize the velocity errors and improve the overall

stability. Among the most famous modifications are the leap-frog and velocity Verlet algorithms.

### 2.1.2.2 Other algorithms

There are several other integration algorithms that were proposed and used [41]. Although the calculation accuracy could be improved, the new algorithms were often heavier than the Verlet algorithms in terms of calculation time. The Verlet algorithms require the least number of stored variables in the memory to determine the trajectory. For example, the Gear predictor-corrector algorithm “guesses” (predicts) the new position from existing information (positions, velocities, accelerations, and jerks) from previous steps. Then, knowing the exact acceleration from Newton’s equation, a correction term can be deduced and applied to the previously guessed values. Another interesting algorithm was proposed by Toxvaerd in 1982 [75]. The integration takes into account the motion of neighboring atoms and achieves better energy conservation than the Verlet algorithm. However, it remains three times slower.

## 2.1.3 Initial conditions

In molecular dynamics, the initial state of the system is usually not yet characteristic for the desired equilibrium. The evolution towards equilibrium can last a few nanoseconds. Assuming  $N$  the number of atoms in a simulation, solving  $3N$  second order differential equations of motion normally requires  $6N$  initial conditions. In practice, these initial conditions can be chosen as the sets of initial positions ( $3N$ ) and velocities ( $3N$ ) of all atoms.

It is preferable to initially position the atoms in a state that is not far from equilibrium. This helps in reducing the time needed for equilibration. However, this is often a hard task to accomplish as not all properties of the equilibrium state are known. In common practice, atoms in crystalline solids are placed on the lattice positions whereas in liquids they are randomly dispersed. Before simulation, a potential energy minimization process can be run to avoid having large interactions at the beginning of the simulations.

As for the initial velocities, they can be sampled from a Maxwell-Boltzmann distribution corresponding to the initial temperature  $T_0$  of the system with a uniform direction distribution of vectors. Each velocity component is sampled from a Gaussian distribution of zero mean and a standard deviation of  $\sqrt{k_B T_0 / m_i}$ ,  $k_B$  and  $m_i$  being the Boltzmann constant and atomic mass respectively. Finally, the set of initial velocities are corrected to make sure that no initial momentum is given to the system.

## 2.2 Construction of the molecular lubrication model

### 2.2.1 Model overview

At the scale of molecular modeling, an explicit system of only a few nanometers wide on each dimension can be simulated. It is thus out of question to molecularly simulate a whole

contact with inlet and outlet conditions. The molecular lubrication model used in this thesis consists of a surface-lubricant-surface configuration as shown in of Fig. 2.1. Periodic boundary conditions in  $x$  and  $y$  allow the elementary model to be repeated along these dimensions. This hypothesis is necessary to ensure the continuity of the model and its integrity and can be justified by the infinitely small  $z$ -dimension of the lubricant film compared to the other two dimensions. This model represents a small region in a real macroscopic contact, for example between two interacting asperities.

Due to computational limitations, only a small thickness  $dz$  of each surface can be considered. The lubricant film is modeled with its real thickness  $h$  and extends infinitely in  $x$  and  $y$  with the periodic boundary conditions.

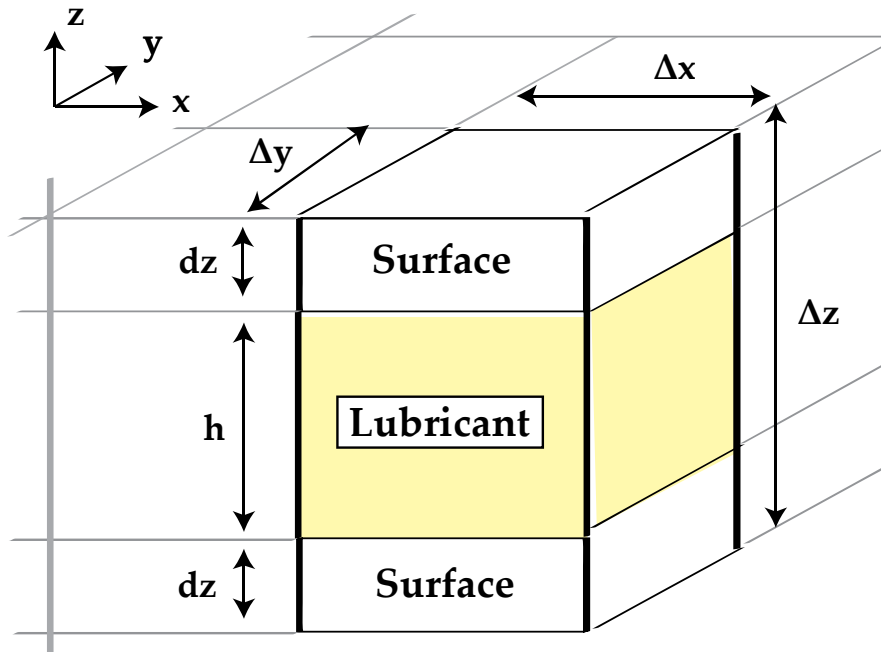


Fig. 2.1: A schematic of the molecular lubrication model. The simulated box is bounded by bold black lines. Grey line extensions represent the copies of the simulation box due to the periodic boundary conditions.

The lubrication model is constructed and characterized in two separate sections. In the model construction section, the elements which constitute the model are studied independently. These elements include the solid surfaces (gold or ferric oxide), the confined lubricant (pentane or hexadecane), and the interface between the two. After this step, the elements are put together in the configuration of Fig. 2.1 to form the molecular lubrication model.

The model is then characterized under static and dynamic conditions. In static conditions, the surfaces are stationary and the focus is on the structural properties of the confined lubricant. In dynamic conditions, the surfaces are moved in opposite directions while pressing on the lubricant. As a result, characteristic fields develop across the film (density, velocity and temperature). These effects are studied in this chapter for an example system of gold ( $Au$ ) surfaces confining an n-pentane lubricant model ( $C_5H_{12}$ ).

## 2.2.2 Solid surfaces

Although the main interest of the lubrication model is in replicating the lubricant behavior, it is important to have an adequately representative model for the surfaces. Examples from the literature [52, 55] show that structureless and smooth surface models fail in capturing the real effects on the lubricant due to confinement. The model which will be used is based on crystalline structured surfaces with, as much as possible, realistic replication of the mechanical and thermal properties. Details of the construction of the surface model and its characterization are the object of this section.

### 2.2.2.1 Crystalline structure and interactions

In modeling crystalline surfaces, atoms are disposed on the equilibrium lattice positions. This corresponds to FCC and Corundum crystals for gold ( $Au$ ) and ferric-oxide ( $Fe_2O_3$ ) respectively. Details on the crystalline structures of these two materials are given in Table 2.1 and a snapshot the unit cell in Fig. 2.2. Gold has been chosen as a model type surface that was widely studied in the literature whereas ferric-oxide is more representative of a real tribological surface. The introduction of dislocations in the crystals is possible. However, the tiny size of the systems (only a few cubic nanometers) and the nature of the problem being studied (confined lubrication) make this an unnecessary complication.

Compound	Lattice structure	Lattice constants	Primitive cell
Gold ( $Au$ )	Face-centred cubic (FCC)	$a = 4.0782 \text{ \AA}$	FCC
Ferric-oxide ( $Fe_2O_3$ )	Corundum	$a = 5.029 \text{ \AA}$ ; $c = 13.730 \text{ \AA}$ $x_O = 0.3056$ ; $z_{Fe} = 0.10534$	rhombohedral

**Table 2.1:** Lattice structure of the crystalline surface models. The constants for gold are from ref. [76] and those for ferric-oxide are from ref.[77]

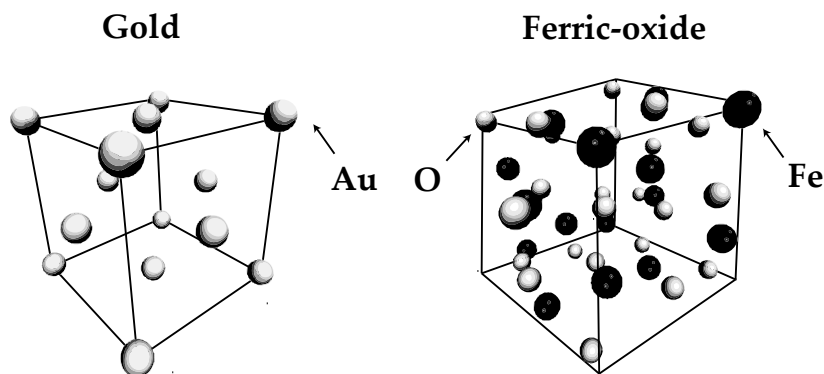


**Fig. 2.2:** Snapshot of the unit cells of gold and ferric-oxide crystals.

In order to construct a surface model from these unit cells, a lattice orientation should also be defined. The orientation influences the surface density and eventually its potential corrugation. The reader is advised to consult the interface modeling section of this chapter and Chapter 4 about the effect of surface potential corrugation on friction in confined lubrication problems.

After the solid atoms are disposed on their lattice structure, the laws of their interactions must be defined. Three interaction models from the literature were considered: harmonic bonds (HB) [41], Lennard Jones (LJ) [41], and the embedded-atom method (EAM) [78].

In the harmonic bonds model, each atom in the surface is connected by unbreakable bonds to its neighboring atoms within a defined cut-off distance. This insures the integrity of the surfaces during the studied interval. In the equilibrium lattice configuration, the force between any two atoms is zero. When the bonds are stretched or compressed, the force between the atoms is equivalent to a harmonic spring model. If  $l$  is the distance between two connected atoms and  $l_0$  is the equilibrium bond length, then the interaction potential energy  $V_{(\text{HB})}$  is given as:

$$(2.5) \quad V_{(\text{HB})} = K(l - l_0)^2$$

$K$  is half the spring stiffness. The knowledge of this parameter is usually not straightforward. A few guidelines, however, can help in this choice such as the Debye frequency and Lindemann melting criterion for solids. The Debye frequency represents the maximum frequency of vibration in a crystal. Since this frequency is proportional to the spring stiffness, a maximum limit can be set for the choice of  $K$ . On the other hand, Lindemann criterion gives the maximum mean square displacement ( $\langle \delta u^2 \rangle$ ) of atoms from their equilibrium lattice positions before melting takes place, this is given by the equation:

$$(2.6) \quad \frac{\langle \delta u^2 \rangle}{\tilde{d}^2} \leq c_L^2 \quad \text{with} \quad c_L \approx 0.18 - 0.25 [79]$$

In this equation,  $\tilde{d}$  is the distance to the nearest atom and  $c_L$  is a universal coefficient that is independent of the lattice. Considering  $c_L = 0.18$ , by isothermal equilibrium simulations a minimum value for  $K$  that satisfies the Lindemann criterion of Eq. (2.6) is calculated. The results for the Debye and Lindemann criteria are given in Table 2.2.

Compound	Debye frequency (rd.s <sup>-1</sup> )	Minimum K (Kcal.mol <sup>-1</sup> .Å <sup>-2</sup> )	Maximum K (Kcal.mol <sup>-1</sup> .Å <sup>-2</sup> )
Gold ( <i>Au</i> )	$2.160 \times 10^{13}$	$8 \times 10^{-3}$	109.8
Ferric-oxide ( <i>Fe<sub>2</sub>O<sub>3</sub></i> )	$5.021 \times 10^{13}$	3	281.2

**Table 2.2: Guidelines for the choice of the spring stiffness in the harmonic bond model for gold and ferric-oxide solids. The minimum K is determined with Lindemann criterion at 400 K. The maximum K is calculated from the Debye frequency determined from the material properties of gold [76] and ferric-oxide [80].**

The range of which satisfies the two criteria remains quite large for both surface types. Additional criteria based on the thermal and mechanical properties of the modeled surfaces will be introduced in the next section which will allow a more precise choice of  $K$ .

The Lennard-Jones (LJ) potential is used to model the electrostatic attraction (Van der Waals) and repulsion (Pauli) forces between atoms. Within a predefined cut-off distance  $r_c$ , an atom interacts with a neighboring atom at a distance  $r$  according to the potential  $V_{(\text{LJ})}$ :

$$(2.7) \quad V_{(\text{LJ})} = 4\epsilon \left[ \left( \frac{\sigma}{r} \right)^{12} - \left( \frac{\sigma}{r} \right)^6 \right] \quad r < r_c$$

$\epsilon$  is the LJ energy and depends on the nature of the interacting atoms. On the other hand, if the interacting atoms are of the same nature, then  $\sigma$  is their atomic diameter. When the atoms approach to a closer distance than  $2^{\frac{1}{6}}\sigma$ , their electronic clouds superpose and a repulsion force is produced Fig. 2.3. For two interacting atoms of different nature,  $\epsilon$  and  $\sigma$  can be concluded using mixing rules from the individual interaction parameters for each atom. Lorentz-Berthelot rules are most widely used and are given as [41]:

$$(2.8) \quad \epsilon_{AB} = \sqrt{\epsilon_{AA} \epsilon_{BB}} \quad \text{and} \quad \sigma_{AB} = \frac{\sigma_{AA} + \sigma_{BB}}{2}$$

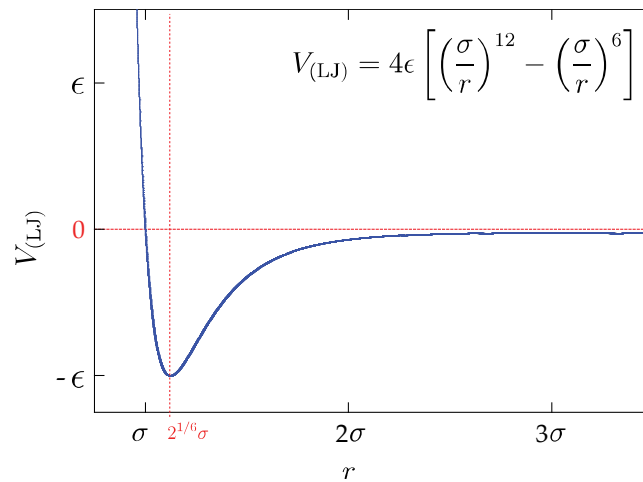


**Fig. 2.3: The Lennard-Jones model for inter-atomic showing repulsion (Pauli's forces) and attraction (Van der Waals forces) at short and large distances respectively.**

Finally, the EAM potential models, in addition to the nucleic pair-wise interactions ( $\phi^{pw}$ ), an embedded energy function ( $F$ ) is considered which depends on the electron density ( $\rho_e$ ) from the surrounding atoms. The EAM potential is widely used to model metals and metal alloys. The interaction energy  $V_{(EAM)}$  on atom  $i$  is given as:

$$(2.9) \quad V_{(EAM)} = F \left( \sum_{j \neq i} \rho_e(r_{ij}) \right) + \frac{1}{2} \sum_{j \neq i} \phi^{pw}(r_{ij})$$

The EAM interaction parameters are often given in tables and can be found for commonly used metals. For gold, the parameters were taken from ref. [78]. However, no EAM potential parameters were found for the ferric-oxide crystal.

Employing harmonic bonds has the advantage that, throughout a simulation, each atom has a fixed number of neighbors. LJ and EAM models require a regular neighbor list update to be determined for each atom. Fig. 2.4 shows a comparison between these three interaction models in terms of calculation time needed to simulate 10ps on a single processor. The results show that the calculations using harmonic bonds model are about 10 times faster than EAM, and 5 times faster the LJ model.

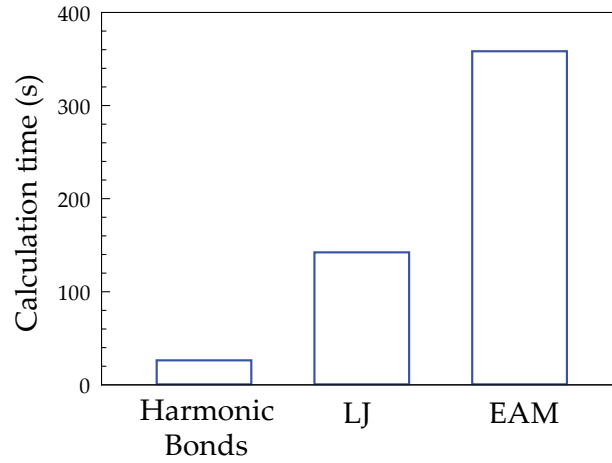


**Fig. 2.4:** Calculation time, in seconds, for a system of 2560 gold atoms in FCC configuration at constant volume and temperature. Simulations are done with a single processor and for a total simulated time of 10 ps.

The calculation speed is not the only criteria for the choice of the interaction model. Thermal and mechanical properties of the surfaces should be representative of the real matter. As will be conveyed in the next section, these properties depend on the values chosen for the interaction parameters.

### 2.2.2.2 Thermal and mechanical properties

Molecular simulations were run in order to characterize the thermal and mechanical properties of solids modeled by each of the three interaction models. The investigated thermal property is the conductivity and the mechanical property is the bulk modulus. In a molecular lubrication problem when the fluid is sheared, heat is generated and must be dissipated properly through the surfaces. A well defined thermal conductivity helps in reproducing the real phenomenon of heat conduction. The bulk modulus represents the response, by volume change, due to a homogeneous pressure. This property was chosen because it is independent of the lattice orientation, unlike the shear or Young modulus which would depend on the relative orientation between the lattice and the applied stress.

In order to calculate the thermal conductivity ( $\lambda$ ), a reversible non-equilibrium simulation was run according to the Muller-Plathe method [81]. This method is based on continuously exchanging heat ( $Q$ ) between two layers at a known rate, giving the heat flux ( $\phi^{\text{ex}}$ ). A temperature gradient, perpendicular to the planes, develops which represents the natural response to the heat exchange (see Fig. 2.5). The ratio of the heat flux to the temperature gradient gives the thermal conductivity:

$$(2.10) \phi^{\text{ex}} = \frac{1}{S} \frac{\partial Q}{\partial t} \quad \text{and} \quad \lambda = -\frac{\phi^{\text{ex}}}{\partial T / \partial z}$$

In this equation,  $S$  is the surface area and  $z$  is the normal direction to the planes where heat is exchanged.

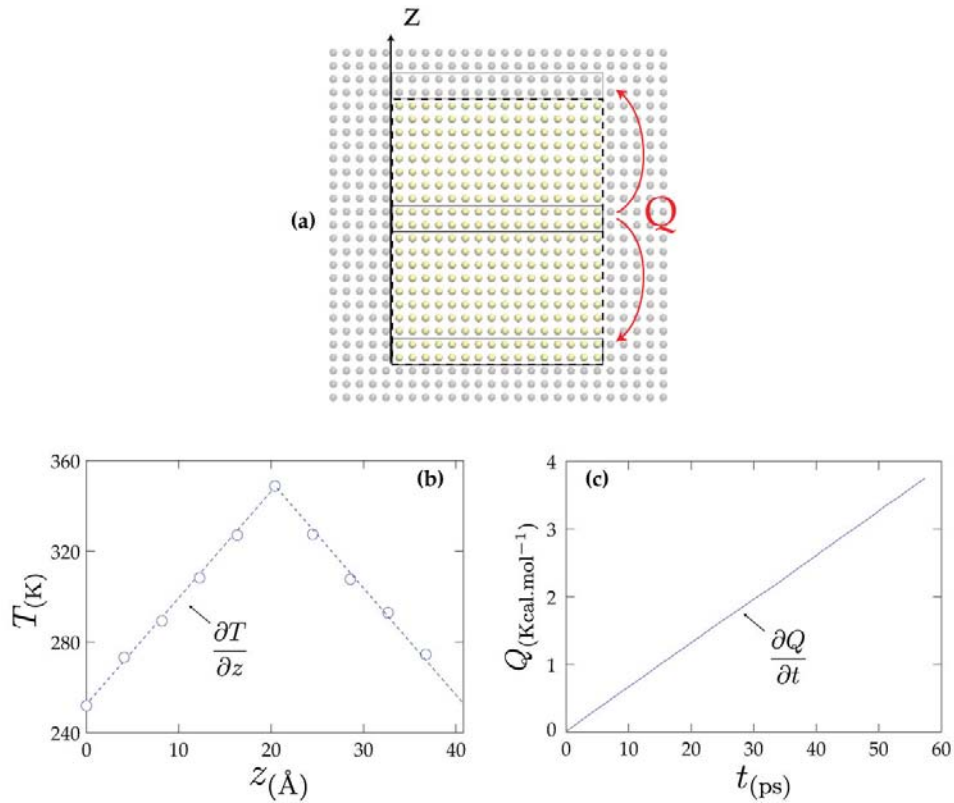


**Fig. 2.5:** The non-equilibrium simulation method for determining the thermal conductivity. Heat is exchanged at a known rate from the center of the box to its sides as explained by the arrows. The system response is through a linear temperature profile. The dotted box represents the periodic boundary conditions.

In order to determine the bulk modulus ( $K_0$ ), simulations were conducted on a bulk system (periodic in three dimensions) within a constant temperature, constant pressure (NPT) thermodynamic ensemble (for more details on the statistical thermodynamic ensembles, please check refs. [41, 82, 43]). A small isotropic pressure change ( $\partial P$ ) produces a volume change ( $\partial V$ ) as shown in Fig. 2.6. The bulk modulus is then calculated by the equation:

$$(2.11) \quad K_0 = -V \frac{\partial P}{\partial V}$$

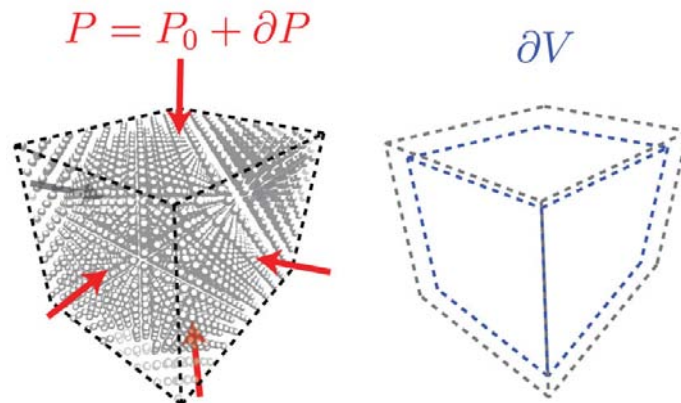


**Fig. 2.6:** A schematic showing the method of calculation of the bulk modulus ( $K_0$ ). From a small isotropic pressure increase, a change in volume is induced which depends only on the bulk modulus.

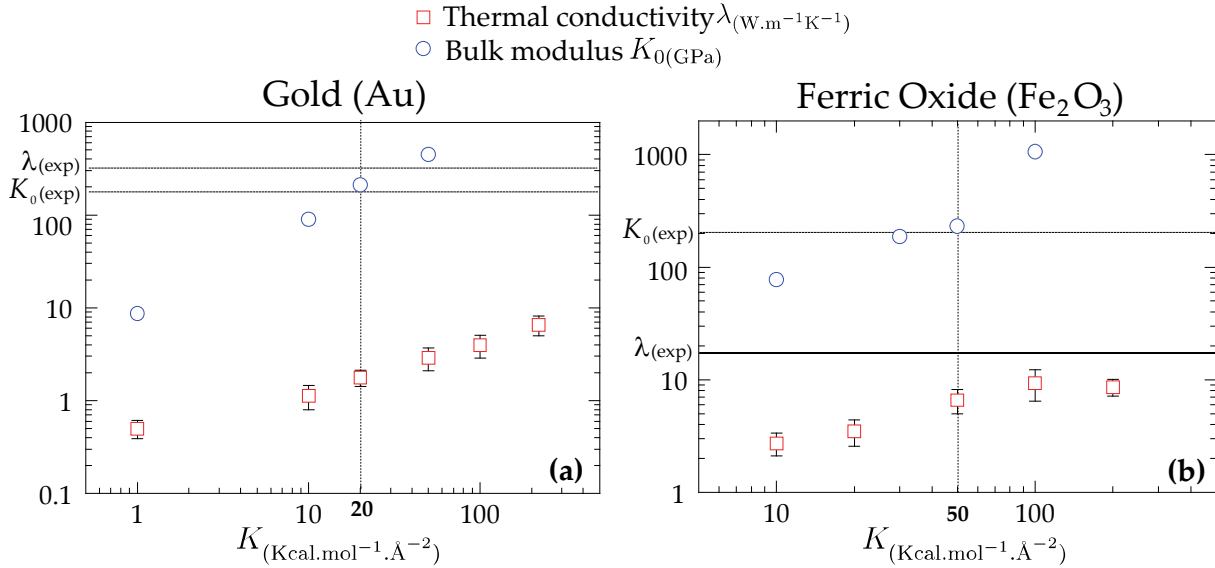


**Fig. 2.7: Variation of the thermal conductivity ( $\lambda$ ) and the bulk modulus ( $K_0$ ) of gold (a) and ferric oxide (b) solids as a function of half the spring stiffness in the HB model. Simulations were run at 300K temperature and 1 atm pressure. Horizontal dashed lines correspond to the results from reference experiments at the same conditions.**

For the harmonic bonds model, the results for the thermal conductivity and the bulk modulus for gold are given in Fig. 2.7-a as a function of half the spring stiffness  $K$ . It can be seen that by increasing  $K$ , both the measured conductivity and bulk modulus increase. However, the thermal conductivity is two orders of magnitude below the experimental value for gold of  $317 \text{ W.m}^{-1}\text{K}^{-1}$  [76]. This difference is due to the deficiency of simulations in modeling conduction through electrons, which has the largest contribution to the thermal conductivity in metals. What is modeled and measured here is only the heat transferred by atomic vibrations (phonons). As for the bulk modulus, the experimental value of  $172.37 \text{ GPa}$  is closely approached for a value of  $K$  of  $20 \text{ Kcal.mol}^{-1}.\text{\AA}^{-2}$ . This value also satisfies the guidelines summarized in Table 2.2 and is considered optimal value for modeling gold surfaces using the harmonic model.

For ferric oxide, the results are given in Fig. 2.7-b. In a similar manner, the conductivity and bulk modulus increase with  $K$  but the conductivity reaches a maximum value for  $K > 100 \text{ Kcal.mol}^{-1}.\text{\AA}^{-2}$ . This saturation in the conductivity can be explained by through the mechanisms of heat transfer by atomic motion on one hand and by inter-atomic interactions on the other. When the springs become very stiff, the transfer through atomic interactions increases. However, the atoms become locked on their equilibrium positions producing a counter effect to the conductivity enhancement by the first mechanism. An optimal value of  $K = 50$  gives the best agreement with the experimental results from refs. [80] and [83].

The same tests were done with the Lennard-Jones and EAM models but only for the case of gold. For the LJ model, the interaction parameters from ref.[84] ( $\epsilon = 529.28 \text{ K}$  and  $\sigma = 2.655 \text{ \AA}$ ) were considered as a reference and  $\epsilon$  was varied over a wide range. The results in Fig. 2.8 show that the thermal conductivity and bulk modulus increase with  $\epsilon$ . The conductivity with both models is still two orders of magnitude smaller than the experimental value. The bulk modulus is also smaller than the experimental value for the LJ and EAM parameters found in the literature. However, an optimal value for  $\epsilon$  between 1000 and 3000 can give a satisfactory bulk modulus but with small conductivity.

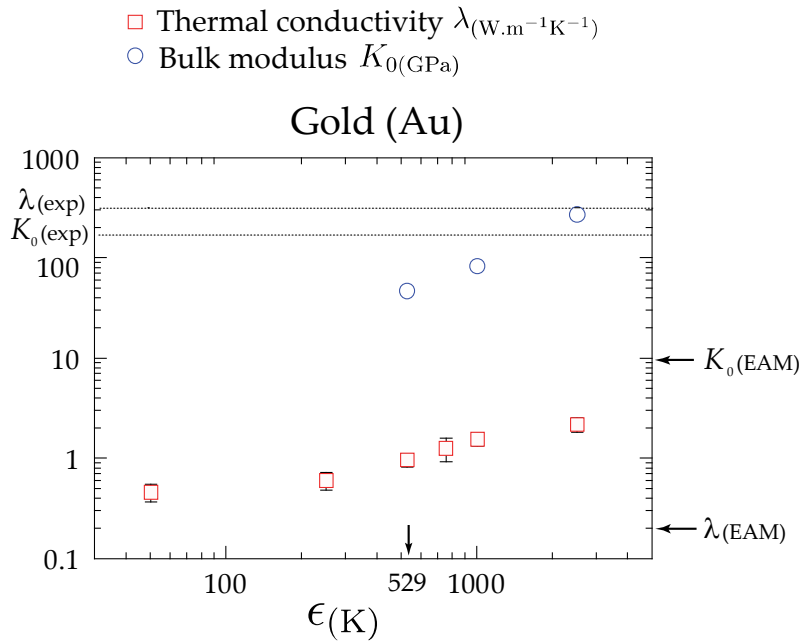


**Fig. 2.8:** Variation of the thermal conductivity ( $\lambda$ ) and the bulk modulus ( $K_0$ ) of gold as a function of Lennard-Jones interaction energy ( $\epsilon$ ). Arrows indicate the results obtained with the Embedded-Atom method. Horizontal dashed lines correspond to the results from reference experiments [76, 80, 83].

As a conclusion, employing LJ and EAM models does not show an improvement in the mechanical and thermal properties of the model. The use of harmonic bonds remains more interesting due to the small calculation time compared to the other models. Table 2.3 summarizes the retained interaction parameters for gold and ferric oxide as well as their corresponding mechanical and thermal properties.

Compound	Bonding cut-off ( $\text{\AA}$ )	K (optimal) ( $\text{Kcal}\cdot\text{mol}^{-1}\cdot\text{\AA}^{-2}$ )	$\lambda$ ( $\text{W}\cdot\text{m}^{-1}\cdot\text{K}^{-1}$ )	$\lambda(\text{exp})$ ( $\text{W}\cdot\text{m}^{-1}\cdot\text{K}^{-1}$ )	$K_0$ (GPa)	$K_0(\text{exp})$ (GPa)
Gold ( <i>Au</i> )	4.08	20	$1.77 \pm 0.35$	317	$210.2 \pm 0.8$	172.4
Ferric-oxide ( <i>Fe</i> <sub>2</sub> <i>O</i> <sub>3</sub> )	3.63	50	$6.58 \pm 1.60$	17.25	$231.2 \pm 4.1$	206.6

**Table 2.3:** Summary on the optimal spring stiffness K for gold and ferric oxide models. The corresponding thermal and mechanical properties are compared to experimental values.

### 2.2.3 Lubricant

The modeling process of a liquid lubricant has three complications compared to that of solid surfaces. First and unlike the well ordered crystalline structure in solids, there is no global ordering inside a liquid. Second, lubricants are able to flow and their molecules are thus able to move past one another during a simulation. Third, lubricant molecules are usually made of flexible chains and thus encounter all sorts of bond stretching and rotations. The molecular architecture of the modeled lubricants: pentane (simple model alkane) and hexadecane (more complex and representative base oil) is presented in the next section.

### 2.2.3.1 Molecular architecture and interactions

Lubricants are modeled as flexible molecules. The molecular architecture includes bond stretching, angle bending, and torsion as shown in Fig. 2.9. The potentials that model these interactions depend on the choice of the force field.

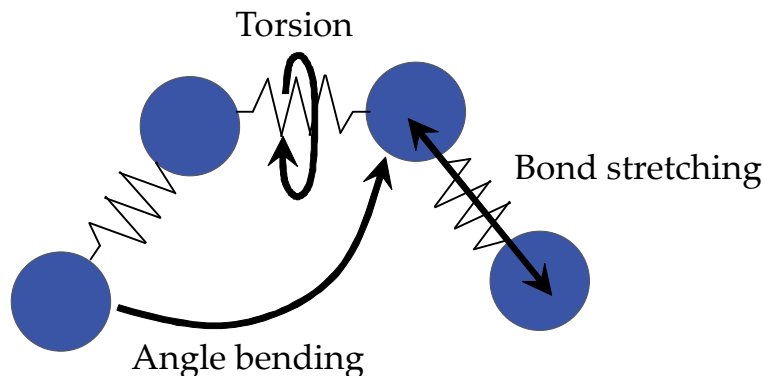


Fig. 2.9: A schematic showing the three kinds of intermolecular interactions used to model the flexibility of lubricant molecules.

Covalent bond stretching and angle bending are usually modeled with simple spring potentials:

$$(2.12) \quad V_{\text{bond}} = K_b (l - l_0)^2$$

$$(2.13) \quad V_{\text{angle}} = C_\theta (\theta - \theta_0)^2$$

where  $l - l_0$  and  $\theta - \theta_0$  represent the deviations from the equilibrium bond length and angle. The dihedral interaction (torsion) can be modeled [85] with either of the following potentials:

$$(2.14) \quad V_{\text{torsion-AMBER}} = K[1 + \cos(n\phi - d)]$$

$$(2.15) \quad V_{\text{torsion-OPLS}} = \frac{1}{2} \sum_{n=1}^4 A_n [1 + (-1)^{n-1} \cos(n\phi)]$$

Moreover, the Lennard-Jones potential as in Eq. (2.7) is used to compute the interactions between atoms that do not interact with intermolecular potentials. These are atoms from different molecules or are separated by more than 4 atoms along the molecular chain.

There are two ways for modeling the structure of liquid alkanes: the All-Atoms and the United-Atoms method. As can be inferred from the name, All-Atoms explicitly model the totality of atoms including Hydrogens. In United Atoms, Hydrogens are compensated in the mass of the  $\text{CH}_2$  and  $\text{CH}_3$  segments to which they are covalently bonded. So instead of having 17 and 50 atoms in the pentane and hexadecane models, only 5 and 16 groups corresponding to  $\text{CH}_2$  and  $\text{CH}_3$  units are considered (Fig. 2.10). This method significantly reduces the calculation time and allows a bigger time step to be used in the simulations.

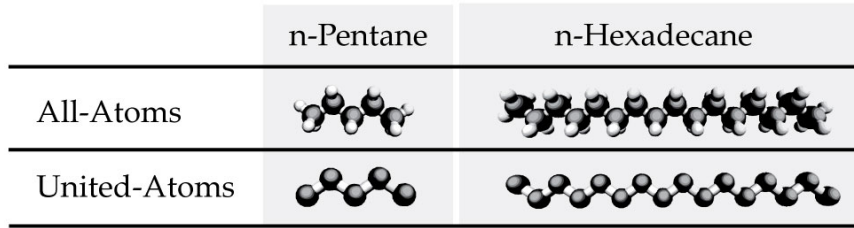


Fig. 2.10: Snapshots of the structures of n-pentane and n-hexadecane molecules using All-Atoms and United-Atoms models.

The interaction coefficients for the all-atoms model were taken from the AMBER96 force-field [86] and those for the united-atoms model were taken from the OPLS force-field [85]. They are presented in Table 2.4.

Interaction/Equation	Type	Coefficients			
<b>All Atoms</b>					
Non-bonded $V_{(LJ)} = 4\epsilon \left[ \left( \frac{\sigma}{r} \right)^{12} - \left( \frac{\sigma}{r} \right)^6 \right]$		$\epsilon$ (Kcal.mol <sup>-1</sup> )	$\sigma$ (Å)		
	Carbon (CT)	0.1093	3.3997		
	Hydrogen (HC)	0.0157	2.6495		
Bond stretching $V_{\text{bond}} = K_b (l - l_0)^2$		$K_b$ (Kcal.mol <sup>-1</sup> .Å <sup>-2</sup> )	$l_0$ (Å)		
	CT-CT	309.7838	1.5260		
	CT-HC	339.7629	1.0900		
Angle bending $V_{\text{angle}} = C_\theta (\theta - \theta_0)^2$		$C_\theta$ (Kcal.mol <sup>-1</sup> .deg <sup>-2</sup> )	$\theta_0$ (deg)		
	CT-CT-CT	39.9721	109.5		
	CT-CT-HC	49.9651	109.5		
	HC-CT-HC	34.9756	109.5		
Torsion $V_{\text{tor}} = K[1 + \cos(n\phi - d)]$		$K$ (Kcal.mol <sup>-1</sup> )	$n$	$d$ (deg)	
	X-CT-CT-X	0.1555	3	0.0	
<b>United Atoms</b>					
Non-bonded $V_{(LJ)} = 4\epsilon \left[ \left( \frac{\sigma}{r} \right)^{12} - \left( \frac{\sigma}{r} \right)^6 \right]$		$\epsilon$ (Kcal.mol <sup>-1</sup> )	$\sigma$ (Å)		
	CH <sub>3</sub>	0.1946	3.7500		
	CH <sub>2</sub>	0.0913	3.9500		
Bond stretching $V_{\text{bond}} = K_b (l - l_0)^2$		$K_b$ (Kcal.mol <sup>-1</sup> .Å <sup>-2</sup> )	$l_0$ (Å)		
	CH <sub>3</sub> -CH <sub>2</sub>	268.09	1.5400		
	CH <sub>2</sub> -CH <sub>2</sub>	268.09	1.5400		
Angle bending $V_{\text{angle}} = C_\theta (\theta - \theta_0)^2$		$C_\theta$ (Kcal.mol <sup>-1</sup> .deg <sup>-2</sup> )	$\theta_0$ (deg)		
	X-CH <sub>2</sub> -CH <sub>2</sub>	62.0570	114.0		
Torsion $V_{\text{tor}} = \frac{1}{2} \sum_{n=1}^4 A_n [1 + (-1)^{n-1} \cos(n\phi)]$		$A_1$ (Kcal.mol <sup>-1</sup> )	$A_2$ (Kcal.mol <sup>-1</sup> )	$A_3$ (Kcal.mol <sup>-1</sup> )	$A_4$ (Kcal.mol <sup>-1</sup> )
	X-CH <sub>2</sub> -CH <sub>2</sub> -CH <sub>2</sub>	1.4101	-0.2708	3.1492	0

Table 2.4: Interaction parameters used to model the lubricant molecules derived from ref. [86] and ref. [85] for the All atoms and United atoms models respectively.

The influence of the lubricant model on its dynamic and thermal properties is presented in the next section.

### 2.2.3.2 Dynamic and thermal properties

Perhaps the most important dynamic property of lubricants is their viscosity. This has been tested for both models using reversible non equilibrium molecular dynamics simulations [81]. The concept is identical to that used to calculate the thermal conductivity but here

the momentum, and not the kinetic energy, is exchanged (see Fig. 2.11). The rate of momentum exchange is used to calculate the shear stress ( $\tau_{xz}^{\text{ex}}$ ) as given in Eq. (2.16). The response of the system is through a linear velocity profile between the layers where momentum is exchanged. The shear rate ( $\dot{\gamma}_{\text{eff}} = \partial u / \partial z$ ) is determined from this profile. Finally, shear viscosity ( $\eta$ ) is calculated as the ratio between the shear stress and the shear rate.

$$(2.16) \quad \tau_{xz}^{\text{ex}} = \frac{1}{2S} \frac{\partial P}{\partial t} \quad \text{and} \quad \eta = \frac{\tau_{xz}^{\text{ex}}}{\dot{\gamma}_{\text{eff}}}$$

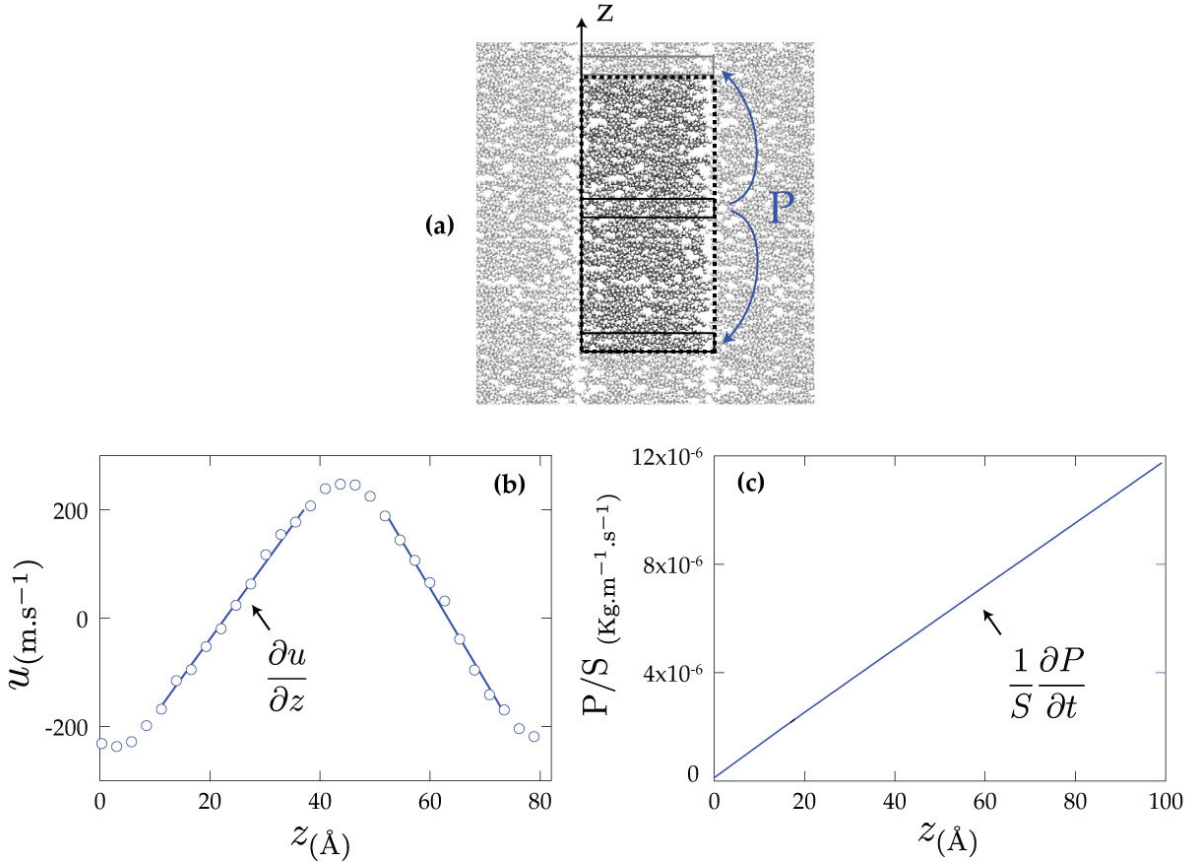


**Fig. 2.11: The non-equilibrium simulation method employed for determining the bulk shear viscosity. Momentum (P) is exchanged at a known rate from the center of the box to its side as explained by the arrows (a). The system response is through a linear velocity profile (b). The dotted box represents the periodic boundary conditions.**

In order to compare with experimental data, a zero-shear (Newtonian) viscosity is needed. In simulations, the zero-shear viscosity can be determined by running a series of simulations at different shear rates and then fitting the data to a Carreau model. The shear viscosity results at different shear rates are given in Fig. 2.12. Shear thinning is observed for both hexadecane and pentane, although the onset of thinning is at a higher shear rate for the latter. It is remarkable also that the United-Atoms model gives a better prediction of the Newtonian viscosity for pentane than the All-Atoms model. However, with hexadecane the predicted shear viscosities are lower than the All-atoms model and experiments.

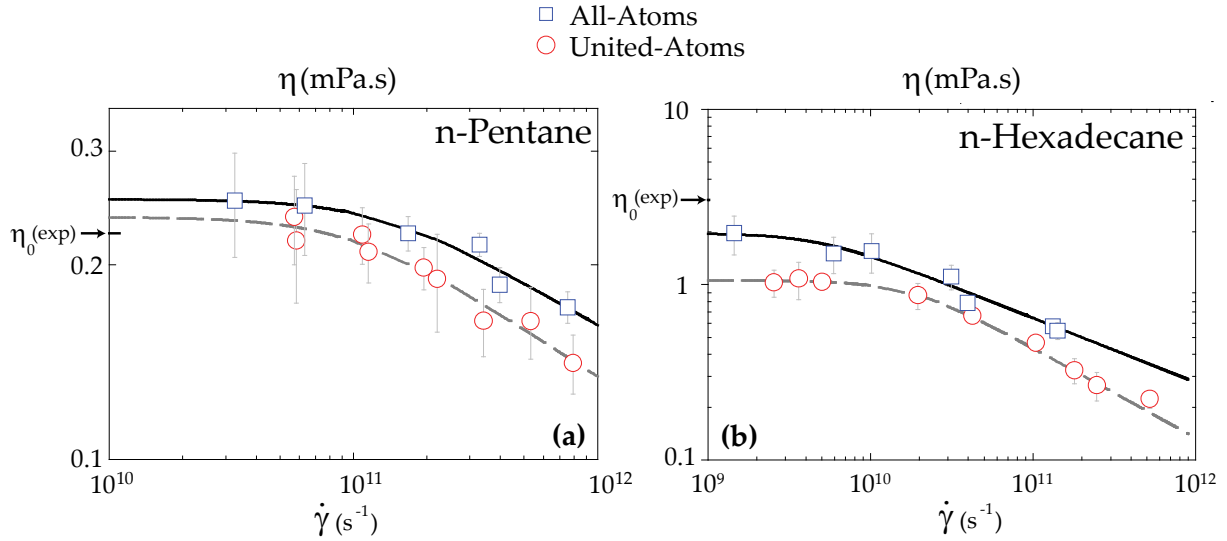


**Fig. 2.12:** Variation of the dynamic viscosity of n-pentane and n-hexadecane with the shear rate determined through molecular simulations. Lines correspond to Carreau fits of the results. The arrows represent the experimental Newtonian viscosities for pentane at 300 K and hexadecane at 298 K. All results are at ambient pressure.

Finally, the thermal conductivity was also calculated in bulk hexadecane and pentane with both models using the non-equilibrium method previously described in the solid modeling section (Fig. 2.5). The results, assembled with the viscosity predictions, are given in Table 2.5. For both lubricants, the measured thermal conductivities are in the same order as those in experiments. For pentane, the All-atom model gives an excellent prediction compared to the United-atoms model. However, for the hexadecane molecule, this model overestimates the conductivity.

Lubricant	Model	$\eta_0$ (mPa.s)	$\eta_0(\text{exp})$ (mPa.s)	$\lambda$ (W.m <sup>-1</sup> .K <sup>-1</sup> )	$\lambda(\text{exp})$ (W.m <sup>-1</sup> .K <sup>-1</sup> )
n-pentane (C <sub>5</sub> H <sub>12</sub> )	United Atoms	0.237	0.224	0.074	0.111
	All Atoms	0.253		0.116	
n-hexadecane (C <sub>16</sub> H <sub>34</sub> )	United Atoms	1.056	3.030	0.097	0.140
	All Atoms	1.962		0.2175	

**Table 2.5:** Dynamic and thermal properties of two types of models (United Atoms and All Atoms) for n-pentane and n-hexadecane. The results, at ambient temperature and pressure, are compared with experimental data from ref.[76].

In this section, the thermal and dynamic properties were determined for pentane and hexadecane with two different models. It was found that explicit and coarse models (all-atoms and united atoms) generally give acceptable predictions of these properties for short molecules. For long molecules, the results are less accurate in comparison with experimental data but remain in the same order of magnitude. While employing either model one should be aware of the influence that this choice has on the properties of the lubricant and whether quantitative comparison with experiments is suitable.

## 2.2.4 Surface-Lubricant interface

The last element in the molecular lubrication model is the surface-lubricant interface. The interfacial interactions determine how the surfaces influence the structure of the confined lubricant. Moreover, these interactions allow the surface loading and sliding to be transmitted into lubricant compression and shear.

The surface-lubricant interfacial interactions are commonly modeled using a Lennard Jones potential (Eq. (2.7)). The potential well-depth (LJ energy), representing the interaction strength between the surface and the lubricant, is chosen as  $\epsilon_{s-f} = \kappa \epsilon_{f-f}$ .  $\epsilon_{f-f}$  is the well-depth of internal fluid interactions and  $\kappa$  is a factor chosen in the range of 0.4 – 4 [55, 87, 11].  $\kappa$  represents the relative interaction strength at the interface with respect to the inside of the fluid. This range (0.4 – 4) covers weakly to highly adsorbing surface types.

In modeling real solid surfaces, justifying the choice of  $\kappa$  is not an easy task. There is only one guideline found in the literature that is based on fitting the interaction strength to experimental data on the molecular adsorption energies on surfaces [87, 88]. In alkanes, experiments with the TPD (Temperature Programmed Desorption) state that the adsorption energy increases by 1 – 1.4 Kcal.mol<sup>-1</sup> per CH<sub>2</sub> segment, for different types of metal surfaces [89, 90, 91]. This criterion has been used by several authors [87, 88] and will be used in the following for choosing the correct surface-lubricant interaction parameters.

The adsorption energies of hexadecane and pentane molecules on gold and ferric-oxide surfaces were determined using molecular simulations. The molecular domain is constituted of a surface that is covered with a 10 Å thickness of lubricant molecules as shown in Fig. 2.13. The surface temperature was fixed at 90K in order to insure that the desorption energy barrier is not surpassed. When the lubricant molecules are adsorbed to the surface, an average potential energy per molecule could be calculated inside the adsorbed lubricant layer. Using the Lorentz-Berthelot mixing rule for the surface and lubricant atoms, the surface-surface interaction well-depth ( $\epsilon_{s-s} = \kappa^2 \epsilon_{f-f}$ ) was changed in a way to yield  $\kappa = 1, 2, 3, 4$  and 5. The distance parameter for gold atoms ( $\sigma_{Au} = 2.655 \text{ \AA}$ ) was taken from ref. [84].

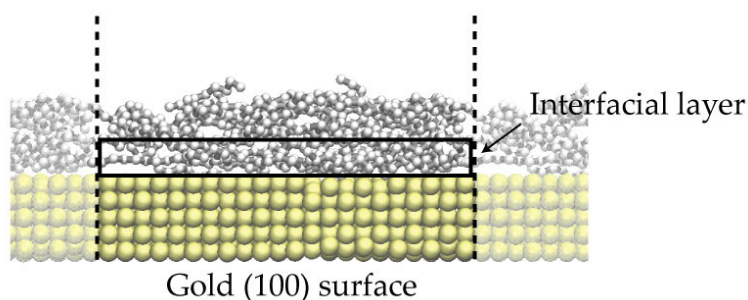


**Fig. 2.13:** The molecular system used for studying the lubricant adsorption in order to determine the interfacial interactions. In this example, hexadecane molecules are adsorbed onto a gold (100) surface. The dotted lines represent the periodic boundary conditions.

Since the lubricant model includes different types of atoms/groups, the average fluid interaction strength ( $\epsilon_{f-f}$ ) was calculated as follows:

$$(2.17) \quad \epsilon_{f-f} = \frac{1}{M} \sum_{i=1}^N m_i \epsilon_i$$

$M$  is the mass of the lubricant molecule,  $N$  is the number of atoms in one molecule,  $m_i$  and  $\epsilon_i$  represent the mass and the LJ well-depth of atom  $i$ . From the interaction parameters reported in Table 2.4, the average fluid interaction strengths are calculated and given in Table 2.6. The surface-fluid interaction is given by " $\kappa$ " multiplied by these values.

Lubricant	Model	$\epsilon_{f-f}$ (Kcal.mol <sup>-1</sup> )
n-pentane (C <sub>5</sub> H <sub>12</sub> )	United Atoms	0.1344
	All Atoms	0.0936
n-hexadecane (C <sub>16</sub> H <sub>34</sub> )	United Atoms	0.1050
	All Atoms	0.0952

Table 2.6: Average fluid interaction strengths calculated according to Eq. (2.17)

As shown in Fig. 2.14, the adsorption energy increases with the interaction strength represented by  $\kappa$  for both pentane and hexadecane, with the United-Atoms and All-Atoms models. The difference in the adsorption energy between these two molecules given experimentally is equal to 11 – 15.4Kcal.mol<sup>-1</sup>. This is satisfied for  $\kappa = 5$  in the United Atoms model and for  $\kappa = 4$  in the All Atoms model. Moreover, the adsorption energies for both types of molecules are in the same order of magnitude for this choice of  $\kappa$ .

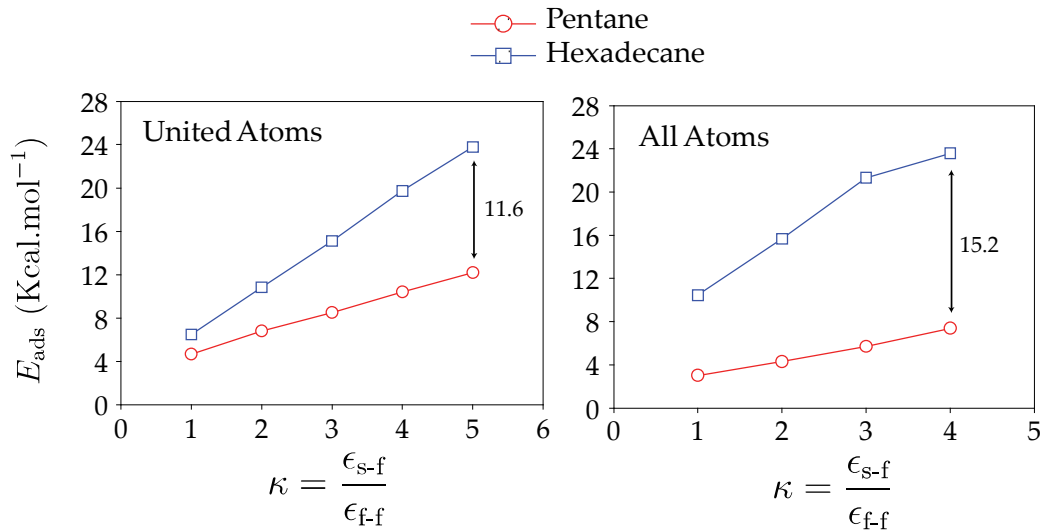


Fig. 2.14: Variation of the adsorption energy on gold surfaces for pentane and hexadecane with the two model types as a function of  $\kappa$  the ratio of interaction strengths at the interface to that inside the fluid.

The same method was applied for the ferric oxide surface. However in this case the Lennard Jones parameters for oxygen atom were taken from the AMBER96 force field [86] as  $\epsilon_O = 0.2098$ Kcal.mol<sup>-1</sup> and  $\sigma_O = 2.960$ Å. As for the iron atom, the distance parameter was taken from ref. [92] as  $\sigma_{Fe} = 2.321$ Å and the energy parameter ( $\epsilon_{Fe}$ ) was varied. Eq. (2.17) was

used to calculate the equivalent  $\text{Fe}_2\text{O}_3$  surface-surface interaction well-depth from the two constituting elements, oxygen and iron, according to the equation:

$$(2.18) \epsilon_{\text{s-s}} = \frac{1}{M_{\text{Fe}_2\text{O}_3}} (2 \times m_{\text{Fe}} \epsilon_{\text{Fe}} + 3 \times m_{\text{O}} \epsilon_{\text{O}}) = \kappa^2 \times \epsilon_{\text{f-f}}$$

( $\epsilon_{\text{Fe}}$ ) was changed in order to regulate the strength of the surface-lubricant interactions ( $\kappa$ ). With a similar analysis to that with the gold surface, it was found that only a value of  $\kappa = 8$  gives correct adsorption energies for both United Atoms and All Atoms models. This is equivalent to the values of  $\epsilon_{\text{Fe}}$  given in Table 2.7.

The obtained interaction parameters for gold and iron atoms, given in Table 2.7, are coherent with the parameters found in the literature (for slightly different systems). These are the parameters which will be used in the remaining part of this manuscript. For cases involving polar molecules, Coulombic interactions are considered in addition to the presented LJ interactions (Chapter 5).

Surface Atom	$\epsilon$ (Kcal.mol <sup>-1</sup> )				Range found in the literature
	Pentane United Atoms	Hexadecane United Atoms	Pentane All Atoms	Hexadecane All Atoms	
Gold (Au)	3.360	2.625	1.498	1.523	1.05 – 1.96
Iron (Fe) in $\text{Fe}_2\text{O}_3$	12.208	9.518	8.475	8.621	12.137

**Table 2.7: The obtained Lennard-Jones interaction parameter for the surface-lubricant interface. The literature range is from refs. [87, 84, 92, 88].**

## 2.3 Initialization and sampling

### 2.3.1 Geometry

The molecular lubrication model is built from the three constitutive elements described previously: the surfaces, the lubricant, and their interface. A snapshot of an example model with gold surfaces confining a 24Å pentane lubricant is given in Fig. 2.15. The surface dimensions are 36.72Å in both x and y dimensions and periodic boundary conditions are used to model an infinitely large contact. (See also section 2.3.5.1 for validation of this choice)

The size of the simulation domain in the z direction is governed by two critical parameters: the thickness of the lubricant film and that of the surfaces. Although in reality the surfaces can be a few micrometres or millimeters thick, in molecular simulations only a few angstroms can be modeled. This choice can be justified physically by the limited cut-off distances of the interfacial interactions. In the example model of Fig. 2.15 which will be used from this point on, the surfaces are chosen to be 10Å thick so that the lubricant molecules (which are usually a few angstroms away from the surfaces) are not influenced by the discontinuity of the solid model.

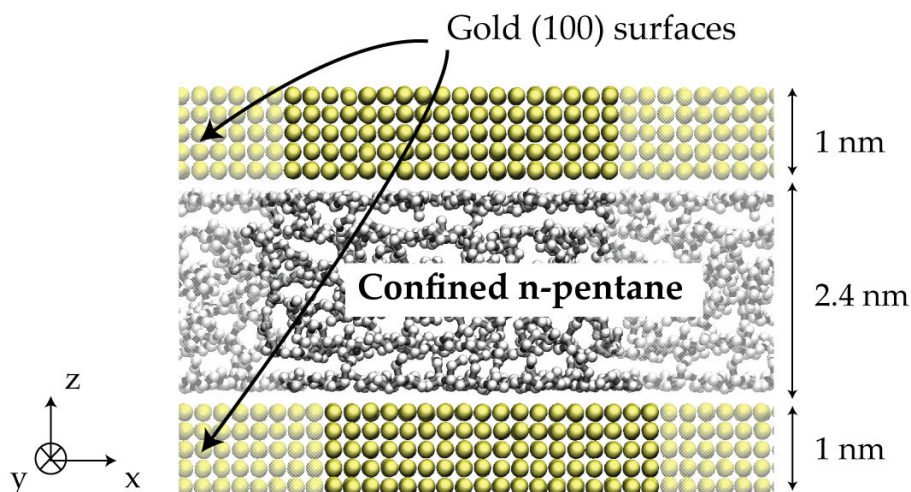


Fig. 2.15: Snapshot of the molecular lubrication model comprising gold (100) surfaces and 2.4 nm thick pentane lubricant. The shaded regions correspond to periodic images of the simulated box.

### 2.3.2 Initial density

It is common to run simulations with a fixed film thickness. Unless the number of molecules of the confined film is allowed to vary [93], an initialization phase (using Monte-Carlo methods) is needed in order to yield a physical initial lubricant density prior to the MD simulation [94].

In constant-thickness simulations with a constant number of molecules, the contact pressure is constant if no shear is applied. The pressure oscillates with the film thickness mimicking the solvation pressure oscillations in SFA experiments [93]. However, when the confined lubricant is sheared in a constant volume, its temperature and pressure increase.

This work, however, is inspired from classical notions in lubrication where the film thickness is seen as the result of the contact conditions of temperature, normal load, and surface motion. The load, instead of the film thickness, is constant. The choice of the initial lubricant density becomes no longer a critical issue since the volume (thickness) may naturally vary with the load. By compression, the lubricant relaxes to a physical density throughout the simulation. Constant load molecular simulations have already been employed by several workers [95, 66].

In constant load simulations, it is preferable to have an initial density that is close to the equilibrium one. This allows a better control of the equilibrium thickness. If the final density is approximately known in advance, the thickness will only change a little with compression. For this purpose, empirical density-pressure relationships can give a good estimation of the initial density needed in the domain so that the thickness varies little by compression.

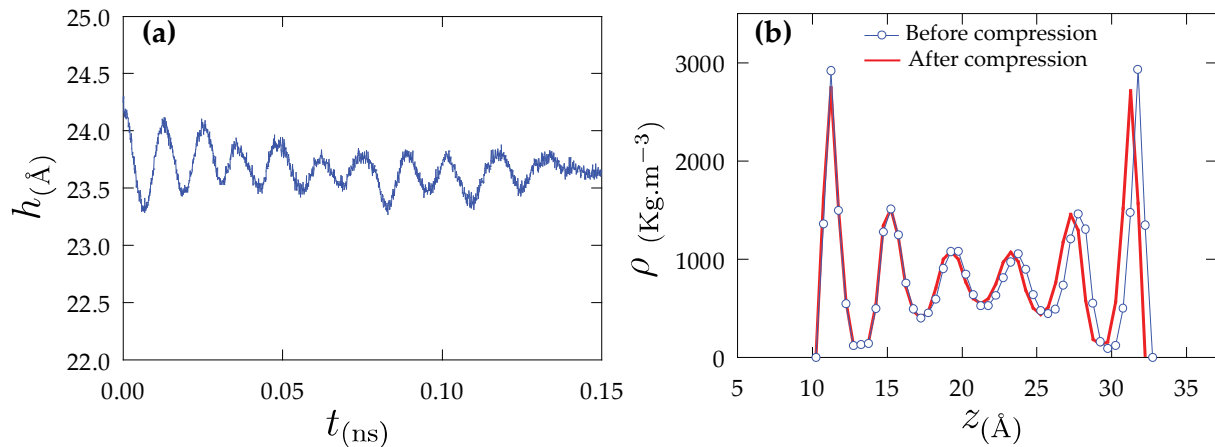
In this work, the initial density is determined by running bulk fluid simulations at constant pressure and temperature (NPT ensemble) corresponding to the normal load and the initial temperature. The equilibrium density is then used as the initial state in confined dynamic simulations.

### 2.3.3 Compression

The lubricant is compressed by applying a unidirectional load normal to the surfaces. The uniform load is applied in the form of elementary forces whose sum divided by the surface area gives the loading pressure. The atoms to which the forces are applied belong to a  $2\text{\AA}$  thick layer, furthest from the solid liquid interface in order to avoid direct influence of this boundary condition on the confined lubricant.

In the following example simulation, the contact load is chosen to be equal to  $500\text{MPa}$  which is common in industrial applications. The initial and the boundary temperatures are set to  $300\text{K}$ . Therefore, the initial density is chosen to be coherent with these two conditions. The calculated density under these conditions for the pentane bulk (United Atoms model) is  $757\text{Kg.m}^{-3}$ .

Under constant load, the film thickness encounters oscillations with time as shown in Fig. 2.16-a. The film thickness reaches an equilibrium value that is constant within 2-3% in less than  $0.2\text{ns}$  of compression. This is because the initial density was chosen to be near the equilibrium density under confinement.



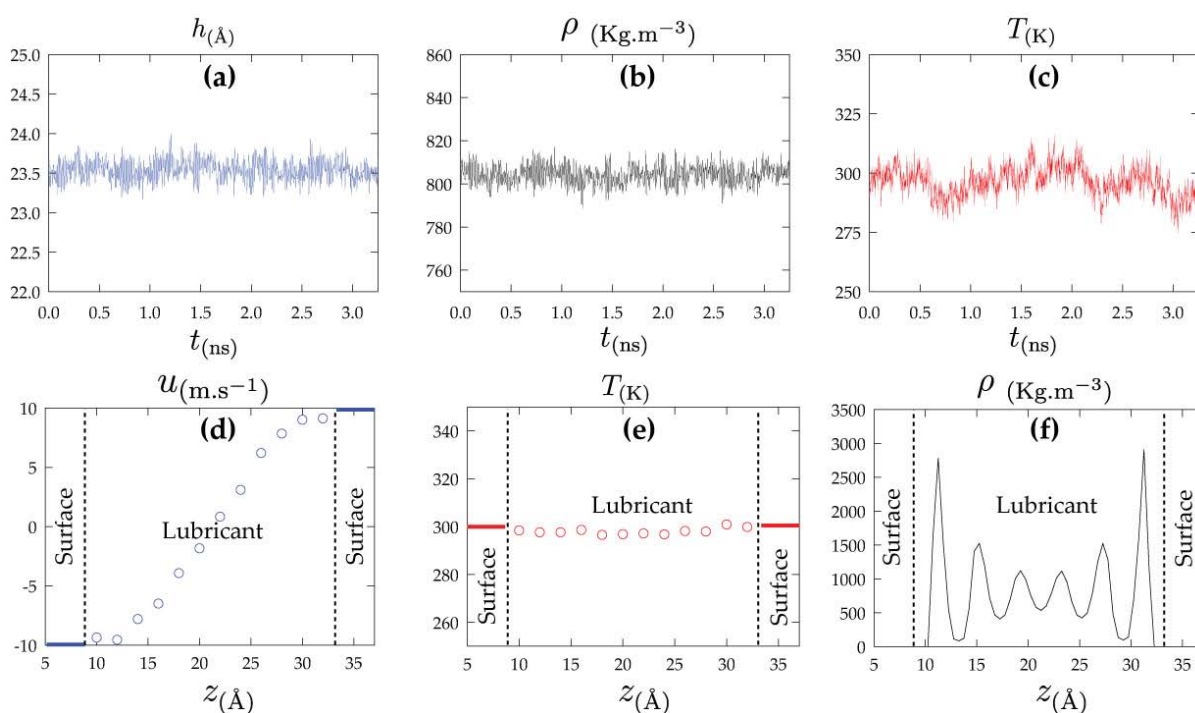
**Fig. 2.16: During the compression phase: a) time evolution of the film thickness ( $h$ ) as a function of time. b) Comparison between the density profiles before and after the compression across the  $2.4\text{nm}$  confined pentane film between Au surfaces.**

Fig. 2.16-b shows a comparison in the density profiles of the pentane film before and after compression. Before applying the normal load but keeping the film thickness constant at  $2.4\text{nm}$ , the pressure in the lubricant oscillated around  $450\text{MPa}$ . When a pressure of  $500\text{MPa}$  was imposed, the lubricant was compressed by about  $0.5\text{\AA}$  (Fig. 2.16-a) and the density profile was a little more compacted. At the same temperature and pressure, a slight density increase thus occurs in the confined film compared to the bulk system which was used to define the initial density.

The obtained density profiles across the pentane film (Fig. 2.16-b) are classical and show the structuring which occur as a result to confinement. The first density peak is about 4 times the bulk (average) density. The structuring becomes less pronounced in the middle of the film. These results are a proof of the model capability of capturing the structural effects in confined lubricants. In the next section, the surfaces are set to move in opposite direction and the dynamics of the confined film are presented.

### 2.3.4 Shear

After the system is compressed and reaches equilibrium, the surfaces are set to move at equal but opposite velocities of  $10\text{m}\cdot\text{s}^{-1}$  each to produce an apparent shear rate in the same order of magnitude as that in tribological applications involving molecular lubrication. The difference in momenta between the two surfaces is transmitted through the interfacial interaction forces, inside the fluid. A momentum flux is built and this is conveyed with a velocity gradient which develops across the sheared film as shown in Fig. 2.17-d. The density profile given in Fig. 2.17-f doesn't show a considerable change with respect to the case without shearing (Fig. 2.16).



**Fig. 2.17:** During the shear phase, time evolution of: a) the film thickness, b) the average lubricant density, and c) the average lubricant temperature. During the shearing steady state, between 2 and 8 ns, the streaming velocity (d), temperature (e), and density (f) profiles across the 2.4nm confined pentane film between Au surfaces.

As for the dynamics of the confined film, the effective shear viscosity in this simulation is  $2.19$  mPa.s. It is calculated as the shear stress, needed to keep moving the surfaces at a constant speed, divided by the apparent shear rate. Although this viscosity is found at an elevated shear rate ( $8.49 \times 10^9 \text{s}^{-1}$ ), it is still higher than the Newtonian bulk viscosity of this lubricant ( $0.237$  mPa.s). This is an indication of a viscosity increase due to the confinement and a deviation from the bulk properties. The investigation of the velocity profile (Fig. 2.17-d) reveals a no-slip boundary condition in these simulations. The lubricant velocity near the solid surfaces is equal to the sliding speed of the surfaces. Finally, the lubricant temperature is constant as an average during the shearing state as shown in Fig. 2.17-e.

## 2.3.5 Sampling effects

The final section of this chapter is dedicated to analyzing the influence of spatial and time sampling on the results of molecular simulations. Spatial sampling is related to the size of the domain in the  $x$  and  $y$  directions, where periodic boundary conditions are applied (Fig. 2.15). Time sampling is related to the choice of the integration time-step as well as the total simulated duration.

### 2.3.5.1 Spatial sampling: system size

Regarding the system size, an evident rule is that the length of the system in any dimension should be at least equal to the molecular length plus the interaction cut-off distance. If this condition is not satisfied, a molecule risks interacting with itself across the periodic boundaries. Moreover, there is an interest in employing larger domains for reducing the statistical uncertainties in the measured quantities since they will be averaged over a bigger number of elements. Unfortunately, increasing the system size can be very heavy in terms of calculation load.

In order to verify the choices taken for the system size of the model from Fig. 2.15, the same system was modeled with double  $x$  and  $y$  dimensions. The total number of molecules is then multiplied by 4. Fig. 2.18 shows a comparison between the results obtained from the two models under compression and shear.

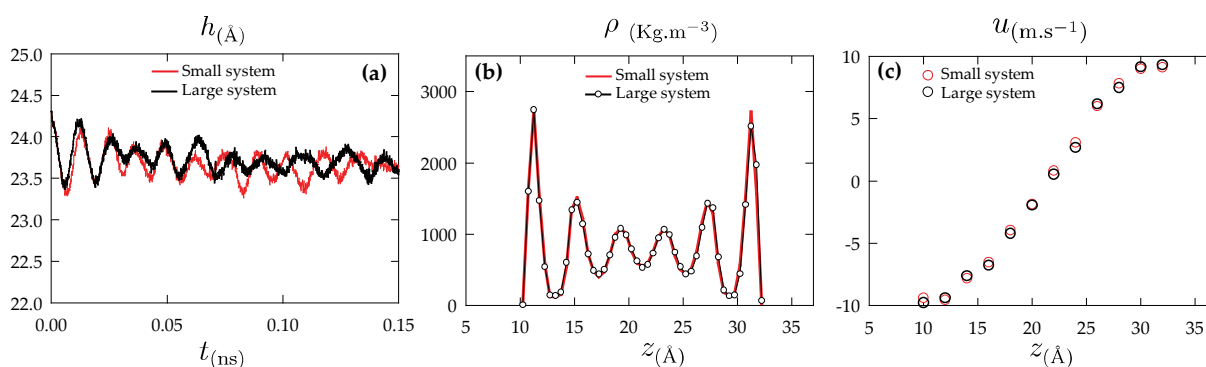


**Fig. 2.18: For a 2.4nm thick pentane film confined between gold surfaces: comparison of the: a) film thickness evolution with time and b) the density profile after compression and c) velocity profile across the film during shear for the same model but with different system size.**

The results show that increasing the system size has no direct influence on the results. The differences are only within statistical uncertainties.

A similar analysis was made for systems with hexadecane lubricant whose molecule (stretched) is nearly 18.5Å i.e. 3.5 times longer than the pentane molecule. Simulations at variables surface sliding velocities from 10m.s<sup>-1</sup> to 200m.s<sup>-1</sup> were conducted on a thick hexadecane film confined between gold surfaces. The sampled surface size was changed between 32.64Å × 32.64Å, 48.96Å × 48.96Å, and 61.20Å × 61.20Å.

In order to compare how the system sampling size influences the results, the velocity profiles across the hexadecane film were given for different sliding velocities and sampled surface area in Fig. 2.19. The results show that the sampled surface had very small influence

on the velocity profiles for sliding velocities greater than or equal to  $20\text{m.s}^{-1}$ . For slower surface sliding, the small surface area gave different results than the larger two. The reason is that with slow sliding velocities, a larger sample needs to be considered in order to eliminate statistical errors.

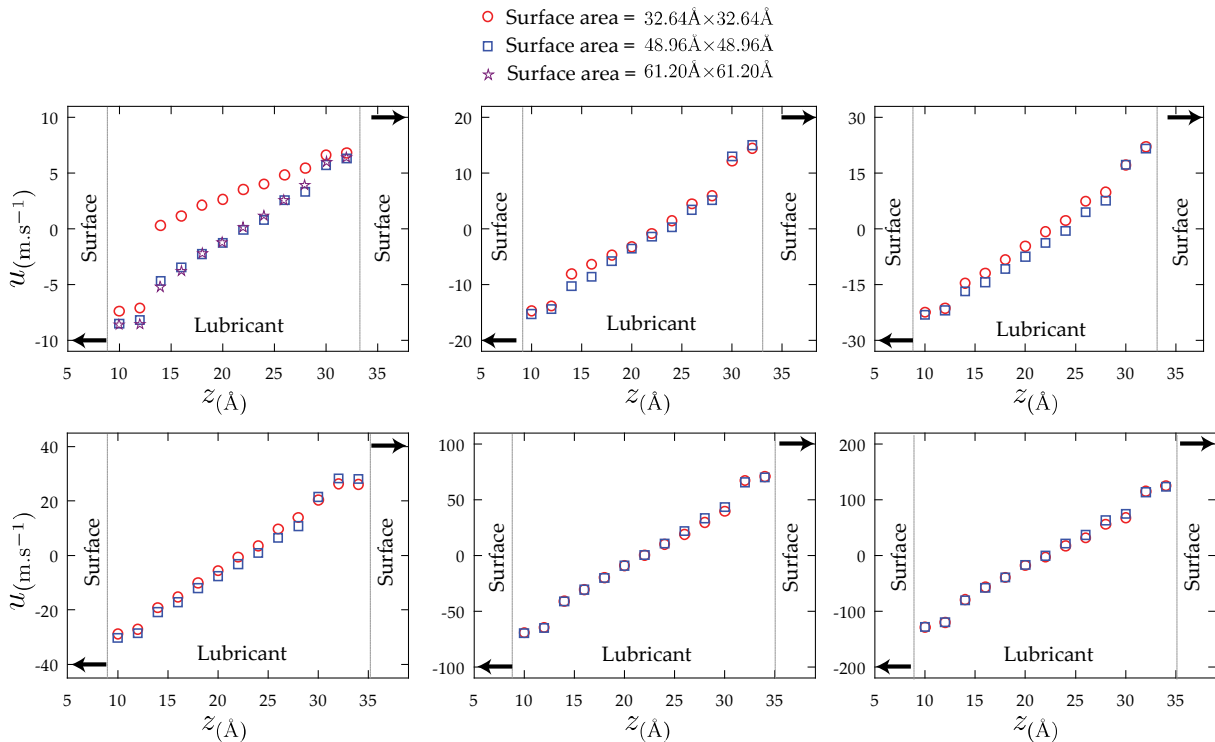


**Fig. 2.19: Velocity profiles obtained across 2.4nm thick hexadecane films confined between gold surfaces for different surface sliding velocities and sampled system sizes.**

In conclusion, it is not possible to set a universal guideline for different molecular systems and operating conditions. According to the system in study, a larger sample may be needed to eliminate statistical errors. A large domain is actually needed for simulating long molecular chains and low sliding velocities. The sampling duration also plays a role in this aspect. For the case of hexadecane with 5ns sampling duration, a gold surface area of  $48.96\text{\AA} \times 48.96\text{\AA}$  was found to give size-independent results for different surface sliding speeds and will thus be used in the rest of this thesis.

### 2.3.5.2 Time sampling: time-step and simulation duration

The choice of the time-step in molecular dynamics simulations is also a critical issue to handle. In principle, the time step should be small enough so that the supposition that all interaction forces are invariant between two steps remains valid. Nevertheless, there is an obvious interest in using large time steps because this allows phenomena to be investigated over a long period of time.

For each type of interactions between atoms, a characteristic time scale can be known in advance. For example in covalent bonds modeled by harmonic springs the period of oscillation can be calculated from the spring stiffness and the atomic masses. In molecular systems with angle bending and torsional interactions, it is often suggested to use a time step of  $2\text{fs} = 2 \times 10^{-15}\text{s}$ . The accuracy of the simulations can be simply tested by decreasing the time

step and watching the quantities that are supposed to be conservative. For example, in molecular systems with conservative Newtonian motion integrations (micro-canonical NVE type simulations [41]), the total energy should be constant.

NVE simulations at different time-steps were conducted for a system of bulk pentane with the united and all-atoms models. The total energy was plotted as a function of time as shown in Fig. 2.20.

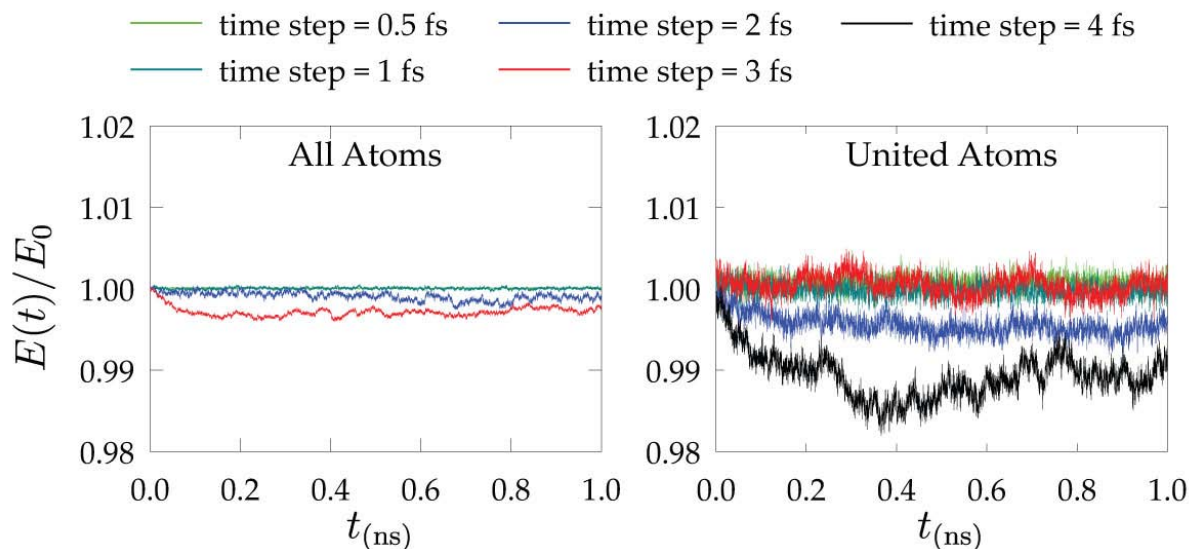


Fig. 2.20: Evolution of the ratio of the total system energy to the initial energy as a function of time for bulk (3D periodic) pentane with the all-atoms and united-atoms models.

The first observation is that the energy variations are more pronounced for the united atoms model. This can be explained by the fact that, for a given system size, a smaller number of elements (united atoms) are present compared to the explicit all-atoms model and this results in statistical uncertainties. The variation of the total energy after 1ns of simulation is found to be inferior to 1% for time steps less than 3fs in both models. However, in order to ensure stability and minimize the numerical errors, a time step of 1fs is chosen for the simulations.

Finally, it is difficult to set a single guideline for choosing the total simulated duration. The longer the sampling duration, the more accurate are the collected statistics. As conveyed in the previous section, the system size also plays a significant role. If the system is large, a shorter duration would be needed. However, in all cases, the simulated duration must be longer than the time scale of the phenomenon being investigated. For instance, in the molecular lubrication model presented previously, the simulation should be longer than the time needed for reaching the shearing steady state of the system.

From the example of Fig. 2.17, it was found that the collected time averages of thickness, temperature, and shear stress over 6ns after the steady state are the same as over 3ns sampling period. Nevertheless the condition remains system specific. It strongly depends on the number of atoms, their nature, the nature of their interactions, in addition to the boundary conditions. This was seen in the case of hexadecane for a sliding speed of  $10\text{m}\cdot\text{s}^{-1}$  (Fig. 2.19). The combination of system size and simulation duration should be large enough to give accurate statistics. This relationship is closely related to the ergodic theory which states that the

averages over large time and space are equivalent for a system in equilibrium. For the time being and for accuracy purposes, 5ns sampling will be considered in the remaining simulations of this thesis.

## Conclusion

In this chapter, the molecular dynamics simulation method was briefly presented. A molecular lubrication model was designed and developed element by element. Each element was studied separately and parameterized in order to yield realistic material and interface properties. The elements were finally compiled to produce the molecular lubrication model. This model was then tested and it succeeded in reproducing many common trends from the literature in both static and dynamic conditions.

The last part of this chapter dealt with sampling issues related essentially to the size of the system, the time step, and the simulation duration. Guidelines were determined for ensuring the stability and accuracy of the simulations as well as the adequacy of the determined statistics from the molecular scale for different operating conditions.

In the purpose of modeling molecular lubrication, one of the weak points of the current model is the method of heat dissipation. The mechanical energy being continuously injected to the system by compression and shear is transformed into heat. The heat is then transferred by conduction and convection inside the lubricant, across the interface, and into the surfaces where it is dissipated. If the method of dissipation is not realistic, due to model related issues like a low conductivity or inappropriate thermostating method, the temperature of the lubricant increases non-physically. This in turn influences the dynamics of the confined lubricant and may give misleading results on friction.

It is thus essential to properly model the dissipation especially in friction and lubrication studies. The next chapter is dedicated to the resolution of this problematic in molecular lubrication problems.

# 3

## Friction and Energetic Dissipation Mechanisms

58

<b>Introduction</b>	<b>58</b>
<b>3.1 Energy balance in confined films under shear</b>	<b>59</b>
3.1.1 Energetic path	59
3.1.2 Balance validation in confined shear simulation	61
3.1.3 Cause-effect relationship between friction and thermostat dissipation	63
<b>3.2 Sliding boundary thermostat method</b>	<b>63</b>
3.2.1 Thermostating algorithms	64
3.2.2 Heating onset by shearing	66
<b>3.3 Advanced dissipation methods</b>	<b>68</b>
3.3.1 The Phantom-Molecules method	69
3.3.2 The variable boundary temperature method	71
3.3.2.1 Principle	71
3.3.2.2 Validation	73
3.3.2.3 Temperature update interval	74
3.3.3 Assessment on the dissipation methods	75
<b>Conclusion</b>	<b>76</b>

# 3. Friction and Energetic Dissipation Mechanisms

---

## Introduction

In the previous chapter, a molecular dynamics model for molecular lubrication problems was constructed and characterized. In this model, all molecular interactions that govern the system evolution with time are conservative. The extra mechanical energy added by surface loading and sliding can only be dissipated as heat in the molecular model. For a lubrication-type study, energy dissipation is a key factor that must be carefully handled. The present chapter is thus dedicated to examining the influence of the energy dissipation method on the thermodynamic state of the confined film and the globally measured friction for different contact operating conditions. A novel model for energy dissipation dedicated for high shear simulations is finally presented which takes into account realistic heat transfer from the confined lubricant to the confining surfaces.

In MD simulations where energy needs to be dissipated, a thermostat is usually employed. The purpose of the thermostat is to define a coupling between the simulated molecules and an imaginary heat bath at a specified temperature. This “coupling” allows the kinetic energy of molecules, due to thermal vibrations, to be controlled.

For simple homogeneous systems such as bulk solids and liquids, temperature can be controlled homogeneously using one of several available algorithms. The simplest and perhaps the oldest method is “velocity-rescaling”. The principle is to scale the atomic velocities at regular intervals to give the required kinetic temperature [41]. Advanced methods employ various constraints to control the temperature in a “smoother” way. For example, the Nosé-Hoover thermostat changes the energy-conservative equations of motion by adding an additional degree of freedom by which the energy transfer with the external heat bath occurs instantaneously.

These methods actually work very well for controlling the temperature in homogeneous systems. However in the case of confined films, some problems may emerge due to the non-homogeneous nature of the system [96]. This non-homogeneity is mainly due to the solid/liquid interface and manifests density fluctuations across the film. The picture becomes even more complicated in the case of shear. The generated viscous heat needs to be dissipated out of the contact. Several energetic transformations thus occur inside the film and characteristic temperature and velocity fields can only be captured if the lubricant molecules are free from any direct thermostating constraints [97]. The extra heat needs to be dissipated from the surfaces level [97].

In order to gain insight on the different energetic transformations occurring inside the lubricant film, the energetic balance in confined lubrication conditions is investigated in the

next section. This analysis will be used to show that there is a close relationship between the thermostat energy dissipation and the frictional force in the contact.

### 3.1 Energy balance in confined films under shear

The energetic study of confined films in molecular lubrication gives very important information on two levels. First, from a numerical simulation point of view, the energy balance is an important verification that the integration method is correct. Second, such analysis allows the energy path inside the molecular system to be understood. As will be illustrated in this section, the understanding of the energetic path permits us to answer several questions related to friction and dissipation in molecular lubrication problems.

#### 3.1.1 Energetic path

From its inlet at the surfaces in mechanical form, the energy undergoes three essential steps: absorption, transformation, and finally dissipation as shown in Fig. 3.1. Energy is added to the system by compression and relative surface motion. The momentum difference between the upper and lower surfaces diffuses inside the lubricant which absorbs this mechanical energy. Energy is transformed into the thermal form as a viscous heat is generated inside the sheared lubricant film. Temperature increases inside the lubricant and results in a gradient with the thermostated surfaces. The result is in a conductive heat flux transporting the thermal energy towards the surfaces where it is finally dissipated.

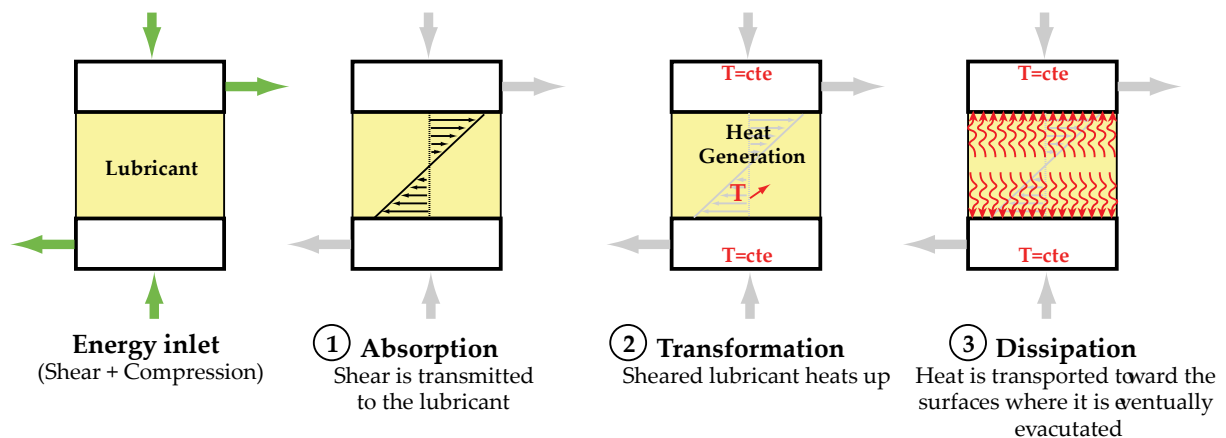


**Fig. 3.1: The energetic path inside a classical molecular lubrication problem. Energy is input in a mechanical form; it is transformed into heat inside the sheared lubricant, conducted inside the fluid and through the surface-lubricant interface to be finally dissipated by the thermostat.**

The input energy represents the work of the compression and shearing forces:

$$(3.1) \quad dE_{\text{in}} = -F_z \cdot (dh) + 2F_x \cdot v_x \cdot dt$$

As shown in Fig. 3.2,  $F_z$  is the normal force representing the contact load and  $F_x$  is the force needed to keep the surfaces going at a constant velocity. Since the sliding velocity is constant, then the sum of tangential forces acting on each surface is zero. Thus  $F_x$  is identical to the frictional force from the lubricant molecules on each surface.  $dE_{\text{in}}$  represents the input mechanical energy during a single time step ( $dt$ ). It is equal to the sum of the works of the normal and tangential forces. Assuming that the origin of the Cartesian coordinates moves with the lower surface, the works of the lower tangential and compression forces are zero. As for the forces on the upper surface, in one time step this surface moves  $dh = h_2 - h_1$  and  $2v_x \cdot dt$  in the normal and tangential directions with respect to the lower one. When  $dh$  is negative, meaning that the fluid is compressed, the work of the normal force must be positive. This explains the negative sign which precedes the first term on the right hand side of Eq.(3.1).

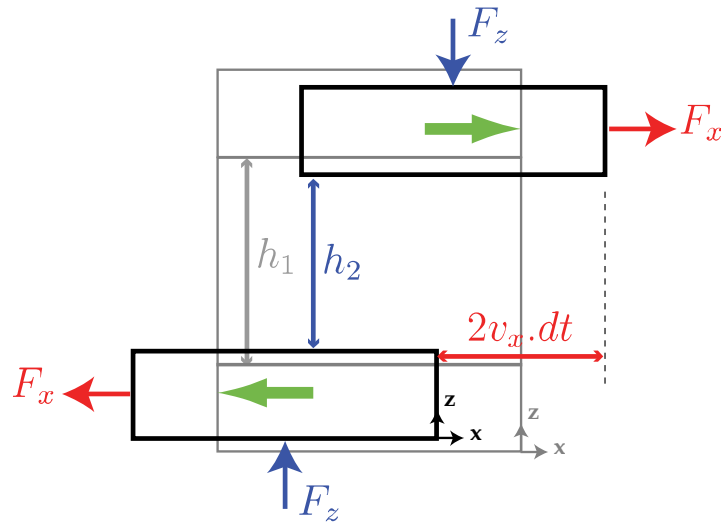


**Fig. 3.2: A schematic illustrating the normal and tangential distances traversed by the surfaces during a single time step. These distances are used to calculate the input energy according to Eq.(3.1).**

The input energy flux ( $\phi_{\text{in}}$ ) can be inferred from the previous equation as:

$$(3.2) \quad \phi_{\text{in}} = \frac{1}{S} \frac{dE_{\text{in}}}{dt} = \frac{1}{S} \left( -F_z \cdot \frac{dh}{dt} + 2F_x \cdot v_x \right)$$

$S$  is the surface area. On the other hand, the output (heat) flux ( $\phi_{\text{out}}$ ) can be determined from the total energy dissipated by the thermostats from both surfaces ( $E_{\text{out}}$ ):

$$(3.3) \quad \phi_{\text{out}} = \frac{1}{S} \frac{dE_{\text{out}}}{dt}$$

Note that in the molecular model with periodic boundary conditions, all mechanical energy is transformed into heat and is then dissipated by the surface thermostat. In reality other forms of energy dissipation may occur such as convection in the contact inlet and outlet and radiation. In the molecular model, the balance between the input and the output fluxes should be valid if the system doesn't "store" any energy. An example of this phenomenon is the lubricant heating up just at the instant when the surfaces are moved. The lubricant temperature increase actually uses a part of the input energy.

### 3.1.2 Balance validation in confined shear simulation

The energetic balance was verified for an example case with a 2.4nm thick hexadecane film confined between gold surfaces. The contact pressure is 500MPa and the surfaces are moved at equal but opposite velocities of  $10\text{m}\cdot\text{s}^{-1}$  each. The surface temperature is held fixed at 300K using a velocity rescaling thermostat of 100fs rescaling interval. No thermostating constraints were used on the lubricant. This method of dissipation is often referred to as the sliding boundary thermostat (SBT) and will be considered in details in the following sections. For the time being, a snapshot of the simulation domain with the boundary conditions is given in Fig. 3.3.

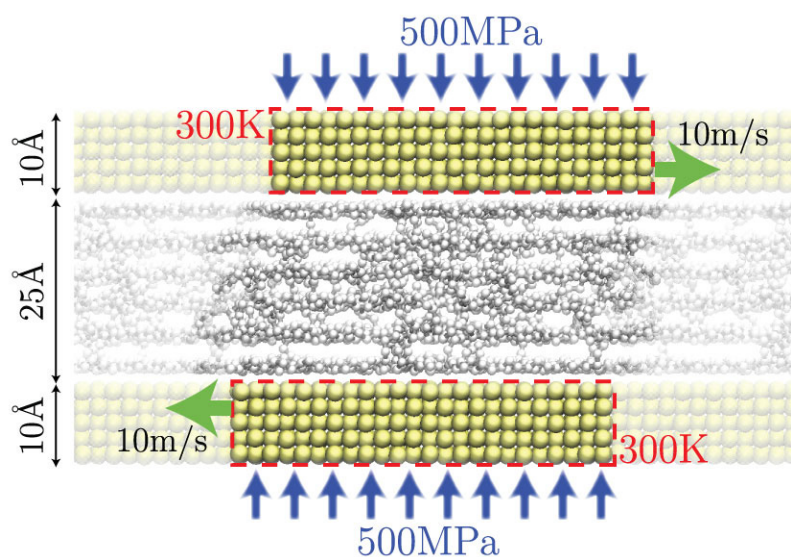


**Fig. 3.3: Snapshot of the simulation domain with the thermal and mechanical boundary conditions. The surfaces are squared and of a side dimension of  $48.96 \text{ \AA}$ . The periodic images of the modeled system are faded out. Temperature is controlled at the surfaces level as illustrated by the red dotted boxes.**

The film thickness, temperature, and various energetic terms of Eqs. (3.2) and (3.3) are given as a function of time in Fig. 3.4. At the beginning of shear ( $t = 0$ ), a transient stage is encountered as the lubricant cools down very fast then heats up gradually as shown in Fig. 3.4-b. The film gently expands (Fig. 3.4-a). For the considered conditions, this stage lasts about 0.1ns. The lubricant then reaches a state of equilibrium where its temperature and volume are constant.

The initial cooling down of the lubricant is due to start of motion of the surfaces. This creates a non-equilibrium state in the system. Since the surface velocities are imposed, the lubricant has no choice but to move along with the surfaces. However for lubricant flow to occur, the lubricant needs to surpass an energy barrier (static friction). The potential energy variation due to the surface motion is not yet enough to surpass this barrier. The only possibility is actually by sucking energy from the thermostat. Of course, heat flows only from high to low temperature zones. Since the surface temperature is constant, the fluid cools down to allow the energy to flow. This phase is very quick and lasts only about 0.03ns. The lubricant temperature drops about 20K. Note that during this phase, the film thickness is nearly constant (Fig. 3.4-a).

This phase ends when the energy barrier is surpassed and the lubricant shear flow begins. By shear, viscous heat is generated and the lubricant finds itself now with an excess of energy causing its temperature to rise. The excess energy is dissipated in two ways. The first way is through the mechanical work required to push the surfaces apart (expansion of the film as shown in (Fig. 3.4-a)). The second way is by thermal dissipation through the thermostats. The latter only occurs when the lubricant temperature rises above the controlled surface temperature (300K). The transient stage ends when all of the generated heat is dissipated thermally. In this example, the lubricant heats up to a temperature of 305.7K. At this temperature, there is equilibrium between the rate of viscous heating and its dissipation rate through the surface thermostat.

The different fluxes are plotted as a function of time in Fig. 3.4-c. Note that the fluxes are smoothed using a negative exponential method for the sake of clarity. During the transient stage ( $t < 0.1\text{ns}$ ), the energy balance between input and output energies is not clearly satisfied. This is normal because several transformations are occurring inside the lubricant (changes in potential energy, cooling then heating). The mechanical work of the normal forces is negative due to the expansion of the film as explained previously and shown in Fig. 3.4-a.

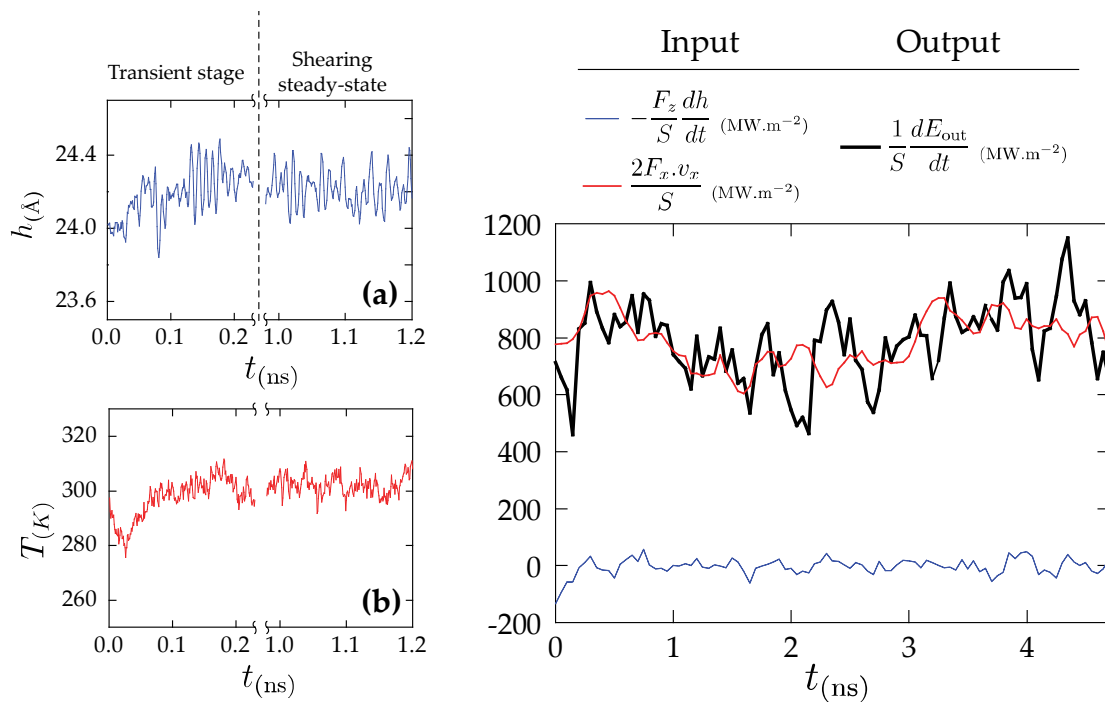


**Fig. 3.4:** Evolution of the lubricant film thickness (a) and temperature (b) in a system composed of a confined hexadecane lubricant between gold surfaces. (c) Comparison among different input and output fluxes for the same system.

At the end of the transient stage ( $t > 0.1\text{ns}$ ), the balance between the input and the output fluxes is established. The input mechanical energy is completely dissipated by the surface thermostat. This is the shearing steady-state. The film thickness is also constant in this steady-state and the power generated by compression is zero (Fig. 3.4-c). The role of the lubricant film is to absorb mechanical energy of shear from the surfaces, transform it into heat, and transmit it back to the surfaces by conduction and convection. It achieves this role per-

fectly and quite its total energy remains constant. The surface-lubricant-surface energetic loop continues endlessly once the shearing steady state is reached.

### 3.1.3 Cause-effect relationship between friction and thermostat dissipation

The analysis of the shearing steady state and especially its energetic balance clearly shows the direct connection between the tangential force (friction) and the thermostat dissipation. As the lubricant thickness is constant (Fig. 3.4-a), the energetic balance in the shearing steady state can be simplified to:

$$(3.4) \quad \frac{1}{S} \frac{dE_{\text{out}}}{dt} = \frac{2F_x \cdot v_x}{S}$$

For given conditions of load and sliding velocity, this equation has only two variables: the dissipated energy ( $E_{\text{out}}$ ) and the frictional force ( $F_x$ ). There are two possible scenarios to describe the cause-effect relationship between these two variables:

1. The dissipated energy is the consequence of friction forces inside the contact. Independent of the numerical parameters of the thermostat, the dissipated energy depends uniquely on the contact operating conditions.

2. The measured friction is the consequence of energy dissipation. For example, numerically if the thermostat is set to remove energy so often, the lubricant temperature will drop. Consequently, flow resistance increases and so does friction.

The purpose of the rest of this chapter is to answer this paradox. This will be accomplished by employing different dissipation methods in the molecular lubrication model and comparing the results. In the next section, different implementations of the classical sliding boundary thermostat are compared. The intriguing results will conduct the research to different cases in order to understand the complex relationship between friction and the thermostat dissipation.

## 3.2 Sliding boundary thermostat method

The classical dissipation method used in simulations of confined films under shear is the sliding boundary thermostat (SBT). In this method, the temperature of the solid surfaces is held fixed and no thermostating constraints are applied to the lubricant. This method has been employed by several authors [96, 97, 65, 94] as a substitute for homogeneous thermostats that directly control the lubricant temperature. It was shown that, by homogeneously dissipating energy from a confined lubricant in shear, its transport properties such as the viscosity are influenced [97]. In reality, the lubricant heats up (at elevated shear rates) and a characteristic temperature field develops across the film which influences its local transport properties and global friction in the contact.

In this section, the sliding boundary thermostat method is employed because, in addition to the previous arguments, it allows physical heat transmission from the lubricant to the surfaces to occur. A realistic energetic evolution, as illustrated previously in Fig. 3.1, can thus

be observed. Nevertheless, it is interesting to see if the different implementations of this method may have an effect on the obtained friction under invariant contact conditions.

### 3.2.1 Thermostating algorithms

In order to implement the sliding boundary thermostat method, a thermostating algorithm must be chosen for controlling the surface temperature. In this section, three algorithms were tested: velocity-rescaling, Nosé-Hoover, and Langevin thermostats. Details about these algorithms are given in Appendix 1.

In the velocity-rescaling algorithm, the Newtonian equations of motion are not modified but at regular intervals the atomic vibrational energies are scaled up or down to yield the target kinetic temperature. Note that this algorithm scales the velocities of all atoms homogeneously. The global surface temperature is thus controlled and a temperature gradient may still occur across the surface. In particular, surface atoms in direct contact with the lubricant may be “hotter” than those further from the interface (Fig. 3.5).

In the Nosé-Hoover algorithm, the Newtonian equations of motion are modified to include an additional degree of freedom by which the interactions with an external heat bath are included in the integration equations. This algorithm allows a smoother temperature control compared to the velocity rescaling algorithm where abrupt rescales are used. This algorithm, as velocity-rescaling, acts on the global temperature. If used to implement a SBT, a temperature gradient may develop across the surface (Fig. 3.5). The exhibited temperature gradient actually depends on the surface thickness. For example, if the simulated surfaces are infinitely thick, the temperature gradient across the surface would be smaller than with thin surfaces. In other words, the thermal inertia of the surfaces depends on their simulated size. (Fig. 3.5)

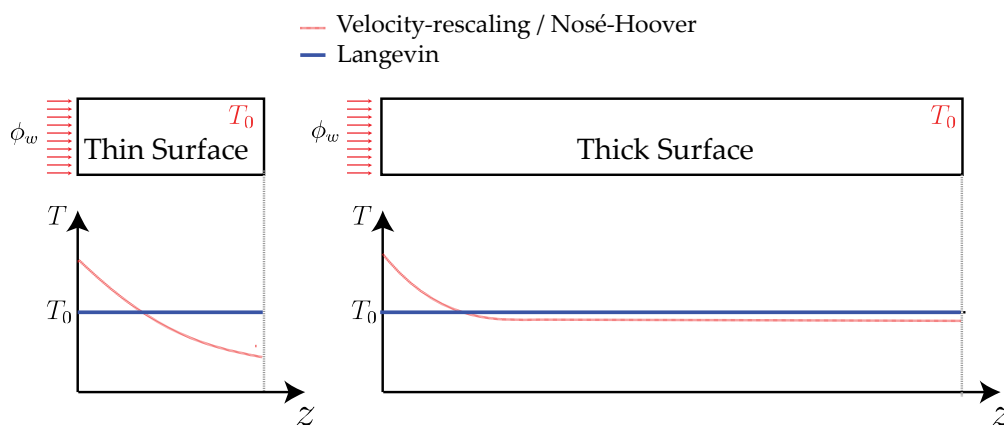


**Fig. 3.5:** A schematic explaining in the SBT method with different implementations how temperature would develop across the surfaces due to a heat flux ( $\phi_w$ ) from the confined lubricant, for two different surface thicknesses.

Implementing the SBT method with a Langevin algorithm allows temperature gradients across the surfaces to be avoided (Fig. 3.5). In this algorithm temperature is controlled on a per-atom basis. This is achieved by adding frictional and random forces to the conservative forces acting on each atom. The frictional force is proportional to the velocity of the surface

atom and the random force represents the collisions of the latter with imaginary particles from the heat bath. More details about these algorithms are given in Appendix 1.

Confined shear simulations were conducted with the hexadecane and gold system described in section 3.2 (see Fig. 3.3). The contact pressure is 500MPa but the sliding velocities were increased to  $\pm 100 \text{m.s}^{-1}$ . Three simulations were conducted using the velocity rescaling algorithm involving different intervals between consecutive rescales (50fs, 100fs, and 200fs). Two additional simulations were also considered for both the Nosé-Hoover and Langevin thermostats with a time relaxation parameter of 100fs.

The results of these simulations are given in Table 3.1. For a shear rate of about  $8 \times 10^{10} \text{s}^{-1}$ , it is remarkable that the temperature control algorithm (velocity rescaling, Nosé-Hoover, or Langevin) influences the temperature increase inside the lubricant as well as the measured friction (shear stress). Highly dissipative thermostats (for example short rescaling intervals) can attenuate the temperature increase inside the lubricant, increasing the force needed to shear the lubricant at a constant velocity (shear stress).

	Velocity Rescaling			Nosé-Hoover	Langevin
	$\Delta t = 50\text{fs}$	$\Delta t = 100\text{fs}$	$\Delta t = 200\text{fs}$	$\tau_{\text{NH}} = 100\text{fs}$	$\tau_{\text{L}} = 100\text{fs}$
Average lubricant temperature <u>increase</u> (K)	116.4	120.4	122.6	121.6	57.8
Total shear stress $\tau_{xz}$ (MPa)	59.3	58.8	58.0	58.6	65.4
Effective shear viscosity $\eta_{\text{eff}}$ (mPa.s)	0.75	0.74	0.73	0.74	0.83

**Table 3.1: For the molecular system of ~2.4nm hexadecane confined between gold surfaces with a loading pressure of 500MPa and a sliding velocity of  $\pm 100 \text{m.s}^{-1}$ , given are the results obtained using the sliding boundary thermostat method with different temperature control algorithms.  $\Delta t$  and  $\tau$  represent the rescaling time interval and the average relaxation time of the respective algorithms.**

The effective shear viscosity was calculated as the ratio of the measured shear stress to the apparent shear rate. For the different cases of velocity rescaling and Nosé-Hoover algorithms, the measured shear viscosity is equal although energy is dissipated in quite different ways (Appendix 1). On the other hand, the Langevin algorithm exhibited a larger dissipation of energy as the lubricant heating was about 50% lower than the other two. Since the steady-state temperature was lower than the other two algorithms, the lubricant effective viscosity and the measured shear stress were about 12% greater (Table 3.1). For a simple SBT, the implemented thermostating algorithm thus influences how the lubricant heats up and its resistance friction to the sliding surfaces.

In order to explain why the Langevin algorithm exhibited a larger dissipation than the velocity rescaling and the Nosé-Hoover algorithms, one should closely examine how energy is transferred between the group of atoms representing a confining surface and the heat bath. While the velocity rescaling and Nosé-Hoover algorithms dissipate energy “globally” from the group, the Langevin algorithm acts on each atom individually. For example, a thermostated body with a Nosé-Hoover thermostat may encounter a temperature gradient around

the controlled temperature. In the case of the Langevin thermostat, no gradient may develop. In consequence, the Langevin thermostat with the parameters used in these simulations dissipated energy faster than the other algorithms.

In conclusion, the dissipation properties of the algorithm employed in the SBT method may influence the lubricant heating and its global dynamics. This was observed in simulations at relatively large sliding velocities and shear rates. It is possible however that the observed effects dominate uniquely for high shear rates. It is thus interesting to define a critical condition for the heating onset inside the confined lubricant. If the critical condition is defined, then it is possible to know in advance for any simulation whether the thermostating method is susceptible of quantitatively altering the results or not.

### 3.2.2 Heating onset by shearing

The literature reports that thermostating methods only become influential in the regime where heating is actually susceptible to occur inside the lubricant [97, 65]. Simulations of simple Lennard-Jones systems find that there is a critical shear rate at which the lubricant starts heating [3]. Its value in reduced units is  $0.2\tau^{-1}$  ( $\tau = \sqrt{m\sigma^2/\epsilon}$  is the characteristic LJ time scale). The system being studied here, however, is different with its complex molecular architecture and degrees of freedom. Nevertheless, for comparison purposes, it was found that literature equation applied to the hexadecane lubricant gives a critical shear rate of roughly  $9.1 \times 10^{10} \text{s}^{-1}$ . However, the results of section 3.2 for all of the tested algorithms showed significant heating while the shear rate ( $8 \times 10^{10} \text{s}^{-1}$ ) was lower than this value. There is thus a necessity to determine, for the particular system in study, the critical shear rate of lubricant heating.

Simulations were thus conducted with the hexadecane and gold model of Fig. 3.3 with varying surface sliding speeds. A range of apparent shear rates could thus be investigated and the lubricant temperature was observed in order to detect heating. Two implementations of the SBT method were used, one with the velocity rescaling algorithm with 100fs rescale interval and another with the Langevin algorithm with a 100fs relaxation time.

The sliding velocity was varied between 1 and 200  $\text{m.s}^{-1}$  giving apparent shear rates between  $8.37 \times 10^8$  and  $1.54 \times 10^{11} \text{s}^{-1}$ . The normal pressure was kept at 500MPa and the boundary temperature was set to 300K.

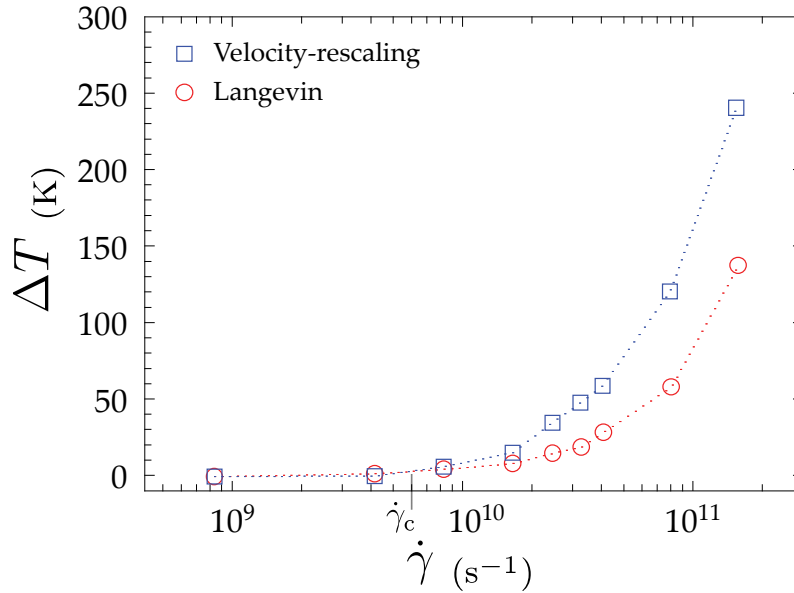


**Fig. 3.6:** Temperature increase ( $\Delta T$ ) inside the confined hexadecane film between gold surfaces at a 500MPa pressure as a function of the apparent shear rate for two different implementations of the SBT dissipation method. The critical shear rate at which heating starts was found to be equal to  $6 \times 10^9 \text{ s}^{-1}$ .

The results for the temperature increase inside the lubricant ( $\Delta T$ ) are given in Fig. 3.6 as a function of the apparent shear rate ( $\dot{\gamma}$ ) for both the velocity rescaling and the Langevin algorithms. For shear rates lower than  $\dot{\gamma}_c = 6 \times 10^9$ , no heating due to shear could be observed with either algorithm and the lubricant temperature was independent of the algorithm employed for the SBT method. The reason is that the rate of heat generation due to lubricant shear is smaller than the maximum dissipation rate that can be handled by the thermostat. On the other hand at shear rates higher than  $\dot{\gamma}_c$ , the lubricant starts heating up. The lubricant temperature increases more gently as a function of shear rate with the Langevin algorithm than with the velocity-rescaling algorithm.

These thermal effects which are thermostat-dependant convey, on Fig. 3.7, their influence on the shear stress. At shear rates lower than the critical one ( $\dot{\gamma}$ ), The SBT method with velocity-rescaling and the Langevin implementations gives the exact same friction. As the shear rate is increased to values higher than  $\dot{\gamma}$ , the Langevin implementation produces a higher shear stress than with velocity-rescaling. As the shear rates are increased, the results diverge even more since thermal effects are susceptible to play a bigger role.

At low shear rates, the relationship between shear stress and shear rate is linear. At high shear rates, the shear stress increase becomes limited. This is due to two combined factors: 1) the lubricant heating (Fig. 3.6) which reduces the effective resistance to flow, and 2) shear thinning which is susceptible to occur, as was presented in Chapter 2, at shear rates as low as  $10^{10} \text{ s}^{-1}$  for the hexadecane bulk model.

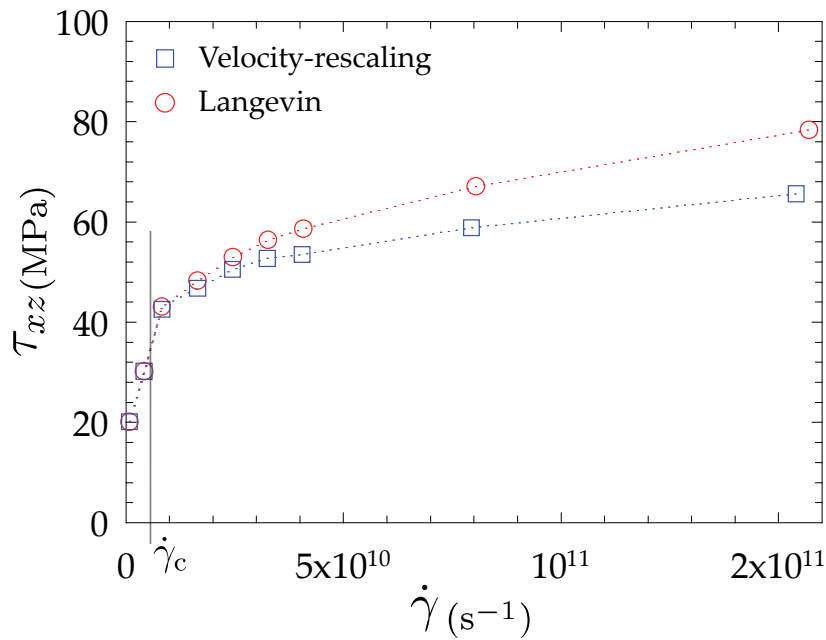


**Fig. 3.7:** Variation of the total shear stress ( $\tau_{xz}$ ) as a function of the apparent shear rate for two different implementation algorithms for the SBT dissipation method. Results for a 2.5nm confined film of hexadecane between gold surfaces with a loading pressure of 500MPa and variable surface sliding speeds.

The results give clear evidence that there exists a critical shear rate ( $\dot{\gamma}_c$ ) at which the lubricant starts heating up. The value of  $\dot{\gamma}_c$  does not depend on the thermostating method but is expected to depend on the lubricant nature and the boundary conditions of pressure and temperature. If the apparent shear rate is smaller than  $\dot{\gamma}_c$ , the dissipation method showed no influence on the friction. When this critical value is surpassed, lubricant starts heating up at different rates according to the thermostating method. If the thermostat is highly dissipative (for example SBT method with Langevin implementation), the lubricant heats up gently as a function of shear rate. If the thermostat is weakly dissipative (for example SBT method with velocity-rescaling implementation) the lubricant heats up faster with the shear rate. These thermal effects have significant influence on the effective viscosity of the lubricant and the friction results can be different according to the thermostating method.

### 3.3 Advanced dissipation methods

In the SBT method with Langevin implementation, the surface temperature is controlled to be equal to the ambient one (outside the contact). Thus for any heat flux generated in the contact, no temperature gradient is modeled in the surfaces. This is equivalent to assuming that the surfaces have infinite thermal conductivities and heat capacities. The side of the surface in direct contact with the lubricant is thus at the same temperature as the outer side which is at the ambient temperature.

In reality, of course, no surface materials have such properties. Moreover, in molecular lubrication problems at severe operating conditions, the generated heat flux can reach extremely high values in the order of a few  $\text{GW}\cdot\text{m}^{-2}$ . These are the cases where the lubricant starts heating up with classical SBT methods (Fig. 3.6). A simple analysis on mono-

directional heat conduction in a semi-infinite solid with a boundary heat flux ( $\phi_w$ ) on the finite end and a constant temperature ( $T_\infty$ ) on the other gives the following analytical solution for the wall temperature ( $T_w$ ) (see Appendix 2 for details):

$$(3.5) \quad T_w = T_\infty + \frac{2\phi_w}{\lambda} \sqrt{\frac{\alpha t}{\pi}}$$

$\alpha$  is the thermal diffusivity of the surface and  $\lambda$  its thermal conductivity. Inserting the properties of gold in this equation ( $\lambda = 318 \text{W}\cdot\text{m}^{-1}\cdot\text{K}^{-1}$  and  $\alpha = 12.732 \times 10^{-5} \text{m}^2\cdot\text{s}^{-1}$ ) [98], the evolution of the wall temperature can be predicted. For example using the heat flux of  $25 \text{GW}\cdot\text{m}^{-2}$  (result of the simulation with  $\pm 200 \text{m}\cdot\text{s}^{-1}$  sliding velocities), the wall temperature is supposed to increase by  $32 \text{K}$  in the first  $1 \text{ns}$ .

In severe contact conditions, the sheared lubricant heats up and a large temperature difference may develop between the film and the bounding surfaces if they do not accommodate to lubricant heating (such as in the case of SBT method). The dissipation heat flux seen in simulation, which is proportional to this temperature difference, may be higher than reality. As the surfaces dissipate more, the lubricant heats up less and gives a higher resistance to flow (friction).

It is thus of great importance to accurately model the dissipation path by conduction not only inside the fluid, but also across the solid surfaces when the contact conditions are severe. It is particularly important to allow the surface temperature to naturally accommodate to the lubricant heating. This requires, however, relatively complicated algorithms to be employed. In the following section, the Phantom Molecules method [99], which allows modeling infinitely thick surfaces, is briefly presented and employed to the molecular system studied previously. Finally, in the last section, a novel dissipation method (Variable Boundary Temperature) which allows accurate heat conduction to be modeled in the solid surfaces is presented. This method is based on updating the boundary temperature, at regular intervals, as a function of the heat flux from the contact.

### 3.3.1 The Phantom-Molecules method

The phantom molecules method is a thermostating technique developed originally for studying simple gas-solid interfaces. It is based on approximating the solution of the generalized Langevin equations (GLE) for the solid atoms in the surfaces (called primary atoms). The effect on the global thermal properties of the infinite number of solid layers which are not considered in the simulations is compensated through "ghost" atoms (or secondary atoms) which have special interactions with the primary atoms. The phantom atoms represent an infinite number of layers at a constant temperature. More details about this method are given in Appendix 1.

The interest of using this thermostating method, compared to the regular sliding boundary thermostat is that it permits a temperature gradient to develop inside the modeled solid surfaces. The surface temperature may thus increase. Moreover, the phantom atoms can reproduce the thermal conductivity and heat capacity of a semi infinite solid. In other words, the dissipation mechanisms are more realistically modeled.

The parameters needed to employ this method can be derived from the material properties of the solid surfaces. For gold, as in the case being studied here, the Debye temperature

of  $\theta_d = 170\text{K}$  for gold [76] is used to calculate the damping parameter for the interactions between the surface and the phantom atoms. The reader is advised to refer to Appendix 1 for more details about this method and its implementation.

This method was applied to the same domain of gold and hexadecane, defined previously with a sliding velocity of  $\pm 100\text{m}\cdot\text{s}^{-1}$ . This corresponds to a shear rate in the order of  $8 \times 10^{10}\text{s}^{-1}$ . The classical SBT with velocity-rescaling and Nosé-Hoover implementations showed that for such shearing, the lubricant temperature may increase by more than  $120\text{K}$  (Fig. 3.6). With the Phantom Molecule method, as shown in Fig. 3.8, the average lubricant temperature increases by only  $84.7\text{K}$ . Moreover, a temperature gradient develops inside the surface and the interface layer temperature increases about  $45\text{K}$ . The temperature profile is continuous across the solid-liquid interface because the surfaces temperature can accommodate naturally to the lubricant heating.

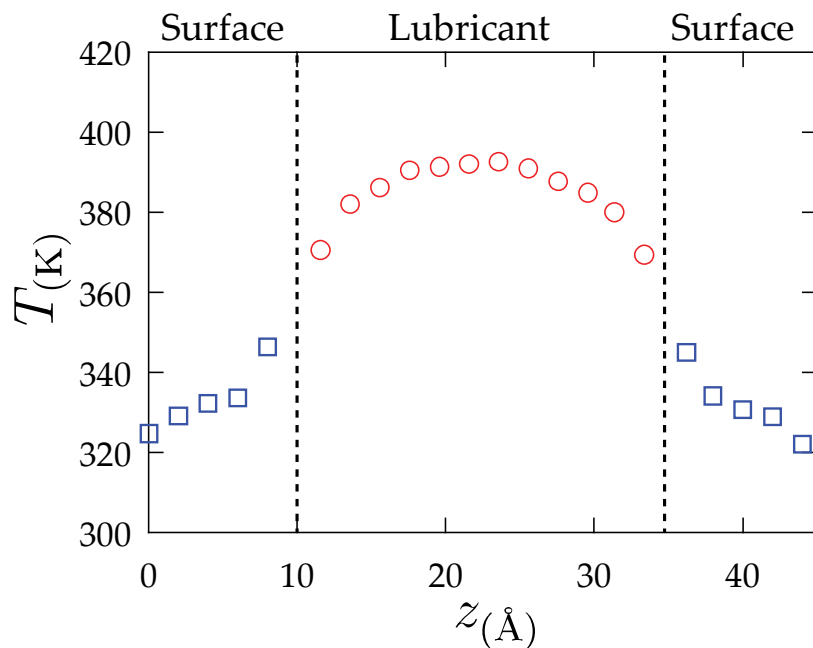


**Fig. 3.8: Temperature profile across the surfaces and lubricant film for a simulation employing the Phantom Molecules thermostating method for contact conditions of  $500\text{MPa}$  pressure and  $8 \times 10^{10}\text{ s}^{-1}$  apparent shear rate.**

The measured apparent shear stress (see Appendix 3) with the Phantom-Molecules method was  $60.6\text{MPa}$ . In comparison with the results from Table 3.1, this method dissipated more energy than the SBT with velocity rescaling and Nosé-Hoover algorithms. The lubricant heated less and the shear stress was higher. The SBT with a Langevin algorithm however exhibited a larger energy dissipation and thus higher shear stress and friction.

The physical significance of the Phantom-Molecules method is in that it simulates a large portion of the solid with bulk thermal properties. The heat conduction and dissipation through the surfaces is thus closer to reality than with the SBT method. The measured shear stress with this method was found to be moderate compared to results using different possibilities for employing a classical SBT. This result proves that quantitative results from molecular simulations can only be considered if a proper dissipation algorithm is used.

The Phantom-Molecules method is however difficult to implement with amorphous surfaces or with complicated lattice structures. Moreover, this method only allows to model, beyond the primary surface layers, an infinitely thick solid surface at a constant temperature. Between the primary surface atoms (explicitly simulated) and the imaginary atoms (not explicitly seen), a thermal discontinuity may emerge as shown in Fig. 3.8 between the outer surface layer and the 300K temperature supposed to be imposed in the remaining part of the solid surfaces. For this purpose, a novel method for energy dissipation in molecular lubrication problems in severe conditions is presented. The idea is to start with a classical sliding boundary thermostat but then allow the thermostat to adapt itself to the heat flux generated inside the contact.

### 3.3.2 The variable boundary temperature method

The variable boundary temperature (VBT) is a novel method of applying the thermal boundary conditions in molecular dynamics simulations for molecular lubrication. It is similar to simple SBT with the difference that the temperature of the sliding boundary evolves during the simulation. The boundary temperature is calculated, on the fly, from the dissipated heat flux and the bulk material properties of the surfaces.

#### 3.3.2.1 Principle

The principle is as follows, starting with a simple thermostat controlling the boundary temperature to the ambient one ( $T_0$ ), the lubricant temperature equilibrates in a way to yield energy balance between heat generation and dissipation rates. The heat flux ( $\phi_w$ ) of this steady state is constant and can be calculated as the energy removed by the thermostat per unit of surface and time. As shown in Fig. 3.9 for the first temperature update ( $t = \Delta\tilde{t}$ ), the new boundary temperature to be imposed is calculated using Eq.(3.5) which is an exact solution of the conduction equation in a semi infinite solid (Appendix 3). During the following update intervals, the new heat flux is measured and a temperature increase/decrease is calculated analytically at regular intervals ( $t_0 = \tilde{n}\Delta\tilde{t}$ ) as follows:

$$(3.6) \Delta T_w(t_0) = \Psi(t_0) \left( \frac{2\phi_w(t_0)}{\lambda} \sqrt{\frac{\alpha t_0}{\pi}} \right)$$

Note that Eq.(3.6) is identical to Eq.(3.5) except for the term ( $\Psi$ ). This equation is determined analytically from the derivative of the wall temperature with time, assuming the possibility of small boundary flux variations between two updates (Appendix 3). This term actually varies with time and with the flux variations between two updates.  $\Psi$  can be positive or negative but is usually close to zero. It is given as:

$$(3.7) \Psi(t_0) = \frac{1}{2} \frac{\Delta\tilde{t}}{t_0} + \frac{\Delta\phi_w(t_0)}{\phi_w(t_0)}$$

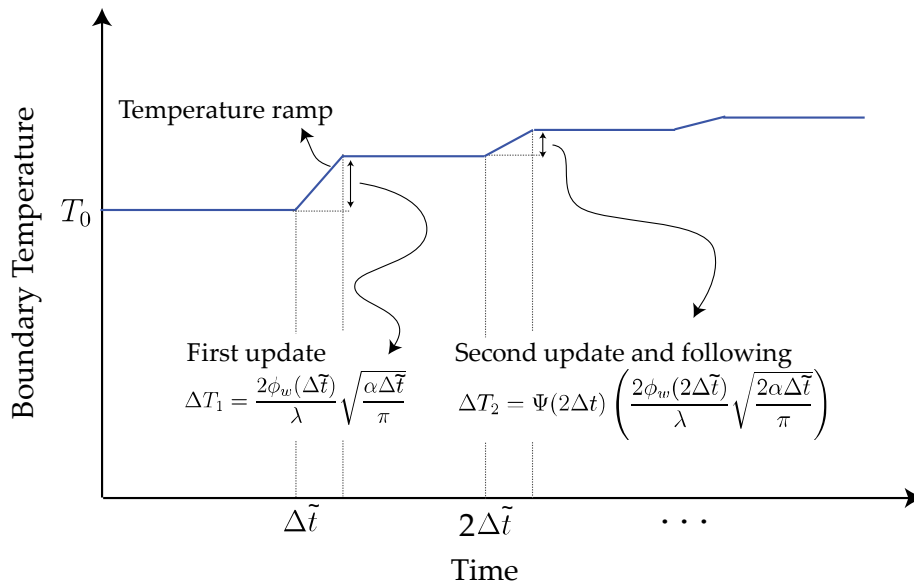


**Fig. 3.9:** Schematic showing the steps in boundary temperature update. The temperature change is calculated from the measured wall flux. The boundary temperature is ramped toward the new value in order to avoid abrupt changes.

If  $\tilde{n}$  is an index of the temperature update such that  $t_0 = \tilde{n}\Delta\tilde{t}$ , then  $\Psi$  can be written purely as a function of  $\tilde{n}$  and the fluxes at the consecutive steps:

$$(3.8) \quad \Psi^{\tilde{n}} = \frac{2\tilde{n} + 1}{2\tilde{n}} - \frac{\phi_w^{\tilde{n}-1}}{\phi_w^{\tilde{n}}}$$

An interesting aspect of this scheme is that a steady state surface temperature can be attained when  $\Psi = 0$ . According to Eq.(3.7), this occurs when the dissipated flux is more or less constant and after a significantly sufficient number of update steps.

In order to control the temperature between two updates, any of the existing temperature control algorithms can be used. The fact that the used algorithm dissipates too much or too little energy has theoretically no difference because the boundary temperature would increase accordingly to produce a counter effect. However, it remains preferable to use a Langevin thermostat because it insures that no temperature gradient develops inside the surfaces.

In order to avoid abrupt changes in the surface temperature, the imposed temperature is ramped during 50 – 100ps between two updates as shown in Fig. 3.9. This allows a natural relaxation of the system to the change in the boundary conditions. In practice, this also allows to improve the stability of the method.

The VBT method works as follows. Starting with a given surface temperature, when the lubricant is sheared it produces a certain heat flux. However this flux (and measured friction) could be over-estimated if the surface thermostat dissipates more energy than in reality. So for the first temperature update, the wall temperature is increased. By doing so, the temperature difference between the film and the boundary surfaces is reduced resulting in a smaller energetic dissipation by the thermostat. On the next update, the wall temperature is adjusted accordingly and so on. The loop continues until the lubricant naturally finds equilibrium with the flexible dissipation rate from the surfaces. This equilibrium depends only on the material properties of the surfaces which give this method a physical importance.

### 3.3.2.2 Validation

The VBT method was tested with different dissipation algorithms for controlling the boundary temperature between two updates. The tested algorithms are the velocity rescaling, Nosé-Hoover, and Langevin thermostats with a velocity rescaling/ temperature relaxation intervals of 100fs. The boundary temperature was updated every 0.25ns according to the measured heat flux as illustrated previously in Fig. 3.9.

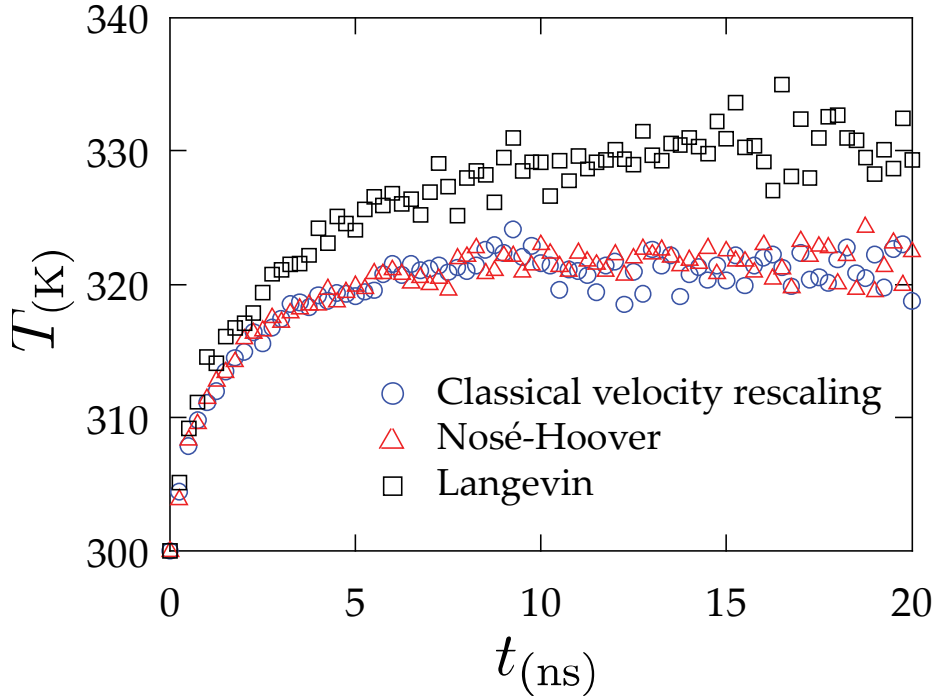


**Fig. 3.10: Surface temperature evolution with time using the Variable Boundary Temperature method for different temperature control algorithms. The results for velocity rescaling and Nosé-Hoover are confounded.**

The boundary temperature evolution during 20ns of shear for the different algorithms is presented in Fig. 3.10. It is remarkable that the surface temperature evolution is the same for the velocity rescaling and the Nosé-Hoover algorithms. In previous simulations with constant boundary temperature (SBT) the two algorithms gave very close dissipation (see Table 3.1). The time evolution of the wall temperature with the VBT method is identical for the two algorithms. On the other hand, with the Langevin thermostat which dissipates more energy (see Table 3.1) the surface temperature increases faster than the other two algorithms. The surface temperature increase plays a role in attenuating the dissipation flux from the Langevin thermostat.

Table 3.2 reports the dissipation flux for the three cases. Indeed, the variable boundary temperature method gives closer results for the dissipation flux and shear stress (friction) among different algorithms compared to the SBT method (Table 3.1).

	Variable Boundary Temperature			Phantom Molecules
	Velocity rescaling	Nosé-Hoover	Langevin	
Dissipation flux (GW.m <sup>-2</sup> )	11.56	11.54	12.01	-
Total shear stress $\tau_{xz}$ (MPa)	58.5	58.5	60.8	60.6

**Table 3.2: Dissipation flux and total shear stress from simulations with the VBT method (implemented with three different temperature control algorithms) and with the Phantom-Molecules method.**

The main influence of this method was when implemented with the Langevin thermostat which exhibited the larger energetic dissipation in the SBT case. With the VBT, as the surfaces were allowed to heat up (Fig. 3.10), the lubricant heated up more than the SBT case. Consequently, its flow resistance decreased and the encountered shear stress in the steady state (60.8MPa) was lower than with the SBT method (65.4MPa).

When implemented with velocity-rescaling and the Nosé-Hoover algorithms, the VBT method, causing surface heating, had no significant effect on the SBT results (Table 3.2). The reason is that the lubricant heating was already elevated (more than 120K) in the SBT case (Table 3.1).

The VBT method can thus adapt to the temperature control algorithm in order to yield dissipation that is a function of the solid bulk thermal properties and the contact conditions.

The only numerical parameter that needs to be chosen in the Variable Boundary Temperature method is the update interval ( $\Delta t$ ). In the previous simulations this parameter was set to 0.25ns. The next section deals with the influence of this parameter on the Variable Boundary Temperature method.

### 3.3.2.3 Temperature update interval

There are two criteria for the choice of the update interval. First the interval should be long enough to insure that energy is balanced between two updates. In section 3.2, this was established in roughly 0.1ns for the system in study (see Fig. 3.4). Second, the update interval must be short enough to insure that the hypothesis that the discrete formulation of Eq.(3.6) remains valid and its numerical resolution is stable.

Three update intervals of 0.1, 0.25, and 0.5ns were tested with the same confined hexadecane system of Fig. 3.3 at  $\pm 100\text{m.s}^{-1}$ . A simple velocity rescaling algorithm of a 100fs rescaling interval was used to set the surface temperature between two updates. As shown in Fig. 3.11, using any of the three temperature update intervals the equilibrium temperature is unchanged and equals approximately 320K. It is remarkable, however, that when the update interval is small relatively large fluctuations in the wall temperature are noted. This is probably due to statistical uncertainties when calculating the heat flux between two updates. This can be dangerous because it results in abrupt temperature changes in very small time that the system may not be able to accommodate to. It is thus preferable to use moderate update intervals in the order of 0.25 – 0.5ns for systems similar to the one in study.

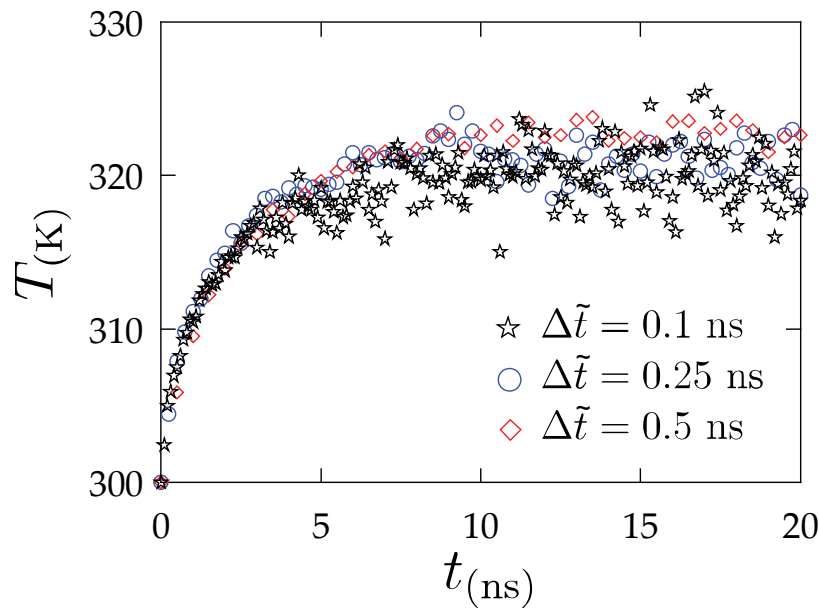


Fig. 3.11: Surface temperature evolution with time using the Variable Boundary Temperature method with three different update intervals.

### 3.3.3 Assessment on the dissipation methods

The results presented in this chapter give clear evidence that the employed method of heat dissipation may quantitatively influence the measured friction. Even with the same dissipation method but with different algorithms for its implementation, the friction was also variable (Table 3.1). The main reason behind this variation was that, if the surfaces dissipate heat so quickly, the lubricant heats up less and thus its effective viscosity is higher. The second scenario, evoked in section 3.1.3 that the measured friction is influenced by the way energy is dissipated from the system seems to be more persuasive.

However, this picture is not complete. It was proven (Fig. 3.6) that the lubricant heating does not always occur. In fact, a critical shear rate needs to be exceeded before any significant heating starts occurring. Thus if the shear rates are low, the dissipation method has no influence on the lubricant film properties and friction (Fig. 3.6 and Fig. 3.7). So in this regime actually the friction is independent of the dissipation method employed and the first scenario from section 3.1.3 is valid.

The friction in molecular simulations is in fact neither the direct result of the numerical dissipation method nor is it always independent of the latter. In severe contact conditions, the methods employed for energy dissipation start interfering. For these cases, two advanced methods were presented that allow realistic physical conduction out of the contact to be modeled.

The most important aspect found in the two advanced thermostating methods is that the surface temperature must increase when the lubricant heats up. It is unphysical to set the surface temperature to the ambient one while the lubricant heats up by more than a hundred degrees (Table 3.1). The surface temperature increase with the Phantom molecules (Fig. 3.8) and the VBT methods (Fig. 3.10) are in the same order of magnitude. In fact, the total shear stress and thus the friction are also very close (Table 3.2).

The Variable Boundary Temperature method, however, has three advantages over the Phantom Molecules method. First it does not require using any additional (phantom) atoms to be inserted inside the system. Second, it is easier to implement especially if the surface crystalline structure is complex. Third, in the Phantom Molecules method a semi-infinite solid is modeled at a constant temperature whereas in the VBT method, such an assumption is not needed. The heat conduction out of the contact is thus more physically modeled.

## Conclusion

In this chapter, the physical mechanisms of heat dissipation in molecular lubrication problems were introduced. The methods of energy dissipation in molecular dynamics simulations were put into several tests at different contact conditions. It was found that for low shear rates, the thermostating method has no effect on the friction inside the contact. However, at higher shear rates, the influence of the thermostating method becomes crucial.

Advanced methods of dissipation were compared to classical ones in this regime. It was found that the temperature increase results from a relatively slow dissipation rate compared to the heat generation rate. The choice of the method and parameters of heat dissipation is critical in such situations and a novel method was developed to tackle this particular issue.

Based on these conclusions, the molecular lubrication model is employed in the low shearing regime to investigate the influence of surface (Chapter 4) and lubricant molecular structures (Chapter 5) on boundary flow and friction. The simulated contact conditions are close to those found in real applications where the surface sliding speed and the film thickness are in the order of  $10\text{m}\cdot\text{s}^{-1}$  and  $4\text{nm}$  respectively.

# 4

## Effect of Surface Adsorption and Corrugation

78

<b>Introduction</b>	78
<b>5.1 Surface characterization</b>	79
5.1.1 Surface scanning method	79
5.1.2 Application to different surface types	81
<b>5.2 Overview of the molecular model</b>	83
<b>5.3 Results and discussion</b>	84
5.3.1 Film structure	84
5.3.2 Boundary flow	85
5.3.3 Shear stress	87
<b>Conclusion</b>	88

# 4. Effect of Surface Adsorption and Corrugation

---

## Introduction

In molecular lubrication problems, lubricants are confined to molecular scale thicknesses. Experiments have shown that in such confinements the structure and dynamics of lubricants are greatly influenced by the nature of the confining surfaces [15, 16]. The well-organized surface structure is reflected, through the interfacial interactions, by a set of potential valleys that lubricant molecules are attracted to occupy [55, 100]. Any surface, no matter how geometrically smooth, manifests a sort of a foot-print over the neighboring lubricant layers.

The surface interaction is a combination of two components: adsorption and corrugation potentials [101]. In a Lennard-Jones model for the surface interactions, the adsorption potential increases with the surface density and with the well-depth energy ( $\epsilon$ ) of the surface-lubricant interaction [55]. Lubricant molecules are more attracted to surfaces with high adsorption potential and a dense lubricant layer forms adjacent to the surfaces. The corrugation potential, on the other hand, depends on the in-plane potential variations which are due to the crystalline structure and density of the surfaces. Corrugation results in epitaxial ordering in the adjacent lubricant layers [55, 87]. In analogy with the footprint-in-sand example, corrugation potential represents the shape of the footprint while the adsorption potential represents how deep the latter is pushed into the sand.

Perhaps one of the most researched effects of surface interactions on a confined film is with respect to the induced density fluctuations in the direction normal to the surfaces. The phenomenon is physically due to the liquid density cut-off at the interface which creates a disorder in the bulk radial distribution function [101]. When the surface adsorption is strong, a dense liquid layer is adsorbed to the surface. The distance between the first liquid layer and the surface corresponds to the minimum stable interaction between the two. Deeper inside the liquid, a second layer is formed under the influence of the first dense layer and so on. This layering phenomenon produces non-homogeneous properties across the confined film and up to 5 liquid layers may be distinguishable near each surface [101]. Liquid layers adjacent to the surfaces may eventually crystallize if the adsorption potential is strong enough [102]. Thus in confinement situations, the layering phenomenon which is caused by the surface adsorption potential influences not only the global structure but also the dynamics of the film.

On the other hand, the corrugation potential of the surface interactions causes in-plane (epitaxial) ordering inside the formed liquid layers parallel to the surfaces. This type of ordering may extend 2 – 3 layers deep inside the film for strong surface interactions [55].

Boundary slip is thought to depend on this ordering [55, 100, 68]. Liquids generally slip more near high-density surfaces because they have small corrugations [55].

In model crystalline surfaces, it is easy to modify the density, interaction well-depth, or any other property for changing the adsorption and corrugation potentials [55]. Increasing the surface density gives stronger adsorption but smaller corrugation. Increasing the well-depth interaction energy for a given lattice increases both the adsorption and corrugation. In realistic lubrication problems, surfaces such as oxides are amorphous. They can be constituted of two or more types of atoms and have quite complex crystalline structures. The classical methods that apply to model surface become inefficient because more factors come into play. There is no clear way in the literature for combining all of these factors in representative parameters that are comparable between different surface types.

A simple method is proposed in the next section which is inspired by this need for quantitative measurements of adsorption and corrugation potentials. The method will be initially used to compare the properties of five different surface types. These surfaces are then used to confine a lubricant film in molecular lubrication conditions. The results for lubricant structuring, boundary flow and friction are eventually analyzed according to the measured adsorption and corrugation.

## 4.1 Surface characterization

The surface characterization method must produce reliable results that allow comparison between different types of surfaces. Moreover, the method should be simple and performed in the absence of a lubricating medium so that the results are intrinsic properties of the surface. The surface characterization method for quantitatively measuring surface adsorption and corrugation potentials is presented in detail in the following section.

### 4.1.1 Surface scanning method

A surface scanning method is developed which allows characterizing adsorption and corrugation potentials of different surface types. The principle is as follows: a set of  $N_x$  scanning atoms are positioned at a distance  $d$  above the surface to be scanned as shown in Fig. 4.1. The atoms are uniformly separated and extend across the x-dimension of the surface. The potential energy, from surface interactions, is then recorded at each atom as the surface is scanned across its y-dimension. If  $N_y$  is the number of snapshots taken during a scan, then a total of  $N_x \times N_y$  data points are collected. The data allows an accurate surface plot of the interaction potential energy.

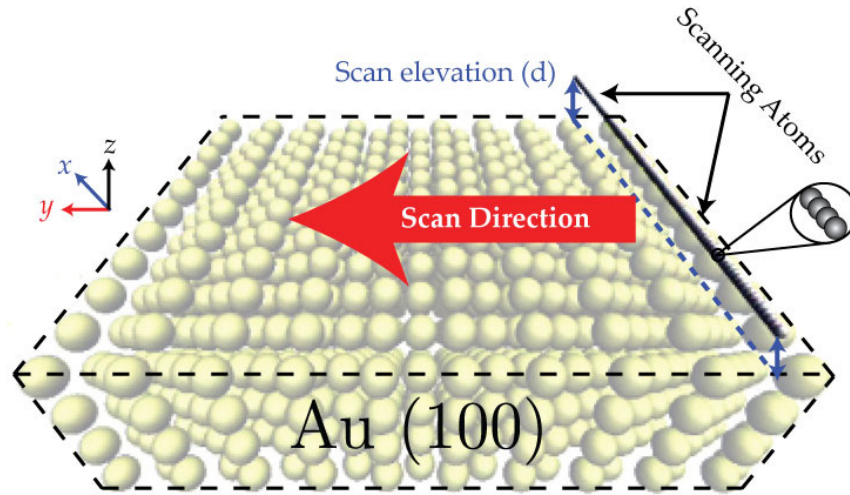


**Fig. 4.1:** Schematic describing the surface scanning procedure applied on a gold Au (100) surface.

The scanning atoms do not interact with one another and are frozen during the scan. For simplification purposes, the interaction properties of the scanning atoms are chosen as:

$$(4.1) \quad \epsilon_{\text{scan}} = 1 \text{Kcal.mol}^{-1} \quad \text{and} \quad \sigma_{\text{scan}} = 1 \text{\AA}$$

According to the Lorentz-Berthelot mixing rules, the surface-scanning atoms interactions are given as:

$$(4.2) \quad \epsilon_{\text{surf-scan}} = \epsilon_{\text{surf}} \quad \text{and} \quad \sigma_{\text{surf-scan}} = \frac{1 + \sigma_{\text{surf}}}{2}$$

$\sigma_{\text{surf}}$  and  $\epsilon_{\text{surf}}$  are the distance and the well-depth energy parameters of the Lennard Jones surface interaction. In the case of multi-atomic surfaces, a mass-weighted average for both parameters is calculated as follows:

$$(4.3) \quad \epsilon_{\text{surf}} = \frac{1}{M} \sum_{i=1}^N m_i \epsilon_i \quad \text{and} \quad \sigma_{\text{surf}} = \frac{1}{M} \sum_{i=1}^N m_i \sigma_i$$

$M$  is the molar mass and the index  $i$  ramps over the surface atom types.  $m_i$  is the atomic mass and  $\sigma_i$  and  $\epsilon_i$  are the LJ distance and well-depth energy parameters respectively.

The scan results depend on the elevation ( $d$ ) of the scanning atoms. In a LJ model, the surface potential is repulsive at small distances and becomes attractive at a distance greater than  $\sigma_{\text{surf-scan}}$ . The minimum potential energy is expected at an elevation of  $2^{1/6} \sigma_{\text{surf-scan}}$ . In practice, the scan elevation ( $d$ ) is chosen to be equal to this value. In molecular lubrication simulations, this corresponds to the position where the first lubricant layer would be present. The adsorption and corrugation potentials are thus characterized at the position.

At any instant, the potential energy of each scanning atom ( $\Phi$ ) represents its interaction with all neighboring surface atoms. This potential energy depends on the position ( $x, y$ ) of the scanning atom with respect to the surface. The adsorption parameter ( $\epsilon_{\text{ads}}$ ) is determined as the average Lennard-Jones well-depth across the surface, calculated as:

$$(4.4) \quad \epsilon_{\text{ads}} = \frac{\langle \Phi(x, y) \rangle}{4 \left[ \left( \frac{\sigma_{\text{surf-scan}}}{d} \right)^{12} - \left( \frac{\sigma_{\text{surf-scan}}}{d} \right)^6 \right]} = \frac{\langle \Phi(x, y) \rangle}{4 [2^{-2} - 2^{-1}]} = - \langle \Phi(x, y) \rangle$$

$\langle \rangle$  represents the average over all data points. The corrugation potential is characterized with a parameter ( $\epsilon_{\text{corr}}$ ) in energy units as the mean deviation of the interaction energy from the average adsorption ( $\epsilon_{\text{ads}}$ ). In mathematical terms:

$$(4.5) \quad \epsilon_{\text{corr}} = \langle |\Phi(x, y) - \langle \Phi(x, y) \rangle| \rangle$$

For example, a top view of a model Au(111) surface is given in Fig. 4.2. The results of the potential energy scan are given on the adjacent figure. Note that the scan shows the presence of periodically repeated valleys of potential energy minima (black spots). These represent the sites that lubricant atoms would preferentially occupy. Moreover, the wave-length of the potential energy fluctuations is equal to the lattice parameter for gold ( $a = 4.08\text{\AA}$ ). From these results, the adsorption and corrugation potentials can be quantitatively characterized according to Eq.(4.4) and Eq.(4.5) respectively. In the case of Au(111), the energy scan gives  $\epsilon_{\text{ads}} = 0.628\text{Kcal.mol}^{-1}$  and  $\epsilon_{\text{corr}} = 0.0622\text{Kcal.mol}^{-1}$ .

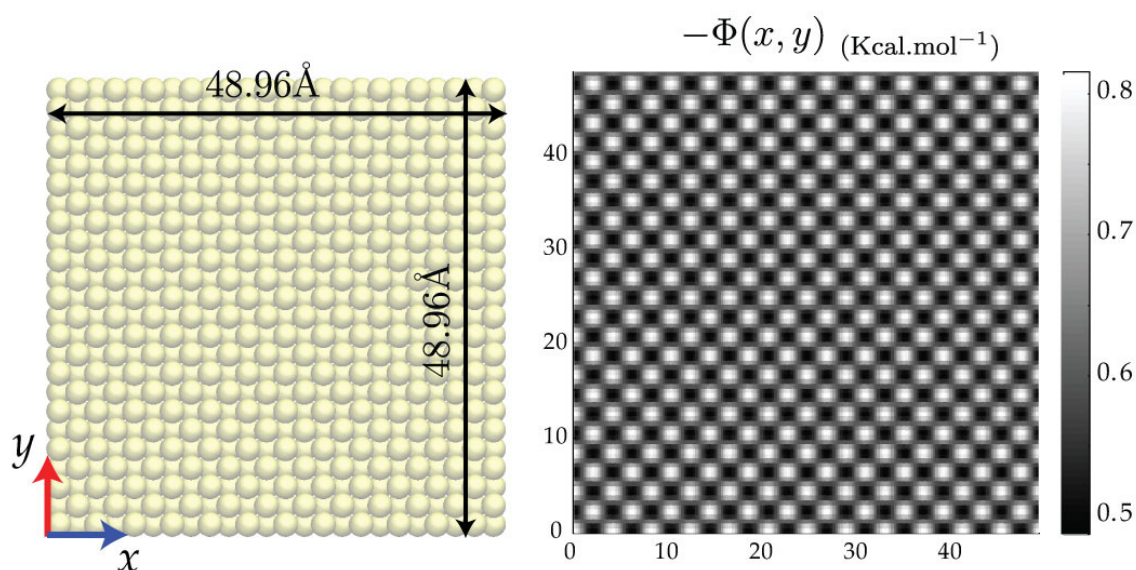


Fig. 4.2: XY snapshot of an Au(111) surface and the respective energy scan results.

### 4.1.2 Application to different surface types

In addition to the Au (111) surface, the scanning procedure was applied to four other surface types: Au (100), Fe (100), Fe<sub>2</sub>O<sub>3</sub> (100), and CuO (100) with oxygen layer termination. The consideration of these particular surfaces allows investigating the influence of lattice orientation as well as the atomic composition on the corrugation and adsorption properties. The interaction parameters for gold, iron, copper, and oxygen atoms in each surface are given in Table 4.1. These have been calculated by adsorption simulations with alkanes using the same method employed for gold and ferric oxide surfaces in section 2.2.4 of Chapter 2.

Surface	Atom type	$m_i$ (amu)	$\epsilon_i$ (Kcal.mol <sup>-1</sup> )	$\sigma_i$ (Å)	$\epsilon_{\text{surf}}$ (Kcal.mol <sup>-1</sup> )	$\sigma_{\text{surf}}$ (Å)	$d$ (Å)
Au (111)	Au	196.966	2.625	2.655	2.625	2.655	2.051
Au (100)	Au	196.966	0.945	2.655	0.945	2.655	2.051

Fe (100)	Fe	55.845	0.945	2.321	0.945	2.321	1.864
Fe <sub>2</sub> O <sub>3</sub> (100)	Fe	55.845	9.518	2.321	6.720	2.513	1.972
	O	15.999	0.210	2.960			
CuO (100)	Cu	63.546	4.679	2.740	3.780	2.784	2.124
	O	15.999	0.210	2.960			

**Table 4.1: Masses and Lennard-Jones interaction parameters for individual solid atoms, calculated by adsorption simulations of hexadecane as explained in Chapter 2. The surface global parameters are calculated according to Eq.(4.3).  $d$  is the scanning elevation corresponding to the energetic minimum above the scanned surface.**

The adsorption and corrugation parameters for all five surfaces are compared in Fig. 4.3. The results are sorted from left to right in a descending order of the adsorption parameter. The surface characterization shows that the five surfaces have different adsorption and corrugation potentials. Such a conclusion would not have been simple using the classical methods of comparing the surface densities and lattice structures.

Gold surfaces with two different lattice orientations have different adsorption but close corrugation. Fe<sub>2</sub>O<sub>3</sub> surface has the largest corrugation and moderate adsorption potential compared to the other surfaces. Finally, CuO has the smallest corrugation but an adsorption potential that is very close to that of Fe<sub>2</sub>O<sub>3</sub> and Fe(100).

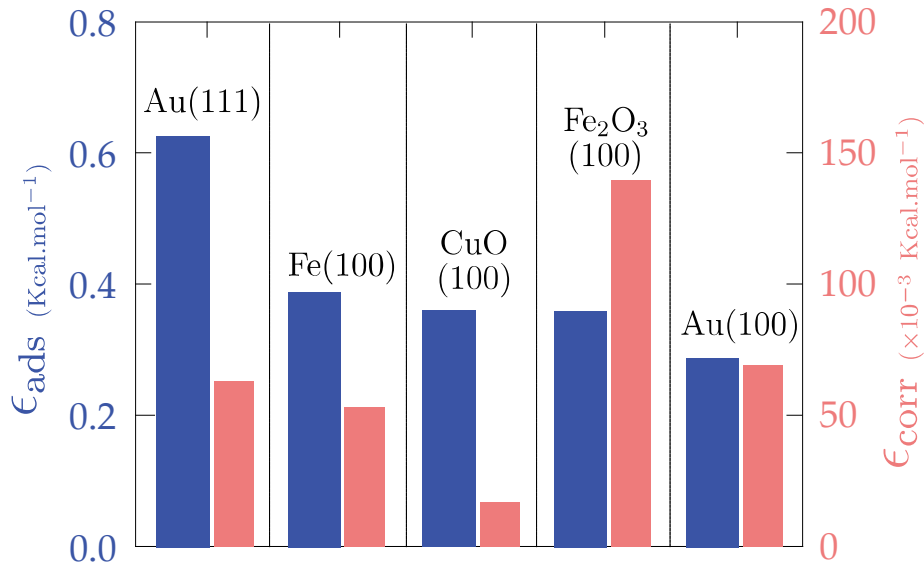


**Fig. 4.3: Adsorption and corrugation parameters for five different surfaces determined using the surface scanning procedure of Fig. 4.1. The results are sorted from left to right in the descending order of adsorption.**

In order to check if the scan results are indicative of the surface influence on the different properties of confined films, the characterized surfaces were put in molecular lubrication conditions for confining a hexadecane film. The relationships between the adsorption and corrugation parameters on one side and the simulation results are then discussed in details.

## 4.2 Overview of the molecular model

Molecular lubrication simulations were conducted on a system of a 4nm hexadecane film confined between each of the five previously characterized surfaces. Snapshots of the molecular systems with the boundary conditions are given in Fig. 4.4. The size of the simulation boxes is around  $50\text{\AA} \times 50\text{\AA} \times 60\text{\AA}$ , this is sufficiently large to insure that the lubricant molecules can flow with properties close to the bulk in the central part of the simulation box. The surface area is slightly changed for each surface type in order to insure perfect repetition of the lattice across the periodic boundaries. A constant load of 500MPa was applied and the surfaces were moved at a sliding speed of  $\pm 10\text{m}\cdot\text{s}^{-1}$  as shown in Fig. 4.4. The expected apparent shear rate in these simulations is  $5 \times 10^9\text{s}^{-1}$ . According to the results from Chapter 3, no surface/lubricant heating is supposed to occur at this shear rate. Thus a simple sliding boundary thermostat SBT with a Langevin implementation is used to keep the surface temperature at 300K.

As detailed in previous chapters, shear is only applied after an initialization phase. This phase includes energy minimization, thermostating, and compression by the application of the normal load. At the end of compression, the film thickness is almost constant. While keeping the load, the surfaces are finally set to move in opposite directions and the thermostat is applied uniquely at the surfaces.

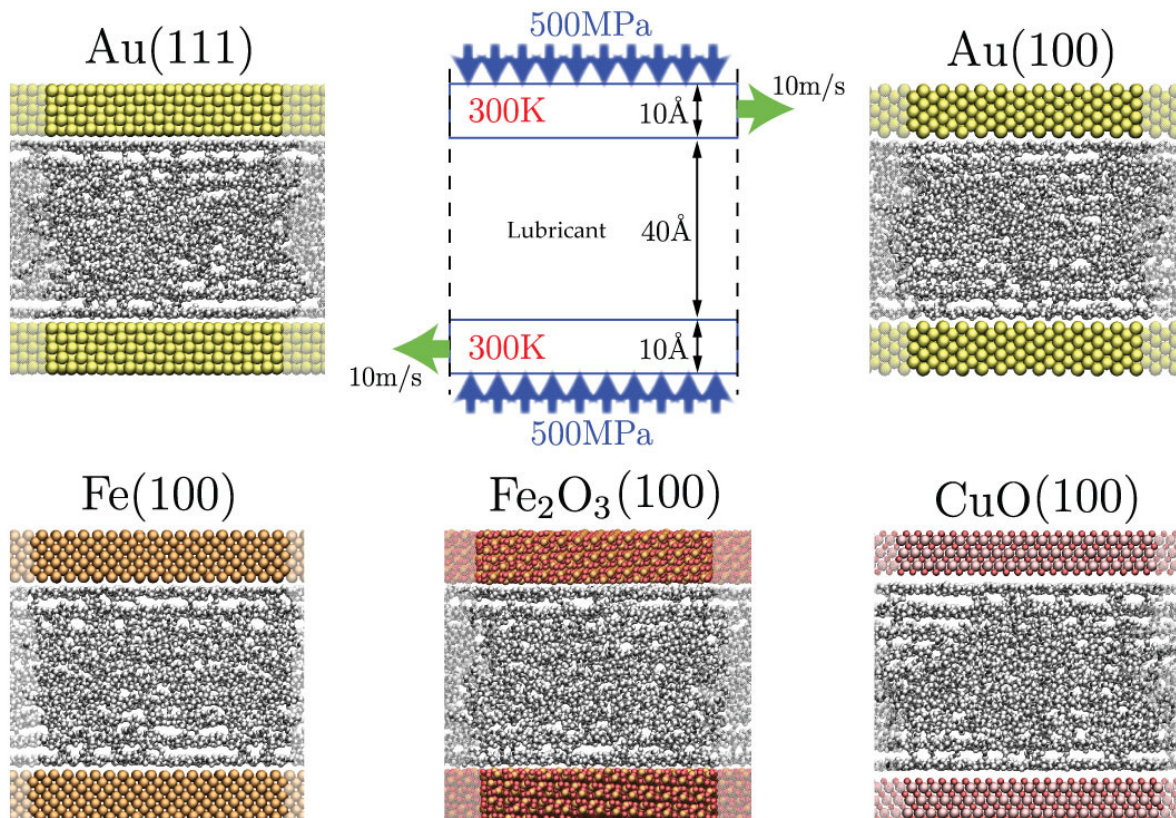


Fig. 4.4: Snapshots of the molecular lubrication systems of 4nm hexadecane film confined between five different surface types. The thermal and mechanical boundary conditions for the shearing phase are shown.

### 4.3 Results and discussion

The results are given in three sections: film structure, boundary flow, and shear stress.

#### 4.3.1 Film structure

The mass density profiles across the sheared hexadecane film for Au(111) and Au(100) surfaces are given in Fig. 4.5. In both cases, the normal density fluctuates across the film indicating lubricant layering and the number of formed layers is 9. Moreover the average lubricant density ( $\bar{\rho}$ ) is independent of the surface type. However, there is a significant difference in the amplitude of the first density peak. This is as a measure of how dense the first lubricant layer adjacent to the surfaces is. Au(111) surface, which has a significantly stronger adsorption potential than Au(100) (see Fig. 4.3), results in denser lubricant layers adjacent to the surfaces.

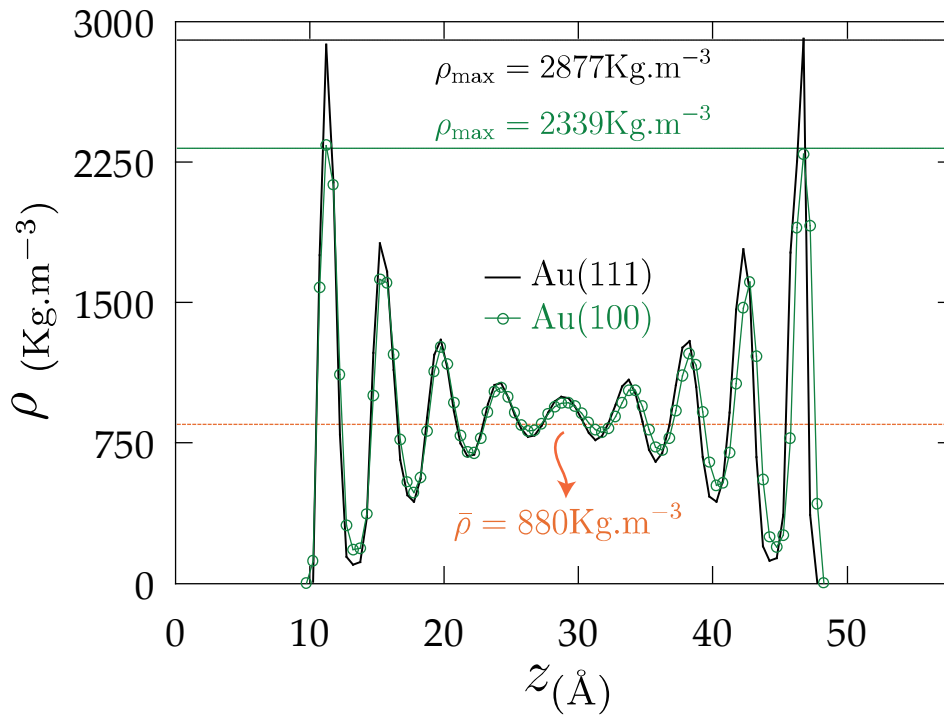


Fig. 4.5: Mass density profiles of a 4nm confined hexadecane film between two gold surfaces of different lattice orientations and different adsorption potential.

This tendency is also observed for the other surface types. As a quantitative substitute to comparing density profiles, the ratio  $\left(\frac{\rho_{\max}}{\bar{\rho}}\right)$  is calculated for each surface and is given as a function of the surface type and its characteristic adsorption parameter in Table 4.2.

Surface	$\epsilon_{\text{ads}}$ (Kcal.mol <sup>-1</sup> )	$\frac{\rho_{\text{max}}}{\bar{\rho}}$
Au (111)	0.628	3.269
Fe (100)	0.390	2.951
CuO (100)	0.362	2.851
Fe <sub>2</sub> O <sub>3</sub> (100)	0.361	2.669
Au (100)	0.289	2.658

**Table 4.2: Variation of the maximum-to-average density ratio (see Fig. 4.5) as a function of the adsorption parameter for different five surface types.**

The maximum-to-average density ratio is clearly an increasing function of the adsorption parameter. Surfaces with strong adsorption actually attract more molecules and the density peak in the first lubricant layer is larger.  $\epsilon_{\text{ads}}$  is thus a representative measure of the surface adsorption potential and is the dominant factor which controls the density of the adjacent lubricant layer.

A thorough examination of the results for Fe<sub>2</sub>O<sub>3</sub> and CuO surfaces (Table 4.2) reveals that another surface-dependant factor has a secondary influence on the lubricant structure. Several authors have already observed that “geometrically corrugated” (rough) surfaces frustrate the film ordering and attenuate the density fluctuations compared to smooth surfaces [63, 64]. In this work, all surfaces are “geometrically” smooth but a potential physical corrugation may actually be playing a similar role to geometrical roughness. Although the two surfaces have almost equal adsorption potentials (Table 4.2), Fe<sub>2</sub>O<sub>3</sub> has a significantly larger corrugation than CuO (see Fig. 4.3). The corrugation of Fe<sub>2</sub>O<sub>3</sub> surface plays a secondary role in partially frustrating the lubricant layering and attenuates the lubricant density peaks.

In conclusion, the surface nature is an essential factor which influences lubricant layering. The results present evidence that this phenomenon is amplified by the surface adsorption potential and slightly attenuated by the corrugation. The analysis of these effects and comparison between the different surface types wouldn’t have been possible without the surface characterization method. In the next section, velocity profiles across the lubricant film are compared for different surfaces in the purpose of revealing the factors which influence the lubricant boundary flow.

### 4.3.2 Boundary flow

The surfaces slide at equal but opposite velocities of  $\pm 10\text{m.s}^{-1}$  creating shear inside the confined hexadecane film. The velocity profiles obtained for the same operating conditions but different surface types are given in Fig. 4.6.

The first two observations that catch the eye in this figure are that the profiles are symmetrical and that the lubricant may slip or not with respect to the surfaces according to their type. The symmetry of the profiles is purely due to symmetrical operating conditions and proves that the sampling time (5ns) is sufficient. As for slip, it is nearly impossible to analyze its origins, as is classically done, by examining the lattice structures, surface densities, and interaction parameters. However, all of these factors can be quantified as done previously

with the surface adsorption and corrugation parameters. It will be shown that these two parameters are essential for understanding the origins of boundary slip and analysing the details of the velocity profiles of Fig. 4.6.

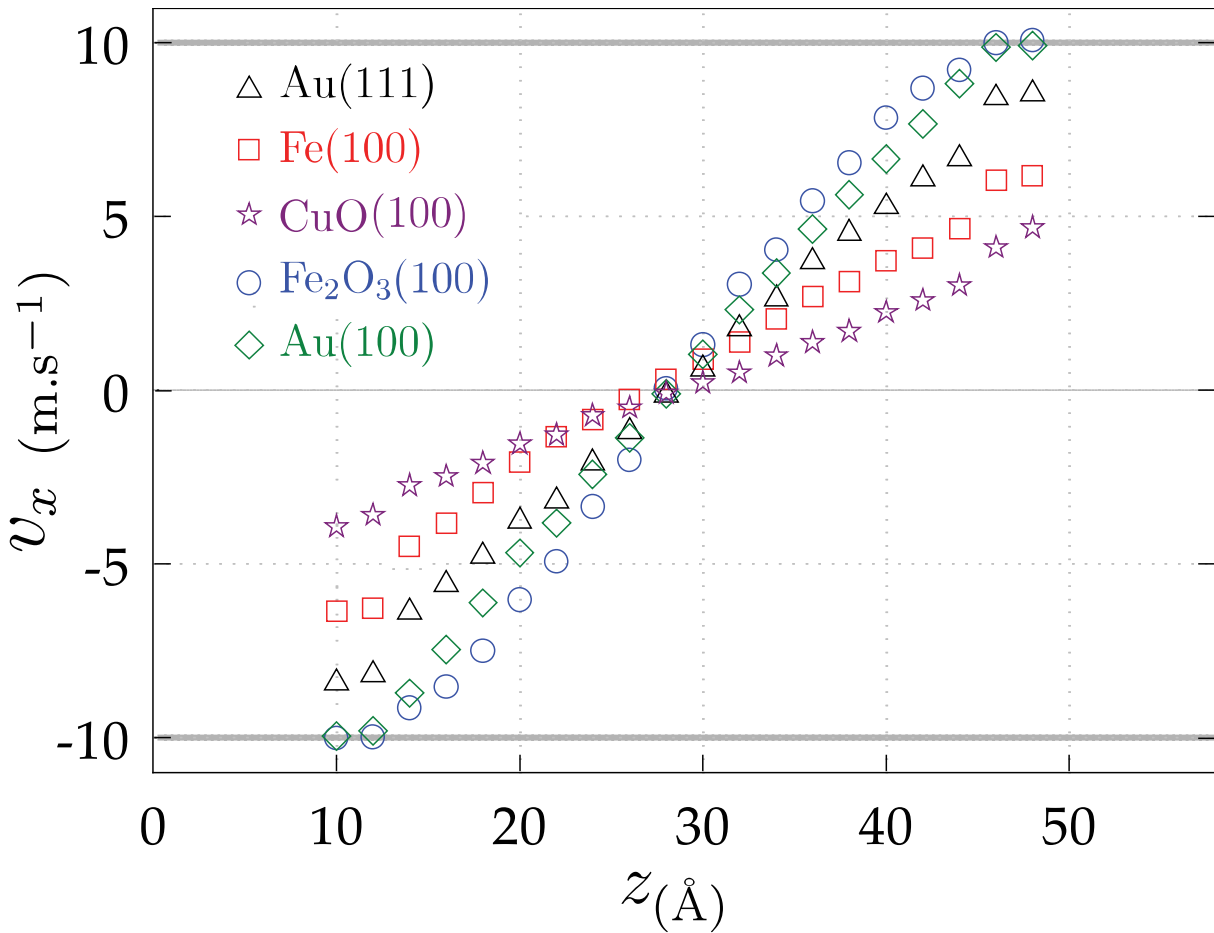


**Fig. 4.6: Streaming velocity profile across a confined hexadecane film between five different types of surfaces. The shearing is due to surface sliding at velocities of  $\pm 10\text{m.s}^{-1}$ .**

The surface types in Fig. 4.6 are sorted vertically in decreasing adsorption parameter (Fig. 4.3). Au(111) surface has the strongest adsorption and is covered by the densest lubricant layer (Fig. 4.5) but the first lubricant layer significantly slips at the interface. Au(100) surface has, on the other hand, the weakest adsorption potential but no boundary slip occurs. Unlike for the layering phenomenon, the surface adsorption potential is actually not a dominant factor which influences boundary slip.

The dominant factor in question here is in fact the surface corrugation. The surface scan results for the corrugation parameter in Fig. 4.3 are completely coherent with the obtained velocity profiles. The lubricant does not slip next to corrugated surfaces such as Au (100) and  $\text{Fe}_2\text{O}_3$ . The other surfaces, with lower corrugation, exhibit boundary lubricant slip. These observations can be presented in a more quantitative manner as shown in Table 4.3 which gives the average shear rate ( $\dot{\gamma}_{\text{av}}$ ) in the center of film as a function of the corrugation parameter ( $\epsilon_{\text{corr}}$ ).

In these simulations the apparent shear rate is  $5.15 \times 10^9 \text{s}^{-1}$ . The average shear rate is smaller than the apparent one when the lubricant slips at the boundary. On the other hand,

the average shear rate is higher than the apparent one when one or more lubricant layers are locked to the surfaces and real shearing starts at a distance inside the film.

Hexadecane molecules slip occurs near surfaces with small corrugation potentials. The reason is that in such cases, the surface interaction potential varies little across the surface. Lubricant atoms thus easily break out of the sites of potential minima and move freely in the opposite direction of surface motion. When surfaces are corrugated, they present a large number of local potential minima. Lubricant molecules almost always find free equilibrium positions and move altogether with the surface.

A closer examination of the velocity profiles of Fig. 4.6 reveals a particular phenomenon occurring near surfaces with strong adsorption potentials such as Au (111) and Fe (100). In these surfaces, the first lubricant layer slips at the interface due to insufficient surface corrugation. However, the particularity is in that the velocity profile is discontinuous inside the film and also shows a slip between the second and the first layer.

The adsorption potential causes a boost in the density of the adjacent lubricant layer as was shown in the previous section. This layer becomes, if not crystallized, of higher order than the lubricant bulk. As a result, the second layer no longer recognizes this adsorbed layer as one of its kind and slip occurs inside the film.

In the case of surfaces with low adsorption but relatively large corrugation potentials such as Au (100), the velocity profile is continuous across the film and at the interface. Slip occurs neither at the boundary nor inside the film.

Surface	$\epsilon_{\text{ads}}$ (Kcal.mol <sup>-1</sup> )	$\epsilon_{\text{corr}}$ ( $\times 10^{-3}$ Kcal.mol <sup>-1</sup> )	$\dot{\gamma}_{\text{av}}$ ( $\times 10^9$ s <sup>-1</sup> )	$\tau_{\text{xz}}$ (MPa)	$\eta_{\text{eff}}$ (mPa.s)
CuO (100)	0.362	17.0	1.81	23.6	13.04
Fe (100)	0.390	53.3	3.04	34.5	11.35
Au (111)	0.628	62.2	4.81	40.9	8.50
Au (100)	0.289	69.6	5.80	42.3	7.29
Fe <sub>2</sub> O <sub>3</sub> (100)	0.361	139.8	7.09	46.0	6.49

**Table 4.3: Average shear rate, apparent shear stress and effective shear viscosity of a confined hexadecane film between different surface types characterized by their adsorption and corrugation potentials. The apparent shear rate in these simulations is equal to  $5.15 \times 10^9$  s<sup>-1</sup>.**

### 4.3.3 Apparent shear stress

The apparent shear stress is determined from the total tangential force acting on the surfaces that oppose their motion. This also represents the total driving force needed on the surfaces to overcome the lubricant flow resistance and enforce their constant-velocity sliding. Fig. 4.7 reports the apparent shear stress for each of the five types of surfaces. It should be noted that the operating conditions for the five cases are identical. The difference in the shear stresses is thus purely due to the difference in the surface properties.

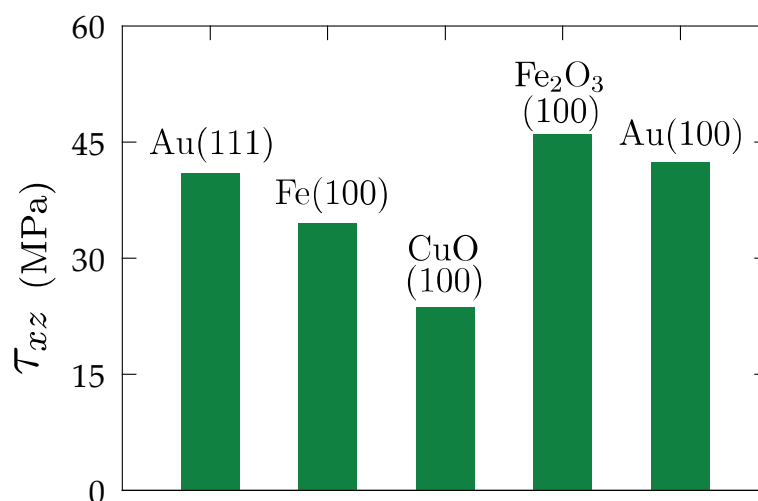


**Fig. 4.7: The measured total shear stress of a 4nm thick hexadecane film confined between five different types of surfaces.**

The highest shear stress is reported for Fe<sub>2</sub>O<sub>3</sub> surface whereas the lowest is seen with CuO. By considering the corrugation results of Table 4.3, it is clear that surfaces with large corrugations give the highest shear stress. This is mainly due to the weak lubricant slip near such surfaces. The lubricant slips more near surfaces with low corrugation. As a result it is practically sheared at a lower rate and thus the shear stress is lower.

## Conclusion

A surface interaction energy scanning method was introduced which allows characterizing and comparing the adsorption and corrugation potentials of different surface types. The method was applied to five realistic surfaces with different densities, crystalline structures, and interaction parameters. The results showed that some surfaces may have a strong adsorption potential with small corrugation and vice-versa.

These surfaces were then used, in molecular lubrication conditions, to confine a 4nm hexadecane film. The simulation results showed different film structure and dynamics with each of the surfaces. Since the surface scans were available, the origins of different factors influencing film structure and boundary flow were identified.

Within the studied operating conditions, surface adsorption potential was found to be the dominant factor which amplifies the density of the adjacent lubricant layer. A secondary effect was found to be related to the surface corrugation which frustrates the layering and thus reduces the adjacent lubricant density. As for boundary flow, lubricant boundary slip is greatly influenced by surface corrugation. Lubricant molecules may even slip at a strongly adsorbing surface if it has a small corrugation. In some surfaces of strong adsorption, an internal slip may occur inside the film between the first and the second lubricant layers adjacent to the surfaces.

Finally, in terms of global friction it was found that corrugation is the most influencing factor through its strong relationship with boundary slip and thus surface wettability. In

comparison between geometrically smooth surface models, low-friction surfaces can be identified as those with the lowest potential corrugation.

It was shown in this chapter that the atomic nature of the surface greatly influences the structure and dynamics of a confined hexadecane lubricant film. In the next and last chapter, the influence of the lubricant molecular structure in pure solutions and mixtures are considered as a function of surface wettability.



# 5

# Effect of lubricant molecular structure

92

<b>Introduction</b>	<b>92</b>
<b>5.1 Effect of molecular chain length</b>	<b>92</b>
5.1.1 Molecular domain	93
5.1.2 Results	94
5.1.2.1 Film structure	94
5.1.2.2 Boundary flow	95
5.1.2.3 Shear stress	96
<b>5.2 Effect of molecular branching</b>	<b>98</b>
5.2.1 Molecular domain	98
5.2.2 Results	99
5.2.2.1 Film structure	99
5.2.2.2 Boundary flow	100
5.2.2.3 Shear stress	101
<b>5.3 Non polar lubricant mixtures</b>	<b>102</b>
5.3.1 Molecular domain	102
5.3.2 Results	103
5.3.2.2 Film structure	103
5.3.2.3 Boundary flow	105
5.3.2.4 Shear stress	106
<b>5.4 Polar lubricant mixtures</b>	<b>107</b>
5.4.1 Molecular domain	107
5.4.2 Molecular migration of ZDDP molecules	109
5.4.3 Effect on the boundary flow and friction	111
<b>Conclusion</b>	<b>112</b>

# 5. Effect of lubricant molecular structure and surface wettability

---

## Introduction

Lubricants are often mixtures of different chemical compounds. Their bulk viscosities can be related to the shape and interactions of their constitutive molecules. Long-chain and branched molecules have higher viscosities than small-chain and linear ones. In classical lubrication problems, the bulk lubricant transport properties are often sufficient for explaining the relationship between friction and the molecular structures of the lubricating fluids.

However, this relationship is more complex in molecular lubrication problems where nanometer thin lubricants are sheared between two surfaces. For instance, the notion of bulk viscosity is totally insufficient for explaining friction at this scale [101]. Due to the small size of the confined domain, the surface-lubricant interactions play an essential tribological role. These interactions actually depend as much on the surfaces as they do on the shape and nature of the confined lubricant molecules.

Commercial lubricants are complex blends of different types of chemical compounds such as mineral oils, anti-wear or friction additives, anti-oxidizing agents, detergents, etc. The constitutive molecules can be saturated with linear or branched chains but can be also polar and encounter special physico-chemical interactions with the bounding surfaces. Unlike the preceding chapter where hexadecane was the only fluid considered, in this chapter the major effects of lubricant molecular nature and shape in confined films between wetting and non-wetting surfaces are studied. There is an essential need for understanding such effects especially for improving the predictive ability of lubricant design in applications operating completely or partially under molecular lubrication conditions. In the line of the preceding chapter, the operating conditions of normal pressure and sliding speed will be kept constant and equal to those chosen previously.

## 5.1 Effect of molecular chain length

The length of lubricant molecules is a crucial factor in determining their tribological performances in molecular confinement [103]. Short molecules have low bulk viscosities but in severe confinement they more easily reach a high-order state (solidification or glassy state) compared to longer ones [61]. They also encounter a smaller boundary slip than longer chains [104] which may also result in a friction increase.

Five types of saturated linear-chain alkane molecules were studied under molecular lubrication conditions in order to detect the effect of chain length on the global behavior of the confined film. The details about these simulations are given in the next section.

### 5.1.1 Molecular domain

A model for molecular lubrication is used including five linear-chain alkane molecules of different lengths: methane, n-pentane, n-decane, n-hexadecane, and n-tetracosane. A snapshot of the five molecules modeled with united atoms is given in Fig. 5.1. Two realistic models of oxide surfaces were considered: copper oxide (CuO) and ferric oxide (Fe<sub>2</sub>O<sub>3</sub>) in the same orientations as the previous chapter (100). These surfaces were shown to have different corrugations and exhibit different boundary flow conditions. The effect of lubricant chain length can thus be understood for the cases of wetting (Fe<sub>2</sub>O<sub>3</sub>) as well as non-wetting (CuO) surfaces.

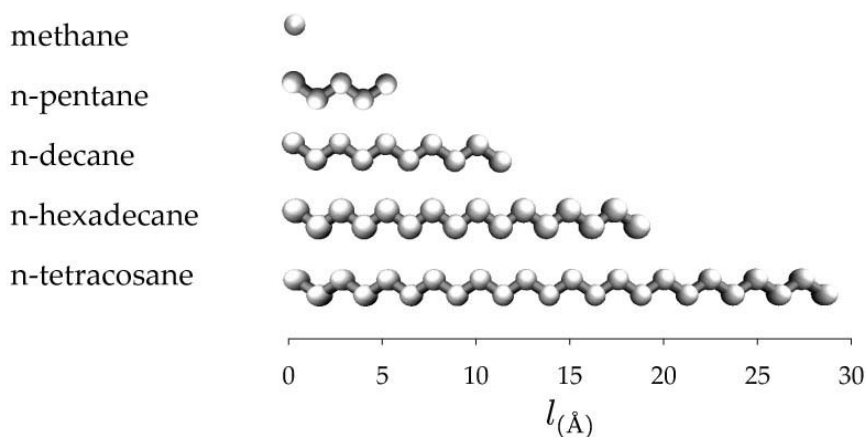


**Fig. 5.1: Snapshot of five lubricant molecules used in molecular lubrication conditions for investigating the effect of chain length on the tribological performance of lubricants.**

In the simulations, the operating conditions are the typical ones used in the previous chapter i.e. a loading pressure of 500MPa and a sliding velocity of  $\pm 10\text{m}\cdot\text{s}^{-1}$ . These conditions represent severe pressure and shear as in many industrial applications. The equilibrium film thickness in the simulations is around 4nm. No significant lubricant heating is susceptible to occur because the apparent shear rate in these simulations is around  $5 \times 10^9\text{s}^{-1}$  which is lower than the critical shear rate ( $\dot{\gamma}_c = 6 \times 10^9\text{s}^{-1}$ ) identified in Chapter 3. A simple SBT with a Langevin implementation is thus convenient to be used.

A united atoms model was used for all interactions inside the system. For all molecules except methane, the molecular architecture and interactions are those given in Chapter 2. For methane, the Lennard-Jones interaction parameters ( $\epsilon = 0.294\text{Kcal}\cdot\text{mol}^{-1}$  and  $\sigma = 3.73\text{Å}$ ) from the OPLS force field were used. As for the surface-lubricant interactions, the employed parameters are those determined by adsorption energy calculations which were given in Chapter 4.

## 5.1.2 Results

### 5.1.2.1 Film structure

The density profiles across the lubricant films are given for methane ( $\text{CH}_4$ ), n-decane ( $\text{C}_{10}\text{H}_{22}$ ), and n-tetracosane ( $\text{C}_{24}\text{H}_{50}$ ) in Fig. 5.2. The results with the other two molecules (pentane and hexadecane) are not given for the sake of presentation clarity. The results show that in all cases, lubricant layering occurs and 9-10 layers are formed for all molecules except methane which forms 12 layers (Fig. 5.2).

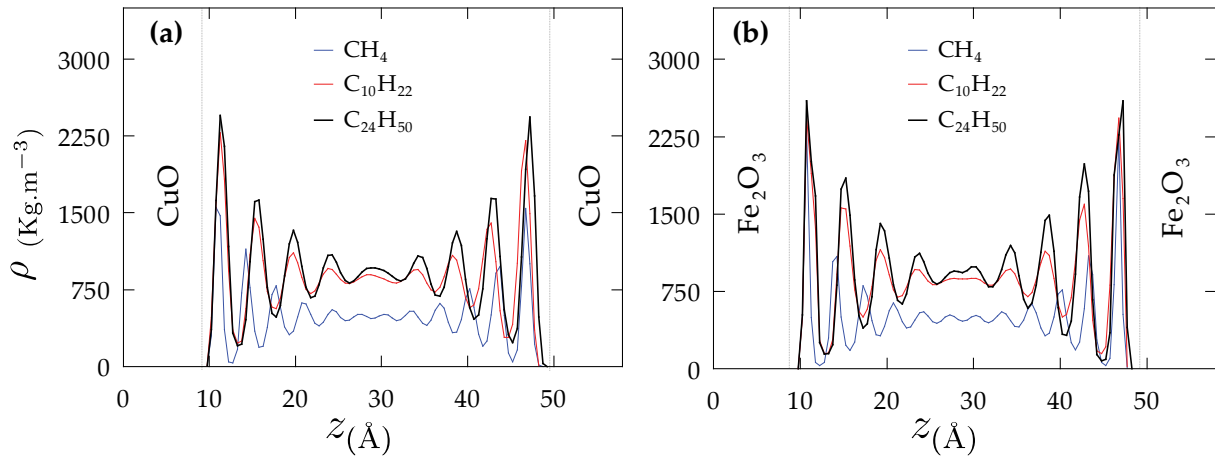


**Fig. 5.2: Mass density profiles across confined lubricant films with molecules of different chain lengths (methane, decane, and tetracosane). The results are given for two types of confining surfaces: CuO and  $\text{Fe}_2\text{O}_3$ .**

The average lubricant density ( $\bar{\rho}$ ) is given as a function of the chain length in Table 5.1.  $\bar{\rho}$  is independent of the surface type but increases with the chain length. The absolute value of the first density peak increases with the chain length as shown in Fig. 5.2. However, the ratio of the maximum-to-average density decreases with the chain length (Table 5.1). This means that, in relative units, layering is more pronounced in lubricant films made of short molecules. For molecules with more than 10 segments, this ratio stabilizes at a minimum value (Table 5.1). This minimum depends only on the type of the confining surfaces.

$\text{C}_n\text{H}_{2n+2}$	CuO		$\text{Fe}_2\text{O}_3$	
	$\bar{\rho}$ ( $\text{Kg.m}^{-3}$ )	$\frac{\rho_{\max}}{\bar{\rho}}$	$\bar{\rho}$ ( $\text{Kg.m}^{-3}$ )	$\frac{\rho_{\max}}{\bar{\rho}}$
n = 1	479.7	4.83	481.0	3.23
n = 5	773.8	3.08	773.6	2.88
n = 10	855.5	2.85	854.5	2.67
n = 16	880.8	2.85	876.4	2.67
n = 24	910.1	2.86	911.0	2.68

**Table 5.1: Average lubricant density and maximum-to-average density ratio across the confined films between CuO and  $\text{Fe}_2\text{O}_3$  surfaces. The film is subject to 500 MPa and its temperature is 300K.**

Finally, the molecular configurations in the plane of the adsorbed layers of methane, pentane, and tetracosane on CuO are given in Fig. 5.3. In long chain molecules ( $C_{24}H_{50}$ ), a preferential alignment parallel to the shear direction is observed. This effect diminishes for shorter molecules ( $C_5H_{12}$ ) and clearly vanishes for methane as shown in Fig. 5.3.

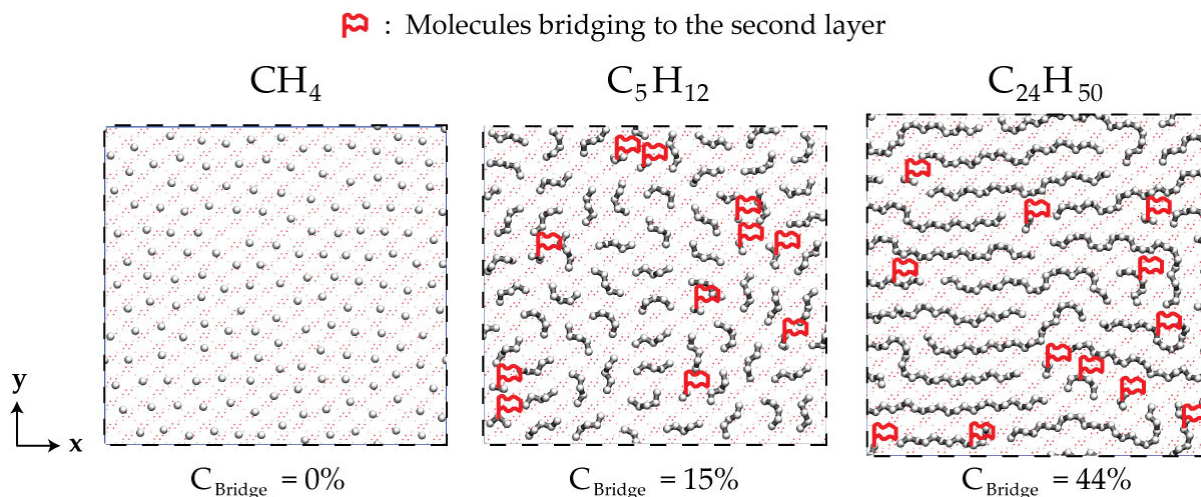


**Fig. 5.3:** XY snapshot of the molecular configuration inside the first lubricant layer, for three different chain lengths, near the CuO surface. The bridging coefficient  $C_{Bridge}$  represents the percentage of lubricant molecules being incompletely present in the first layer adjacent to the surfaces.

In lubricant films constituted of long chains, moreover, the percentage of molecules contained in more than a single layer is high. For instance with tetracosane (Fig. 5.3), 44% of the molecules in the first lubricant layer form bridges to the next layers inside the film compared to only 15% with pentane. The bridge formation is representative of the internal fluid cohesion which is also related to its flow resistance (viscosity) [103].

### 5.1.2.2 Boundary flow

The velocity profiles across each of the five lubricant films are given in Fig. 5.4. For the CuO (non-wetting) surface, boundary slip occurs for all cases but significantly increases with the chain length (Fig. 5.4-a). For hexadecane ( $n=16$ ) and tetracosane ( $n=24$ ) molecules, an additional slip occurring inside the lubricant, between the first and second adsorbed layers, can be observed. These effects are not observed with the wetting surface ( $Fe_2O_3$ ). In this case, a no-slip boundary condition is seen for all molecules considered (Fig. 5.4-b).

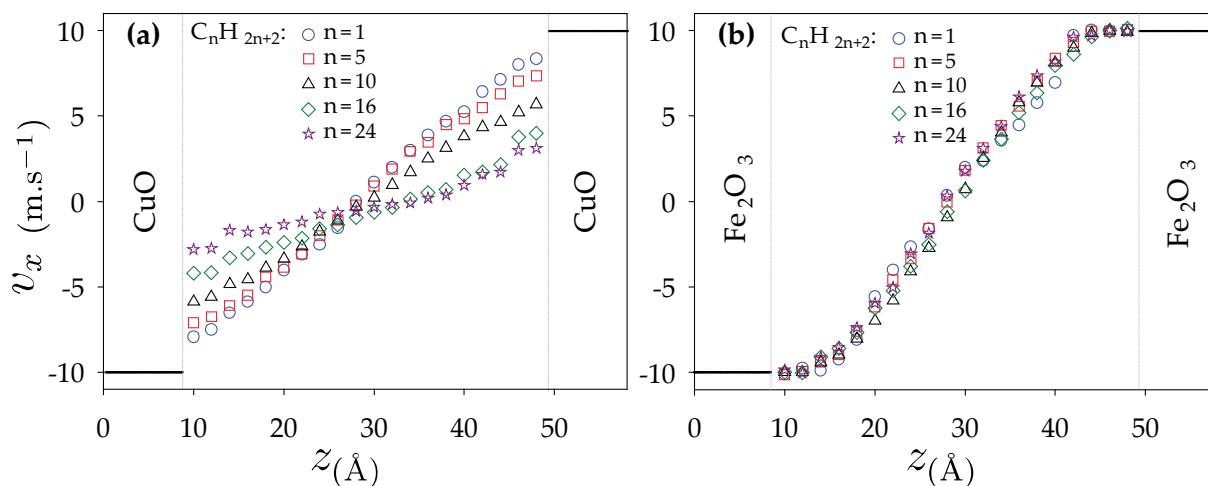


**Fig. 5.4: Velocity profiles across five different alkane lubricant films of different chain lengths confined between two types of surfaces.**

Long molecules slip near the non-wetting surfaces (CuO) due to the strong internal cohesion between their layers. This was manifested by an important degree of interlayer bridging (Fig. 5.3). When the internal lubricant cohesion is weak, as in the case of short molecules, the adsorbed layers preferentially follow the sliding surfaces and a smaller slip is encountered. There is thus a competition between the internal fluid cohesion and that with the surfaces and slip occurs when the former is stronger than latter. This explains why the same molecules did not show any slip near the wetting surface ( $\text{Fe}_2\text{O}_3$ ). The surface corrugation results in a strong cohesion with the lubricant molecules which attenuates the boundary occurring slip.

The chain length thus plays an important role in increasing slip near non-wetting surfaces (i.e. surfaces with low corrugations). This result, for realistic surfaces, is coherent with a molecular dynamics study which was conducted with model surfaces [104]. This effect vanishes if the surfaces are wetting. In this case, no slip occurs for molecules with different chain lengths.

### 5.1.2.3 Apparent shear stress

The average shear rate in the central part of the film is given as a function of  $n$ , the number of lubricant chain segments in Fig. 5.5-a. With the non-wetting (CuO) surface, the average shear rate (undergone by the lubricant) decreases with the chain length (number of segments) and is well below the apparent shear rate (imposed by the surfaces). This is due to the boundary slip which directly influences the rate by which the confined film is actually sheared. As for the wetting ( $\text{Fe}_2\text{O}_3$ ) surface, the average shear rate is almost constant for all cases and is slightly greater than the apparent one. This is due to the lubricant layer locking to this corrugated surface which displaces the shear plane inside the lubricant.

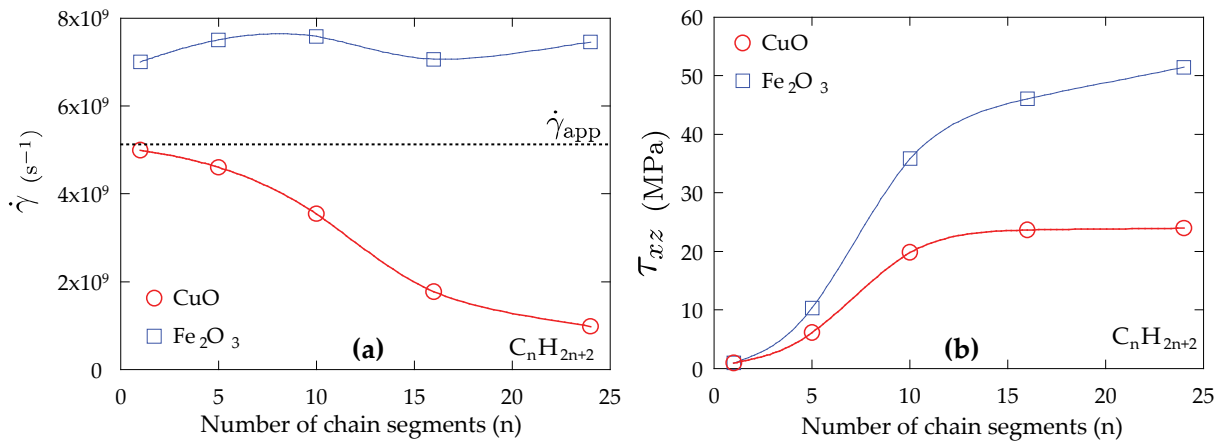


**Fig. 5.5:** As a function of the number of chain segments, (a) the average shear rate in the center of the film and (b) the apparent shear stress required to maintain the lubricant shear.

The apparent shear stress represents the lubricant resistance to surface sliding which produces the shear. It represents the friction in the molecularly confined contact. The shear stress is influenced by two main factors: the flow resistance of the lubricant and the actual shear rate across the film. First, increasing the chain length gives an increase in the flow resistance due to the bridge formation and the strong internal lubricant cohesion. Second, boundary slip which also increases with the chain length results in a smaller average shear rate in the central part of the film. The total shear stress is eventually the product of the flow resistance and the average shear rate, factors which are differently influenced by the chain length.

The shear stress results are given in Fig. 5.5-b for exactly the same contact conditions. The results show that shear stress increases with the chain length for both surface types but not at the same degree. The general increase is a direct result of the enhanced flow resistance with long chain molecules. However, with non-wetting surfaces such as CuO, boundary slip, which increases with the chain length, plays an important role in limiting the shear stress as the lubricant becomes effectively sheared at a lower rate than the apparent one.

In conclusion, the lubricant chain length is an important factor which influences the general structure and dynamics in confinement conditions. Long chains align parallel to the shear direction and slip more than short molecules with respect to non-wetting surfaces. The boundary slip which increases with the chain length counteracts the viscosity increase and results in friction stabilization. Near wetting surfaces, no lubricant slip is observed and friction globally increases with the chain length due to viscosity enhancement in films with such molecules.

These results with the CuO surface are coherent with the simulation results of Priezjev et al. [104] which were conducted on model non-wetting surfaces and bead-spring polymers of different lengths. In this work, realistic tribological surfaces and complex molecular architecture (including bending and twisting rotations) were considered. The results with the wetting surface show that the molecular length effects depend also of the surface type. It is actually the competition between the molecular nature of the lubricant and that of the surfaces that concludes the friction in molecular lubrication.



as united atoms for computational efficiency. The same interaction parameters for the lubricant molecules, surfaces, and their interface (given in Chapters 2 and 4) were used.

## 5.2.2 Results

As previously, the results will be exposed in three separate sections regarding film structure, boundary flow, and shear stress.

### 5.2.2.1 Film structure

The mass density profiles across films of linear and branched decane for the two surface types are given in Fig. 5.7. In both surfaces, the results show that the density of the first adsorbed layer is not influenced by the molecular branching. However, for both surfaces a significant attenuation of layering is observed deeper inside the fluid, in the case of branched decane. The effect of the surface interactions vanishes at only 3 molecular diameters distance and a homogeneous (bulk-like) density persists in the center of the film. In the case of linear decane, well-defined layers are distinguishable at 5 molecular diameters from both surfaces. Due to their strong internal cohesion, branched molecules are actually less influenced by the surface interactions and recover bulk-like behavior at a closer distance from the confining surfaces.

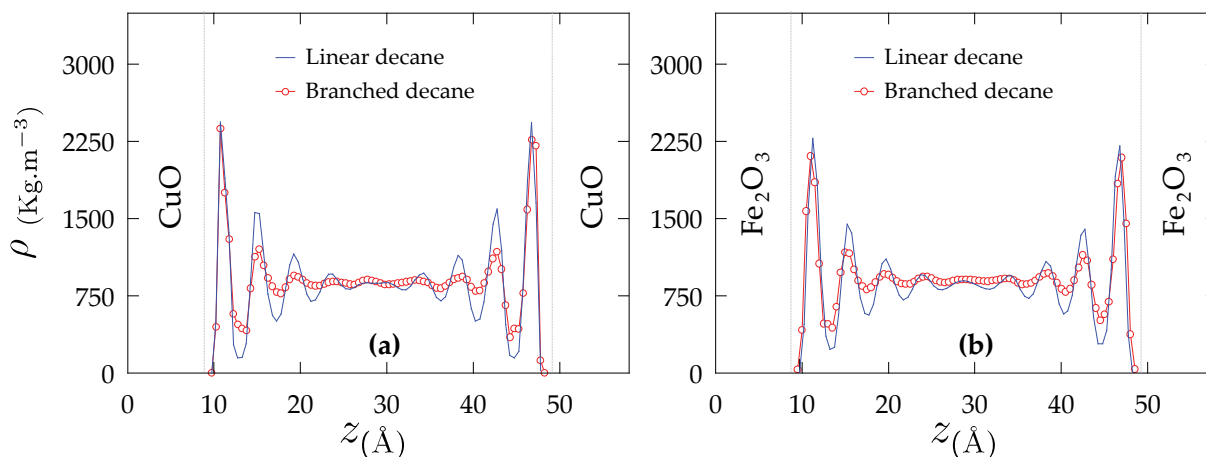


**Fig. 5.7:** Mass density profiles across confined films of linear and branched decane molecules between CuO and Fe<sub>2</sub>O<sub>3</sub> surfaces.

As for the in-plane order, a snapshot of the molecular configuration inside the first lubricant layer adjacent to the CuO surface is given in Fig. 5.8.

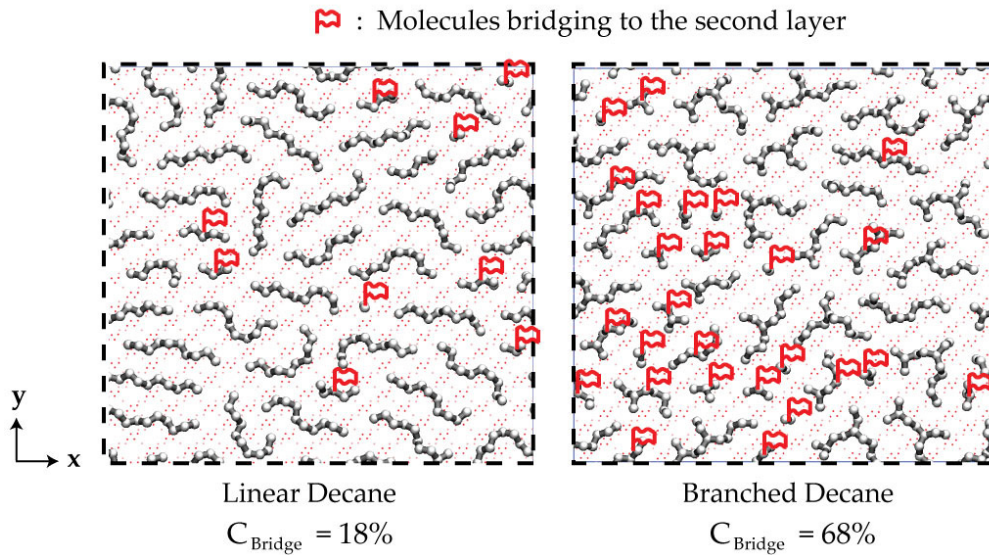


**Fig. 5.8: XY snapshot of the first lubricant layer near the CuO surface for linear and branched Decane molecules. Small red flags indicate the molecules that form bridges to the second lubricant layer. The coefficient of bridging represents the ratio of these molecules to the total number of molecules.**

Linear decane molecules are aligned parallel to the surfaces and thus form very few bridges with the second layer. A preferential alignment parallel to the shear direction can also be observed. In the case of branched decane, the molecules do not show to have a preferential alignment. Moreover, a large percentage of these molecules are actually shared between more than one layer. In other words, they form bridges with the internal layers. The internal cohesion of the molecules is thus stronger than in the linear molecule and a bulk-like homogeneity is seen at a closer distance from the surfaces.

### 5.2.2.2 Boundary flow

The velocity profiles are given for the two surface types (CuO and Fe<sub>2</sub>O<sub>3</sub>) and lubricant molecules in Fig. 5.9. No slip is observed for both linear and branched decane films between the wetting Fe<sub>2</sub>O<sub>3</sub> surface. The obtained velocity profile shows that branching has no significant effect on the local flow near wetting surfaces. However, a remarkable influence on the velocity profiles can be observed with the non-wetting CuO surface. The boundary slip is significantly increased in the case of branched molecules.

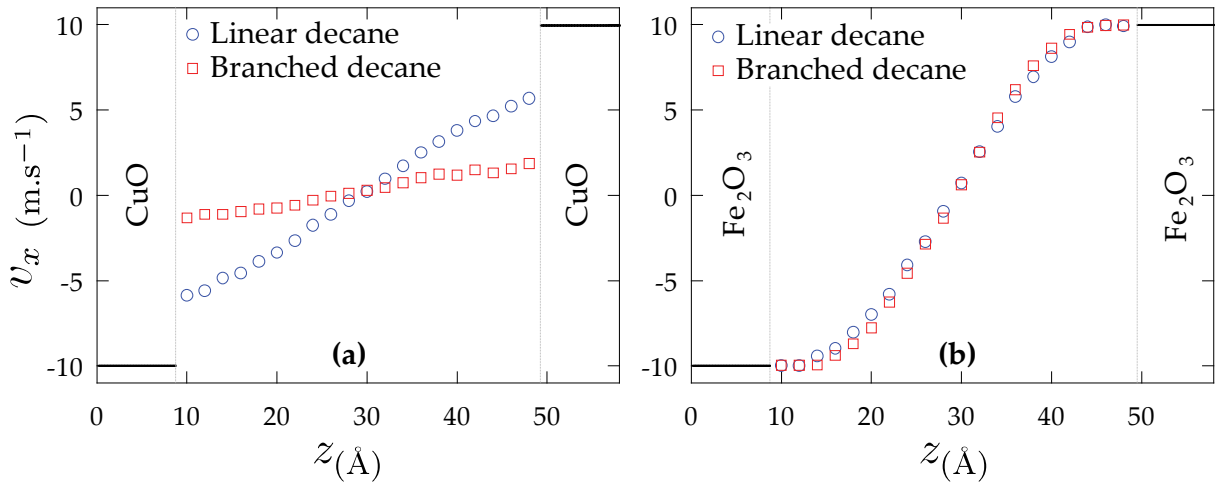


Fig. 5.9: Velocity profiles across a linear and branched decane films confined between CuO and Fe<sub>2</sub>O<sub>3</sub> surfaces.

When the internal lubricant cohesion becomes stronger than its cohesion with the bounding surface, it slips. The enhanced bridging between the layers of branched molecules (Fig. 5.8) plays an important role in increasing the internal cohesion of the film. For the case of the non-wetting surface, this cohesion became stronger than the lubricant adsorption with the surface causing a significant boundary slip to occur.

### 5.2.2.3 Apparent shear stress

In analogy with the effect of the chain length, branching influences the apparent shear stress and friction through two factors. First, branched molecules generally have higher bulk viscosities than linear ones. Second, near non-wetting surfaces they enhance the boundary slip and their films are thus sheared at a lower rate than the apparent one. The increasing viscosity and decreasing average shear rate with the degree of branching have the total shear stress as their product. Depending on the nature of the surface and the molecular structure of the lubricant, more or less friction may be encountered.

In the studied case, the average shear rate in the central part of the film and total shear stress for linear and branched decane films are given in Table 5.2. Although, due to branching the average shear rate was reduced in the case of the non-wetting surface (CuO), the encountered total shear stress remains about 40% higher than for the linear molecule. In the case of the wetting surface (Fe<sub>2</sub>O<sub>3</sub>), the total shear stress is about 70% higher than the linear molecule case. This suggests that the intrinsic viscosity enhancement in branched molecules remains the dominant factor which influences the global friction, at least for the simulated molecular confinement conditions.

Molecule type	CuO		Fe <sub>2</sub> O <sub>3</sub>	
	$\dot{\gamma}$ ( $\times 10^9 \text{s}^{-1}$ )	$\tau_{xz}$ (MPa)	$\dot{\gamma}$ ( $\times 10^9 \text{s}^{-1}$ )	$\tau_{xz}$ (MPa)
Linear	3.54	19.8	7.68	35.8
Branched	1.00	27.2	7.92	61.2

Table 5.2: Average shear rate and total shear stress for linear and branched decane 4nm thin films confined between CuO and Fe<sub>2</sub>O<sub>3</sub> surfaces.

In conclusion, molecular branching frustrates the layering phenomenon in confined lubricant films under molecular lubrication conditions. Bridge formation is encouraged between the lubricant layers and bulk-like homogeneity is seen at a close distance from the bounding surfaces. These observations are coherent with the literature [60, 61, 62]. The bridging enhances the internal fluid cohesion and viscosity resulting in a significantly higher friction near wetting surfaces. In the case of non-wetting surfaces, the strong internal fluid cohesion in branched molecules encourages boundary slip which limits the friction.

Within the limits of the studied operating conditions, the friction was always higher for branched molecules. For higher sliding velocities, it is expected that the boundary slip becomes of increased importance and then the friction enhancement in branched molecules may become more limited.

## 5.3 Non polar lubricant mixtures

The simplest of commercial lubricants are mixtures of saturated hydrocarbons of different molecular structures. As has already been shown in this chapter, the molecular shape of lubricant molecules influences their tribological performances in both bulk and confined conditions. In molecular confinement, this performance also depends on the nature of the confining surfaces. The problem becomes even more complicated when combinations of different molecules are considered.

In bulk lubricants, Khare et al. [106] found that the mixing of long chain (20%) and short chain molecules (80%) results in a significant increase of viscosity. Such non trivial complexities, depending on the molecular structures of lubricant molecules, make the design of new lubricants more of an art than a science [107].

In this section, the mixing of long and short alkane chains to formulate a lubricant blend is considered. The mixture is then put in molecular lubrication conditions. The structure and dynamics of the confined mixture are then compared to those of its constituent molecules in pure solution.

### 5.3.1 Molecular domain

A lubricant mixture is formulated using equal mass concentrations of methane and n-hexadecane molecules. A 4nm thick film of this mixture was confined between CuO and Fe<sub>2</sub>O<sub>3</sub> surfaces. A snapshot of the initial configuration of the system is given in Fig. 5.10-a. Methane molecules are painted in yellow color to distinguish them from the hexadecane molecules.

Initially, the different constituent molecules are homogeneously distributed across the confined domain. With an applied normal pressure of 500MPa, the surfaces are set to move at 10m.s<sup>-1</sup> in opposite directions, creating lubricant shear.

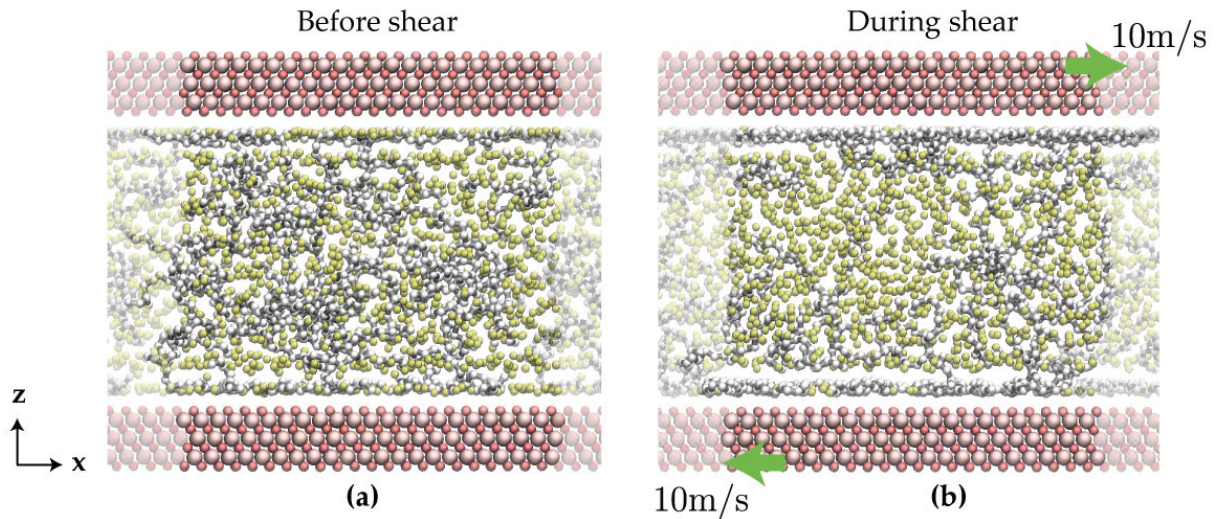


Fig. 5.10: Snapshots of the 4nm molecular confined film of methane-hexadecane mixture before (a) and during shear (b) between CuO surfaces. Methane is represented in yellow while hexadecane is represented in black and white colors.

## 5.3.2 Results

### 5.3.2.2 Film structure

Snapshots of the confined lubricant mixture film before and during shear are given in Fig. 5.10. A quite interesting phenomenon of molecular separation seems to occur inside the film. The long molecular chains of hexadecane (black and white colors) migrate toward the surfaces while the short methane molecules remain in the center of film. The initially homogeneous mixture becomes heterogeneous in the course of shear.

For more quantitative analysis, the mass concentration of hexadecane during shear for the two surface types is given in Fig. 5.11. The migration tendency observed in the snapshots of Fig. 5.10 is conveyed by a large mass concentration near the surfaces and a below-the-average concentration in the center of the film. This effect is seen with both types of wetting ( $\text{Fe}_2\text{O}_3$ ) and non-wetting (CuO) surfaces.

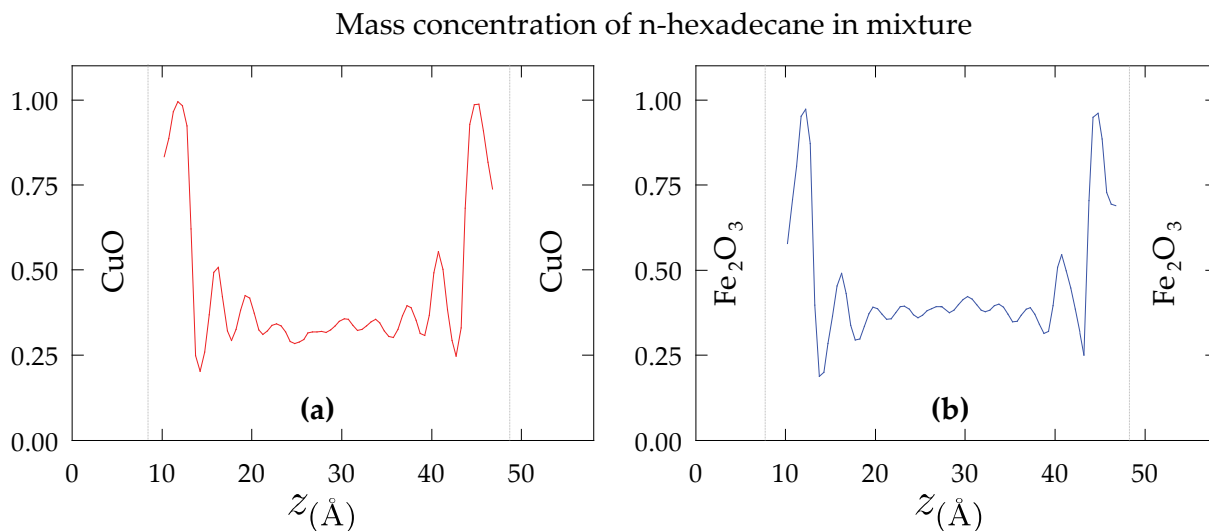


**Fig. 5.11:** Mass concentration of n-hexadecane in the lubricant mixture containing an equal concentration of methane. The results are given for the two surface types CuO and Fe<sub>2</sub>O<sub>3</sub>.

This phenomenon influences the global lubricant density profile. The latter is given in Fig. 5.12 in comparison with the separate density profiles obtained with pure n-hexadecane and methane. The pure hexadecane and mixture density profiles coincide in the first adsorbed layer ( $10 < z < 14 \text{ \AA}$ ). This is logical since this layer is mainly constituted of only hexadecane molecules (Fig. 5.11). From that point on, however, the mixture density no longer follows the hexadecane curve neither in periodicity nor amplitude (Fig. 5.12). In the mixture case, a homogeneous bulk density is reached at a closer distance from the surfaces. In analogy with the density profile of branched molecules (Fig. 5.7), the phenomenon of lubricant layering is actually frustrated by any form of non-homogeneity in the lubricant molecular structure whether this involves molecular branching or molecular mixing as in this case.

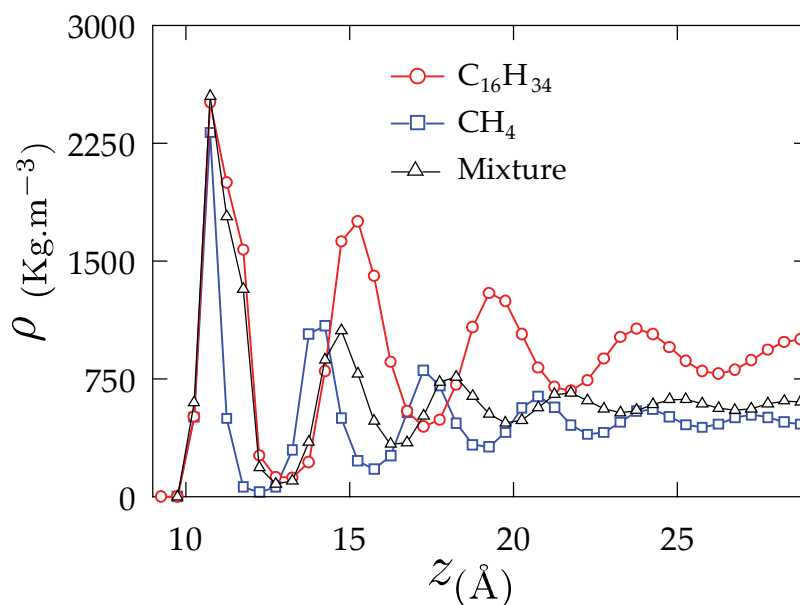


**Fig. 5.12:** Mass density profile in half of the confined films of hexadecane, methane, and their mixture (equal mass fraction of each molecule) confined between CuO surfaces.

### 5.3.2.3 Boundary flow

There is often a close relationship between the film structure and the boundary flow condition of slip or no-slip. This was seen in the case of branched molecules where the bridging between layers caused an attenuation of the layering phenomenon (Fig. 5.7). Moreover, the boundary slip (near the non-wetting surface) increased as the internal lubricant cohesion was enforced (Fig. 5.9). In the case of lubricant mixture and due to shear, a particular “molecular filtering” occurred. The molecular system is heterogeneous with the long chain molecules preferentially concentrated near the surfaces while the short ones remained in the center of the film (Fig. 5.11). So, how does this particular configuration influence the boundary flow?

Fig. 5.13 presents the velocity profiles across the confined mixture in comparison with the velocity profiles obtained with pure solutions of its constitutive molecules (hexadecane and methane).

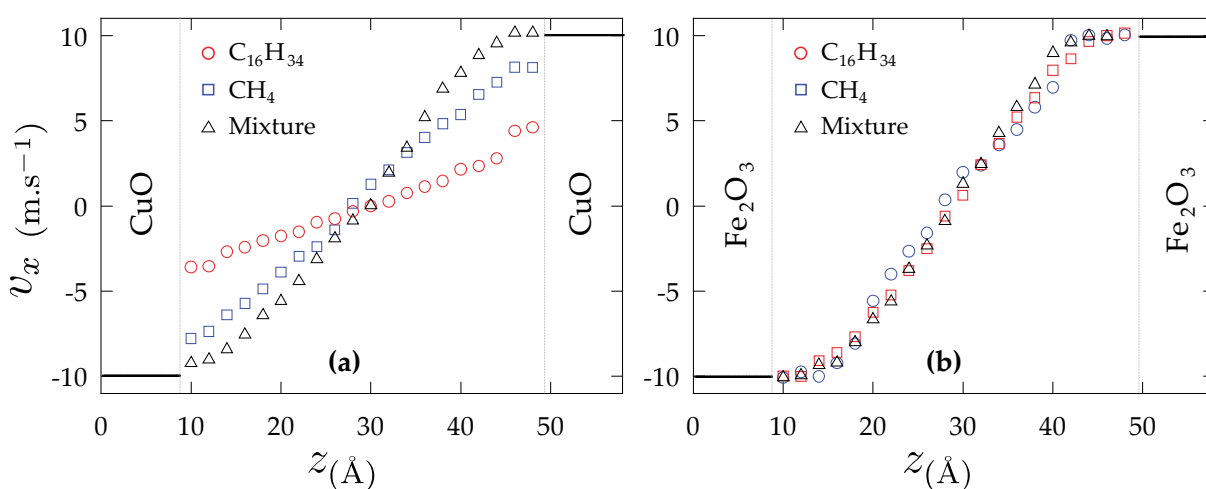


**Fig. 5.13: Velocity profiles across hexadecane, methane, and their mixture in 4nm molecular confinement between CuO and Fe<sub>2</sub>O<sub>3</sub> surfaces.**

With the wetting surface (Fe<sub>2</sub>O<sub>3</sub>), the mixture velocity profile coincides with the profiles for pure hexadecane and methane films. However, a particular phenomenon occurs with the non-wetting surface (CuO). Since pure films of both methane and hexadecane slip, one would expect that their mixture would also slip up to a moderate degree. However, in reality their mixture does not slip at all near the boundary (Fig. 5.13-a). Due to the heterogeneity of the domain (Fig. 5.11), the hexadecane adsorbed layer masks the wetting surface morphology for the internal lubricant layers which are mainly composed of methane. So instead of interacting with a slippery surface potential, the methane (and some hexadecane) molecules interact with a corrugated hexadecane layer which is adjacent to the real solid surface.

But there is another mechanism responsible of the intriguing no-slip boundary condition with the lubricant mixture. In the pure hexadecane simulation, a very similar dense first layer was present and yet the film encountered significant boundary slip. The same applies for the case of branched decane where a dense lubricant layer was present and yet the film slipped at the CuO boundary. Indeed a given dense lubricant layer may or not slip at the boundary depending on two competing cohesion forces. The first represents that with the surface which can be seen as the surface corrugation potential. The second force is that occurring between the consecutive lubricant layers. In the case of branched decane for example,

the internal lubricant cohesion was enhanced by layer bridging and was stronger than the surface corrugation. So, the dense first layer slipped at the boundary. The same reasoning applies for the pure hexadecane film. However, in the case of methane-hexadecane mixture the film composition is heterogeneous. The internal methane layers do not have remarkably strong cohesion with the dense hexadecane layer as shown in Fig. 5.14. In comparison with pure hexadecane, bridge formation is reduced for the mixture case. In this case, the adsorbed hexadecane layer prefers sticking to the surfaces and boundary slip eventually vanishes (Fig. 5.14).

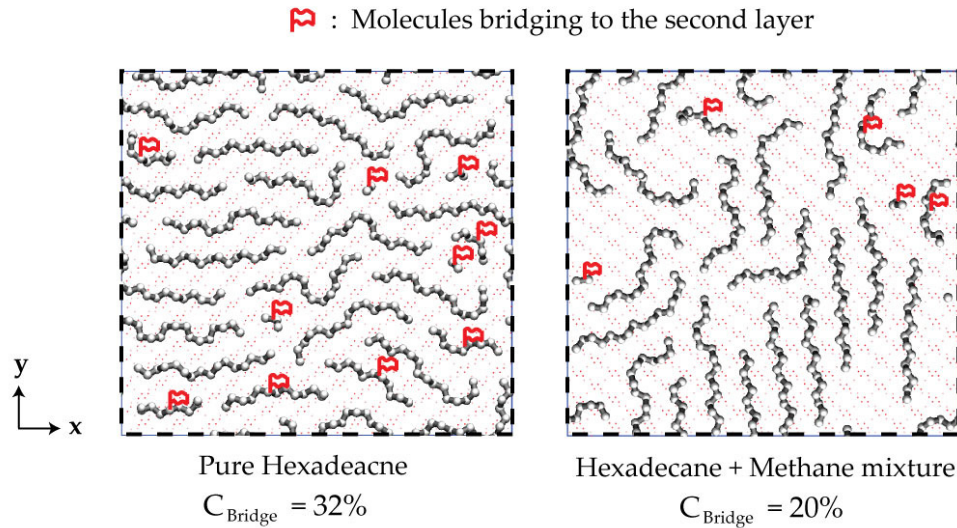


Fig. 5.14: XY snapshot of the first lubricant layer near the CuO surface for pure hexadecane and hexadecane+methane mixture. Small red flags indicate the molecules that form bridges to the second lubricant layer. The coefficient of bridging represents the ratio of these molecules to the total number of molecules in the layer.

#### 5.3.2.4 Apparent shear stress

The results for the average shear rate in the center of the film and the total shear stress are given for both pure and mixture films in Table 5.3. Near the non-wetting (CuO) surface, although boundary slip was significantly reduced in the mixture case, the total shear stress remains remarkably low compared to the pure hexadecane case. The reason is that the majority of the film molecules being sheared in the central part of the film are methane. Due to its low viscosity, the measured shear stresses for the mixture case are very low.

Film composition	CuO		Fe <sub>2</sub> O <sub>3</sub>	
	$\dot{\gamma}$ ( $\times 10^9 \text{s}^{-1}$ )	$\tau_{xz}$ (MPa)	$\dot{\gamma}$ ( $\times 10^9 \text{s}^{-1}$ )	$\tau_{xz}$ (MPa)
100% methane	4.99	0.9	7.00	0.9
100% n-hexadecane	1.77	23.6	7.06	46.0
50% methane + 50% n-hexadecane	6.22	2.8	7.64	3.3

Table 5.3: Average shear rate and total shear stress for pure methane and hexadecane and their mixture in 4nm confined films between CuO and Fe<sub>2</sub>O<sub>3</sub> surfaces.

These results seem to contradict the results of Khare et al. [106] who state that the addition of short molecules to longer ones significantly increase their viscosity. However, their results were given for simulations with bulk lubricants. In the confined simulations considered here, the mixture behaves differently. The film composition becomes heterogeneous with long chain molecules being attracted to the surfaces. Consequently, the major constituents of the central part of the film which is actually in shear are the short molecules which have low viscosities. Once again, this result shows that the bulk properties of lubricants (pure or mixtures) can be misleading in molecular confinement conditions. The tribological performance in these conditions depends on effects that can only be identified at the molecular scale.

## 5.4 Polar lubricant mixtures

Commercial lubricants are mixtures of different chemical compounds. The global performance of a lubricant depends on how each of its constituents behave in all the encountered operating conditions. Engine oils that are designed to lubricate during regular operation may fail for example at the moment of starting or in extreme weather conditions. Many industrial applications encounter molecular lubrication conditions during critical operation periods. The tribological performance of the employed lubricants should be characterized and maintained in such conditions.

Among the chemical compounds which are added to improve the tribological performance of oils are anti-wear additives. These additives protect the interacting surfaces by processes of physical or chemical adsorption to form protective layers (tribo-layers). These layers significantly reduce wear, friction, and improve the lifetime of the machine elements.

ZDDP (Zinc dialkyl-dithio-phosphate) is a representative example of a classical anti-wear additive used in commercial engine oils [108]. Despite its excellent anti-wear properties, this additive is known to produce undesirable high friction in the conditions of mixed lubrication [108]. Recent experimental studies [109] have shown that the addition of 5% in mass concentration of ZDDP with hexadecane base oil results in about 40% increase of friction compared to pure hexadecane. Using molecular dynamics simulations, this section aims to identify the main reasons of the high friction behavior of ZDDP mixtures in molecular confinement conditions.

### 5.4.1 Molecular domain

Molecular dynamics simulations were conducted on a confined system of linear chain hexadecane base oil in the presence as well as the absence of 5% mass concentration of C4-ZDDP additive. A snapshot of the additive molecule is given in Fig. 5.15. The simulated system consists of a 3nm confined film between  $\text{Fe}_2\text{O}_3$  surfaces used to model the oxidized layer on steel, the surface material from the experiments of ref.[109]. The experimental pressure of 1.3GPa is reproduced in the simulations and the surfaces are set to slide at a constant velocity of  $\pm 10\text{m.s}^{-1}$ . Finally, a SBT with a Nosé-Hoover implementation is used to dissipate the generated heat. Although heating is suspected to occur under the operating conditions of pres-

sure and shear, for computational efficiency reasons a simple thermostat was used. This choice is justified by the purpose of the simulations which is to perform qualitative comparison with experiments on the friction in the presence and absence of the ZDDP additive.

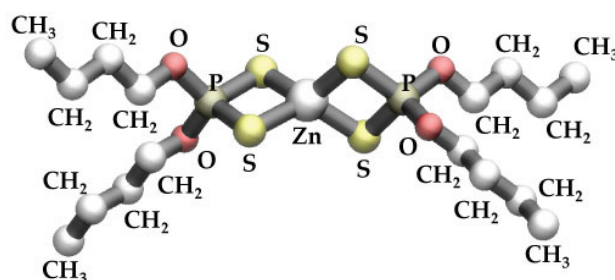


Fig. 5.15: Snapshot of the C4-ZDDP molecule modeled with united atoms.

Hexadecane and ZDDP molecules are modeled using united atoms. The ZDDP molecule model is flexible and has a similar molecular architecture as hexadecane. However, ZDDP includes non-neutral atoms for which electrostatic forces are computed using a particle-particle particle-mesh solver [110]. The element charges and other pairwise interaction parameters used in the simulations are all given in Table 5.5.

		$m$ (amu)	$\epsilon$ (Kcal.mol <sup>-1</sup> )	$\sigma$ (Å)	$q$ (e)
Surface	Fe	55.845	0.0850 (non-wetting) 2.5485 (wetting)	2.20	+0.771
	O	15.999	0.1699	2.96	-0.514
Hexadecane and ZDDP	CH <sub>2</sub>	14.027	0.0933	3.93	0.000
	CH <sub>3</sub>	15.035	0.2264	3.93	0.000
ZDDP	O	15.999	0.1699	2.96	-0.514
	P	30.974	0.1999	3.74	+1.858
	S	32.974	0.2498	3.56	-0.830
	Zn	65.370	0.2500	1.95	+1.600

Table 5.4: masses, Lennard Jones energies ( $\epsilon$ ) and distances ( $\sigma$ ), as well as atomic charges ( $q$ ) for the pair-wise interactions used in the simulations.

A wetting and a non-wetting surface model were created based on the ferric oxide (Fe<sub>2</sub>O<sub>3</sub>) lattice structure. These models were created by artificially changing the LJ energy parameter for the Fe atom in the surfaces. For the non-wetting model, the energy parameter was taken as 0.0850Kcal.mol<sup>-1</sup> while for the wetting one this parameter was increased to 2.5485Kcal.mol<sup>-1</sup>. This permits to study the effect if the ZDDP additives near two types of physically wetting and non-wetting surfaces. A snapshot of the whole molecular domain with the operating conditions is given in Fig. 5.16.

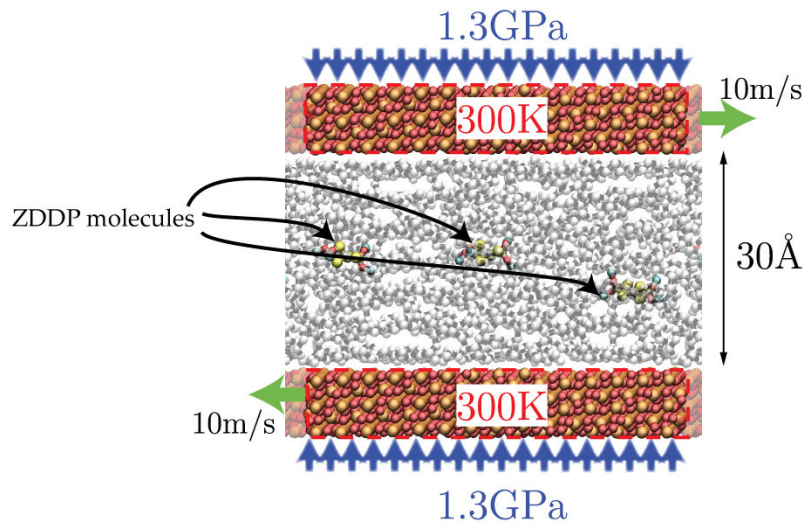


Fig. 5.16: A snapshot of the initial state of the molecular domain used to study the influence of the polar additive (ZDDP) in molecular lubrication.

#### 5.4.2 Molecular migration of ZDDP molecules

In the initial molecular configuration (Fig. 5.18) the ZDDP additive molecules are positioned in the center of the film. However, as soon as the surfaces start sliding and a shear is imposed across the film, the ZDDP molecules migrate toward the oxide surfaces. This occurs with both wetting and non-wetting surface models. Snapshots during the course of shear of the molecular system for the non-wetting surface case are given in Fig. 5.17.

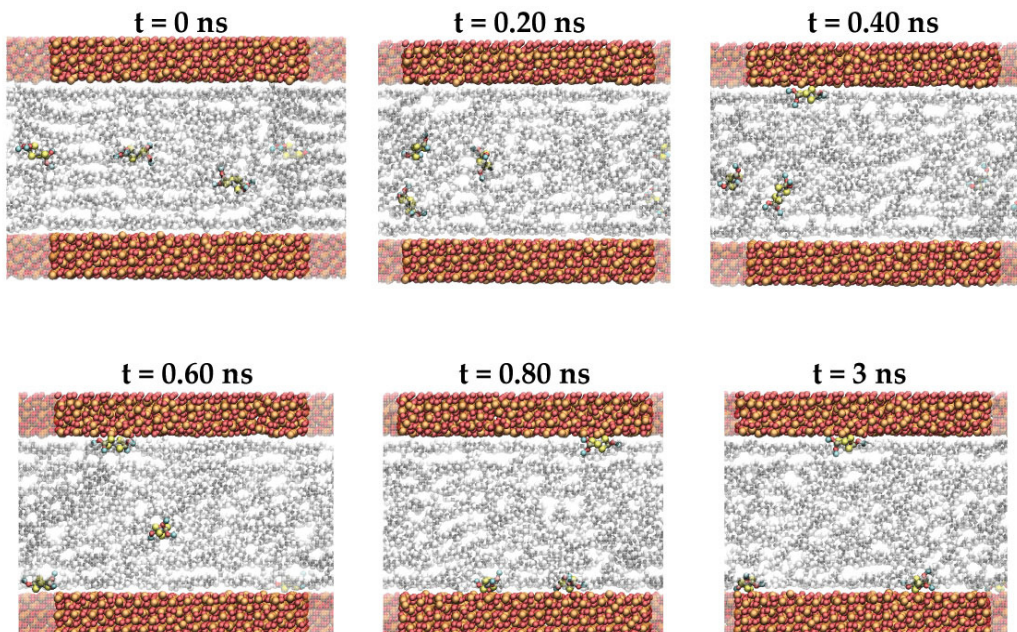


Fig. 5.17: Molecular system snapshots during shear for the case of non-wetting ferric oxide surface model. The ZDDP molecules are in vivid colour while the hexadecane molecules are represented in shaded white and grey. ZDDP molecules are seen migrating and completely adsorbed to the oxide surface after about 0.8ns of shear. These molecules stick to the surfaces for the total duration of the simulation (6ns).

This phenomenon can be explained by the polar nature of the ZDDP molecules. The charges in these molecules result in long-range electrostatic interactions with the oxide surfaces. Saturated hexadecane molecules do not exhibit such long-range interactions with the surfaces. Shear, moreover, plays an important role in encouraging the molecular migration of ZDDP as it causes preferential alignment of the lubricant molecules and global film thinning.

In order to quantitatively describe the migration phenomenon, a non-dimensional parameter  $\bar{d}_c$ , which represents the reduced average distance of the ZDDP molecules from the centre of the film, is calculated as follows:

$$(1) \quad \bar{d}_c = \sum_{i=1}^N \frac{2|Z_i - Z_c|}{N \cdot h}$$

$N$  is the number of ZDDP molecules and  $Z_i$  is the z-coordinate (in the film thickness direction) of the center of mass of molecule  $i$ ,  $h$  is the average film thickness and  $Z_c$  is the elevation of the central plane of the film. A value of  $\bar{d}_c$  near zero means that the ZDDP molecules are aligned in the center of the film whereas a value near unity means that they are located near the surfaces.

A similar non-dimensional parameter  $\bar{v}$  representing the ratio of the average streaming velocity of the ZDDP molecules to the surface sliding speed is calculated by the equation:

$$(2) \quad \bar{v} = \sum_{i=1}^N \frac{|\bar{v}_i/v_s|}{N}$$

$\bar{v}_i$  is the streaming velocity (in the shear direction) of molecule  $i$  and  $v_s$  is the surface sliding velocity. A value of  $\bar{v}$  near unity means that the ZDDP molecules move at the same velocity as the surface which indicates that they are actually sticking to the surfaces. The time evolution of  $\bar{d}_c$  and  $\bar{v}$  for the simulation with the non-wetting oxide surface is given in Fig. 5.18.

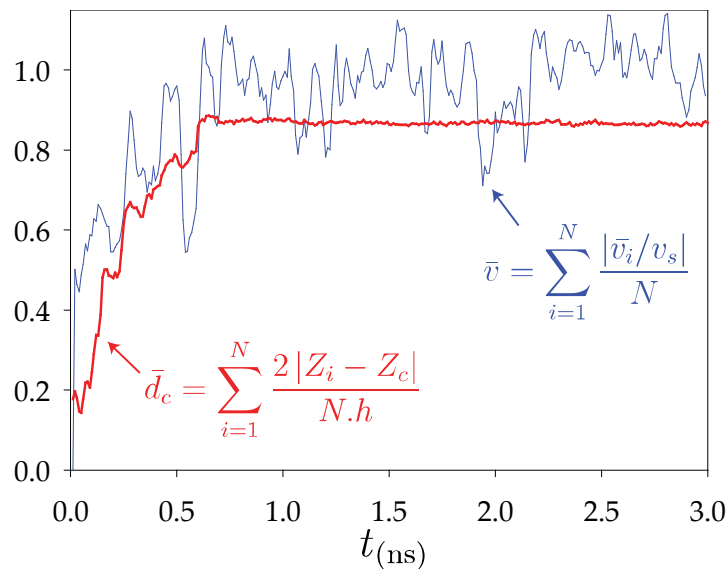


**Fig. 5.18:** Time evolution of: (1) the reduced average distance of the ZDDP molecules from the centre of the film and (2) the reduced average velocity  $\bar{v}$  of the ZDDP molecules with respect to the non-wetting surface sliding velocity  $v_s$ . A similar evolution was observed with the wetting surface.

In the initial state ( $t = 0$ ), the ZDDP molecules are in the center of the film. The reduced average distance from the centre of the film ( $\bar{d}_c$ ) is close to zero. The average streaming velocity in the center ( $\bar{v}$ ) is also close to zero. When the film is sheared, the additive molecules move toward the surface. This is quantified by  $\bar{d}_c$  which increases in time until it reaches a maximum value near unity after about  $0.7 - 0.8$  ns. The maximum is not exactly one because of the 3D shape of the ZDDP molecule and the repulsive part of the surface potential which keeps the molecules from penetrating the surfaces. As for the streaming velocity of the molecules, it increases as the molecules move closer to the surfaces. When all the ZDDP molecules reach the surfaces, they move at the surface sliding speed ( $t > 0.8$  ns). This is an indication that these molecules do not encounter boundary slip.

### 5.4.3 Effect on the boundary flow and friction

The velocity profiles across the hexadecane and hexadecane-ZDDP mixture films for the two surface models are given in Fig. 5.19. With the wetting surface, the velocity profiles are very close with and without ZDDP and no boundary slip is seen. In the case of ZDDP a slight locking can be observed which means that the adsorbed lubricant layer completely sticks to the surface and the shearing plane is displaced inside the film. In the case of non-wetting surfaces, the presence of ZDDP results in a significant attenuation of boundary slip compared to pure hexadecane lubricant case.

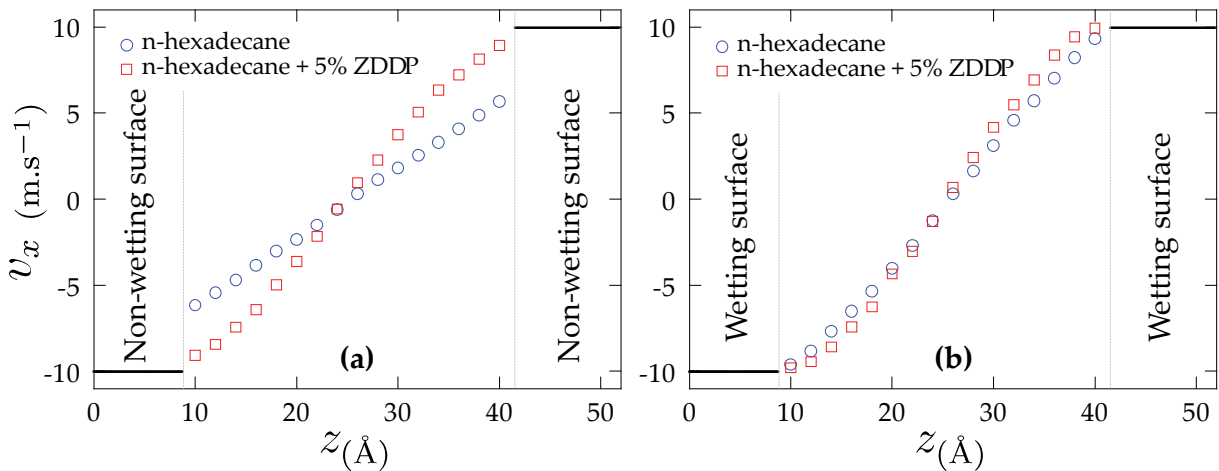


Fig. 5.19: Velocity profiles across pure hexadecane and hexadecane-ZDDP mixtures confined between two types of surfaces. The apparent shear rate in all simulations is  $6.88 \times 10^9 \text{ s}^{-1}$ .

The reduction of slip in this case is due to the ZDDP molecular migration described in the previous section. As the additive molecules move toward the surfaces and stick to them (Fig. 5.18), they enhance the effective molecular corrugation of the surfaces. This improves the momentum transfer across the hexadecane film.

As a result of the change in the boundary flow condition from slip to no slip with the non-wetting surface and slight locking with the wetting one, the presence of ZDDP influences the value of the average shear rate in the center of the film. The average shear rates are reported with the corresponding shear stresses in Table 5.5.

Film composition	Non-wetting surface		Wetting surface	
	$\dot{\gamma}$ ( $\times 10^9 \text{s}^{-1}$ )	$\tau_{xz}$ (MPa)	$\dot{\gamma}$ ( $\times 10^9 \text{s}^{-1}$ )	$\tau_{xz}$ (MPa)
100% n-hexadecane	4.30	93.6	8.18	118.3
95% n-hexadecane + 5% C4-ZDDP	8.26	115.7	9.31	126.1

**Table 5.5: Average shear rate and total shear stress for pure hexadecane and hexadecane-ZDDP mixture in 3nm confined films between wetting and non-wetting oxide surfaces.**

The simulation results with both wetting and non-wetting surfaces show that the addition of ZDDP results in an increase of friction. The high friction behavior of ZDDP seems to be more significant for non-wetting sliding surfaces. The adsorption of ZDDP molecules at the surfaces result in an attenuation of boundary slip, increased average shear in the confined film and consequently higher friction.

## Conclusion

As much as the surface properties influence the friction in molecularly confined films, the molecular nature of the lubricant film is also an important factor. In pure lubricant films, the effects of molecular chain length and branching on boundary flow and friction were explicitly considered. Lubricant mixtures of polar and non-polar nature were also studied in order to develop a realistic idea of how lubricants behave in confinement conditions. The operating conditions were unchanged in order to eliminate their influence in the simulations.

In pure confined lubricants, the increase of chain length and branching results in an attenuation of the layering phenomena. The structure of the film becomes bulk-like homogeneous in branched molecules at only three molecular diameters distance from the confining surfaces. Long and branched chains encounter an increased level of inter-layer bridging which results in a stronger internal lubricant cohesion. When no boundary slip occurs as in the case of wetting surfaces, molecular length and branching increase the friction because of the enhanced effective viscosity of the film. However near non-wetting surfaces, the internal film cohesion in long and branched chains may become stronger than their cohesion with the surfaces. This results in a larger boundary slip and an attenuation of friction in these films.

In lubricant mixtures of long and short saturated chains, the film becomes heterogeneous under shear. Long-chain molecules are located in high density layers near the bounding surfaces and the central part of the film remains occupied by shorter molecules. The central part of the film, mainly constituted of short molecules, presents a low flow resistance (viscosity). Although the heterogeneity of the film composition results in an attenuation of the slip near non-wetting surfaces, the apparent shear stress encountered in such mixtures remains lower than in pure long chain molecules.

Finally, commercial-like lubricant mixtures including hexadecane and ZDDP polar anti-wear additives were simulated in molecular lubrication conditions. In agreement with experiments, the presence of ZDDP resulted in a higher friction compared to pure hexadecane oil. It was found that the molecular migration and adsorption of ZDDP molecules at the surfaces

are the cause of this phenomenon. When ZDDPs stick to the non-wetting surfaces, they significantly reduce the boundary slip which normally occurs with pure hexadecane oil. Moreover in the case of wetting surfaces, the whole adsorbed layer becomes locked to the surfaces. This results in a global increase of the average shear rate in the middle of the film. The central hexadecane film becomes sheared at a higher rate giving rise to a higher shear stress and friction, in agreement with experimental findings.



# General conclusion and prospects

---

In this thesis, a numerical approach based on molecular dynamics simulations was developed in the purpose of investigating the local mechanisms of lubrication at nano-scales. The model elements were explicitly introduced and characterized in order to yield the most realistic material and interfacial behavior of the molecular system.

A particular attention was given to the methodology of heat dissipation in the simulations especially because of its relationship with friction. The mechanisms of energy transformation and dissipation in a confined film were thus studied in details. When the surfaces slide at moderate speeds, the total mechanical energy adsorbed by the lubricant and converted into heat is completely dissipated by the thermostat. As a result, the global temperature remains constant in the simulations. However, when a critical shear rate is surpassed, heating starts to occur and from this point an appropriate energetic dissipation method becomes necessary.

Advanced methods were compared in the heating regime and the results showed that if the surfaces are allowed to heat up, they accommodate more gently to the lubricant temperature increase. A novel method of applying the thermal boundary conditions was introduced for this purpose. The principle is that the outer surface temperature can be updated during simulation according to the heat flux coming from the confined contact.

The molecular model and the acquired knowledge on the thermal effects were put into application in order to study various molecular effects that give molecular lubrication its particularity.

First, the influence of the surface nature on friction was investigated. For this purpose, a novel procedure was developed for characterizing realistic surfaces with two parameters that represent adsorption and corrugation potentials. MD simulations showed that a given lubricant film, confined between five different surfaces, exhibits different structural and dynamic properties. Although lubricant layering is present with all surfaces, this phenomenon was more pronounced with surfaces characterized by a high adsorption potential. On the other hand, the simulations showed that in-plane variations of the surface interaction potential (corrugation) influence the lubricant boundary slip. Physically corrugated surfaces encountered a smaller slip than less corrugated ones. The lubricant resistance to surface sliding and shear, giving the contact friction, was shown to depend essentially on the flow condition at the boundary (wettability). In the case of surfaces with low corrugations (non-wetting surfaces), simulations showed that the lubricant slips at the surfaces and the confined film becomes effectively sheared at a lower rate than the apparent one. This results in a low friction.

Second, the influence of lubricant molecular structure on the lubrication properties were studied for both physically corrugated (wetting) and non-corrugated (non-wetting) surfaces. The considered effects were: the chain length, molecular branching, non-polar lubricant mixing, and polar lubricant mixing. The chain length was found to substantially influence the boundary slip in the simulations. Long molecules slipped more easily at solid interfaces. This

could be explained by the strong internal cohesion that was manifested by bridge formation between consecutive lubricant layers. Despite their higher viscosities, lubricant films constituted of long molecules did not show a significantly higher friction than shorter molecules for the case of non-wetting surfaces because of the boundary slip. On the other hand with wetting surfaces, since no lubricant slip took place friction naturally increased with the lubricant chain length due to their high viscosities. Molecular branching was found to have a similar consequence as chain length in molecular confinement. While branched molecules exhibited a larger friction than linear ones, they showed a larger slip near non-wetting surfaces due to their strong internal cohesion.

In lubricant mixtures of non-polar linear alkane molecules of different lengths, shearing caused a sort of molecular segregation to occur. The long chain molecules were attracted to the surfaces while shorter ones remained in the middle of the film. This heterogeneous structure had crucial effects on the flow properties and friction in the confined mixture. On one hand, slip was suppressed even for the case of non-wetting surfaces. On the other hand, the central part of the film was mainly constituted of short molecules with low viscosity. In consequence, the measured friction in the lubricant mixture was relatively low.

Finally, a model lubricant mixture including hexadecane as a base oil and ZDDP anti-wear additive was considered. The surface nature, lubricant composition, and simulation conditions were chosen to be representative of an industrial application. The MD simulations showed that the polar additive molecules were attracted to the surfaces where they finally got adsorbed. With non-wetting surfaces this caused a complete attenuation of boundary slip which resulted in an increase of the effective shear rate of the central hexadecane film. MD simulations showed that the measured friction was higher in the presence of ZDDP, as observed in reference experiments under similar conditions.

There are numerous opportunities to exploit the developed molecular dynamics model for investigating a wide selection of surface and lubricant structures. More extensive studies about the influence of lubricant molecular shape and polarity near realistic surfaces can be undertaken for generalizing the effects presented in this thesis. Moreover, by studying more surface models it could be interesting to find universal laws that relate boundary slip to the corrugation and adsorption potential from the molecular scale. Such laws could be integrated in large scale simulations as in continuum EHL to account for boundary slip which plays an important role at molecular scales.

Although the molecular effects presented in this thesis were given for a limited range of operating conditions, they could also be investigated under more severe conditions of surface sliding, loading pressure and confinement. For accessing these high shear regimes, the appropriate energetic dissipation methods developed in this thesis would form a strong basis.

It would also be interesting to investigate the effect of real surface (geometrical) roughness on the structure and dynamics of the confined lubricant. This would be complementary to the studied effects of physical corrugation in this thesis. In geometrically rough surfaces, the molecular model can be employed for investigating the conditions of local lubrication failure and provide insights for lubricant design dedicated for severe operating conditions as those encountered in the mixed lubrication regime.

<b>Appendix 1: Temperature- control Algorithms</b>	<b>118</b>
<b>A1.1 Introduction</b>	<b>118</b>
<b>A1.2 Thermostating algorithms</b>	<b>119</b>
A1.2.1 Velocity-rescaling	119
A1.2.2 Nosé-Hoover algorithm	119
A1.2.3 Langevin algorithm	121
<b>A1.3 Phantom-Molecules method</b>	<b>122</b>
A1.3.1 Scope of applicability	122
A1.3.2 Practical application	122
A1.3.2.1 Primary-Phantom atoms interactions	123
A1.3.2.2 Phantom-Fixed atoms interactions	125

# Appendix 1: Temperature-control Algorithms

---

## A1.1 Introduction

Classical molecular dynamics involves solving Newton's equations of motion on a system of molecules interacting with purely conservative forces [41]. Classical MD thus produces system configurations in the NVE (micro-canonical) thermodynamic ensemble where the total number of molecules, the volume, and the total energy are constant. Unfortunately, the experimental conditions often involve constant temperature rather than constant energy conditions. In order to control the temperature in MD simulations, several algorithms have been developed which vary in their level of simplicity of application and statistical thermodynamic significance and accuracy [41, 111].

In the first part of this appendix, three thermostating algorithms classically used to control the temperature in MD simulations are presented. These are the direct velocity-rescaling, Nosé-Hoover, and the Langevin algorithms. In the second part of this appendix, the Phantom Molecules thermostating method which allows modeling an infinitely large thermostated solid is introduced and general guidelines of its application for modeling realistic crystalline surfaces are presented.

However, before getting into the details of these methods, it is important to define the notion of temperature in MD simulations. The experimental (equilibrium) temperature is actually the time average of an "instantaneous" temperature often referred to as the kinetic temperature because it is closely related to the total atomic kinetic energy by thermal vibrations ( $E_k$ ). The kinetic temperature at any instant ( $T(t)$ ) can be given in general with the formula:

$$(A1.1) \quad E_k = \sum_{i=1}^N \frac{|p_i|^2}{2m_i} = \frac{k_B T(t)}{2} (3N - N_c)$$

In this equation,  $N$  is the number of atoms.  $p_i$  and  $m_i$  represent the linear momentum and mass of atom "i".  $N_c$  is the number of constraints and  $(3N - N_c)$  is thus the number of degrees of freedom.  $k_B$  is the Boltzmann constant.

In order to control this kinetic temperature ( $T(t)$ ), various algorithms have been developed. They are presented in the next section. In the last section of this appendix, the "Phantom Molecules" method for solid surfaces thermostating is explained in details.

## A1.2 Thermostating algorithms

The oldest and simplest way is the velocity-rescaling algorithm. More details about this method are given in the next section, followed by the two other algorithms: Nosé-Hoover and Langevin thermostats.

### A1.2.1 Velocity-rescaling

The velocity-rescaling method is the simplest method of temperature control. It is based on scaling the atomic velocities of the thermostated group at regular time intervals in order to give a global kinetic temperature  $T(t)$  equal to the target one ( $T_t$ ) [41]. Note that all the atomic velocities are multiplied by the same factor  $\tilde{\lambda}$ . By doing so, the kinetic temperature (Eq. A1.1) is multiplied by a factor of  $\tilde{\lambda}^2$ .

Thus the rescaling factor is exponentially proportional to the ratio of the instantaneous kinetic temperature  $T(t)$  (Eq.(A1.1)) and the target temperature  $T_t$ .

$$(A1.2) \quad \tilde{\lambda} = \sqrt{\frac{T(t)}{T_t}}$$

The kinetic energy dissipated (or added) by the thermostat is equal to:

$$(A1.3) \quad \Delta E = E_k(\tilde{\lambda}^2 - 1)$$

Where  $E_k$  is the total thermal kinetic energy of atoms from the thermostated group as given in Eq. (A1.1).

In this method, all atomic velocities are rescaled with the same factor. Heat is thus removed in a homogeneous manner from all atoms even if some atoms are “hotter” than others. One example for this is a thermostated group of atoms to a temperature  $T_t$  using a velocity rescaling algorithm where only one side of the group is in contact with a heat source. In this case, the atoms near the heat source will exhibit a larger kinetic energy (and temperature) than those on the other side. But rescaling all atomic velocities, the atoms near the heat source would have a higher temperature than the target ( $T_t$ ) and those on the other side would have a lower temperature than  $T_t$ . Thus, a temperature gradient may develop in some cases with the velocity-rescaling algorithm.

The velocity-rescaling algorithm moreover controls the temperature in a “brutal” way. The temperature doesn’t fluctuate as it should in the NVT (canonical) thermodynamic ensemble. The extended system method, originally presented by Nosé and developed by Hoover, is capable of probing a correct canonical ensemble. The details about this method are given in the next section.

### A1.2.2 Nosé-Hoover algorithm

The idea of the Nosé-Hoover thermostat is to consider the external heat bath to be an integral part of an extended system [41, 111]. The extended system contains the real molecules and the heat bath. The coupling between the two is accomplished by adding an artificial degree

of freedom ( $\tilde{s}$ ) with an artificial thermal inertia ( $Q_b$ ) and velocity ( $\dot{\tilde{s}}$ ). The magnitude of  $Q_b$  determines the coupling between the real system and the heat bath. The artificial variable ( $\tilde{s}$ ) is a time scaling parameter. The time ( $d\tilde{t}$ ) in the extended system (= real system + artificial heat bath) is stretched by the factor of  $\tilde{s}$ :

$$(A1.4) \quad d\tilde{t} = \tilde{s}dt$$

The coordinates ( $r$  and  $s$ ) are identical in the real and the extended systems but the velocities depend on  $\tilde{s}$  according to:

$$(A1.5) \quad \dot{\tilde{r}} = \frac{\dot{r}}{\tilde{s}} \quad \dot{\tilde{s}} = \frac{\dot{s}}{\tilde{s}}$$

The Nosé equations of motion in the extended system can be written as:

$$(A1.6) \quad \ddot{\tilde{r}}_i = \frac{\tilde{F}_i}{m_i \tilde{s}^2} - \frac{2\dot{\tilde{s}}\dot{\tilde{r}}_i}{\tilde{s}}$$

$$(A1.7) \quad \ddot{\tilde{s}} = \frac{1}{Q_b \tilde{s}} \left( \sum_i m_i \tilde{s}^2 \dot{\tilde{r}}_i^2 - (N_{dof} + 1)k_B T_0 \right)$$

In this equation,  $N_{dof}$  is the number of degrees of freedom which depend on the molecular constraints employed in the system. The Nosé equations of motion can also be reformulated in terms of the real system variables by substituting  $\gamma = \dot{s}/s$ :

$$(A1.8) \quad \ddot{r}_i = \frac{F_i}{m_i} - \gamma r_i$$

$$(A1.9) \quad \dot{\gamma} = \frac{-k_B N_{dof}}{Q_b} T(t) \left( \frac{N_{dof} + 1}{N_{dof}} \frac{T_0}{T(t)} - 1 \right)$$

The choice of  $Q_b$  defines the level of coupling between the real system and the heat bath. If  $Q_b$  is very large ( $Q_b \mapsto \infty$ ), the coupling is very weak and very little energy is exchanged between the two systems. The Nosé equations (A1.6 and A1.7) then generate micro-canonical NVE ensemble trajectories. If  $Q_b$  is very small, a tight coupling is used and high frequency temperature oscillations may occur. A more intuitive choice for the numerical parameters is through the relaxation time ( $\tau_{NH}$ ) which can be defined as [111]:

$$(A1.10) \quad \tau_{NH} = \sqrt{\frac{Q_b}{k_B N_{dof} T_0}}$$

Eq. (A1.9) becomes:

$$(A1.11) \quad \dot{\gamma} = \frac{-1}{\tau_{NH}^2} \frac{T(t)}{T_0} \left( \frac{N_{dof} + 1}{N_{dof}} \frac{T_0}{T(t)} - 1 \right)$$

$\tau_{NH}$  has time units and is roughly the time needed for temperature relaxation in the system. Exponentially proportional to  $Q_b$ , when a large relaxation time ( $\tau_{NH}$ ) is chosen the heat is transferred very slowly between the real system and the heat bath. With small relaxation times the transfer occurs more rapidly. The choice of  $\tau_{NH}$  is done by trial and error. In practice for molecular systems, a value around 100fs usually insures that the canonical thermodynamic integration is correct.

In comparison with the velocity-rescaling algorithm, here the temperature evolves more smoothly and the system trajectory can be proven to belong to a canonical NVT thermodynamic ensemble. The two methods have a point in common as the heat transfer depends on the ratio of the instantaneous kinetic temperature  $T(t)$  to the target one ( $T_t$ ). Both of which

are global to the system. Thus local temperature differences may be found in systems with non-homogeneous conditions.

There are several other algorithms that are based either on the classical velocity-rescaling or the Nosé-Hoover extended system methods. More details about thermostating methods can be found in refs.[41, 111]. In what follows, the Langevin thermostating method is presented. This method has the particularity of transferring heat independently for each atom in the thermostated group. This allows temperature gradients in non-homogeneous systems to be avoided. More details about the method are given in the next section.

### A1.2.3 Langevin algorithm

The Langevin thermostating algorithm uses Brownian dynamics to solve the many-particle 3D Langevin equations [112]. The equations of motions are modified to include a friction and a random force that act on each atom in the thermostated group. The friction force represents the drag acting on the atom due to its surrounding medium. The random force corresponds to collisions occurring between the atom and heat bath atoms at a constant temperature. The differential equations of motion thus include in addition to the conservative intermolecular force ( $F_c$ ), a friction force ( $F_f$ ) and a random force ( $F_r$ ) as follows:

$$(A1.12) \quad \ddot{\mathbf{r}}_i = \frac{\mathbf{F}_t}{m_i}$$

$$(A1.13) \quad \mathbf{F}_t = \mathbf{F}_c + \mathbf{F}_f + \mathbf{F}_r$$

The friction force acting on each atom is proportional to the atomic velocity. It is given as:

$$(A1.14) \quad \mathbf{F}_f = \left( \frac{m_i}{\tau_L} \right) \dot{\mathbf{r}}_i$$

$\tau_L$  is a damping parameter in time units. It represents roughly the temperature relaxation time. The random force corresponding to the heat bath atoms bumping into the real atoms is given according to the fluctuation-dissipation theorem to be proportional to:

$$(A1.15) \quad \mathbf{F}_r \propto \sqrt{\frac{k_B T_0}{dt} \frac{m_i}{\tau_L}}$$

The importance of this method is that it treats each atom in the thermostated group individually. Thus no matter what conditions are present in the system, the Langevin algorithm would remove heat locally from where it is needed. As a result, no temperature gradient may develop in a system thermostated by a Langevin algorithm.

These three thermostating algorithms can be used to control the temperature in homogeneous systems of solids, liquids, and gases. In the next section, an advanced method is presented which, unlike the previous algorithms that perform global thermostating, is used for thermostating solid surfaces in problems that involve solid-liquid or solid-gas interfaces.

## A1.3 Phantom-Molecules method

The Phantom-Molecules method was originally proposed by Tully in 1980 [113], and it was originally referred to as the “ghost atom technique”. This method is in fact simply a computationally feasible solution to the 3D-GLE (Generalized Langevin Equations) developed initially by Zwanzig, Mori, and Kubo and then formulated for a three dimensional system by Tully himself. As was shown in the previous section, The Langevin equations propose that the interactions of an atom with an infinitely large heat bath can be accounted for by adding random force and friction terms to the atomic equations of motion. This allows reducing the number of atoms needed to be considered explicitly in the constant-temperature simulations. However, the exact determination of the parameters for the random force and friction terms on each atom remains complicated.

In the Phantom-Molecules method, the modeled system is limited to atoms that are in “real action” (usually called the primary atoms, see Fig. A1.1). Unlike the classical Langevin method where per atom friction and random forces are added, in the Phantom-Molecules method no external forces acting on the primary atoms are used. However, a number of “ghost” atoms are added directly in the simulations. The special motions and interactions between the “ghost” atoms and the primary atoms produce the exact same effect as the Langevin friction and random terms.

The interest in using the Phantom-Molecules method is that it can be parameterized according to experimental data about surface vibrational properties. The Debye frequency (representing the maximum vibration frequency possible for a given lattice) is used for choosing the parameters for this temperature control model.

Moreover, the model size reduction does not affect the heat capacity and conduction properties of the infinitely large thermostated surface. The premier application of this technique by Tully was for gas desorption on solid surfaces. The technique allowed simulating a few number of atoms of the solid surface in the area where the gas impact was probable (primary lattice atoms) where the whole remaining part of the solid surfaces was represented by only a few ghost atoms.

### A1.3.1 Scope of applicability

This method of temperature control is uniquely applicable for solid surfaces with regular crystalline atomic structure [113]. This method has only been applied for mono-atomic FCC [113, 99] or BCC crystal structures [113]. Nevertheless, this method was shown to be flexible enough to be applied not only for harmonic but also Lennard-Jones bounded surface atoms [114].

### A1.3.2 Practical application

The Phantom-Molecules method is used to model mono-directional heat conduction in an infinitely thick solid surface by only simulating a limited number of atoms. As explained by

Blomer et al. [114] and Maruyama et al. [99], the application of this method involves the addition of two imaginary atomic layers perpendicular to heat transfer direction. As shown in Fig. A1.1, the first layer from the side of the primary atoms is the phantom molecules layer. The second is a fixed layer. The fixed layer must be exactly at the lattice equilibrium position of the primary atoms layer which is directly interacting with the phantom molecules. The phantom molecules layer is initially in the same position but is excited by a random force and a friction term during the course of the simulation as will be demonstrated later on.

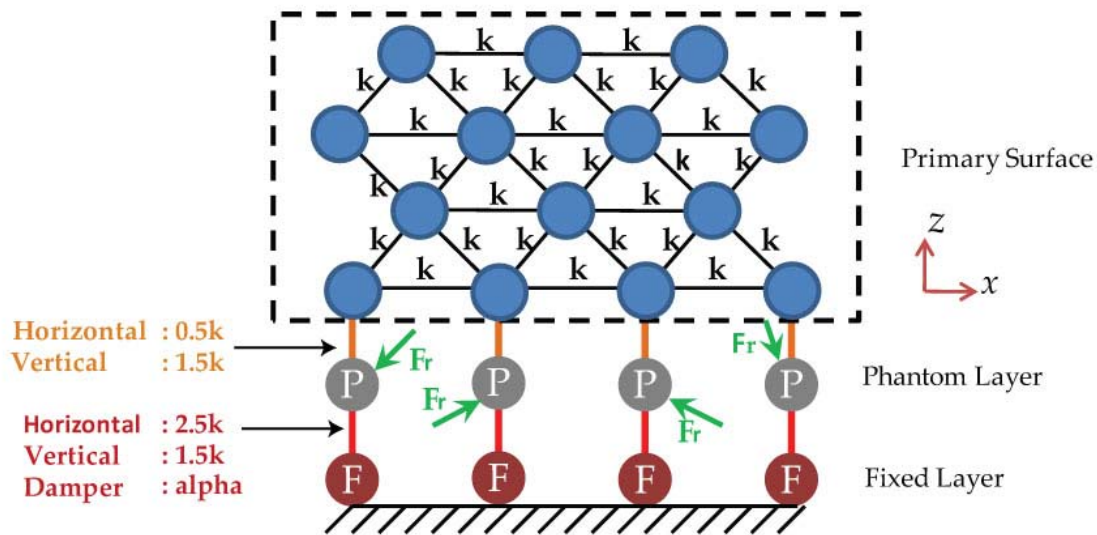


Fig. A1.1: 2D schematic showing how the ghost atoms in the phantom and fixed layers are used to replace an infinite number of atoms at constant temperature. This is possible using particular positioning of the ghost atoms and special interactions between each other and with the atoms of the primary surface.

### A1.3.2.1 Primary-Phantom atoms interactions

All interactions between the primary and phantom atoms (in both the phantom and fixed layers) must be of the same nature as those between the primary atoms. For example if the primary atoms are connected by harmonic springs, then harmonic springs must be used between the primary and the phantom atoms, and between the phantom and the fixed atoms, although some characteristics of the springs can be different as will be explained later.

The initial positions of the phantom layer atoms are chosen to be exact projections of the primary layer on the  $Z$ -plane of the phantom layer. The initial  $Z$ -coordinate of the phantom layer is of no significance (this will be proven later) because of the special nature the springs connecting the primary and phantom atoms.

The interactions between the primary and phantom layer atoms should be sufficient to account for all interactions that this atom would have had with an imaginary second layer of the non-modeled solid. As a demonstration example, consider the 2D atomic system shown in Fig. A1.2. Atom (1) belongs to the furthest layer of the primary surface where the introduction of the phantom atoms is required. By imagining that the solid extends to infinity, this atom would have interacted with 6 atoms (2-7), including two atoms (6 and 7) that belong to an imaginary layer, neither the primary surface nor the phantom layer. The principle

is that the phantom atom to be introduced thereafter (atom (P)) should interact with atom (1) identically to the sum of interactions of atoms (6) and (7).

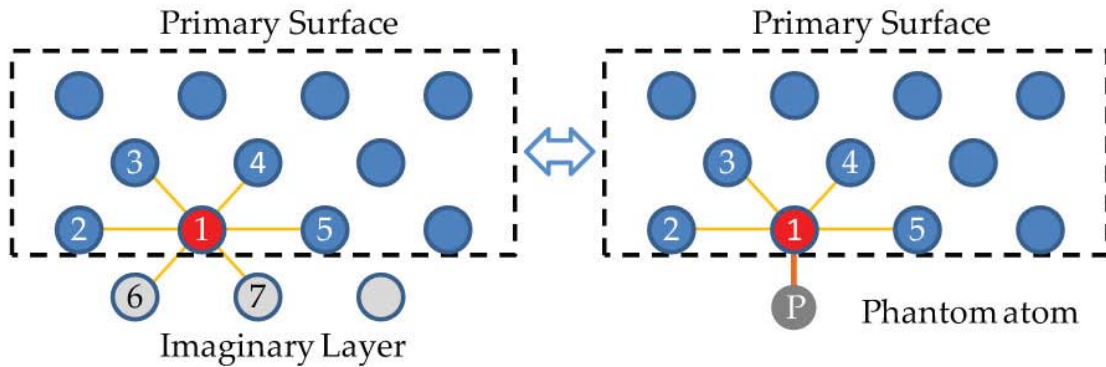


Fig. A1.2: An example showing the calculation method of the interactions between the primary atoms and the phantom layer atoms.

Assuming for this example that all bonds have the same length ( $a$ ). The procedure is as follows. Atoms (1), (6), and (7) are isolated as shown in Fig. A1.3. When atom (1) is displaced by a small  $dz$  ( $dz \ll a$ ) on the  $z$ -direction, it will no longer be in equilibrium with its surroundings. Atoms (6) and (7) will exert two forces along the bond direction. These two forces will have a magnitude of  $k(a + dr)$  where  $dr$  is the extension in the bond length from the equilibrium position.

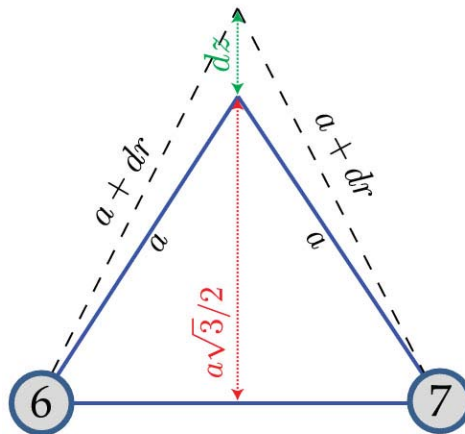


Fig. A1.3: The primary atom (1) is displaced by  $dz$  in order to determine the  $z$ -component of the equivalent special spring to be used with the phantom atom (P) that will replace atoms 6 and 7.

The sum of the forces acting from atoms (6) and (7) on atom (1) from its displacement by  $dz$  in this case is equal to  $\frac{3}{2}k dz \vec{e}_3$ . A vertical spring of  $\frac{3}{2}k$  stiffness is thus chosen in order to replace the effects of the two imaginary atoms on the primary atom of the surface. The same analysis with a small  $dx$  displacement of atom (1) gives an equivalent horizontal spring of a  $\frac{k}{2}$  stiffness.

### A1.3.2.2 Phantom-Fixed atoms interactions

The interactions between the atoms in the phantom and fixed layers are calculated in a similar manner to the preceding ones between the primary and phantom layer atoms. The horizontal and vertical springs acting between the primary and phantom layer atoms have already been characterized. However, as shown in Fig. A1.4, for a given atom (P) in the phantom layer, interactions with atoms from the same layer as well as from a lower imaginary layer need also to be taken into consideration.

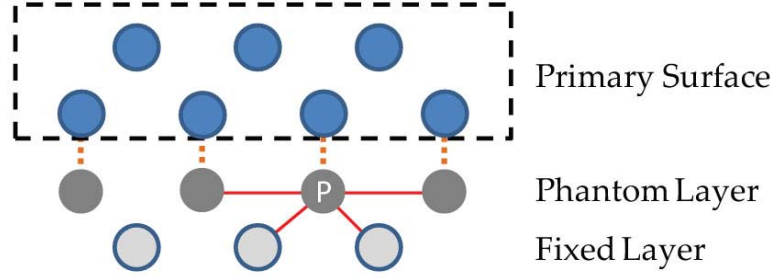


Fig. A1.4: An example showing the calculation method of the interactions between the phantom and the fixed layer atoms.

Exactly as done previously, the phantom layer atom (P) is moved with small displacements in the  $x$  and  $z$  directions (as well as the  $y$  direction in case of 3D lattices). The parameters of the horizontal and vertical springs can thus be calculated. In this example, horizontal and vertical spring stiffness of  $\frac{5k}{2}$  and  $\frac{3k}{2}$  respectively are used to replace all of the interactions that a phantom layer atom exhibits in the real lattice system.

The molecular system can finally be constructed with the Phantom-Molecules method in the 2D example by using horizontal ( $x$ ) springs of  $\frac{k}{2}$  and vertical springs of  $\frac{3k}{2}$  between the primary surface and phantom layer atoms. Moreover, horizontal springs of  $\frac{5k}{2}$  and vertical springs of  $\frac{3k}{2}$  are used between the phantom layer and the fixed layer atoms (Fig. A1.1).

All of these forces are conservative. However, additional friction terms need to be used in the interactions between the phantom layer and the fixed layer atoms. According to Tully [113], the friction terms can be chosen as independent for each phantom atom (meaning no dampers between phantom atoms) but have a damping coefficient ( $\alpha_d$ ) of:

$$(A1.16) \quad \alpha_d = m \frac{\pi}{6} \omega_B$$

$m$  is the mass of one surface atom, and  $\omega_B$  is the bulk Debye frequency (in  $rd/s$ ) for the surface. In case the Debye frequency information is absent, it can be calculated from the Debye temperature ( $\theta_d$ ) according to:

$$(A1.17) \quad \omega_B = \frac{k_B \theta_d}{\hbar}$$

In this equation,  $k_B$  and  $\hbar$  are Boltzmann and Planck's angular constants. The phantom layer atoms are finally excited by a random Gaussian force ( $F_r$ ) of a standard deviation of:

$$(A1.18) \quad \sigma_{F_r} = \sqrt{\frac{2\alpha_d k_B T_0}{dt}}$$

$T_0$  is the temperature of the infinitely thick surface and  $dt$  is the MD integration time step. This choice for the random force allows the fluctuation-dissipation theorem to be accomplished for totally uncorrelated random forces [114].

<b>Appendix 2: Heat Conduction in a Semi-infinite Solid with a Constant Boundary Flux</b>	<b>128</b>
<b>A2.1 Introduction</b>	<b>128</b>
<b>A2.2 1-D Heat conduction with constant boundary flux</b>	<b>128</b>
A2.2.1 Integration	129
A2.2.2 Time evolution of the wall temperature	130
<b>A.2.3 Discrete formulation of the boundary temperature change with flux</b>	<b>130</b>

# Appendix 2: Heat Conduction in a Semi-infinite Solid with a Constant Boundary Flux

---

## A2.1 Introduction

In simulations of confined lubricant shear, a viscous heat flux is generated and can be measured. The purpose of this section is to find an exact (analytical) formula giving the surface temperature ( $T_w$ ) evolution as a function of the dissipated heat flux ( $\phi_w$ ).

Each surface is supposed to be equivalent to a semi-infinite solid whose infinite end is at a constant (ambient) temperature ( $T_\infty$ ) as shown in Fig. A2.1. The finite end (wall) is that at the lubricant interface at which the heat flux is considered to be known.

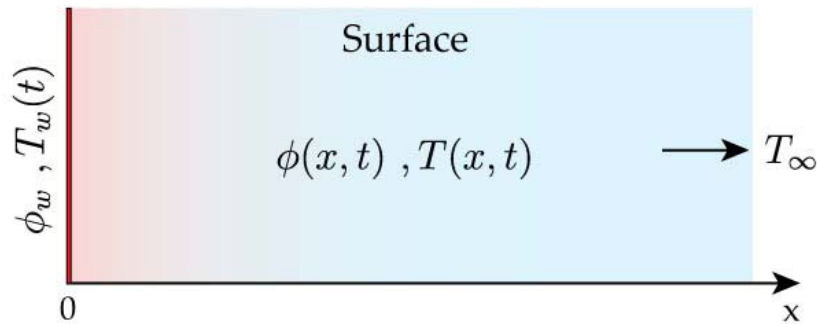


Fig. A2.1: A schematic of the mono-directional heat conduction problem solved in a semi-infinite solid representing the solid surfaces.  $\phi_w$  and  $T_w$  represent the heat flux at the surface and the wall temperature respectively.  $T_\infty$  is the ambient temperature (far away from the surface/lubricant interface).

## A2.2 1-D Heat conduction with constant boundary flux

The mono-directional heat conduction differential equation in a solid of thermal diffusivity  $\alpha$  and no internal heat generation is given as:

$$(A2.1) \quad \frac{\partial^2 T}{\partial x^2}(x, t) - \frac{1}{\alpha} \frac{\partial T}{\partial t}(x, t) = 0$$

The initial and boundary conditions from Fig. A2.1 can be translated in mathematical terms to:

$$(A2.2) \quad \begin{aligned} \frac{\partial T}{\partial x}(x=0, t > 0) &= -\frac{\phi_w}{\lambda} \\ T(x \rightarrow \infty, t) &= T_\infty \\ T(x, t=0) &= T_0 \end{aligned}$$

$\lambda$  is the thermal conductivity of the solid.  $T_\infty$  is the ambient temperature and  $T_0$  is the initial temperature of the solid.

## A2.2.1 Integration

The standard solving method of Eq.(3.5), by temperature decomposition into transient and steady state terms, does not work in this case since there is no steady state temperature distribution. However, an alternative is by using Fourier's equation for mono-directional heat conduction for rewriting Eq.(3.5) in terms of the heat flux ( $\phi$ ): [98]

$$(A2.3) \quad \frac{\partial^2 \phi}{\partial x^2}(x, t) - \frac{1}{\alpha} \frac{\partial \phi}{\partial t}(x, t) = 0$$

The initial and boundary conditions from Eqs.(A2.2) give for the heat flux:

$$(A2.4) \quad \begin{aligned} \phi(x=0, t > 0) &= \phi_w \\ \phi(x \rightarrow \infty, t) &= 0 \\ \phi(x, t=0) &= 0 \end{aligned}$$

By defining the two variables  $a$  and  $b$ :

$$(A2.5) \quad a = \frac{\phi_w - \phi}{\phi_w} \text{ and } b = \frac{x}{\sqrt{\alpha t}}$$

Eq.(A2.3) becomes:

$$(A2.6) \quad \frac{\partial^2 a}{\partial b^2} + \frac{b}{2} \frac{\partial a}{\partial b} = 0$$

The initial and boundary conditions translate to:

$$(A2.7) \quad a(0) = 0 \text{ and } a(\infty) = 1$$

Considering  $U = \partial a / \partial b$ , Eq.(A2.6) becomes:

$$(A2.8) \quad \frac{\partial U}{\partial b} = \frac{-b}{2} U \Rightarrow U(b) = e^{-(\frac{b}{2})^2}$$

$$(A2.9) \quad a = C \int_0^b e^{-(\frac{m}{2})^2} dm + a(0) = 2C \int_0^{b/2} e^{-(\frac{m}{2})^2} d(\frac{m}{2}) = \frac{C}{\sqrt{\pi}} \operatorname{erf}\left(\frac{b}{2}\right)$$

Since  $\operatorname{erf}(\infty) = 1$ , then the second boundary condition from Eq.(A2.7) gives  $C = \sqrt{\pi}$

Hence:

$$(A2.10) \quad a = \operatorname{erf}\left(\frac{b}{2}\right)$$

Considering Eq.(A2.5), the heat flux can be written as:

$$(A2.11) \quad \phi(x, t) = \phi_w \left(1 - \operatorname{erf}\left(\frac{x}{2\sqrt{\alpha t}}\right)\right) = \phi_w \operatorname{erfc}\left(\frac{x}{2\sqrt{\alpha t}}\right)$$

## A2.2.2 Time evolution of the wall temperature

According to Fourier's conduction law, Eq.(A2.11) gives for the temperature:

$$(A2.12) \quad \frac{\partial T}{\partial x}(x, t) = -\frac{\phi_w}{\lambda} \operatorname{erfc}\left(\frac{x}{2\sqrt{\alpha t}}\right)$$

Integrating Eq.(A2.12) with respect to  $x$  from 0 to  $\infty$ :

$$(A2.13) \quad T_\infty - T_w(t) = -\frac{\phi_w}{\lambda} \int_0^\infty \operatorname{erfc}\left(\frac{x}{2\sqrt{\alpha t}}\right) dx$$

Since  $\int_0^\infty \operatorname{erfc}(m) dm = 1/\sqrt{\pi}$ , then:

$$(A2.14) \quad T_\infty - T_w(t) = -\frac{2\phi_w}{\lambda} \sqrt{\frac{\alpha t}{\pi}}$$

Finally:

$$(A2.15) \quad T_w(t) = T_\infty + \frac{2\phi_w}{\lambda} \sqrt{\frac{\alpha t}{\pi}}$$

This equation shows that if a constant flux is imposed on one side of a semi-infinite body, the boundary temperature increases endlessly. This equation will be used to update the boundary temperature with the generated flux from the contact. However, the heat flux may change when the boundary temperature is modified. In the next section, a time discrete formulation for updating the wall temperature as a function of the boundary flux is presented.

## A.2.3 Discrete formulation of the boundary temperature change with flux

The definite derivative of the wall temperature with time from Eq.(A2.15) gives:

$$(A2.16) \quad \frac{dT_w}{dt} = \frac{\partial T_w}{\partial t} + \frac{\partial T_w}{\partial \phi_w} \frac{\partial \phi_w}{\partial t}$$

At an instant  $t_0$ , the variation of the wall temperature and the heat flux with time over a small time period  $\Delta t$  is approximated as:

$$(A2.17) \quad \frac{dT_w}{dt} = \frac{\Delta T_w}{\Delta t} \quad \text{and} \quad \frac{\partial \phi_w}{\partial t} = \frac{\Delta \phi_w}{\Delta t}$$

Eq.(A2.16) can thus be written in the following discrete forms:

$$(A2.18) \quad \Delta T_w = \frac{\phi_w \Delta t}{\lambda} \sqrt{\frac{\alpha}{\pi t}} + \frac{2\Delta \phi_w}{\lambda} \sqrt{\frac{\alpha t}{\pi}}$$

$$(A2.19) \quad \Delta T_w = \frac{2\phi_w}{\lambda} \sqrt{\frac{\alpha t}{\pi}} \left( \frac{1}{2} \frac{\Delta t}{t} + \frac{\Delta \phi_w}{\phi_w} \right)$$

<b>Appendix 3: Calculation methods of macroscopic quantities from microscopic data</b>	<b>132</b>
<b>Introduction</b>	<b>132</b>
<b>A3.1 Characteristic profiles</b>	<b>132</b>
A3.1.1 Lubricant density profile	132
A3.1.2 Lubricant velocity profile	133
A3.1.3 Lubricant temperature profile	134
<b>A3.2 Time-variable quantities</b>	<b>134</b>
A3.2.1 Lubricant film thickness	134
A3.2.2 Lubricant density	135
A3.2.3 Apparent shear rate	135
A3.2.4 Apparent shear stress	135
A3.2.4 Lubricant temperature	136
<b>A3.3 Deduced quantities</b>	<b>136</b>
A3.3.1 Effective shear rate	136
A3.3.2 Effective viscosity	136

# Appendix 3: Calculation methods of macroscopic quantities from microscopic data

---

## Introduction

Molecular Dynamics simulations generate the atomic trajectories of a molecular system. At each time step, the atomic positions, velocities, and accelerations are known and represent the bulk output of MD simulations. Statistical mechanics provides the necessary tools for relating the microscopic information to macroscopic variables of interest.

In this appendix, the calculation methods of the macroscopic variables and fields from atomic velocities and positions are presented. These variables are grouped into three sections: profiles, time-variables, and deduced quantities. Profiles such as density, velocity, and temperature are time averages of spatially defined fields. Time-variables are system properties whose variation with time is regarded. Deduced quantities are obviously calculated from the profiles and time variables: for example the average shear rate in the central part of the film and the effective film viscosity.

## A3.1 Characteristic profiles

Characteristic density, velocity, and temperature profiles are determined in layers normal to the film thickness. Spatial averaging is performed inside each layer in order to determine the instantaneous profiles and then time averaging is performed during 5ns in the shearing steady state to determine the average characteristic profiles in the confined lubricant films.

### A3.1.1 Lubricant density profile

In order to determine the mass density profile, the confined film volume is cut, along the film thickness direction, into thin layers of  $1\text{\AA}$  thickness ( $\delta$ ) parallel to the surface sliding direction as shown in Fig. A3.1. At each time step and in each layer, the masses of all lubricant atoms that lie within the layer ( $m_i$ ) are summed up and then divided by the elementary volume of each layer ( $\delta \times S$ ) giving the instantaneous mass density profile.  $S$  is the surface area.

The obtained profile is then averaged over the sampling duration which follows the shearing steady state.

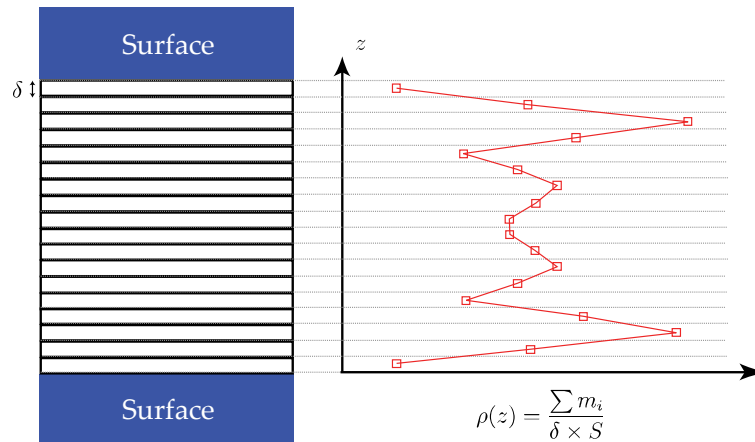


Fig. A3.1: Illustration of the calculation method of the lubricant density profile.

### A3.1.2 Lubricant velocity profile

In the molecular lubrication model, the lubricant molecules are grouped in layers according to the surface interactions. In a previous work [115], local thermodynamic equilibrium was shown to exist inside these molecular layers. Moreover, it was shown that proper kinetic energy decomposition into shear flow and peculiar thermal components for each layer can be obtained from flow velocities calculated as the layer total linear momentum divided by the layer total mass, rather than the conventional methods by simple averaging of atomic velocities by the number of atoms [115].

The instantaneous velocity profile is thus determined in  $2\text{\AA}$  thick layers as the total layer linear momentum on the surface sliding direction divided by the layer mass as shown in Fig. A3.2.

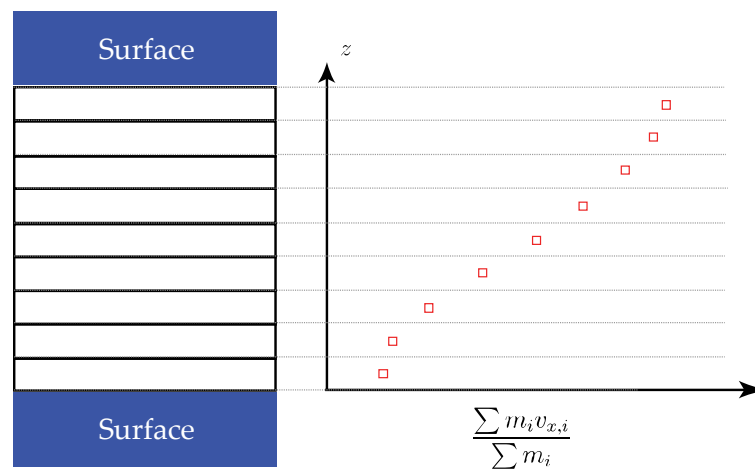


Fig. A3.2: Illustration of the calculation method of the lubricant velocity profile.

### A3.1.3 Lubricant temperature profile

The Hybrid Diffusion method, as described in ref.[115], is used to decompose atomic velocities into shear flow and peculiar thermal terms in each molecular layer. The peculiar velocities are used for calculating the kinetic layer temperatures. The time average of the kinetic temperatures during the steady state is reported in each layer to yield the lubricant temperature profile as shown in Fig. A3.3.

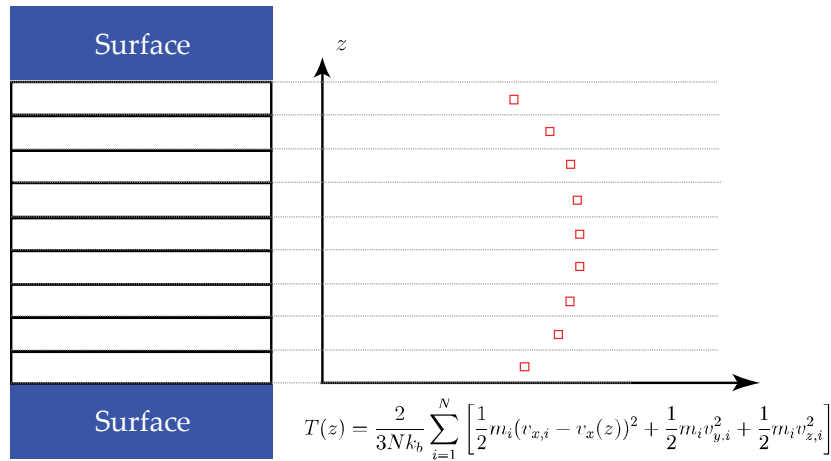


Fig. A3.3: Illustration of the calculation method of the lubricant temperature profile according to the Hybrid Diffusion approach [115].

## A3.2 Time-variable quantities

The time-variable quantities defined in this section are system properties whose instantaneous values can be significant without necessary averaging. For example, the film thickness, lubricant density, and apparent shear rate are quantities that can be defined at each instant. Nevertheless, in MD simulations these quantities are often reported as averages during the sampling period which extends over 5ns during the shearing steady state.

### A3.2.1 Lubricant film thickness

The procedure for calculating the film thickness ( $h$ ) is presented in Fig. A3.4. Near each surface, a central plane is positioned at the center distance between the two lubricant and surface atoms that are closest to one another. The instantaneous film thickness is then defined as the absolute distance between the central planes from each of the two surfaces.

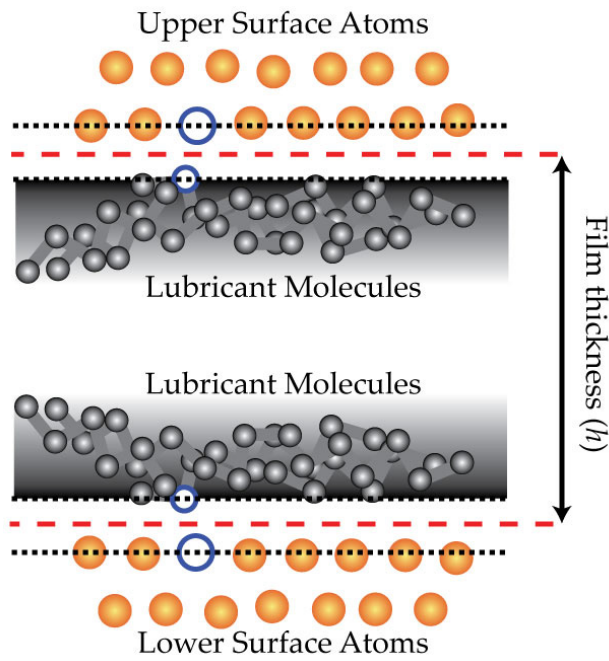


Fig. A3.4: Illustration of the calculation method of the lubricant film thickness.

### A3.2.2 Lubricant density

The lubricant density ( $\rho$ ) is defined as the total mass of lubricant molecules divided by the volume of the film. The volume is determined as the surface area multiplied by the lubricant film thickness as defined in Fig. A3.4:

$$(A3.1) \quad \rho = \frac{\sum m_i}{h \times S}$$

### A3.2.3 Apparent shear rate

The apparent shear rate ( $\dot{\gamma}_{\text{app}}$ ) is determined as the velocity difference between the surfaces ( $\Delta U$ ) divided by the lubricant film thickness ( $h$ ):

$$(A3.2) \quad \dot{\gamma}_{\text{app}} = \frac{\Delta U}{h}$$

### A3.2.4 Apparent shear stress

The apparent shear stress ( $\tau_{xz}$ ) is determined as the sum of all elementary forces in the surface sliding direction, opposing the constant speed motion of the surfaces, divided by the surface area:

$$(A3.3) \quad \tau_{xz} = \frac{\sum f_{x,i}}{S}$$

### A3.2.4 Lubricant temperature

In molecular lubrication problems, lubricant molecules belonging to different layers exhibit different streaming velocities. In order to calculate an average (global) film temperature, the velocities perpendicular to the surface sliding directions are only considered. The lubricant temperature is defined according to the equation:

$$(A3.4) \quad T(t) = \frac{1}{Nk_b} \sum_{i=1}^N \left[ \frac{1}{2} m_i v_{y,i}^2 + \frac{1}{2} m_i v_{z,i}^2 \right]$$

## A3.3 Deduced quantities

### A3.3.1 Effective shear rate

The lubricant velocity profile corresponding to all layers except the two that are adjacent to the surfaces is fitted to a linear regression function as shown in Fig. A3.5. The slope of this line represents the effective shear rate in the central part of the film.

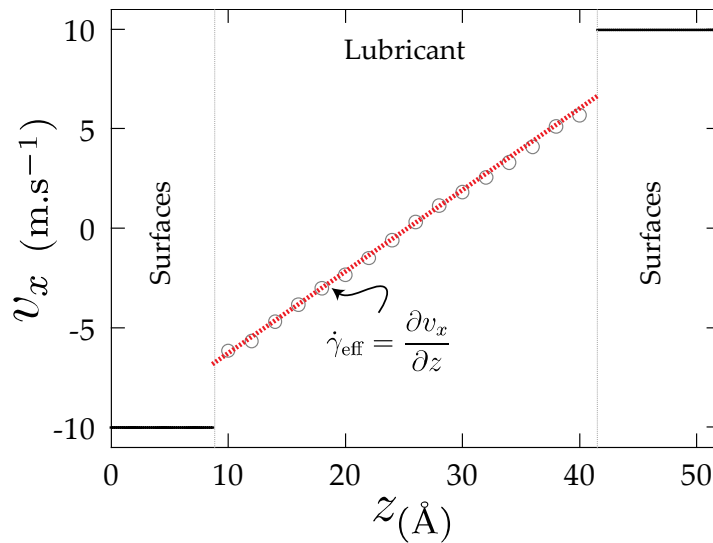


Fig. A3.5: Illustration of the calculation method of the effective shear rate.

### A3.3.2 Effective viscosity

The effective viscosity is determined as the ratio between the apparent shear stress and the effective shear rate in the center of the film:

$$(A3.5) \quad \eta_{\text{eff}} = \frac{\tau_{xz}}{\dot{\gamma}_{\text{eff}}}$$

# References

---

- [1] D. Dowson, *History of Tribology*, Longman, London, 1979.
- [2] J. Frêne, D. Nicolas, B. Degeurce, D. Berthe, M. Godet, *Lubrification Hydrodynamique: Paliers et Butées*, Eyrolles, Paris, 1990.
- [3] J. M. Georges, *Frottement, Usure, et Lubrification : La Tribologie ou Science Des Surfaces, Sciences et techniques de l'ingénieur*, Eyrolles, 2000.
- [4] O. Reynolds, On the theory of lubrication and its application to Mr. Beauchamp Tower's experiments, including an experimental determination of the viscosity of olive oil, *Philosophical Transactions of the Royal Society of London* 177 (1886) 157–234.
- [5] B. Jacobson, The Stribeck memorial lecture, *Tribology International* 36 (2003) 781–789.
- [6] A. D. Berman, J. N. Israelachvili, *Modern Tribology Handbook*, Vol. 1, CRC Press LLC, 2001, Ch. 16: Microtribology and Microrheology or Molecularly Thin Liquid Films, pp. 567–616.
- [7] T. Mang, *Lubricants and Lubrication*, Chapter 1: Lubricants in the Tribological System, 2nd Edition, Wiley, 2007.
- [8] Y. Hori, *Hydrodynamic Lubrication*, Springer-Verlag, Tokyo, 2006.
- [9] W. Habchi, A full-system finite element approach to elastohydrodynamic lubrication problems: application to ultra-low-viscosity fluids, Ph.D. thesis, MEGA, INSA de Lyon (2008).
- [10] R. W. Carpick, M. Salmeron, Scratching the surface: Fundamental investigations of tribology with atomic force microscopy, *Chemical Reviews* 97 (4) (1997) 1163–1194.
- [11] M. J. Stevens, M. Mondello, G. S. Grest, S. T. Cui, H. D. Cochran, P. T. Cummings, Comparison of shear flow of hexadecane in a confined geometry and in bulk, *Journal of Chemical Physics* 106 (17) (1997) 7303–7314.
- [12] J. N. Israelachvili, *Intermolecular and Surface Forces*, 2nd Edition, Colloid Science, Academic Press Inc, 1991.
- [13] J. V. Alsten, S. Granick, Molecular tribometry of ultrathin liquid films, *Physical Review Letters* 61 (22) (1988) 2570–2573.
- [14] P. Frantz, N. Agrait, M. Salmeron, Use of capacitance to measure surface forces. 1. measuring distance of separation with enhanced spatial and time resolution, *Langmuir* 12 (13) (1996) 3289–3294.
- [15] D. Y. C. Chan, R. G. Horn, The drainage of thin liquid films between solid surfaces, *The Journal of Chemical Physics* 83 (10) (1985) 5311–5324.

- [16] R. G. Horn, J. N. Israelachvili, Direct measurement of structural forces between two surfaces in a nonpolar liquid, *The Journal of Chemical Physics* 75 (3) (1981) 1400–1411.
- [17] H. K. Christenson, R. G. Horn, J. N. Israelachvili, Measurement of forces due to structure in hydrocarbon liquids, *Journal of Colloid and Interface Science* 88 (1) (1982) 79 – 88.
- [18] H. Christenson, R. Horn, Direct measurement of the force between solid surfaces in a polar liquid, *Chemical Physics Letters* 98 (1) (1983) 45 – 48.
- [19] H. K. Christenson, D. W. R. Gruen, R. G. Horn, J. N. Israelachvili, Structuring in liquid alkanes between solid surfaces: Force measurements and mean-field theory, *The Journal of Chemical Physics* 87 (3) (1987) 1834–1841.
- [20] H. K. Christenson, Experimental measurements of solvation forces in nonpolar liquids, *The Journal of Chemical Physics* 78 (11) (1983) 6906–6913.
- [21] J. Klein, Surface interactions with adsorbed macromolecules, *Journal of Colloid and Interface Science* 111 (2) (1986) 305 – 313.
- [22] J. N. Israelachvili, P. M. McGuiggan, Forces between surfaces in liquids, *Science* 241 (4867) (1988) 795–800.
- [23] M. L. Gee, P. M. McGuiggan, J. N. Israelachvili, A. M. Homola, Liquid to solidlike transitions of molecularly thin films under shear, *The Journal of Chemical Physics* 93 (3) (1990) 1895–1906.
- [24] A. Dhinojwala, L. Cai, S. Granick, Critique of the friction coefficient concept for wet (lubricated) sliding, *LANGMUIR* 12 (19) (1996) 4537–4542, workshop on the Physical and Chemical Mechanisms of Tribology, BAR HARBOR, ME, AUG 28-SEP 01, 1995.
- [25] S. Granick, Motions and relaxations of confined liquids, *Science* 253 (5026) (1991) 1374–1379.
- [26] H.-W. Hu, G. A. Carson, S. Granick, Relaxation time of confined liquids under shear, *Physical Review Letters* 66 (21) (1991) 2758–2761.
- [27] M. Urbakh, L. Daikhin, J. Klafter, Dynamics of confined liquids under shear, *Physical Review E* 51 (3, Part A) (1995) 2137–2141.
- [28] G. Luengo, F. Schmitt, R. Hill, J. Israelachvili, Thin film rheology and tribology of confined polymer melts: Contrasts with bulk properties, *Macromolecules* 30 (8) (1997) 2482–2494.
- [29] B. Bhushan, J. N. Israelachvili, U. Landman, Nanotribology: friction, wear and lubrication at the atomic scale, *Nature* 374 (1995) 607–616.
- [30] G. Luengo, J. Israelachvili, S. Granick, Generalized effects in confined fluids: New friction map for boundary lubrication, *Wear* 200 (1-2) (1996) 328 – 335.
- [31] E. T. Watts, J. Krim, A. Widom, Experimental observation of interfacial slippage at the boundary of molecularly thin films with gold substrates, *Physical Review B* 41 (6) (1990) 3466–3472.
- [32] A. Khurana, Numerical simulations reveal fluid flows near solid boundaries, *Physics Today* 41 (5) (1988) 17–19.
- [33] M. Mooney, Explicit formulas for slip and fluidity, *Journal of Rheology* 2 (2) (1931) 210–222.

- [34] C. J. S. Petrie, M. M. Denn, Instabilities in polymer processing, *American Institute of Chemical Engineers Journal* 22 (2) (1976) 209–236.
- [35] E. Lauga, M. P. Brenner, H. A. Stone, Microfluidics: The no-slip boundary condition, *ArXiv Condensed Matter e-prints* (0501557).
- [36] L. Bocquet, J.-L. Barrat, Flow boundary conditions from nano- to micro-scales, *Soft Matter* 3 (2007) 685–693.
- [37] A. V. Ramamurthy, Wall slip in viscous fluids and influence of materials of construction, *Journal of Rheology* 30 (2) (1986) 337–357.
- [38] S. G. Hatzikiriakos, J. M. Dealy, Wall slip of molten high density polyethylene. i. sliding plate rheometer studies, *Journal of Rheology* 35 (4) (1991) 497–523.
- [39] K. B. Migler, H. Hervet, L. Leger, Slip transition of a polymer melt under shear stress, *Physical Review Letters* 70 (3) (1993) 287–290.
- [40] Y. Zhu, S. Granick, Superlubricity: A paradox about confined fluids resolved, *Physical Review Letters* 93 (9-96101) (2004) 1–4.
- [41] M. P. Allen, D. J. Tildesley, *Computer Simulations of Liquids*, Clarendon Press, Oxford, 1987.
- [42] U. Landman, Materials by numbers: Computations as tools of discovery, *PNAS* 102 (19) (2005) 6671–6678.
- [43] J. W. Halley, *Statistical Mechanics: From First Principles to Macroscopic Phenomena*, Cambridge University Press, 2007.
- [44] W. F. Saam, C. Ebner, Classical fluid structure near solid substrates: A comparison of different theories, *Physical Review A* 17 (5) (1978) 1768–1773.
- [45] G. A. Chapela, G. Saville, J. S. Rowlinson, Computer simulation of the gas/liquid surface, *Faraday Discussions of the Chemical Society* 22.
- [46] J. E. Lane, T. H. Spurling, B. Freasier, J. W. Perram, E. R. Smith, Inconsistency of the Density-Functional Theory of adsorption when using computer simulations, *Physical Review A* 20 (5) (1979) 2147–2153.
- [47] S. Toxvaerd, The structure and thermodynamics of a solid-fluid interface, *Journal of Chemical Physics* 74 (3) (1981) 1998–2005.
- [48] F. F. Abraham, The interfacial density profile of a Lennard-Jones fluid in contact with a (100) Lennard-Jones wall and its relationship to idealized fluid/wall systems: A Monte Carlo simulation, *The Journal of Chemical Physics* 68 (8) (1978) 3713–3716.
- [49] I. K. Snook, W. van Megen, Solvation forces in simple dense fluids, *Journal of Chemical Physics* 72 (5) (1980) 2907–2913.
- [50] J. J. Magda, M. Tirrell, H. T. Davis, Molecular dynamics of narrow, liquid-filled pores, *Journal of Chemical Physics* 63 (4) (1985) 1886–1901.
- [51] I. Bitsanis, J. J. Magda, M. Tirrell, H. T. Davis, Molecular dynamics of flow in micropores, *The Journal of Chemical Physics* 87 (3) (1987) 1733–1750.
- [52] U. Heinbuch, J. Fischer, Liquid flow in pores: Slip, no-slip, or multilayer sticking, *Physical Review A* 40 (2) (1989) 1144–1146.

- [53] I. Bitsanis, S. A. Somers, H. T. Davis, M. Tirrell, Microscopic dynamics of flow in molecularly narrow pores, *The Journal of Chemical Physics* 93 (5) (1990) 3427–3431.
- [54] S. A. Somers, H. T. Davis, Microscopic dynamics of fluids confined between smooth and atomically structured solid surfaces, *The Journal of Chemical Physics* 96 (7) (1992) 5389–5407.
- [55] P. A. Thompson, M. O. Robbins, Shear flow near solids: Epitaxial order and flow boundary conditions, *Physical Review A* 41 (12) (1990) 6830–6837.
- [56] S. K. Kumar, M. Vacatello, D. Y. Yoon, Off-lattice Monte Carlo simulations of polymer melts confined between two plates, *The Journal of Chemical Physics* 89 (8) (1988) 5206–5215.
- [57] P. Padilla, S. Toxvaerd, Fluid alkanes in confined geometries, *Journal of Chemical Physics* 101 (2) (1994) 1490–1502.
- [58] I. Bitsanis, G. Hadziioannou, Molecular dynamics simulations of the structure and dynamics of confined polymer melts, *The Journal of Chemical Physics* 92 (6) (1990) 3827–3847.
- [59] M. Vacatello, D. Y. Yoon, B. C. Laskowski, Molecular arrangements and conformations of liquid n-tridecane chains confined between two hard walls, *The Journal of Chemical Physics* 93 (1) (1990) 779–786.
- [60] P. Padilla, Chemical structure effects on the equilibrium and under shear properties of thin films in confined geometries: A molecular dynamics simulation study, *The Journal of Chemical Physics* 103 (6) (1995) 2157–2168.
- [61] J. Gao, W. D. Luedtke, U. Landman, Layering transitions and dynamics of confined liquid films, *Physical Review Letters* 79 (4) (1997) 705–708.
- [62] A. Jabbarzadeh, J. D. Atkinson, R. I. Tanner, The effect of branching on slip and rheological properties of lubricants in molecular dynamics simulation of Couette shear flow, *Tribology International* 35 (2002) 35–46.
- [63] J. Gao, W. D. Luedtke, U. Landman, Structures, solvation forces and shear of molecular films in a rough nano-confinement, *Tribology Letters* 9 (2000) 3–13.
- [64] A. Jabbarzadeh, J. D. Atkinson, R. I. Tanner, Effect of the wall roughness on slip and rheological properties of hexadecane in molecular dynamics simulation of Couette shear flow between two sinusoidal walls, *Physical Review E* 61 (1) (2000) 690–699.
- [65] R. Balasundaram, S. Jiang, J. Belak, Structural and rheological properties of n-decane confined between graphite surfaces, *Chemical Engineering Journal* 74 (1999) 117–127.
- [66] P. A. Thompson, G. S. Grest, M. O. Robbins, Phase transitions and universal dynamics in confined films, *Physical Review Letters* 68 (23) (1992) 3448–3451.
- [67] A. Jabbarzadeh, P. Harrowel, R. I. Tanner, Crystal bridge formation marks the transition to rigidity in a thin lubrication film, *Physical Review Letters* 96 (206102) (2006) 1–4.
- [68] A. Jabbarzadeh, J. D. Atkinson, R. I. Tanner, Nanorheology of molecularly thin films of n-hexadecane in Couette shear flow by molecular dynamics simulation, *Journal of Non-Newtonian Fluid Mechanics* 77 (1-2) (1998) 53 – 78.
- [69] M. Schoen, S. Hess, D. J. Diestler, Rheological properties of confined thin films, *Phys. Rev. E* 52 (3) (1995) 2587–2602.

- [70] S. A. Gupta, H. D. Cochran, P. T. Cummings, Shear behavior of squalane and tetracosane under extreme confinement. iii. Effect of confinement on viscosity, *The Journal of Chemical Physics* 107 (23) (1997) 10335–10343.
- [71] J. Ding, J. Chen, J. Yang, The effects of surface roughness on nanotribology of confined two-dimensional films, *Wear* 260 (2006) 205–208.
- [72] J. Gao, W. D. Luedtke, U. Landman, Friction control in thin-film lubrication, *Journal of Physical Chemistry B* 102 (1998) 5033–5037.
- [73] A. Jabbarzadeh, J. D. Atkinson, R. I. Tanner, Wall slip in the molecular dynamics simulation of thin films of hexadecane, *The Journal of Chemical Physics* 110 (5) (1999) 2612–2620.
- [74] A. Martini, H.-Y. Hsu, N. A. Patankar, S. Lichter, Slip at high shear rates, *Physical Review Letters* 100 (206001) (2008) 1–4.
- [75] S. Toxvaerd, A new algorithm for molecular dynamics calculations, *Journal of Computational Physics* 47 (3) (1982) 444 – 451.
- [76] D. Lide (Ed.), *Handbook of Chemistry and Physics*, 85th Edition, CRC Press, 2004-2005.
- [77] G. Rollmann, A. Rohrbach, P. Entel, J. Hafner, First-principles calculation of the structure and magnetic phases of hematite, *Physical Review B* 69 (16) (2004) 165107.
- [78] S. M. Foiles, M. I. Baskes, M. S. Daw, Embedded-Atom-Method functions for the FCC metals Cu, Ag, Au, Ni, Pd, Pt, and their alloys, *Physical Review B* 33 (12) (1986) 7983–7991.
- [79] J. Kierfeld, V. Vinokur, Lindemann criterion and vortex lattice phase transitions in type-II superconductors, *Physical Review B* 69 (024501) (2004) 1–21.
- [80] D. L. Anderson, O. L. Anderson, The bulk modulus-volume relationship for oxides, *Journal of Geophysical Research* 75 (17) (1970) 3494–3500.
- [81] F. Muller-Plathe, D. Reith, Cause and effect reversed in non-equilibrium molecular dynamics: an easy route to transport coefficients, *Computational and Theoretical Polymer Science* 9 (1999) 203–209.
- [82] D. J. Evans, G. P. Morriss, *Statistical Mechanics of Nonequilibrium Liquids*, 2nd Edition, Australian National University E Press, 2007.
- [83] T. Akiyama, H. Ohta, R. Takahashi, Y. Waseda, J. ichiro Yagi, Measurement and modeling of thermal conductivity for dense iron oxide and porous iron ore agglomerates in step-wise reduction, *ISIJ International* 32 (1992) 829–837.
- [84] L. Zhang, R. Balasundaram, S. H. Gehrke, S. Jiang, Nonequilibrium molecular dynamics simulations of confined fluids in contact with the bulk, *The Journal of Chemical Physics* 114 (15) (2001) 6869–6877.
- [85] W. L. Jorgensen, J. Tirado-Rives, The OPLS forcefield for proteins. Energy minimizations for crystals of cyclic peptides and crambin, *Journal of the American Chemical Society* 110 (1988) 1657–1723.
- [86] W. D. Cornell, P. Cieplak, C. I. Bayly, I. R. Gould, K. M. Merz, D. M. Ferguson, D. C. Spellmeyer, T. Fox, J. W. Caldwell, P. A. Kollman, A second generation force field for the simulation of proteins, nucleic acids and organic molecules., *Journal of the American Chemical Society* (117) (1995) 5179–5197.

- [87] T. K. Xia, J. Ouyang, M. W. Ribarsky, U. Landman, Interfacial alkane films, *Physical Review Letters* 69 (13) (1992) 1967–1970.
- [88] A. Jabbarzadeh, R. Tanner, Thin lubricant films confined between crystalline surfaces: Gold versus mica, *Tribology International* In Press, Corrected Proof (2010) –.
- [89] A. Hamza, R. Madix, The activation of alkanes on Ni(100), *Surface Science* 179 (1) (1987) 25 – 46.
- [90] Q. Dai, A. J. Gellman, A hreels study of C1–C5 straight chain alcohols on clean and pre-oxidized ag(110) surfaces, *Surface Science* 257 (1-3) (1991) 103 – 112.
- [91] S. M. Wetterer, D. J. Lavrich, T. Cummings, S. L. Bernasek, G. Scoles, Energetics and kinetics of the physisorption of hydrocarbons on au(111), *The Journal of Physical Chemistry B* 102 (46) (1998) 9266–9275.
- [92] C. Minfray, T. L. Mogne, J.-M. Martin, T. Onodera, S. Nara, S. Takahashi, H. Tsuboi, M. Koyama, A. Endou, H. Takaba, M. Kubo, C. A. D. Carpio, A. Miyamoto, Experimental and molecular dynamics simulations of tribochemical reactions with ZDDP: Zinc phosphate-iron oxide reaction, *Tribology Transactions* 51 (2008) 589–601.
- [93] J. Gao, W. D. Luedtke, U. Landman, Origins of solvation forces in confined films, *Journal of Physical Chemistry B* 101 (1997) 4013–4023.
- [94] A. Martini, Y. Liu, R. Snurr, Q. Wang, Molecular dynamics characterization of thin film viscosity for EHL simulation, *Tribology Letters* 21 (3) (2006) 217–225.
- [95] M. Lupkowski, F. van Swol, Ultrathin films under shear, *Journal of Chemical Physics* 95 (3) (1991) 1995–1998.
- [96] S. Y. Liem, D. Brown, J. H. R. Clarke, Investigation of the homogeneous-shear nonequilibrium-molecular-dynamics method, *Phys. Rev. A* 45 (6) (1992) 3706–3713.
- [97] R. Khare, J. de Pablo, A. Yethiraj, Molecular simulation and continuum mechanics study of simple fluids in non-isothermal planar Couette flows, *The Journal of Chemical Physics* 107 (7) (1997) 2589–2596.
- [98] J. H. Lienhard-IV, J. H. Lienhard-V, *A Heat Transfer Textbook*, 3rd Edition, Phlogiston Press, Cambridge Massachusetts, 2008.
- [99] S. Maruyama, T. Kimura, A study on thermal resistance over a solid-liquid interface by the molecular dynamics method, *Thermal Science and Engineering* 7 (1) (1999) 63–68.
- [100] A. Martini, *Molecular dynamics simulation of engineering applications*, Doctoral School IJTC 2008 Miami (2008).
- [101] M. O. Robbins, M. H. Müser, *Modern Tribology Handbook*, Vol. 1, CRC Press LLC, 2001, Ch. 20: Computer Simulations of Friction, Lubrication, and Wear, pp. 717–765.
- [102] T. K. Xia, U. Landman, Structure and dynamics of surface crystallization of liquid n-alkanes, *Physical Review B* 48 (15) (1993) 11313–11316.
- [103] D. Kamei, H. Zhou, K. Suzuki, K. Konno, S. Takami, M. Kubo, A. Miyamoto, Computational chemistry study on the dynamics of lubricant molecules under shear conditions, *Tribology International* 36 (2003) 297–202.
- [104] N. V. Priezjev, S. M. Troian, Molecular origin and dynamic behavior of slip in sheared polymer films, *Physical Review Letters* 92 (1) (2004) 018302.

- [105] J. Gao, W. D. Luedtke, U. Landman, Structure and solvation forces in confined films: Linear and branched alkanes, *The Journal of Chemical Physics* 106 (10) (1997) 4309–4318.
- [106] R. Khare, J. de Pablo, A. Yethiraj, Rheological, thermodynamic, and structural studies of linear and branched alkanes under shear, *The Journal of Chemical Physics* 107 (17) (1997) 6956–6964.
- [107] L. I. Kioupis, E. J. Maginn, Rheology, dynamics, and structure of hydrocarbon blends: a molecular dynamics study of n-hexane/n-hexadecane mixtures, *Chemical Engineering Journal* 74 (1999) 129–146.
- [108] H. Spikes, The history and mechanisms of ZDDP, *Tribology Letters* 17 (2004) 469–489(21).
- [109] A. Naveira-Suarez, M. Grahn, R. Pasaribu, R. Larsson, The influence of base oil polarity on the tribological performance of zinc dialkyldithiophosphate additives, in: ICAT376, 2008.
- [110] R. W. Hockney, J. W. Eastwood, *Computer simulation using particles*, Taylor & Francis Inc., Bristol, 1988.
- [111] P. H. Hünenberger, Thermostat algorithms for molecular dynamics simulations, *Advances in Polymer Science* 173 (2005) 105–149.
- [112] T. Schneider, E. Stoll, Molecular-dynamics study of a three-dimensional one-component model for distortive phase transitions, *Phys. Rev. B* 17 (3) (1978) 1302–1322.
- [113] J. C. Tully, Dynamics of gas–surface interactions: 3D generalized Langevin model applied to FCC and BCC surfaces, *The Journal of Chemical Physics* 73 (4) (1980) 1975–1985.
- [114] J. Blomer, A. Beylich, Molecular dynamics simulation of energy accommodation of internal and translational degrees of freedom at gas–surface interfaces, *Surface Science* 423 (1999) 127–133.
- [115] H. Berro, N. Fillot, P. Vergne, Hybrid diffusion: an efficient method for kinetic temperature calculation in molecular dynamics simulations of confined lubricant films, *Tribology Letters* 37 (1) (2010) 1–13.

## Publications

Berro H., Fillot N., Vergne P., "Hybrid Diffusion: An Efficient Method for Kinetic Temperature Calculation in Molecular Dynamics Simulations of Confined Lubricant Films", *Tribology Letters*, vol. 37, 1, January 2010, p. 1-13, <http://dx.doi.org/10.1007/s11249-009-9484-9>

Berro H., Fillot N., Vergne P., "Molecular Dynamics simulation of surface energy and ZDDP effects on friction in nano-scale lubricated contacts", *Tribology International*, vol. 43, 10, October 2010, p. 1811-1822, <http://dx.doi.org/10.1016/j.triboint.2010.02.011>

Berro H., Fillot N., Vergne P., "Towards an appropriate modelling of energy balance in molecular dynamics simulations of confined lubrication films", *ASME/STLE Int. Joint Tribology Conference IJTC2008*, 20-22 October 2008, Miami (Florida), CD Rom, paper IJTC2008- 71162, ISBN 978-0-7918-3837-2

Berro H., Fillot N., Vergne P., Naveira-Suarez A., Zaccheddu M., Pasaribu R., "Nanoscale simulation of additive effects on friction in a lubricated contact", presented at the *36<sup>th</sup> Leeds-Lyon Symposium on Tribology "Multi-Facets of Tribology"*, Lyon 1-4 September 2009

Berro H., Fillot N., Vergne P., Tokumasu T., Ohara T., Kikugawa G., "The Effect of Different Thermostating Techniques on Friction and Dissipation in Molecular Dynamics Simulations of Confined Lubricant Films", *World Tribology Conference WTC2009*, Kyoto, 6-11 September 2009, proceedings p. 622

Fillot N., Berro H., Habchi W., Vergne P., "Complementary scales and models to better describe lubricated contacts", Keynote Presentation at the *World Tribology Conference WTC2009*, Kyoto, 6-11 September 2009, proceedings p. 825

Berro H., Fillot N., Vergne P., "Surface corrugation: a relevant concept to assess lubricated friction at the nanometer scale", oral presentation at the *Cargèse School "Theoretical modeling and experimental simulation in Tribology"*, Institut d'Etudes Scientifiques de Cargèse, 22-26 March 2010

Fillot N., Berro H. and Vergne P., "Surface Corrugation: a Relevant Concept to Assess Lubricated Friction at the Nanometer Scale", to be presented at the *ASME/STLE Int. Joint Tribology Conference IJTC2010*, 17-20 October 2010, San Francisco (California)

Berro H., Tokumasu T., Ohara T., Kikugawa G., Fillot N. and Vergne P., "Assessment of different thermostating techniques in the simulation of molecular lubrication", to be presented at the *Collaborative Research Forum AFI/TFI, 7<sup>th</sup> International Conference on Flow Dynamics*, Sendai, November 1-3, 2010

Berro H., Fillot N., Vergne P., "The role of interfaces in the molecular dynamics simulation of molecular lubrication", Invited Talk at the session *"Molecular and Nanoscale Phenomena in Fluids and Interfaces"*, *7<sup>th</sup> International Conference on Flow Dynamics*, Sendai, November 1-3, 2010

Berro H., Fillot N. and Vergne P., "Heat dissipation in MD simulation of nano-scale lubrication", to be presented at the *ASIATRIB 2010 "Frontiers in Tribology – knowledge & friendship"*, December 5-9, 2010, Perth, Western Australia.

## FOLIO ADMINISTRATIF

### THESE SOUTENUE DEVANT L'INSTITUT NATIONAL DES SCIENCES APPLIQUEES DE LYON

NOM : BERRO

DATE de SOUTENANCE : 11/10/2010

Prénoms : Hassan

TITRE : Approche Dynamique Moléculaire de la Lubrification à l'Echelle Nanométrique

NATURE : Doctorat

Numéro d'ordre : 2010- ISAL-0084

Ecole doctorale : MEGA

Spécialité :

Cote B.I.U. - Lyon : T 50/210/19 / et bis

CLASSE :

RESUME :

Une approche numérique basée sur des simulations Dynamique Moléculaire a été développée dans le but d'étudier les mécanismes locaux de la lubrification à l'échelle nanométrique. Les éléments du modèle ont été présentés et caractérisés afin de reproduire les propriétés les plus réalistes des matériaux et de l'interface du contact. En raison de leur relation étroite avec le frottement, les méthodes de dissipation énergétique pour la dynamique moléculaire ont été revisitées et des recommandations ont été proposées pour le choix d'une méthode correcte adaptée aux différentes conditions opératoires. Pour le régime de fort cisaillement et donc de forte dissipation, une nouvelle méthode mieux fondée physiquement a été développée, combinant simplicité et vitesse de calcul.

Le modèle a ensuite été utilisé pour étudier les effets liés à la structure moléculaire des surfaces et du lubrifiant confiné. Afin d'étudier différentes surfaces tribologiques, une méthode originale a été utilisée pour mesurer quantitativement les potentiels physiques d'adsorption et de corrugation. Ces propriétés influencent directement la stratification dans le film et son glissement à l'interface solide. D'autre part, l'influence de la forme moléculaire du lubrifiant sur sa performance tribologique a été étudiée, en solution pure et en mélange, pour les surfaces mouillantes et non-mouillantes. Les simulations moléculaires ont permis une analyse locale du frottement lubrifié à l'échelle moléculaire et ainsi une meilleure compréhension des interactions physiques entre les éléments mis en jeu.

MOTS-CLES : TRIBOLOGIE, FROTTEMENT, LUBRIFICATION, DISSIPATION D'ENERGIE, DYNAMIQUE MOLECULAIRE

Laboratoire (s) de recherche : Laboratoire de Mécanique des Contacts et des Structures (LaMCoS)

Directeurs de thèse: Dr. Philippe VERGNE  
Dr. Nicolas FILLOT

Président de jury :

Composition du jury : Prof. Lydéric BOCQUET  
Prof. Patrice CHANTRENNE  
Dr. Nicolas FILLOT  
Prof. Jean-François MOLINARI  
Prof. Susan SINNOTT  
Dr. Philippe VERGNE  
Dr. Maurizio Zaccheddu